ASSESSMENT OF FLEXURAL BEHAVIOUR OF CONCRETE BEAM WITH CORRODED STEEL REBAR USING ACOUSTIC EMISSION TECHNIQUE

AHMAD ZAKI

FACULTY OF ENGINEERING
UNIVERSITY OF MALAYA
KUALA LUMPUR

2018

ASSESSMENT OF FLEXURAL BEHAVIOUR OF CONCRETE BEAM WITH CORRODED STEEL REBAR USING ACOUSTIC EMISSION TECHNIQUE

AHMAD ZAKI

THESIS SUBMITTED IN FULFILMENT OF THE REQUIREMENTS FOR THE DEGREE OF DOCTOR OF PHILOSOPHY

FACULTY OF ENGINEERING
UNIVERSITY OF MALAYA
KUALA LUMPUR

2018

UNIVERSITI MALAYA

ORIGINAL LITERARY WORK DECLARATION

Name of Candidate**: Ahmad Zaki**

Registration/Matric No**: KHA140036**

Name of Degree**: PhD of Engineering**

Title of Project Paper/Research Report/Dissertation/Thesis ("this Work")**:**

Assessment of flexural behaviour of concrete beam with corroded steel rebar using acoustic emission technique

Field of Study**: Structural Engineering and Materials**

I do solemnly and sincerely declare that:

(1) I am the sole author/writer of this Work;
(2) This Work is original;
(3) Any use of any work in which copyright exists was done by way of fair dealing and for permitted purposes and any excerpt or extract from, or reference to or reproduction of any copyright work has been disclosed expressly and sufficiently and the title of the Work and its authorship have been acknowledged in this Work;
(4) I do not have any actual knowledge nor do I ought reasonably to know that the making of this work constitutes an infringement of any copyright work;
(5) I hereby assign all and every rights in the copyright to this Work to the University of Malaya ("UM"), who henceforth shall be owner of the copyright in this Work and that any reproduction or use in any form or by any means whatsoever is prohibited without the written consent of UM having been first had and obtained;
(6) I am fully aware that if in the course of making this Work I have infringed any copyright whether intentionally or otherwise, I may be subject to legal action or any other action as may be determined by UM.

Candidate's Signature Date

Subscribed and solemnly declared before,

Witness's Signature Date

Name:
Designation:

ASSESSMENT OF FLEXURAL BEHAVIOUR OF CONCRETE BEAM WITH CORRODED STEEL REBAR USING ACOUSTIC EMISSION TECHNIQUE

ABSTRACT

Corrosion of reinforced concrete (RC) structures has been one of the major causes of structural failure. Early detection of the corrosion could help limit the location and the extent of necessary repair, as well as reduce the cost associated with rehabilitation work. Non-destructive testing (NDT) method has been found to be useful for corrosion assessments of civil infrastructures, where the effect of steel corrosion can be assessed effectively. The acoustic emission (AE) technique, one of the NDT methods, is more effective for assessing steel corrosion in the RC structures. The AE technique successfully monitors and analyse energy signals released from the fracture of the concrete matrix by steel corrosion activity using AE sensors placed on the concrete surfaces. The main objective of this study is to utilize the AE technique for flexural behaviour assessment of corroded RC beams under load testing. Three different types of experiment sets were performed for evaluation of corroded specimens using the AE technique. During the experiments, the corroded specimen was flexurally loaded together with data acquisition by AE technique. The data obtained were processed and AE parametric-based analysis was carried out. The first experiment was carried out subjected to monotonic loading by looking into the primary AE signals. Thereafter, based on the experience gained in the first experiment, the second and third experiments were utilized for small scales of corroded specimens subjected to cyclic load and monotonic loading, for secondary and primary AE signals, respectively. The second experiment was pre-corrosion beam specimens while the third experiment was post-corrosion beam specimens. The primary AE signal is typically due to changes of concrete material such as crack growth and fracture. The secondary AE signal is related to activity that was not part of original fabrication such as friction between the interface of steel reinforcement and concrete. The AE technique of the first experiment was successfully conducted for fracture mechanisms monitoring of the corroded specimen under flexure load. The RA value of AE parameters was used to evaluate the fracture mode in the corroded specimens. The Control and LC specimens exhibited the highest RA value at the final damage stage, however, the HC specimen exhibited the highest RA value at the damage stage 2. Therefore, the highest RA value was associated with the shear cracks which further explain that high intensity events occurred at the tension reinforcement area in the concrete. Moreover, the index of damage (ID) derived from the AE energy parameters obtained during the damage stage 1 was found to be useful as an indicator for evaluating the extent of corrosion damage of beam specimens at initial loadings. For the result of the second and third experiments, the primary AE parameters include the AE hits, RA value, AF, *I*b-value, historic index (Hi), and severity index (Sr) of AE data were successfully introduced to assess the flexure behavior of the corroded beam specimen. For secondary AE, the cumulative signal strength (CSS) ratio of experiment 3 increases from 17.42 % to 116.22 % with the increase in corrosion level. It indicates that the occurrence of damage was generated due to loss in cross-section (mass loss) of the specimen before first visible crack occurs. The experiments conducted in this research helped to understand the flexural behavior of the corroded specimen under loading test using the AE technique. The secondary AE result of the second and third experiments were successfully found as the indicator of the damage occurrence of the corroded specimen at an early stage of the damage.

Keywords: Reinforced concrete, corrosion, non-destructive testing, acoustic emission, corrosion assessment

PENILAIAN KELAKUAN LENTURAN KONKRIT DENGAN KAKISAN TETULANG MENGGUNAKAN TEKNIK PELEPASAN AKUSTIK

ABSTRAK

Kakisan struktur konkrit bertetulang (RC) telah menjadi salah satu punca utama kegagalan struktur. Pengesanan awal kakisan boleh membantu mengehadkan lokasi dan sejauh mana pembaikan yang diperlukan, serta mengurangkan kos yang berkaitan dengan kerja pemulihan. Kaedah ujian tidak merosakkan (NDT) telah didapati berguna untuk penilaian kakisan infrastruktur awam, di mana kesan kakisan keluli dapat dinilai dengan berkesan. Teknik AE, salah satu daripada kaedah NDT, lebih berkesan untuk pemantauan kakisan dan menilai kakisan keluli dalam struktur RC kerana keupayaannya untuk mengesan kakisan keluli. Teknik AE berjaya memantau dan menganalis isyarat tenaga yang dikeluarkan dari matriks konkrit yang patah disebabkan oleh aktiviti kakisan keluli menggunakan sensor AE yang diletakkan di permukaan konkrit. Objektif utama kajian ini adalah untuk menggunakan aplikasi teknik AE untuk penilaian tegang lenturan rasuk RC berkarat di bawah ujian beban lenturan. Tiga jenis eksperimen yang berbeza dilakukan untuk penilaian kakisan rasuk RC menggunakan teknik AE. Semasa eksperimen, RC berkarat telah dibebankan secara lenturan bersama dengan pemerolehan data oleh teknik AE. Data yang diperoleh telah diproses dan analisis berasaskan parametrik AE telah dijalankan. Eksperimen pertama dilakukan untuk pemantauan AE bagi RC berkarat yang dikenakan beban monotonik dengan melihat kepada isyarat utama AE. Selepas itu, berdasarkan pengalaman yang diperolehi dalam eksperimen pertama, eksperimen kedua dan ketiga digunakan untuk RC berkarat yang berskala kecil tertakluk kepada beban berkitar dan beban monotonik, untuk masing-masing isyarat sekunder dan utama AE. Ekperimen kedua adalah pre-corrosion rasuk dan eksperimen ketiga adalah post-corrosion rasuk. Isyarat utama AE biasanya disebabkan oleh perubahan kekal bahan konkrit seperti pertumbuhan retak dan patah. Isyarat sekunder AE berkaitan dengan aktiviti yang bukan sebahagian daripada fabrikasi asal seperti geseran antara permukaan tetulang keluli dan konkrit.Keputusan ujian eksperimen pertama menunjukkan bahawa tingkah laku rasuk di bawah beban lentur menggunakan teknik AE telah berjaya dilaksanakan. Nilai parameter RA dari teknik AE digunakan untuk menilai mod patah dalam rasuk. Nilai RA tertinggi diperolehi dari peringkat kerosakan terakhir (untuk spesimen Kawalan dan LC) dan kerosakan tahap 2 (untuk spesimen HC) dikaitkan dengan retakan ricih yang menunjukkan bahawa kejadian intensiti tinggi berlaku dalam konkrit di kawasan tetulang tegangan. Selain itu, indeks kerosakan (ID) yang diperoleh daripada parameter AE, semasa peringkat pertama kerosakan didapati berguna sebagai penunjuk untuk tahap kerosakan kakisan rasuk pada pembebanan awal. Bagi hasil eksperimen kedua dan ketiga, AE utama termasuk AE hit, RA value, AF, *I*b-value, historic indeks (Hi), dan indeks keterukan (Sr) data AE telah berjaya diperkenalkan untuk menilai tingkah laku lenturan rasuk RC berkarat. Untuk AE sekunder, kekuatan isyarat kumulatif (CSS) daripada eksperimen 3 meningkat daripada 17.42 % hingga 116.22 % dengan kenaikan paras kakisan. Ia menunjukkan bahawa berlakunya kerosakan yang terhasil akibat kehilangan keratan rentas (kehilangan jisim) sebelum retakan nampak pertama berlaku. Eksperimen yang telah dijalankan membantu memahami perilaku lenturan bagi rasuk di bawah beban lenturan menggunakan teknik AE. Keputusan sekunder AE pada eksperimen kedua dan ketiga didapati sebagai penunjuk berlakunya kerosakan rasuk berkarat pada peringkat awal kerosakan.

Kata kunci: Konkrit bertetulang, kakisan, ujian tidak merosakkan, pelepasan akustik, penilaian kakisan

ACKNOWLEDGEMENTS

In the name of Allah, the most compassionate, the most merciful. I would like to express my gratitude to the following people and organization for their help and valuable contribution to the completion of this thesis. First and foremost, I would like to thank Assoc. Prof. Dr. Zainah Ibrahim, Dr. Chai Hwa Kian and Prof. Dr. Dimitrios G. Aggelis their invaluable supervisory support and guidance during the duration of this study. I would also like to thank Tan Jun Ying, Mei Leng, Maria, Omar, Dr. Lee, Liu Kit Fook, Dr. Pahjehpoor, and Dr. Arash for their help during preparing the experiments. I am greatly indebted to the University of Malaya for its financial support under the High Impact Research (HIR), grant No. UM.C/625/1/HIR/MOHE/ENG/54 and the Postgraduate Research Fund (PPP), grant No. PG164-2015A. I would like to thank technicians in Concrete Technology and Timber Laboratory for friendly conservation and insightful advice during sample preparation and data acquisition in this study. Most importantly, I'd like to thank my wonderful wife, Dr. Yessi Jusman, for her constant love, for motivating me in loving and caring ways, for supporting and helping me in this study, and for the happiness she has brought into my life during our Ph.D Journey with our kids Fatin Sahira Ahmad, Firas Faiq Ahmad, Filzah Delisha Ahmad, and Faruq Umar Ahmad. My special acknowledgments for my brothers M. Abrar and M. Hanif for their love and hope which encourage me all along without hesitation. I would especially like to thank Dr. dr. Susiana Tabrani, M.Pd, Dr. Arisman Adnan, team management, and lecturer and staff from Universitas Abdurrab, Pekanbaru, Indonesia for the support. Finally, I would like to express my greatest appreciation to my Ph.D journey friends in Forum Ukhuwah Studi Islam (FUSI) in UM (especially Dr. Asmuliadi Lubis, Dr. Choirin, Abdul Haris, Hadi, Zaki, Ashdiq, Ryan Kurnia, Sohenuddin, Kukuh, Muliadi, Dodi, Rohim, Suhaeri, Farah, Mirta, Ira, and Fitri) and thanks to valuable supports from my halaqoh members.

DEDICATION

To my (late) mother and (late) father whose love is the eternal motive of my life.

TABLE OF CONTENTS

LIST OF FIGURES

LIST OF TABLES

LIST OF SYMBOLS AND ABBREVIATIONS

Δ m	Mass of steel consumed
M	Atomic or molecular weight of metal
I	Current
t	Time Applied
z	Ionic charge
F	Faraday’s constant
N	Number of AE emission (referred to as “hits”) up to time t
S_{0i}	Signal strength of the *i*th event
K, *J*	Empirical constants based on the material under investigation
α	Empirical constants
μ	Mean amplitude
Ơ	Standard deviation
α1	the coefficient related to the smaller amplitude
α2	coefficient related to the fracture level
Ϭ	Stress
ε	Strain
Ml	the mass loss (%)
Mi	the mass of non-corroded specimen (g)
Mf	the mass of corroded specimen (g)
Rct	polarization resistance
RΩ	ohmic resistance
Cdl	double layer capacitance
Rn	noise resistance
σV	standard deviation for the potential
σI	standard deviation for the current obtained by statistical analysis of the noise data
λB	Bragg wavelength
M	Richter magnitude of the event
N	Incremental frequency, “a” is an empirical constant
b	b-value
Xˆ∈ Rdxn	the data matrix in which the columns are training samples

Xˆ_c	the data matrix of training samples belonging to the class c
m	the mean vector of all training samples
mc	the mean vector of training samples belonging to the class c
T	denotes matrix transpose
NDT	Non-destructive testing
RC	Reinforced concrete
AE	Acoustic emission
HCP	Half-cell Potential
GPM	Galvanostatic Pulse Method
EN	Electrochemical Noise
UPV	Ultrasonic Pulse Velocity
IE	Impact Echo
EM	Electromagnetic
FBG	Fibre Bragg Grating
IRT	InfraRed Thermography
GPR	Ground Penetrating Radar
ASTM	American Society of Testing Materials
BS	British Standard
SHM	Structural health monitoring
DC	Direct current
SiGMA	Simplified Green’s functions for moment tensor analysis
IA	Intensity analysis
Hi	Historic index
Sr	Severity
CSS	Cumulative signal strength
OPC	Ordinary Portland Cement
NaCl	Sodium chloride
*i*b-value	Improved b-value
ID	Index of Damage
MPa	Mega Pascall
GPa	Giga Pascall
kN	Kilo Newton
MHz	Mega Hertz
dB	Decibels

ABS	Absolute Energi
AF	Average Frequency

CHAPTER 1: INTRODUCTION

1.1 Introduction

Reinforced concrete (RC) structures have been used in a great variety of building and civil engineering works since the last century. RC structures have high tensile and compressive strength. In addition, the RC structures are effective for various ideal shapes, sizes, and forms, besides being relatively cheap in comparison to other structural materials and systems. Based on their potential, RC structures have been proven to be a reliable structural system with very good durability performance. However, deterioration such as corrosion, cracks, honeycombs and etc. which are caused by environment, inadequate planning, wrong estimation, and bad workmanship affects the durability of the RC structures. In addition, the deterioration severely affects the service life and maintenance costs of the RC structures.

Repair of deteriorated structures is nearly as important as new constructions. It is reported that the costs of repair and maintenance of the corroded RC structures exceed billions of dollars per year (Song. & Shayan, 1998). The costs vary depending on the conditions of RC structures including the cause of damage, level of damage, and the effect of damage on structural behavior (Almusallam, 2001). Therefore, a reliable inspection method is required at an early stage before the functionality of a structure is seriously damaged due to the deterioration. The inspection method usually provides information about the present condition of the structures, so that their future performance can be predicted.

NDT method is one of many inspection methods for steel corrosion monitoring in RC structures. For new structures, the principal applications of the NDT methods are likely to quality control of the concrete conditions, while in old structures, the methods expected to provide the needed feedback in monitoring, detection, and identification of the damage (Büyüköztürk, 1998). Recently, various NDT methods have been implemented for steel corrosion monitoring in the RC structures. They are classified into six main categories as follows: visual inspection, electrochemical methods (i.e. half-cell potential (HCP)), electromagnetic (EM) methods (i.e. ground penetrating radar (GPR)), infrared thermography (IRT) method, optical sensing method (i.e. fiber Bragg grating (FBG)), and elastic wave methods (i.e. ultrasonic pulse velocity (UPV), acoustic emission (AE), and impact echo (IE)).

However, the NDT methods have some limitations, such as visual inspection can only give information pertaining to the presence of corrosion damage in advanced stage, the GPR and IRT only presents the qualitative interpretation for assessing the corrosion damage, the FBG method only conducts localized inspection of steel corrosion in the RC structures, the UPV method needs for advanced study of steel corrosion monitoring in the RC structures, the main application of the IE method is detection of voids and delamination in the RC structures.

The AE technique is more effective for corrosion monitoring and assessing steel corrosion in RC structures due to its capability to detect steel corrosion. The AE technique successfully monitors and analyses energy signals released from the fracture of the concrete matrix by steel corrosion activity by AE sensors placed on the concrete surface. The AE parameters such as accumulated hits, signal strength, and energy were successfully used to identify and characterize the process of steel corrosion in the RC structures (Yoon et al., 2000; Ohtsu & Tomoda, 2007a; Ohtsu & Tomoda, 2007b; Ohtsu & Tomoda, 2008a; Kawasaki et al., 2010). The AE sources were also classified in terms of RA value and average frequency (AF) to distinguish the type of failure. Besides, the *b*-value and *Ib*-value of AE amplitude distribution were also proposed for assessing the damage severity in the RC structures (Ohtsu & Tomoda, 2007b; Kawasaki et al., 2013; Behnia et al., 2014a; ElBatanouny et al., 2014b). The use of AE technique enables localization of steel corrosion damage in addition to detecting micro- and macro-cracking (Leelalerkiet et al., 2005; Aggelis et al., 2011; Behnia et al., 2014b).

In this study, the AE technique is proposed to monitor and evaluate the corroded beam specimens subjected to flexural loading. In order to characterize the damage of the corroded beam specimens, the AE parameters, namely AE hits, RA value and AF, *I*b-value and etc. have been carried out. Furthermore, the examination of secondary AE signal, namely CSS and *I*b-value were also conducted to evaluate the corroded beam specimens subjected to flexural loading.

1.2 Problem Statements

Steel corrosion is a global problem that leads to deterioration in the RC structures. Damage induced by steel corrosion usually requires proper repair, followed by maintenance. Furthermore, NDT method is almost a prerequisite for an efficient and cost-effective rehabilitation of corroded RC structures which was one of the major considerations in this study. The AE technique has become a valuable method for monitoring of RC structures over the past few years. Previous studies have shown the applicability of the AE technique for monitoring and detecting the steel corrosion in the RC structures. However, there is no guarantee that the AE technique can be easily implemented to the RC structures under flexural test, particularly for corroded RC structures in which the level of uncertainty is considerably high. In addition, limited studies have been attempted to evaluate the flexural behaviour of corroded RC structures under loading test using the AE technique. Therefore, the application of the AE technique to assess overall flexural behaviour of the corroded RC structures under loading test is required. For instance, AE data variation such as primary and secondary AE with respect to different corrosion level of the RC structures has not been investigated yet. So far, there are also limited studies in applying the AE technique to corroded RC structures at an early stage of damage. To overcome this shortcoming, the importance of developing a reliable methodology for assessment the flexural behaviour of corroded RC structures under cyclic load at an early stage is required.

1.3 Objectives of the study

The main objective of the study is to develop an NDT scheme for corroded RC beams using the AE technique. The specific objectives of the study are as follows:

1. To analyze the fracture mechanisms of corroded RC beams using AE technique under loading test.
2. To characterize the damage in the corroded RC beams using AE technique by primary and secondary AE.
3. To investigate the two factors contributing to the loss of concrete strength by steel corrosion of RC beams, i.e. loss of cross section (mass loss) and loss of ultimate strength (bond strength).
4. To establish statistical and numerical signal processing for identification and quantification of corroded RC beams with the aid of the AE parameters.

1.4 Scope and Limitation of the Research

This study consists of three sets of experimental works which are experiments 1, 2, and 3. The experiment 1 is post-corrosion specimen while the experiment 2 and 3 with the same batch of concrete casting are pre-corrosion and post-corrosion specimens, respectively. The steel corrosion process of the beam specimens were accelerated using the impressed current technique. Monitoring of the flexural behaviour of the corroded concrete beams using acoustic emission technique under loading test was performed. This research does not include the assessment of corrosion process of the beam specimens as there are many established studies in applying the AE technique for assessing the corrosion process in the beam specimens (i.e. Yoon et al., 2000; Ohtsu & Tomoda, 2007a; Ohtsu & Tomoda, 2007b; Ismail et al., 2008; Ohtsu & Tomoda, 2008b; Kawasaki et al., 2010; Calabrese et al., 2013b; Kawasaki et al., 2013; Yu et al. 2014).

1.5 Significance of the Research

Previous researchers used AE technique to detect steel corrosion in the RC structures. However, this application does not simulate the actual conditions in the field where the RC structures are normally externally loaded. This research proposed the AE parameters (e.g. RA value, AF, *I*b-value, signal strength, and etc.) for assessing of the corroded RC beam specimens under flexural loading test. This study determined the fracture mechanisms and indicated an early damage of the corroded RC beam specimens. It is known that different levels of corrosion of the RC beam specimens will have different failure properties, then the variations in fracture mechanisms must be manifested in the AE response of the different beam specimens. This hypothesis was tested through the quantitative analysis of AE activity in the RC beam specimens of varying level corrosion. This analysis produced fracture mechanisms that could be compared to the specimens' bulk fracture response. In addition, the application of AE technique for evaluating the corroded RC structures at an early stage is needed, so that an early warning can be given to allow for repair work before the structural RC element is seriously damaged and the functionality is lost due to steel corrosion in the RC structures. This effective corrosion assessment method will reduce the maintenance costs by early repairing works earlier as well as saving lives.

1.6 Thesis Outline

This thesis is presented in a conventional format and comprises of 7 chapters. Chapter one briefly introduces the characteristics of the RC structures and the current state of AE technique to monitor these structures. The principal issues which still suffer from a lack of sufficient information were listed for which relevant objectives were considered in this study.

Chapter two provides a comprehensive exploration of the general existing literature review of NDT for corrosion monitoring and application of AE technique for corrosion monitoring to show the trend and direction of studies in this field. This chapter is a part of a review paper published in an ISI journal (Sensors).

Chapter three describes the materials and methodologies of three different experiments through which the objectives of this research were studied.

Chapter four discusses the results and analysis associated with the first experiments. The first test conducted the study of fracture mechanisms of corroded concrete beams subjected to flexural loading using the AE technique, which addresses the objectives of 1, 2 and 4. The first experiment is a part of a research paper published in an ISI journal (Construction and Building Materials).

Chapter five and six present the results, analysis, and discussions associated with the second and third experiments. The second experiment studies about pre-corrosion concrete prisms while the third experiment study about post-corrosion concrete prisms. The second and third test carried out a study of damage classification for corroded concrete prisms of the AE-based parameters. The corroded concrete prisms subjected to cyclic and monotonic flexural loading, which also addresses the objectives of 1 to 4.

Chapter seven draws the final conclusions and recommendations for future study.

CHAPTER 2: LITERATURE REVIEW

2.1 Corrosion of Reinforced Concrete Structures

Reinforced concrete (RC) structures have been utilized widely throughout the world and they are exposed to different exposure and climatic conditions. In RC structures, the concrete provides reinforcing steel with excellent corrosion protection under normal conditions. Steel reinforcement remains in the passive state in a highly alkaline environment with pH above 13 (Neville, 1996). This highly alkaline environment is achieved as a result of the hydration process of cement releasing calcium hydroxide as one of the hydration products. Under these high alkalinity conditions, steel reinforcement in concrete is normally passive and stable as a thin passive oxide layer is developed on the surface of the reinforcement, hence providing protection to the reinforcement (Page & Treadaway, 1982).

Corrosion of steel reinforcement is a worldwide problem that affects the durability and integrity of RC structures. Corrosion primarily occurs when steel reinforcement is placed too close to the concrete surface in a situation of insufficient concrete cover or due to poor quality of the concrete cover. Steel corrosion happens when the reinforcement is oxidized in the presence of moisture. This could happen as a result of depassivation of the passive oxide layer surrounding the reinforcement. Depassivation could occur as a result of a reduction in alkalinity of concrete due to carbonation. In addition, the presence of chloride could induce localized damage to the passive oxide layer. Once the passive layer loses its protective ability, corrosion could initiate with the presence of moisture and oxygen (Neville, 1996).

2.1.1 Factor Affecting Steel Corrosion

Once steel corrosion of the concrete structure is initiated, cracking, spalling and delamination of concrete cover could occur as the corrosion product is having a greater volume than the good steel reinforcement. The expansive pressure generated by the increase in steel reinforcement volume induces cracking, spalling and possibly also delamination of the concrete cover zone (Figure 2.1).

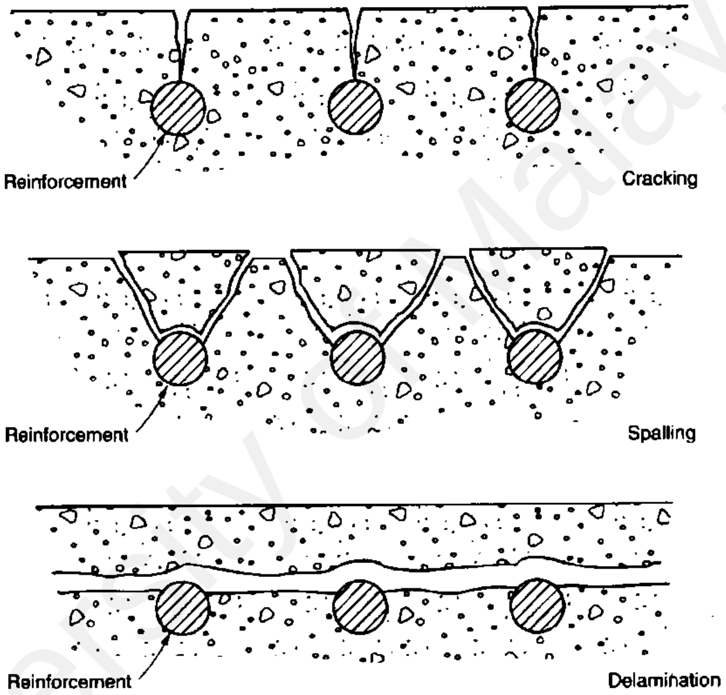

Figure 2. 1: Concrete deterioration process as a result of steel corrosion (Neville, 1996)

Carbonation is a reaction of the alkalis in concrete with carbon dioxide in the air. Carbonation in itself does not cause deterioration of concrete but it has important effects on the durability of RC structures. It gradually reduces the alkalinity of the concrete (pH value). The reduction in the pH value to certain levels may cause commencement of steel corrosion, loss of passivity of concrete against steel corrosion, and catastrophic reinforcement corrosion (Ahmad, 2003), as indicated in Table 2.1. The deterioration rate of concrete due to carbonation depends on the thickness and permeability of the concrete cover, type of binder, curing, density, water cement-ratio, and environmental effects such as temperature, relative humidity, and etc. (Parameswaran et al., 2008).

Tabel 2. 1: State of reinforcement corrosion at various pH levels (Ahmad, 2003)

pH of concrete	State of reinforcement corrosion
Below 9.5	Commencement of steel corrosion
At 8.0	Passive film on the steel surface disappears
Below 7	Catastrophic corrosion occurs

The carbon dioxide diffuses from the atmosphere into the capillary pores of the concrete and combines with water forming carbonic acid which then reacts with the alkali hydroxide, sodium, potassium and calcium, forming carbonates. Since the concentration of calcium hydroxide in normal concrete is usually higher than the concentration of the other hydration products, the reaction of CO_2 with $Ca(OH)_2$ predominates, and the carbonation process could simply be described by the following chemical reaction as in Equation 2.1:

$$CO_2 + Ca(OH)_2 \xrightarrow[H_20]{} CaCO_3 + H_20 \qquad (2.1)$$

The above reaction severely reduces the pH value to as low as 8 and as a result, the passive oxide film is broken out. Diffusion of carbon dioxide both in dry environments and water saturated concrete is a very slow process and the above Equation 2.1 cannot be sustained. Carbonation is a common problem for car parks and buildings and typically occurs in environments with a relative humidity between 50-70% (Saetta et al., 1993; Christodoulou, 2009).

The steel corrosion due to chloride ingress progresses at a much higher rate than that due to carbonation. In extreme cases, the corrosion rate in real structures can be 5 mm/year compared to 0.05 mm/year for carbonation induced corrosion (Basheer et al., 2001). Chlorides lead to corrosion of steel reinforcement inside concrete and it is the type of corrosion that has become the major causes of deterioration of RC structures. There are two possible sources of chlorides: internal, from the ingredients of the concrete mix (i.e. contaminated aggregate from sea water and admixtures containing chloride) and external from the environment (i.e. deicing salt and concrete structures in the marine environment). The use of ingredients containing chlorides for concrete is nowadays severely restricted and thus it may be assumed that the major source of chlorides is from outside.

Chloride ions activate the surface of the steel to form an anode, the passive surface being the cathode. The reactions involved are as follows:

$$Fe^{2+} + 2C1^{-} \rightarrow FeC1_2 \tag{2.2}$$

$$FeCl_2 + 2H_2O \rightarrow Fe(OH)_2 + 2HC1 \tag{2.3}$$

Thus, $C1^-$ is regenerated so that the rust contains no chloride, although steel chloride is formed at the intermediate stage (Neville, 1995).

Figure 2.2 illustrates schematically a plot representing a deterioration of RC structures due to steel corrosion. The corrosion-induced deterioration of RC can be modelled in terms of two-component steps: first, initiation period (T_0), which represents the time from initial exposure to chloride until chlorides have penetrated the concrete cover via diffusion to come into contact with the steel reinforcement. When the concentration of chloride exceeds a threshold value, the pH level is low enough that oxidation of steel reinforcement may take place. The second step involves the propagation period (T_{cr}), which represents the time from when the steel reinforcement starts to corrode until a critical limit of a material property (such as mechanical strength) has been reached (Tuutti, 1979; Liang et al., 1999; El Maaddawy & Soudki, 2007). The propagation period consist of: (i) internal cracking around the steel reinforcement due to the build-up of corrosion products; (ii) surface cracking due to further progression of corrosion induced cracks; (iii) spalling or delamination of the concrete cover; and finally (iv) rehabilitation or replacement of the concrete deck, depending on the amount of concrete damage to the deck that can be tolerated (Cusson et al., 2011).

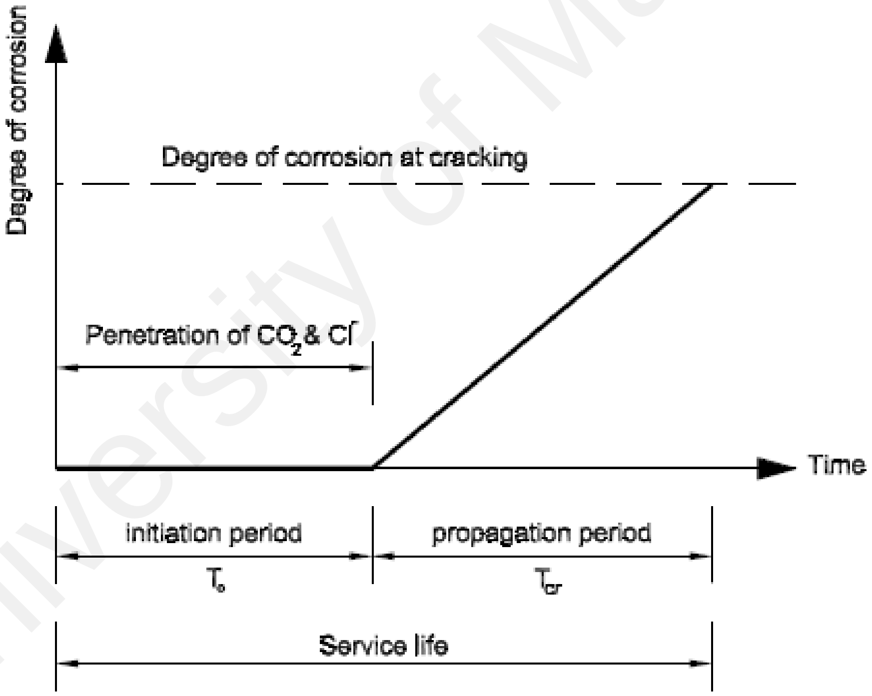

Figure 2. 2: Schematic representation of concrete deterioration process as a result of reinforcement corrosion (Tuutti, 1979)

The initiation period is a function of the diffusivity of chloride or carbon dioxide and temperature, the propagation period is dependent on oxygen diffusion, temperature, resistivity of concrete, depth of cover and its quality, diameter and spacing of steel reinforcement, moisture content, and tensile strength of concrete (Rasheeduzzafar et al., 1992). Based on the conceptual model illustrated in Figure 2.2, the service life (T_S) can be defined as the total time to reach a given corrosion-induced damage level, which is the sum of the corrosion-initiation time (T_0) and the propagation time (T_{cr}).

Corrosion is an electrochemical reaction represented by two half-cell reactions; an anodic reaction and a cathodic reaction. The electrode at which chemical oxidation occurs is called the anode. The electrode at which chemical reduction occurs is called the cathode. The anodic reaction releases electrons, while the cathodic reaction consumes electrons. Figure 2.3 shows schematically the process of steel corrosion in concrete (Ahmad, 2003).

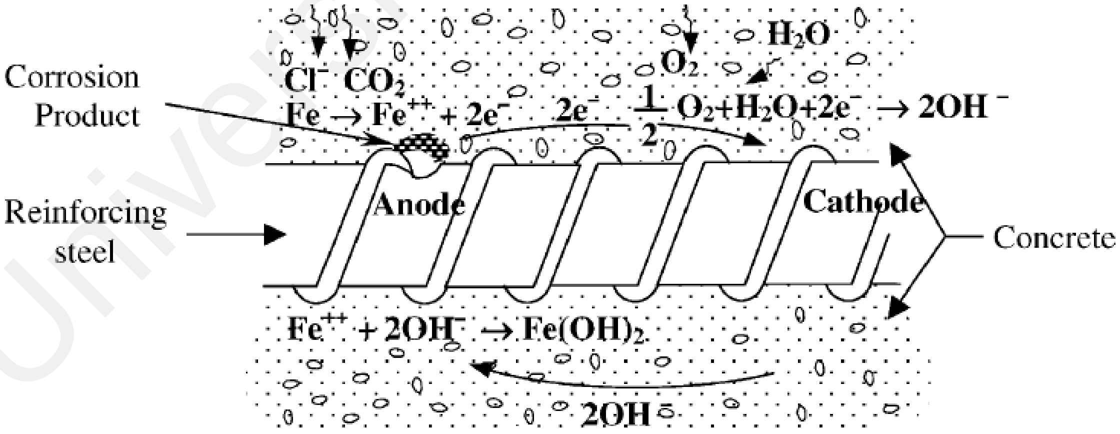

Figure 2. 3: Process of corrosion of steel in concrete (Ahmad, 2003)

The anodic reaction depends on the pH of the electrolyte and the existence of anions. The anodic reaction could be represented by Equation 2.4.

$M \rightarrow M^{n+} + ne^-$ (2.4)

$Fe \rightarrow Fe^{2+} + 2e^-$ (for iron and steel)

The corresponding oxygen reduction at the cathode that uses the electrons generated by the metal dissolution in its reaction is shown in Equations 2.5 to 2.8.

$O_2 + 4H^+ + 4e^- \rightarrow 2H_2O$ (oxygen reduction in acidic solution) (2.5)

$1/2\ O_2 + H_2O + 2e^- \rightarrow 2OH^-$ (oxygen reduction in neutral or basic solution) (2.6)

$2H^+ + 2e^- \rightarrow H_2$ (hydrogen evolution from acidic solution) (2.7)

$2H_2O + 2e^- \rightarrow H_2 + 2OH^-$ (hydrogen evolution from neutral water) (2.8)

The total reaction that leads to the steel corrosion product rust:

$Fe^{2+} + 2OH^- \rightarrow Fe(OH)_2$ (2.9)

$4Fe(OH)_2 + O_2 + 2H_20 \rightarrow 4Fe(OH)_3$ (2.10)

$2Fe(OH)_3 \rightarrow Fe_2O_3.H_2O + 2H_2O$ (2.11)

Where they meet electrically to neutralize each other and form ferrous hydroxide $Fe(OH)_2$ which when mixed with oxygen will form haematite, $Fe_2O_3.H_2O$ (hydrated ferric oxide) a by-product of the corrosion circle. The “rust” has a lower density than steel reinforcement. Hence, as corrosion takes place, the volume increases and since the expansion is restrained by the surrounding concrete, bursting stresses are induced, resulting in spalling, cracking, or delamination of the concrete cover. This makes it easier for aggressive agents to ingress towards the steel reinforcement, with a subsequent increase in the rate of the steel corrosion. In other words, once corrosion starts, it will accelerate (Poonguzhali et al., 2008; Christodoulou, 2009).

2.1.2 Accelerated Corrosion Techniques

The mechanism of steel corrosion of RC structures is a long-term process. It takes realistically long time for the initiation and progression of steel corrosion. It is not easy to achieve steel corrosion with different degree in short time duration for a research study. Therefore, various methods for accelerated corrosion of the RC structure have been used by the researchers (Ahmad, 2009). Many researchers have used impressed current technique to study the mechanical behaviour of corroded RC structure (Almusallam, 2001), the bond behaviour of corroded steel reinforcement (Almusallam et al., 1996; Mangat & Elgarf, 1999; Lee et al., 2002; Fang et al., 2004), the structural behaviour of the corroded elements (Almusallam & Al-Gahtani, 1996; Al-Dulaijan et al., 2002; Chung et al., 2008; Al-Saidy et al., 2010), and the performance of the RC structure (Saricimen et al., 1998; Lee et al., 2000; Sakr, 2005; Ha et al., 2007). The advantages of using this technique are achieving a high degree of steel corrosion within a short period of time and the easy control of the desired corrosion level. The alternative method for accelerated corrosion is artificial climate environment (Yuan et al., 2006; Zhang et al., 2006; Yingshu et al., 2007; Yuan & Ji, 2009).

The impressed current technique is a technique for accelerating corrosion of steel reinforcement in RC by applying direct current (DC) power supply. The positive terminal of a DC power supply should be connected to steel reinforcement as an anode, while the negative terminal should be connected to a counter electrode as cathode. The counter electrode which serves as cathode could be in the forms of internal steel (Yingshu et al., 2007), external mesh (Nounu & Chaudhary, 1999) or external plate (Almusallam et al., 1996; Almusallam & Al-Gahtani, 1996; Maslehuddin et al., 2002; Fang et al., 2004).

The RC samples should be partially immersed in sodium chloride (NaCl) solution in a suitable tank, where the NaCl solution is in contact with the bottom of the structure. The majority of previous studies have used NaCl solution that are from 3% to 5% of solution volume (Uomoto et al., 1985; Tachibana et al., 1989; Mangat & Elgarf, 1999; Maslehuddin et al., 2002; Abul et al., 2007; Yingshu et al., 2007). Here, the NaCl solution functioned as an electrolyte. Figure 2.4 shows a typical schematic representation of an impressed current technique (Almusallam, 2001).

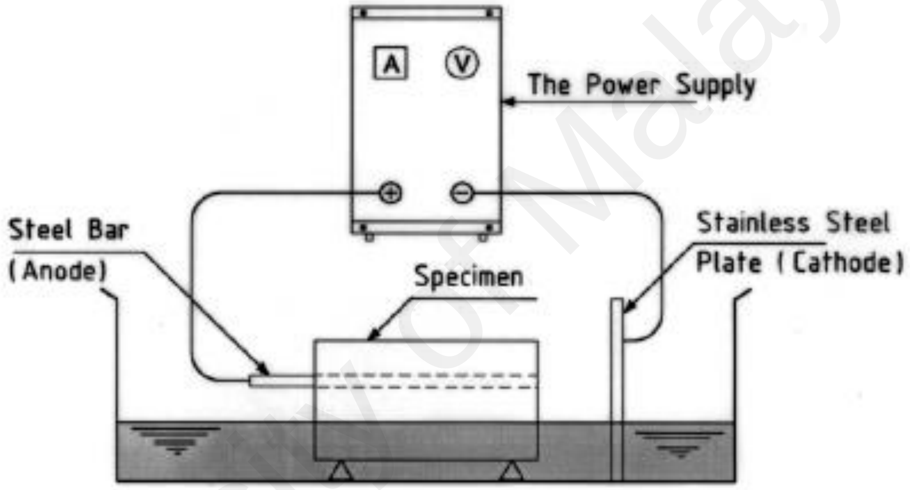

Figure 2. 4: Schematic representation of impressed current technique of accelerating steel corrosion (Almusallam, 2001)

The amount of steel corrosion is related to the electrical energy consumed, which is a function of voltage (V), amperage (A), and time interval. A constant voltage and ampere are normally applied from the DC power supply between the anode and cathode. In many cases, the steel corrosion was accelerated by constant voltage from 2.5 V to 30 V (Cabrera, 1996; Saricimen et al., 1998; Lee et al., 2000; Ballim & Reid, 2003) and current output from 0.4 A to 3 A (Almusallam et al., 1996; Lee et al., 2000; Ballim & Reid, 2003; Yingshu et al., 2007). The principle of the method is described in ASTM G1-03 (ASTM, 2003b) and ASTM G31-72 (ASTM, 2004b). A summary of some of the previous accelerated corrosion tests on RC members is presented in Table 2.2.

Tabel 2. 2: Summary of some previous accelerated corrosion tests

Study	Concrete structure	V	A	Type of cathode	Corrosion Environment
Almusallam *et al.*, 1996[a]	Slab	-	2	External stainless steel plate	5% NaCl solution
Almusallam *et al.*, 1996[b]	Bond pull-out	-	0.4	External stainless steel plate	Salt solution
Cabrera, 1996	Slab	3	-	External cathode	5% NaCl solution
Lee *et al.*, 2002	Cube	-	1	External copper plate	3% NaCl solution
Maslehuddin *et al.*, 2002	Mortar	2.5	-	External copper plate	5% NaCl solution
Fang *et al.*, 2004	Cube	-	0 - 2	External stainless steel plate	5% NaCl solution
Yuan *et al.*, 2007	Beam	-	1	Internal bar	5% NaCl solution

Figure 2.5 shows the electrochemical process using the impressed current technique (Yingshu et al., 2007). In the reaction, the whole surface of the steel reinforcement in concrete is the anode; the corrosion occurred almost entirely around the whole surface of steel reinforcement.

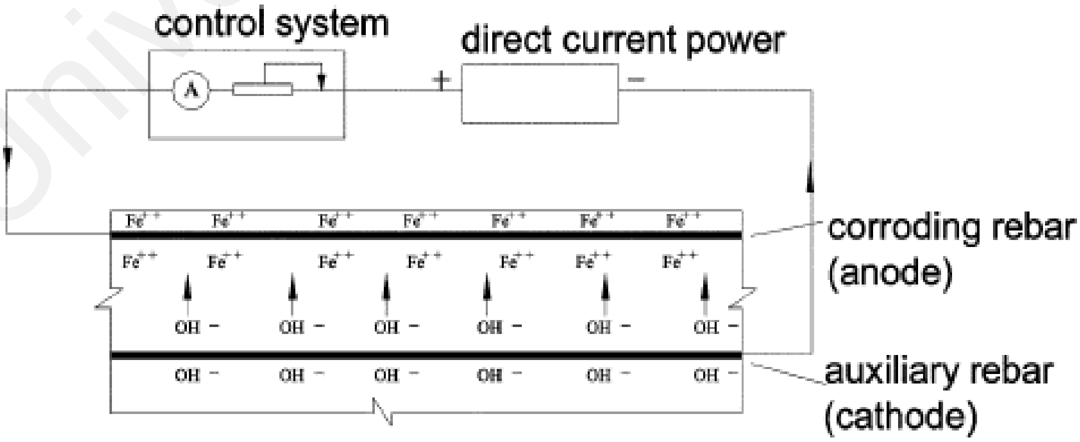

Figure 2. 5: The electrochemical process of impressed current technique (Yingshu et al., 2007)

2.1.3 Assessment of Corrosion Degree

Steel corrosion is often reported in terms of weight loss per unit time or thickness loss per unit time. The corrosion rate is directly proportional to the measured electrical current. The mass loss is related to the measured electrical current by Faraday's Law as shown in Equation 2.12 (El Maaddawy & Soudki, 2003):

$$\Delta \mathrm{m} = \frac{MIt}{zF}, \tag{2.12}$$

Where:

Δm = mass of steel consumed (g);

M = atomic or molecular weight of metal (56 g for Fe);

I = current (amperes);

t = time current or potentials applied (seconds);

z = ionic charge or electrons transferred in the half-cell reaction (2 for Fe); and

F = Faraday's constant (96,500 amperes/seconds).

Furthermore, the actual corrosion level for the corroded RC specimen could be measured as the mass loss of the steels before and after testing as shown in Equation 2.13 (Apostolopoulos & Michalopoulos, 2007):

$$\mathrm{M}l = \frac{Mi - Mf}{Mi} \text{ x } 100 \quad , \tag{2.13}$$

Where:

Ml = the mass loss (%);

Mi = the mass of non-corroded specimen (g); and

Mf = the mass of corroded specimen (g).

2.2 NDT methods for corrosion monitoring

Recently, various methods have been implemented for corrosion monitoring in RC structures. They are classified into six main categories as follows: visual inspection, electrochemical methods (i.e. half-cell potential (HCP) monitoring, resistivity method, polarization resistance, galvanostatic pulse method (GPM), electrochemical noise (EN)), elastic wave methods (i.e. ultrasonic pulse velocity (UPV), acoustic emission (AE), and impact echo (IE)), electromagnetic (EM) methods (i.e. ground penetrating radar (GPR)), optical sensing methods (i.e. fiber Bragg grating (FBG)), and infrared thermography (IRT). Visual inspection, HCP, polarization resistance, and other electrochemical methods are found to be more commonly used for steel corrosion monitoring in RC structures.

2.2.1 Visual Inspection

Visual inspection is a regular inspection method to assess steel corrosion damage on the surface of RC structures. The appearance of the corroded area often provides valuable insight into the cause and the extent of steel corrosion. However, the method is very dependent on the inspector’s experience. In addition, visual inspection is limited in its effectiveness to detect surface discontinuities due to steel corrosion and the unseen corrosion is difficult to spot (Elsener et al., 2003; Rhazi et al., 2007; Arndt & Jalinoos, 2009; Wiggenhauser & Reinhardt, 2010).

2.2.2 Electrochemical methods

Electrochemical methods are by far the most suitable for steel corrosion monitoring in RC structures. Electrochemical methods, in general, can provide fast and reliable information on the probability of steel corrosion, the corrosion rate of steel reinforcement, and the resistivity of the RC structure (Rodriguez et al., 1994; Carino, 1999; Lu & Peiyu, 2000; Law et al., 2001; Holloway et al., 2004; Gonzalez et al., 2005; Koleva et al., 2007; Poursaee & Hansson, 2008; Holloway et al., 2009; Vedalakshmi et al., 2010; Xu & Yao, 2010; Shi et al., 2011).

Electrochemical methods are related to the interrelation of the electrical and the chemical effects. An electrochemical system measures the potential and current of oxidation and reduction reactions (Andrade & Gonzalez, 1978; Baronio et al., 1996; Swarup & Sharma, 1996; Andrade et al., 2001; Song & Saraswathy, 2007; Fang et al., 2014). The principles of the five electrochemical methods are shown in Figure 2.6.

In the half-cell potential (HCP) monitoring, one of the electrochemical methods, the electrical potential (in mV or V) between a steel reinforcement and a reference electrode (i.e. a copper/copper sulphate cell), in contact with the concrete surface, is measured (Ohtsu. & Yamamoto, 1997; Yeih & Huang, 1998; Assouli et al., 2008; Sadowski, 2013). The principle of OCP method is shown in Figure 2.6. The HCP provides information pertaining to the probability and potential level of steel corrosion in the RC structures (Elsener et al., 2003; Arndt & Jalinoos, 2009).

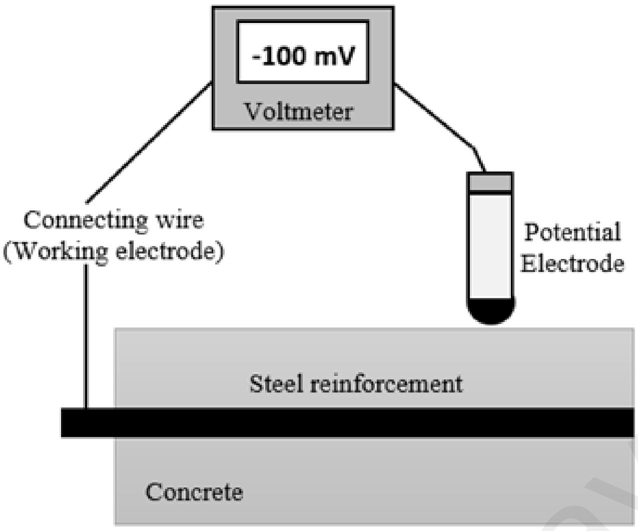

Figure 2. 6: Half-cell potential monitoring (HCP) (Elsener et al., 2003)

Table 2.3 gives the potential ranges for different corrosion conditions of steel inside the RC. The method is often unconvincing in terms of interpretation because the measurement depends on the condition of the RC structure. Moisture levels and amount of chloride concentration can affect the potential readings and give erroneous results (Elsener et al., 2003; Ismail et al., 2006). The changes in moisture content (i.e. wet condition of the concrete surface) lead to a shift in potential values so they become more negative value (i.e. a shift of 100 mV was found on a bridge deck measured in the dry condition and the wet condition after rainfalls).

The potential gradients and the local potential do not change, difference was found only in the magnitude of potential gradients. In a structure with a high chloride concentration, there is usually low resistivity in the concrete. The readings are often mismatched when there is low resistivity in the concrete, but it has readings with high passive potential. This is due to the fact that chlorides are transported more easily in lower resistivity of concrete, high contents of chlorides depassivated the steel reinforcement, and active potentials were measured (Elsener et al., 2003).

On the other hand, the polarization resistance method is commonly used for measuring the corrosion rate in the RC structures. The method records the current generated and consumed by anodic and cathodic reactions. The change in potential during reactions is known as polarization, which is used to evaluate the steel corrosion. However, this electrochemical method has some limitations, such as the method assumes uniform corrosion while pitting corrosion is a highly probable form of steel corrosion in the RC structure, which might lead to misleading results. In addition, the area of steel measured in concrete is not precisely known which creates some errors in the polarization resistance calculations. Another error in the polarization resistance method is the IR drop introduced by high resistive medium and high separation of the reference electrode from the steel reinforcement of the RC structures (Clear., 1989; Andrade et al., 1990; Broomfield, 1996). Figure 2.7 shows the principle of polarization resistance method.

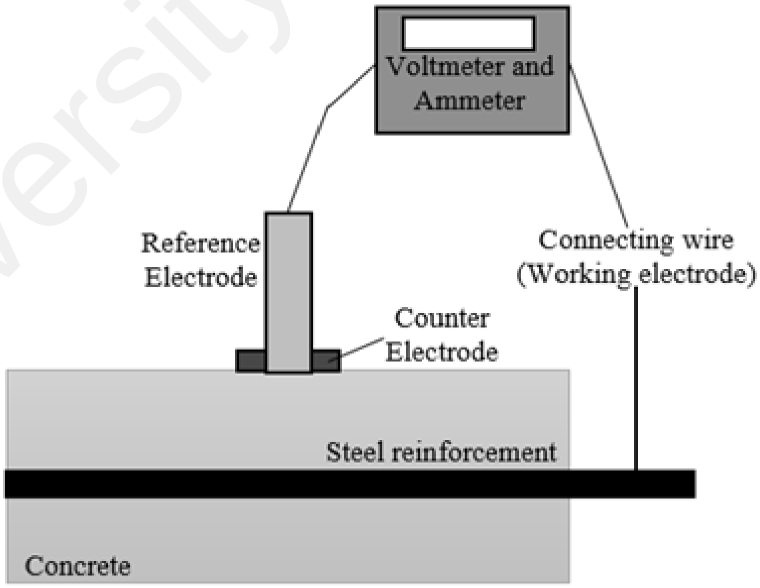

Figure 2. 7: Polarization resistance (Song & Saraswathy, 2007)

The other practical method for measuring the corrosion rate is GPM. This generally involves impressing a small amplitude, short time anodic current pulse, to be applied galvanostatically on the steel reinforcement from the external counter electrode over the concrete surface (Newton & Sykes, 1988; Elsener et al., 1994). The anodic current is usually in the range of 5 to 100μA and the typical pulse duration is between 5 and 30 seconds (Poursaee & Hansson, 2008). The steel reinforcement is anodically polarised and there is a resulting change in the electrochemical potential. The potential is recorded by a reference electrode (usually in the centre of the counter electrode) as a function of polarization response. Figure 2.8 shows a schematic setup for the GPM test.

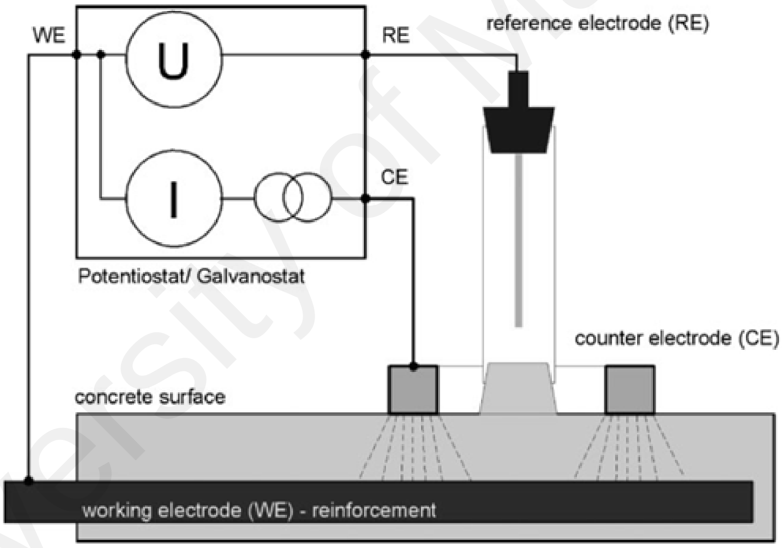

Figure 2. 8: Galvanostatic pulse method (GPM) (Reichling et al., 2013b)

When the constant current Iapp is applied to the system, the polarised potential of reinforcement (η_t), at given time t can be expressed as (Newton & Sykes, 1988):

$$\eta_t = I\text{app}\ [\ R_{ct}\ [\ 1 - \exp\ (-t\ /\ R_{ct} \mathrm{x} C_{dl}))\ ] + R_{\Omega}\ ], \tag{2.14}$$

Where:

R_{ct} = polarization resistance,
C_{dl} = double layer capacitance, and
R_{Ω} = ohmic resistance.

The GPM results are much closer to the corrosion rate produced by the gravimetric method than those produced by polarization resistance, electrochemical impedance spectroscopy (EIS), the Tafel extrapolation method (TEM), and the harmonic analysis method (HAM) (Sathiyanarayanan et al., 2006; Poursaee & Hansson, 2008; Holloway et al., 2009; Vedalakshmi et al., 2010; Vedalakshmi & Thangavel, 2011). Uncertainty about the polarized area of steel reinforcement is one of the major sources of error when measuring the corrosion rate of steel reinforcement in RC structures affected by the electrical signal from the counter electrode and the non-uniform current distribution of the steel reinforcement (Wojtas, 2004).

The resistivity method is another electrochemical method, which relies upon the principle that corrosion is an electrochemical process. An ionic current must pass between the anode and cathode areas for corrosion monitoring of the RC structures (Bungey & Millard, 1996). The resistivity is an indirect indication of active corrosion of the steel reinforcement (Cavalier & Vassie, 1981; Clear, 1982; Sadowski, 2010). The steel corrosion process will be slower if the resistivity of the concrete is high. The resistivity of concrete exposed to chloride indicates the risk of early corrosion damage because low resistivity is always associated with rapid chloride penetration (Polder, 2001).

Concrete resistivity is generally measured using the Wenner four-probe method, as illustrated in Figure 2.9. However, this method has limitations due to the heterogeneities (i.e. steel reinforcement, resistivity layers, cracks, and large aggregates) which would influence the shape of the electric lines in the concrete. In addition, the low distance of the electrode probe (< a few tens of centimeters) and weather conditions (i.e. wet, temperature, and humidity) which influence the resistivity thus having a huge influence on the results (Polder et al., 2000; Reichling et al., 2013a).

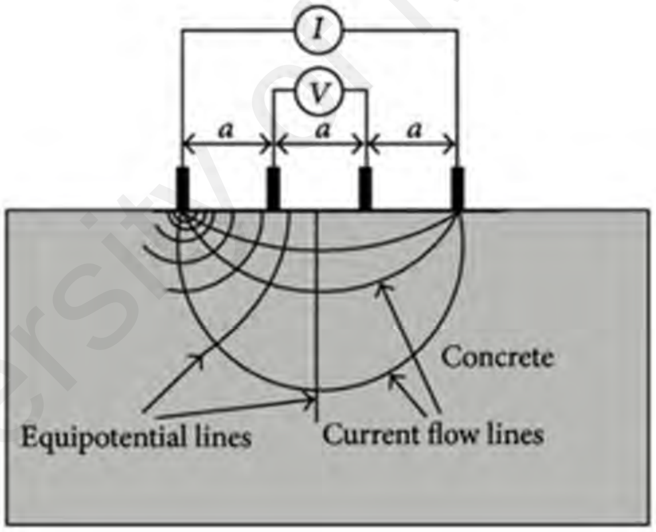

Figure 2. 9: Resistivity method (Broomfield, 1996)

On the other hand, the electrochemical noise (EN) is an emerging technique for monitoring the mechanisms and estimating the rate of corrosion in RC structures. Electrochemical noise is used to describe fluctuations in the potential and current generated by corrosion reactions (Legat & Govekar, 1994; Legat, 2007). The phenomenon whereby the potential of the electrodes fluctuates due to current vibration is also referred to as noise (Inoue et al., 2008). The current vibration of electrodes due to the fluctuation of the oxide-reduction reaction on the surfaces of the electrodes (Fukuyama et al., 2009).

A noise source is located within the probable corroding area. A noise signal is transformed from the time domain to the frequency domain displayed in the form of amplitude and frequency based on the fast Fourier transform (FFT). The noise resistance (Rn), which is believed to be similar to the polarization resistance, is given by (Mansfeld & Xiao, 1993; Xiao & Mansfeld, 1994; Bertocci & Huet, 1995):

$$Rn = \sigma V / \Sigma i, \tag{2.15}$$

Where:

σV = the standard deviation for the potential and

σI = the standard deviation for the current obtained by statistical analysis of the noise data.

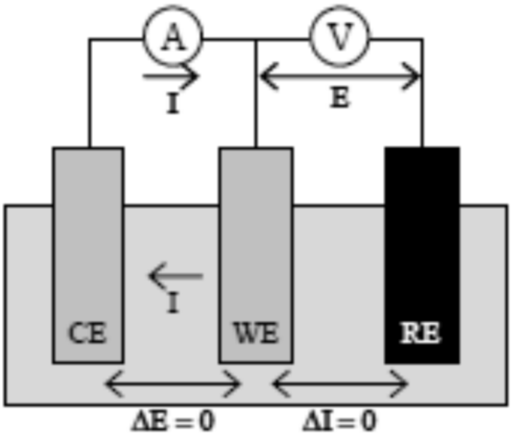

Figure 2. 10: Electrochemical noise (EN) (Fukuyama et al., 2009)

The main advantage of the EN technique is its lack of intrusiveness. It can avoid artificial disturbances to the system during measurement (Yu et al., 2002). The EN measurement has been used to study the onset of localized corrosion (Hashimoto et al., 1992; Mansfeld et al., 2001). However, only a few studies of EN for measuring corrosion in RC structures have been carried out (Mariaca et al., 1997; Legat et al., 2004). Previous work using this technique on reinforcing bars has only studied the steel corrosion process of various metallic materials (Nagiub & Mansfeld, 2001; Mills et al., 2003; Aballe et al., 2004; Zhao et al., 2007). Table 2.3 provides a summary of the qualitative corrosion activity of the above electrochemical methods. However, there is no standardization for the evaluation of the corrosion activity by EN method. Therefore, most of the electrochemical methods require direct connection with the steel reinforcement in the RC structure as the electrode, which makes it an intrusive method (Hong et al., 2014). It requires a localized breakdown in the concrete surface to provide the direct connection (Patil et al., 2014).

Tabel 2. 3: Interpretation of corrosion activity of electrochemical methods

Corrosion Activity	Potential level (mV) (Bertocci & Huet, 1995)	Resistivity (Ω-m) (Legat & Govekar, 1994)	Corrosion Rate	
			LPR (I_{corr} (A/cm^2)) (Sathiyanarayanan et al., 2006)	GPM (R_{ct} (kΩcm^2)) (Sathiyanarayanan et al., 2006)
Very High	-	-	10-100	0.25-2.5
High	<-350	<100	1.0-10	2.5-25
Moderate/Middle	-200 to -350	100-500	-	-
Low	>-200	500-1000	0.1 - 1	25-250
Negligible/passive	-	>1000	< 0.1	>250

2.2.3 Electromagnetic (EM) waves

Another NDT method of corrosion monitoring is ground penetrating radar (GPR), which is based on the propagation of an EM wave into an RC structure. Part of the EM wave is reflected back to the receiving antenna whenever it encounters an interface of two media with differing dielectric constants (Halabe, 1990; Sbartai et al., 2007; Lai et al., 2011b). A GPR antenna receives direct and reflected waves, which are recorded as amplitude-time signals (*a*-scan) by the system. The direct wave signal (S_d) represents the EM energy transmitted directly to the receiving antenna, and the reflected wave (S_r) is the EM energy reflected from the steel reinforcement-concrete interface (Sbartai et al., 2007). The propagation of EM waves depends on the corresponding dielectric permittivity of concrete, which is a quantity related to the ability of concrete to resist the flow of an electrical charge (Halabe, 1990; Robert, 1998; Soutsos et al., 2001; Sbartai et al., 2006b). The permittivity, in turn, depends on the EM properties, which are influenced by temperature, moisture content, chloride content, pore structure, and deterioration (i.e. corrosion) (Maierhofer, 2003).

Despite its capability, GPR only presents a qualitative assessment of the steel corrosion damage. Moreover, the presence of chloride content and corrosion products would attenuate the GPR waves (Kim, 2003; Klysz et al., 2004; Sbartai et al., 2006b; Lai et al., 2009), which decrease the amplitude of the wave and the average velocity of reflected wave (Sbartai et al., 2006a; Barnes et al., 2008) and increasing the travel time of the wave (Lai et al., 2011a; Hong et al., 2012). In addition, the GPR method is carried out periodically to monitor the corrosion process in RC structures and cannot be used for real-time monitoring (Hong et al., 2014). Figure 2.11 shows a 3D image of GPR data in an RC slab with four different degrees of corrosion (i.e. no corrosion, low corrosion, medium corrosion, and high corrosion from the left to the right side).

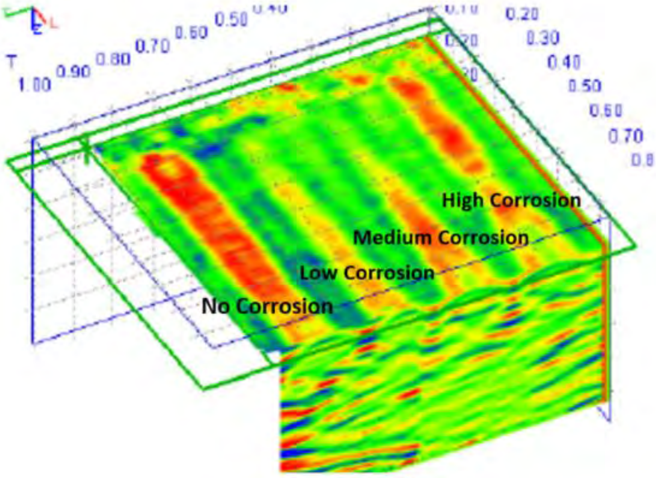

Figure 2. 11: 3D image of GPR of concrete slab with different level of steel corrosion, unit (m) (Kabir & Zaki, 2011)

2.2.4 Infrared thermography (IRT)

As a sub-surface inspection method, IRT has been found to be capable of detecting steel corrosion in the RC structures. The method is based on the resulting perturbations in the heat transfer characteristics of concrete materials (Manning & Holt, 1980; Clark et al., 2003; Kobayashi & Banthia, 2010; Washer et al., 2010; Kordatos et al., 2011; Bagavathiappan et al., 2013; Pieper et al., 2014).

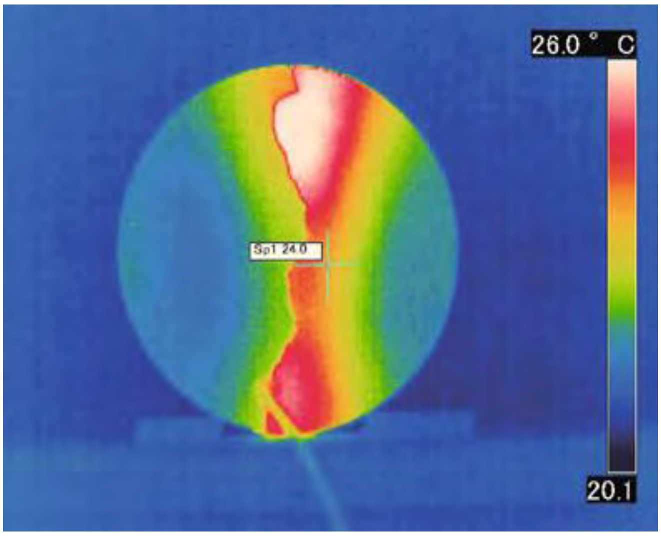

Figure 2. 12: IRT image of the concrete surface of a cylinder, unit (^{0}C) (Kobayashi & Banthia, 2010).

Temperature is one of the most common indicators of the structural health of the RC structures. Cracks, alkali-aggregate reaction (AAR), corrosion, and other deterioration forms could cause abnormal temperature distribution (Bagavathiappan et al., 2013). With the advent of newer generations of IR cameras, IRT is becoming a more accurate, reliable, and cost-effective technique for corrosion monitoring in RC structures (Pieper et al., 2014). However, like GPR method, the interpretation of IRT is also qualitative, i.e. a higher degree of steel corrosion results in stronger IR thermal distribution on the concrete surface (Ii et al., 2004; Chung et al., 2006; Kobayashi & Banthia, 2010, 2011; Washer, 2012), which would exhibit higher peaks of IR intensity and faster rates of heating (Kwon et al., 2011; Baek et al., 2012), and hence increase the temperature of the concrete materials (Chung et al., 2006). Figure 2.12 shows an IRT image of the temperature distribution of a 10 % degree of steel corrosion of the concrete cylinder.

2.2.5 Optical sensing methods

The optical sensing technology of the NDT methods, the fibre Bragg grating (FBG) method, involves creating periodic variations in the refractive index of the core of an optical fibre (Vallee et al., 2004). When light is made to pass through the grating at a particular wavelength, called the Bragg wavelength, the light reflected by the varying zones of refractive indices would be in phase and amplified (Chen & Dong, 2012; Hassan et al., 2012). During corrosion, the formation of corrosion products less dense than steel increases the volume and diameter of the bars, leads to an increase in fibre strain, which is measured by a shift in the wavelength of the FBG. The extent of corrosion is quantitatively evaluated through the change in the wavelength of the FBG (Zheng et al., 2009; Lee et al., 2010; Gao et al., 2011).

Although it has advantages such as linear reaction, small volume, high anti-erosion capability, and automatic signal transmission (Lau, 2003; Geng et al., 2009), the FBG method also has limitations in corrosion monitoring in the RC structures. The method can only conduct localized inspection of steel corrosion in the RC structures. It is expected the distributed and long-gauge FBG technique will be developed for the solution of this problem, which make this method less effective for steel corrosion monitoring in the RC structures (Lei & Zheng, 2013).

2.2.6 Elastic wave methods

In order to enhance reliability, elastic wave methods should be adopted to complete the assessment of steel corrosion in the RC structures. Elastic wave methods are essential when estimating mechanical properties and inhomogeneous characterization due to steel corrosion in the RC structures. Wave-based damage detection excites transient waves to propagate into the concrete structure using sensors since the waves are reactive to damage such as cracks, voids, and also corrosion products (Sohn et al., 2004). There are three major wave-based methods for steel corrosion monitoring in the RC structures, i.e. ultrasonic pulse velocity (UPV), impact echo (IE), and acoustic emission (AE).

The UPV test is an NDT method that involves measuring the speed of sound through concrete in order to detect the condition of the concrete and the presence of steel corrosion (ASTM, 1989; Bungey, 1991; John et al., 1992; Raad et al., 1997; Yeih & Huang, 1998; Ervin et al., 2009; Sharma & Mukherjee, 2010), in chloride and oxide environments (Jung et al., 2000; Sharma & Mukherjee, 2010; Sharma & Mukherjee, 2011; Sharma & Mukherjee, 2013). The principle of the UPV method is shown in Figure 2.13. Ultrasonic waves can propagate a long distance along the steel reinforcement and have been found to be sensitive to the interface conditions between the steel reinforcement and the concrete (Miller et al., 2009; Sharma & Mukherjee, 2010).

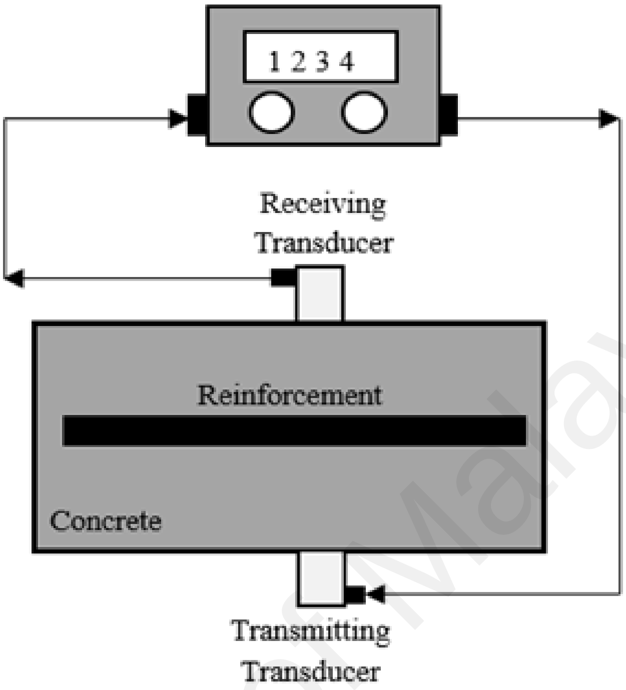

Figure 2. 13: Ultrasonic pulse velocity (Komlos et al., 1996)

Cracking due to steel corrosion results in wave attenuation and a decrease in UPV. It has been reported that the amplitude attenuation has good a correlation with the damage due to steel corrosion (Yeih & Huang, 1998; Goueygou et al., 2004; Aggelis et al., 2010). In addition, UPV, as measured by the first wave peak, could describe the process of steel corrosion. As the corrosion damage level increases, the relative variation for the first wave peak value of UPV first increases and then decreases (Li et al., 2014). This condition occurs because the corrosion products are increased during the process of steel corrosion, resulting in an increase in the delamination degree between the steel reinforcement and the concrete. As the RC corrosion level increases, the pit on the steel reinforcement becomes larger. This condition would lead to great reflection in the first wave energy, and the direct transmission wave energy would become low. The first wave peak value then decreased slowly. However, the method needs an advanced study. The study could come from the use of surface and other, guided waves, with features other than longitudinal pulse velocity, and stemming from advanced signal processing techniques (Komlos et al., 1996).

The stress wave method, IE is employed to detect steel corrosion in structural elements using mechanical impact and then monitoring the displacement (d), detected by sensors placed on the concrete surface. The impulse is reflected by the arrival of reflections of the pulse from the crack and other internal defects under investigation (Carino et al., 1986; Sansalone & Streett, 1997), as shown in Figure 2.14. In an early study by Liang and Su (2001) more than a decade ago, the IE method was certainly able to detect the development of micro-cracks due to steel corrosion in RC blocks.

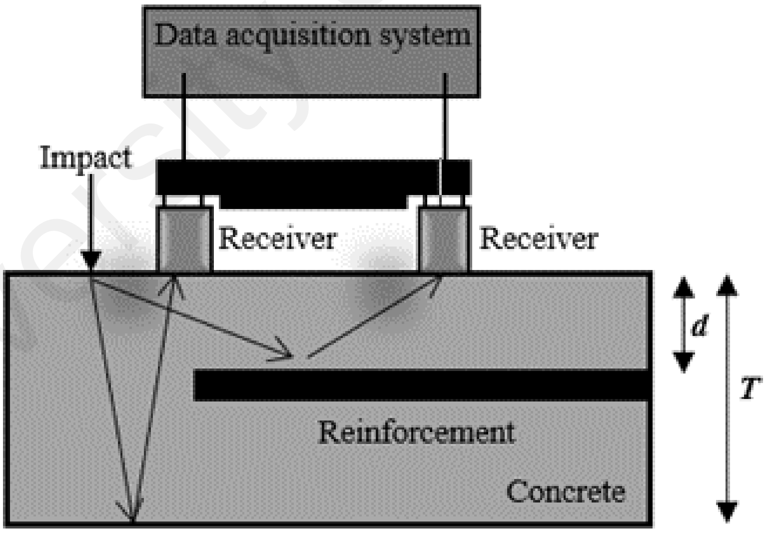

Figure 2. 14: Impact echo (Sansalone & Streett, 1997)

In the latest studies, Samarkova et al. (2014a; 2014b; 2014c; 2014d) have indicated that the dominant frequencies of the response signal are the main criteria used to detect the occurrence and position of steel corrosion in the RC structures. However, only a number of limited studies have attempted to monitor steel corrosion in the RC structures because the main application of the IE method is in the detection of voids and delamination. In addition, the proposed method is not as mature as electrochemical methods for steel corrosion monitoring.

Therefore, AE is considered a good complementary method to UPV and IE. The AE technique is a unique, non-invasive, and passive NDT method. AE is a class of phenomena whereby transient elastic waves (ultrasonic frequency range) from a localised source within a material and conversion of the waves into electrical signals through coupled piezoelectric sensors (Beattie, 1983; Miller & Mc Intire, 1987; Shiotani, 2006; Lapitz et al., 2007; Alvarez et al., 2012). The sources of AE are deformation processes such as crack growth, void closure, plastic deformation, corrosion, and other material degradation. Localised energy release gives rise to elastic waves that are detected by sensors placed on the concrete surface (Wells, 1970; Luo X et al., 2002). The principle of AE is shown in Figure 2.15.

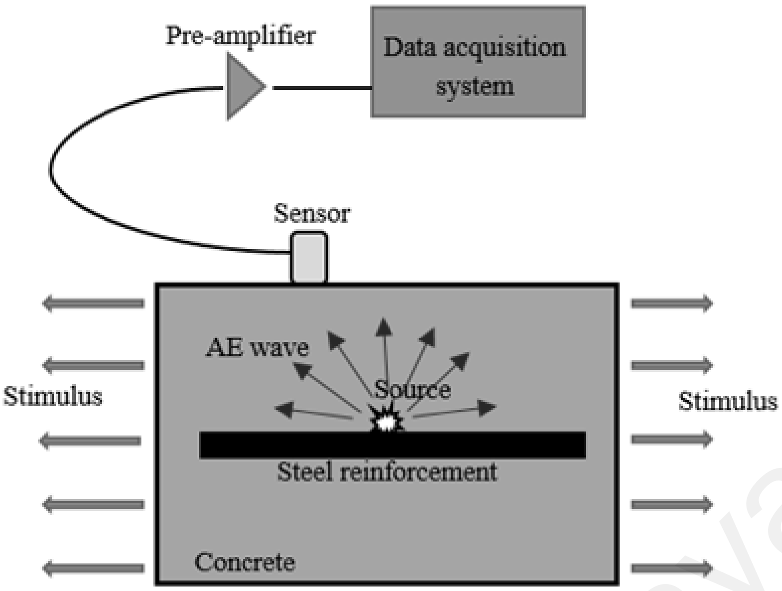

Figure 2. 15: Acoustic emission (ASTM, 1998)

2.2.7 Summary of NDT methods for Corrosion Monitoring

A number of NDT methods for the corrosion monitoring of steel reinforcement in concrete structures have been reviewed. There are six major NDT methods for corrosion monitoring: i.e. visual inspection, electrochemical methods (i.e. HCP, resistivity method, LRP, and GPM), elastic wave methods (i.e. UPV, AE, and IE), the electromagnetic (EM) method (i.e. GPR), the optical sensing method (i.e. FBG), and the IRT method. Table 2.4 shows a summary of NDT methods for corrosion evaluation. Each technique was reviewed in relation to principles, certain applications, and limitations.

Therefore, AE technique is chosen due to its capability of detecting steel corrosion in the early stages of corrosion, so that an early warning can be given to allow for repair work before the RC concrete is seriously damaged and the functionality is lost due to steel corrosion. This study reviews comprehensively the capability of the AE technique in monitoring the corrosion activity and it discusses the distinct advantages of the AE technique as following sections.

Tabel 2. 4: Resume of NDT methods for corrosion evaluation

NDT Methods	Principles	Advantages	Disadvantages	Corrosion Evaluation	Specific Equipment
Electrochemical method					
Open circuit potential (OCP) monitoring	Electrical potential value (in mV or V) is measured between steel reinforcement of RC and reference electrode (indicates corrosion potential of the steel inside RC).	The results are not in the form of equipotential contours, rather a single value that gives an indication of the steel condition.	Time-consuming and need to be closed several hours during the inspection.	Potential level (mV or V)	Potential electrode, Voltmeter, and connecting wires (working electrode).
Resistivity method	Resistivity (ρ) of RC which the current can easily pass between anode and cathode areas of the concrete.	An easy, fast, portable, and inexpensive technique, which can be used for routine inspection.	Reinforcement in the test region can provide a "short-circuit" path and cause an erroneous reduction in the measurement.	Resistivity (Ω.cm.)	Current and potential electrodes, Voltmeter or resistivity unit, and insulated wire (working electrode).
Polarization resistance	The change in current upon a small linear potential sweep (+-10 mV) in turn of the corrosion potential of the concrete.	Short time for measurement and applies small perturbations that do not interfere with the existing electrochemical processes.	It takes time to obtain a full response because of the electrical capacitance across the steel and concrete interface. The voltage error introduced by IR drop in the concrete between working (steel reinforcement) and a reference electrode.	Corrosion current (I*corr* (A/cm^2))	Reference electrode, counter electrode, Voltmeter, Ammeter, and connecting wire (working electrode).

Tabel 2. 4: Continued

NDT Methods	Principles	Advantages	Disadvantages	Corrosion Evaluation	Specific Equipment
Galvanostatic pulse method (GPM)	The anodic current pulse is applied galvanostatically on the steel reinforcement from a counter electrode placed on the concrete surface.	A rapid device for determining the corrosion rate of steel reinforcement in RC, it enables display of corrosion rate, electrical resistance, and potential value simultaneously.	Unstable reading due to parallel or crossing of the steel reinforcement also cracks and delamination is often the reason for wrong readings.	Potential resistance (R_{ct} (kΩcm^2))	The reference electrode, a counter electrode, guard ring, and connecting wire (working electrode).
Electrochemical noise (EN)	EN describe the fluctuations of current and potential spontaneously generated by corrosion reactions.	Simple to use, no interference with the system and measured signals can be analyzed by mathematical analysis.	The complicated kinds of noise (i.e. physical origin) due to corrosion of steel reinforcement make mathematical analysis unsuccessful.	Noise resistance (Rn (kΩcm^2))	Electrodes (reference, counter, and working), Voltmeter, Ammeter, amplifier, and data acquisitions board.
Elastic wave method					
Ultrasonic pulse velocity (UPV)	Mechanical energy propagates through the concrete as stress waves and is converted into electrical energy by a second transducer.	A large penetration depth and it is easy to use for estimating the size, shape, and nature of the concrete damage.	The evaluation of UPV data is a highly specialized task which requires careful data collection and expert analysis.	Pulse velocity (V)	Transducers (transmitter and receiver), amplifier, and oscillator.

Tabel 2. 4: Continued

NDT Methods	Principles	Advantages	Disadvantages	Corrosion Evaluation	Specific Equipment
Acoustic emission (AE)	Elastic waves are generated due to the rapid release of energy from a localized source within an RC structure.	A cost-effective and sensitive technique that can detect and locate the active defects.	Passive defects cannot be effectively detected.	AE parameters	Transducer, preamplifier, filter, amplifier, and storage equipment.
Impact echo (IE)	Stress wave is propagated within the RC structure through vibrations and impact load.	A simple, fast, reliable method for inspecting the concrete is to impact the surface with a hammer and listen to the results.	The reliability of the IE method decreases with an increase in thickness.	Wave velocity (Vp)	Mechanical impactors, high-fidelity receiver, and data acquisition-signal analysis system.
Electromagnetic Method					
Ground penetrating radar (GPR)	Transmission of electromagnetic (EM) waves into the RC structure under investigation.	Equipment portable and effective for investigating one large area from one surface.	Difficult interpretation of the results and needs post-processing analysis.	EM wave velocity (V)	Antennas (transmitter and receiver), a control unit, and computer.

Tabel 2. 4: Continued

Optical Sensing Method					
Fiber Bragg grating (FBG)	The shift of FBG wavelength measures the increase in fibre strains with an increase in the cross-section of steel reinforcement of corroded RC structures.	Small physical dimensions and suitable for embedding into structures.	The equipment has a high cost and there is no standardization of the procedure.	Bragg wavelength (λB)	Optical fibre sensor, Bragg meter, and computer.

2.3 Acoustic Emission (AE) Technique

The AE technique is one of the NDT methods to monitor the structural health of concrete. The phenomenon of AE is defined as the propagation of elastic waves due to the release of localized internal energy, such as a micro-fracture in elastic material. The sources of AE include structural deformation processes such as crack growth, plastic deformation, and other kinds of material degradation. The AE technique involves the use of sensors to detect the strain energy released which generated from growing cracks which attached to the surface of the specimen provided (Behnia et al., 2014a). The application of AE is far more sensitive than other NDT methods with respect to inspection of time and preparation, which also results in the cost savings.

2.3.1 AE for corrosion monitoring

The AE technique has been widely used in the field of civil engineering for structural health monitoring (SHM), especially the monitoring of steel corrosion (Malhotra, 1991; Ohtsu & Yuyama, 2000; Carpinteri et al., 2011; Calabrese et al., 2013a). The advantage of the AE technique is that can be used without intruding into any of the processes associated with the RC structures (Ohtsu, 1987; Colombo et al., 2003; Grosse et al., 2003; Ohno & Ohtsu, 2010).

The first recorded application of the AE technique for corrosion monitoring was by Dunn et al. (1984). The AE technique was used to monitor and characterize the corrosion process in a series of controlled laboratory tests. The study illustrated the sensitivity of the AE technique to evaluate the ongoing corrosion process, suggesting its feasibility as a technique for monitoring corrosion in the RC structures. There are two different approaches in analyzing AE data, one is the classical or parameter-based AE technique and the second is the quantitative or signal-based AE technique (Shiotani et al., 2001; Ohno & Ohtsu, 2010). These approaches could be used for monitoring corrosion in the RC structures, in the following sections.

2.3.2 AE parameters for corrosion monitoring

The parameter-based technique is useful for better characterization of the AE source (Titus et al., 1988; Ohtsu, 1996; Ohtsu, 2010). AE parameter analysis of hits or events, signal strength, and energy demonstrate that AE is readily applicable to the detection of corrosion in steel reinforcement, in order to identify the corrosion process, i.e. initiation of cracks and propagation of cracks, and to locate the early stages of steel corrosion (Yoon et al., 2000; Ohtsu & Tomoda, 2007b; Ohtsu & Tomoda, 2007a; Ismail et al., 2008; Ohtsu & Tomoda, 2008b; Kawasaki et al., 2010; Calabrese et al., 2013b; Elfergani et al., 2013; Kawasaki et al., 2013; Yu et al., 2014).

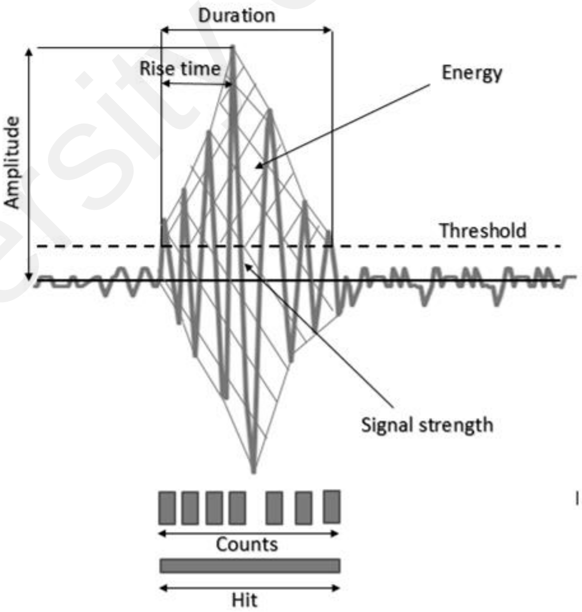

Figure 2. 16: Parameters reflecting of an AE waveform

The AE sources are also classified in terms of RA value and average frequency to classify the type of failure and the *b*-value or *Ib*-value of AE amplitude distribution for assessing the damage severity (Ohtsu & Tomoda, 2007b; Kawasaki et al., 2013; Behnia et al., 2014a; ElBatanouny et al., 2014b). The above AE parameters will be reviewed in the following sections. A simplified representation of an emitted signal as well as of commonly used parameters is shown in Figure 2.16. A summary of AE parameters and their contribution in providing information about the source event are listed in Table 2.5.

Table 2. 5: AE parameters and the applications of source events information

Variables	Parameter	Description
Time domain	Hit	Detection of an AE signal
	Event	Local material change, an event is a number of hits
	Amplitude	Largest voltage peak in the waveforms
	Rise time	Time elapsed from signal start and peak amplitude
	Duration	Time between signal start and signal end
	Threshold	Electronic compactor such that signals with amplitude larger than this level will be recorded
	Counts	Number of times AE signal crosses threshold
	Signal Strength	Area under the positive and negative envelope of linear voltage signal
	Energy	Area above threshold level
Frequency domain	Frequency spectrum	Nature of source event
Time-frequency domain	Spectrogram	Energy distribution of source event through time

2.3.2.1 AE hits

Many researchers have considered AE hits to be one of AE parameters used to study the onset of corrosion and the nucleation of crack in the RC structures (Yoon et al., 2000; Ohtsu & Tomoda, 2007a; Kawasaki et al., 2010; Kawasaki et al., 2013). Yoon et al. (2000) carried out AE monitoring in the RC beams subjected to four different levels of steel corrosion. It was observed that AE hits increased with an increase in the degree of corrosion. This trend could provide important information for estimating the degree of corrosion.

Ohtsu and Tomoda (2007a, 2008b) investigated AE hits of the RC specimens in sodium chloride (NaCl) concentration. Corresponding to two high AE activities, two periods the onset of corrosion and nucleation of cracks were observed. This could suggest that the AE activity observed corresponds to the corrosion loss of steel reinforcement in a marine environment observed by Melcher and Li (2006), and shown in Figure 2.17(a). At Phase 1, the onset of corrosion is initiated and the phase is dominated by the presence of oxygen and water. Then, corrosion loss decreases and stabilizes at Phase 2. The mass loss of steel corrosion increases again at Phase 3 and 4, where the corrosion penetrates inside and the expansion of corrosion products occurs due to anaerobic corrosion. Thus, based on the four phases of corrosion loss, two stages of corrosion activity are characterized, i.e. the onset of corrosion and the growth of corrosion products (nucleation of cracks).

On the other hand, Kawasaki et al (2010; 2013) showed cumulative AE hits and number of AE events in the corrosion process in a cyclic wet-dry test. The generating process of AE hits observed is classified into two stages, which refer to the process of corrosion loss of steel reinforcement due to chloride immersion as observed by Melcher and Li (2006), and previously by Ohtsu and Tomoda (2007a, 2008b). Stage 1 (onset of corrosion) corresponds to Phase 1 and 2 and Stage 2 (nucleation of crack) corresponds to Phase 3 and 4. Thus, the AE technique could detect corrosion at an early stage and AE activities from the beginning, as in Figure 2.17(b).

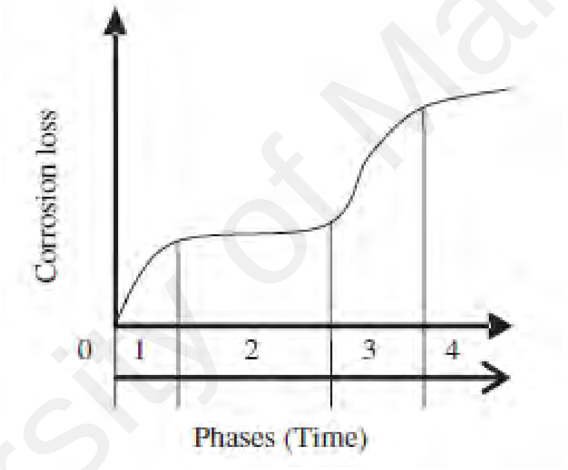

(a) Typical corrosion loss of steel reinforcement due to chloride immersion (Melchers & Li, 2006)

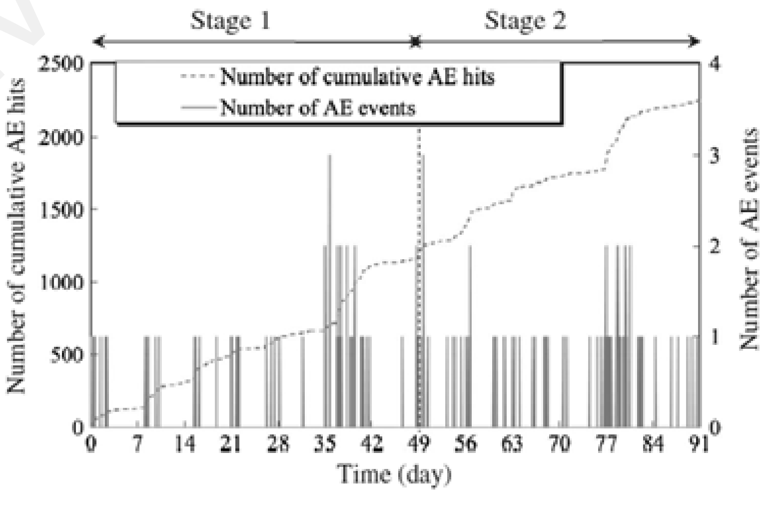

(b) Cumulative AE hits and number of AE events during corrosion test (Kawasaki et al., 2013)

Figure 2. 17: Typical corrosion loss and cumulative AE hits

2.3.2.2 Signal Strength (SS) and Cumulative Signal Strength (CSS)

Signal strength (SS) is one of the AE parameters, it is defined as the area under the voltage signal of AE over the duration of the waveforms. Since it provides a measure of the waveform energy released by the specimen, it is a rational damage indicator (Patil et al., 2014; Velez et al., 2014). Velez et al. (2014) show plots of the SS and cumulative signal strength (CSS) of corroded specimens in Figure 2.18. The dashed line indicates the onset of corrosion according to the results of the electrochemical methods (i.e. HCP and LPR). The SS of the prestressed specimen (P1) is attributed to the nucleation of cracks caused by the accumulation of corrosion products at the steel-concrete interface, as shown in Figure 2.18(a) (Velez et al., 2013).

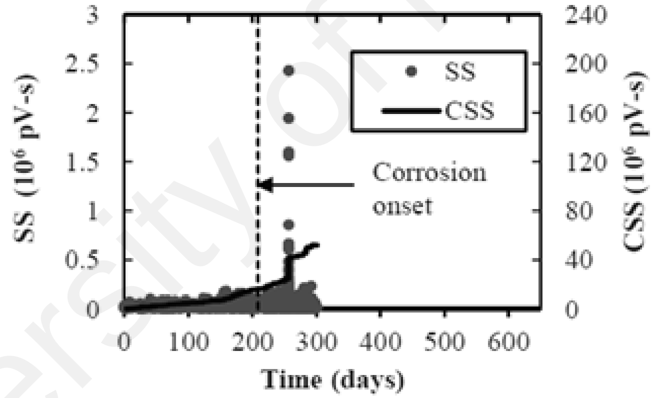

(a) prestressed (P1)

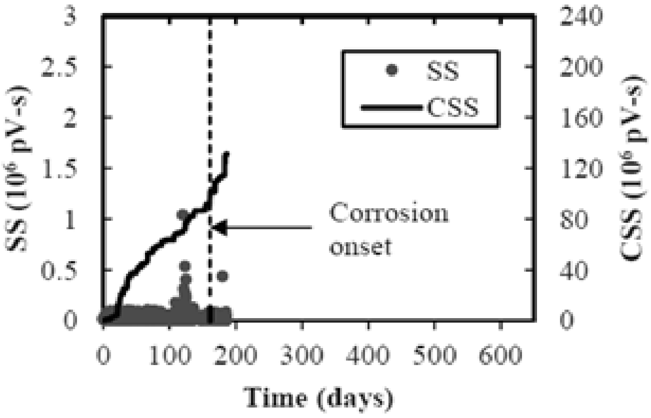

(b) non-prestressed (N3)

Figure 2. 18: SS and CSS of corroding specimens (Velez et al., 2014)

A different analysis is conducted on the SS of the non-prestressed specimen (N3) in Figure 2.18(b), which suggests that it could be an indicator of early crack formation due to corrosion. On the other hand, Figure 2.18(a) and (b) show that the cumulative signal strength (CSS) exhibits a clear rate change before the onset of corrosion according to electrochemical methods, which suggests that the AE technique could detect the onset of corrosion.

Patil et al. (2014) show the curve of CSS with a time of a concrete specimen in Figure 2.19. The curve clearly distinguishes the AE activity recorded for the concrete specimen under active corrosion. The CSS rate increases slowly in Phase 1 indicating de-passivation of the layer surrounding the steel reinforcement and the onset of corrosion. The presence of a sudden rise at the end of Phase 1 might indicates crack initiation due to steel corrosion. The rise of CSS in Phase 2 indicates corrosion activity. The sudden rise at the end of Phase 2 seems to be crack propagation leading to a macro-crack. Further phases are a repetition of Phase 2 continuing in the same manner. According to the phenomenological model of corrosion loss in a marine environment, the CSS curve obtained could also be divided into four phases, but the curve shows two sudden rises at the end of Phase 1 and 2. If these sudden rises are excluded from the CSS curve, the curve shown by the dotted line will be obtained and if connected by a smooth line, the curve would be exactly in agreement with the conventional curve (as shown in Figure 2.17(a)).

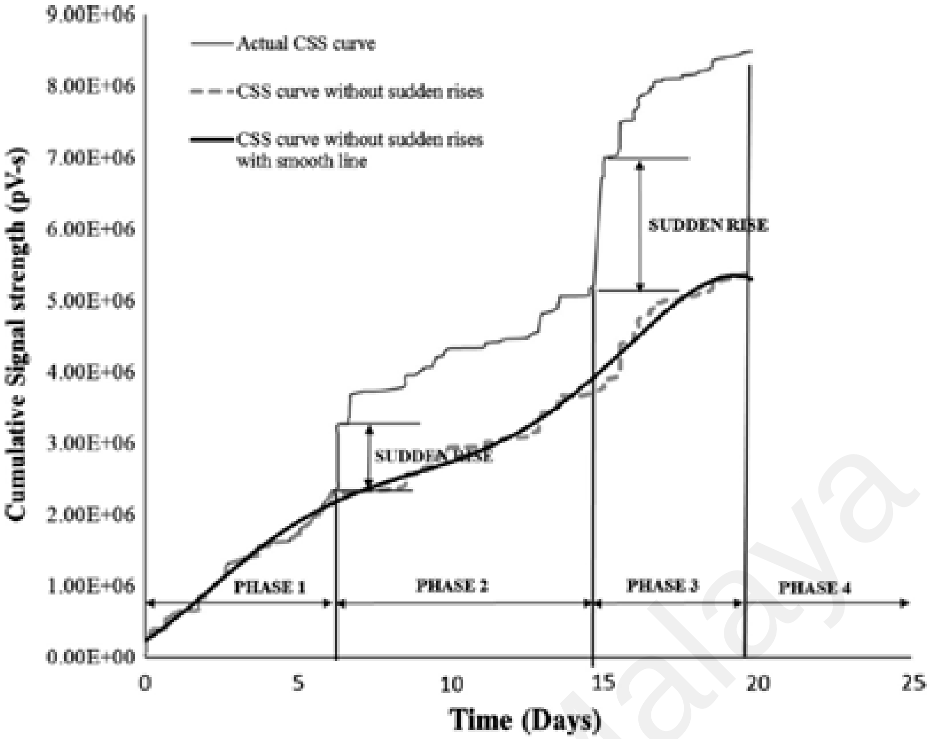

Figure 2. 19: The variations in CSS parameter which are similar to the curve of typical corrosion of steel reinforcement (Patil et al., 2014)

2.3.2.3 Absolute (ABS) Energy

The feature of ABS energy is a quantifiable measurement of energy obtained from all the AE events or hits. Ing et al. (2005) demonstrated the potential of ABS energy for identifying corrosion at an early stage before any external signs (i.e. cracking) of corrosion occur. The thickness of the concrete cover is found to have a significant effect on ABS energy in the early stages of steel corrosion. An exponential relationship has been established between the compressive strength and ABS energy, which shows that AE detects the sudden release of micro-fractures in the RC structure. In addition, increasing the steel diameter due to corrosion is found to increase the ABS energy of AE data.

2.3.2.4 RA values and Average Frequency

The characteristics of AE signals are estimated using two parameters: RA value and average frequency. The RA value and average frequency are defined from the AE parameters, i.e. rise time, maximum amplitude, counts, and duration (Ohtsu & Tomoda, 2007b; Ohtsu & Tomoda, 2008b), as shown in Equations 2.16 and 2.17.

RA value = Rise Time/Amplitude (2.16)

Average frequency = Counts/Duration (2.17)

A crack type is classified by the relationship between RA value and average frequency as shown in Figure 2.20. A tensile-type crack is referred to as an AE signal with a high average frequency and low RA value. A shear-type crack is identified by low average frequency and high RA value. This criterion is used to classify AE data detected in the corrosion process.

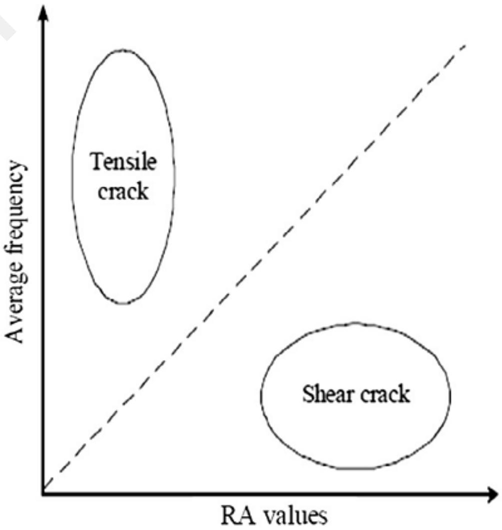

Figure 2. 20: Classification of cracks by AE indexes (JCMS-IIIB5706, 2003)

The RA values and the average frequency were used by Ohtsu and Tomoda (2008b) to classify AE sources, in two weeks of wet and dry tests in an RC slab. At 40 days, the RA value was high and the AF was low indicating shear cracking and later the RA value decreased and AF increased showing tensile cracking, as shown in Figure 2.21(a). However, on the other hand, Kawasaki et al. (2013) showed different trends for RA values and average frequency, as shown in Figure 2.21(b). The trendlines proposed to classify the onset of corrosion and nucleation of cracks in an RC beam.

At Stage 1, at 14 days to 21 days, RA values drastically increase and the average frequencies become smaller. The crack could be classified as a tensile crack due to the onset of corrosion in the RC beam. At Stage 2, an increase in RA values and a decrease in average frequencies were observed. This implies that generations of nucleation of a crack due to corrosion were induced in the concrete specimen. From the above references, the trends for RA value and average frequency which were proposed by Ohtsu and Tomoda (2008b) for an RC slab seem similar to the trends for RA value and average frequency proposed by Kawasaki et al. (2013) for an RC beam at Stage 1. The RA value is low and the average frequency is fairly high.

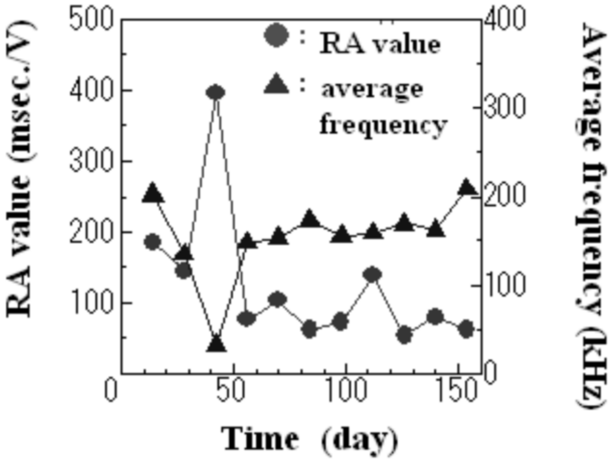

(a) Ohtsu and Tomoda (2008b)

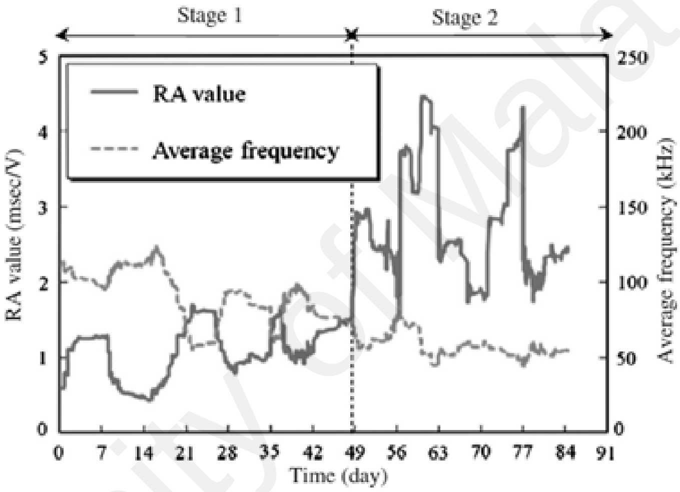

(b) Kawasaki et al. (2013)

Figure 2. 21: Variations in RA values and average frequency

2.3.2.5 *b*-value and *Ib*-value

Gutenberg and Richter have developed the *b*-value in seismology to understand the relationship between the magnitude and frequency of earthquakes (Gutenberg & Richter, 1954; Colombo et al., 2003; Rao & Prasanna Lakshmi, 2005), as shown in Equation (2.18):

$$Log_{10} N = a - bM, \tag{2.18}$$

Where:

M = the Richter magnitude of the event,

N = the incremental frequency, "*a*" is an empirical constant and

b = the *b*-value.

The value of M is proportional to the logarithm of the maximum amplitude A_{max} recorded in a seismic trace.

In the AE method, the same principle can be applied to determine the scaling of the amplitude distribution of the AE waves during the fracture process. In term of AE technique, the formula was modified by Colombo et al. (2003). Where, A_{max} is peak amplitude of the AE events in decibels (dB).

$$Log_{10} N = a - b(Amax) \tag{2.19}$$

However, to evaluate the slope failure and fracture process, Shiotani et al. (1999) improved the formula to improve b-value (*Ib*-value). This formulation is more based on statistical analysis such as mean and standard deviation for each of the AE amplitude sets. The formula is defined as:

$$Ib = \frac{Log\,N(\mu - \alpha 1\sigma) - Log\,N(\mu - \alpha 2\sigma)}{(\alpha 1 + \alpha 2)\sigma}, \tag{2.20}$$

Where:

σ = the standard deviation,

μ = the mean value of the amplitude distribution,

$\alpha 1$ = the coefficient related to the smaller amplitude, and

$\alpha 2$ = coefficient related to the fracture level.

In an RC structure application, the *b*-value is used as an indication and demarcation of degradation in the integrity of the RC specimen and is associated with cracks (Colombo et al., 2003). When cracks are forming, the large number of events increases causing a decrease in the *b*-value. When the distributed micro-crack occurs at an early stage of corrosion, the *b*-value is large and when the macro-crack begins to localize the *b*-value is small. Previous research has indicated that *b*-values below 1.0 correspond to the transition from micro-crack to macro-crack (Ono, 2010; ElBatanouny et al., 2012a).

Figure 2.22(a) shows an example of *b*-value distribution in acyclic wet-dry test in an RC slab by Ohtsu and Tomoda (2008b). The *b*-value becomes large at the 1st period and then the *b*-values keep fairly low. This result might imply a generation of small shear cracks at the 1st period. Then, nucleation of fairly large tensile cracks follows, leading to the 2nd period. For the latter, the *Ib*-value is adopted for calculation, based on cumulative distribution as proposed by Shiotani (2001). In contrast, the case where the *Ib*-values become small implies nucleation of large AE hits. The variations in the *Ib*-value are given by Kawasaki et al. (2013), as shown in Figure 2.22(b)**.** Large drops are observed between 21 days and 35 days, before the first dramatic increase in *Ib*-value. This might imply that the micro-cracks are generated at the onset of corrosion on the surface of the steel reinforcement. Due to high AE activity at Stage 2, the *Ib*-values decrease. Since the results of *Ib*-values at 56 and 84 days are comparatively lower than those of Stage 1, large-scale cracks are considered to be actively generated as corrosion-induced cracks in the RC beam. Furthermore, the fluctuations in *Ib*-values in Stage 2 are even bigger than in Stage 1. These results imply that the cracks are repeatedly generated due to corrosion products expansion.

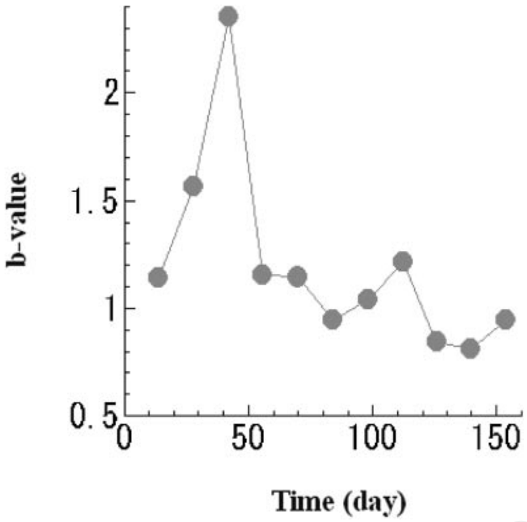

(a) b-value analysis (Ohtsu & Tomoda, 2008b)

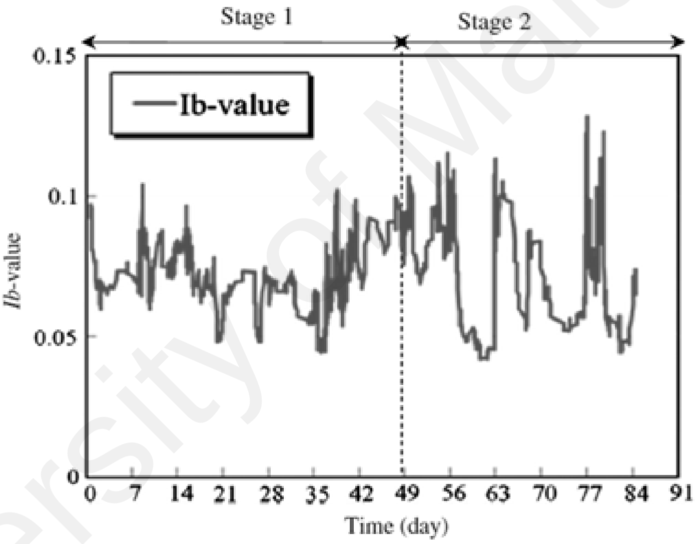

(b) *I*b-value analysis (Kawasaki et al., 2013)

Figure 2. 22: b-value and *I*b-value analysis

2.3.2.6 Intensity Analysis

Intensity analysis (IA) is used to quantify corrosion rate and level (Yuyama et al., 2007; ElBatanouny et al., 2012b; Mangual et al., 2012; ElBatanouny et al., 2014a). Intensity analysis evaluates the structural significance of an AE event by calculating two values called the historic index (*Hi*) and the severity index (*Sr*) from the signal strength

(Fowler et al., 1992; Gostautas et al., 2005; Mangual et al., 2013), as shown in Equation (2.8) and (2.9).

The historic index is used to estimate changes of the slope in the CSS plotted as a function of time. The severity index is the average of the large signal strength received at a sensor (i.e. 50 events having the highest signal strength) (Colombo et al., 2005). An increase in severity index often corresponds to structural or material damage.

$$\mathrm{Hi} = \frac{\mathrm{N}}{\mathrm{N} - \mathrm{K}_{\square}} + \left(\frac{\sum_{i=k+1}^{N} \mathrm{Soi}}{\sum_{n=1}^{N} Soi}\right), \tag{2.19}$$

$$\mathrm{Sr} = \frac{1}{\mathrm{J}_{\square}}\left(\sum_{m=1}^{\mathrm{J}} \mathrm{Som}\right), \tag{2.20}$$

Where:

Hi = Historic index,

N = Number of hits up to time t,

S_{oi} = Signal strength of the *i*th hit,

K = empirically derived constant based on material,

Sr = Severity index,

J = empirically derived constant based on material,

S_{om} = signal strength of the *m*th hit where the order of m is based on the magnitude of the signal strength.

The K and J value are related to N by the relations: K=0, N≤50; K=N−30, 51≤N≤200; K=O.85N, 201≤N≤500 and J=0, N<50; J=50, J≥50.

Velez et al. (2014) developed IA-based criteria for assessing steel corrosion in prestressed concrete (PC) piles. An assessment chart divides the criteria into three areas, i.e. no corrosion, early corrosion, and cracking, as shown in Figure 2.23. The figure shows that corroding and non-corroding specimens can be distinguished. In addition, the values of *Hi* (or *H(t)*) and *Sr* are consistent with the levels of corrosion.

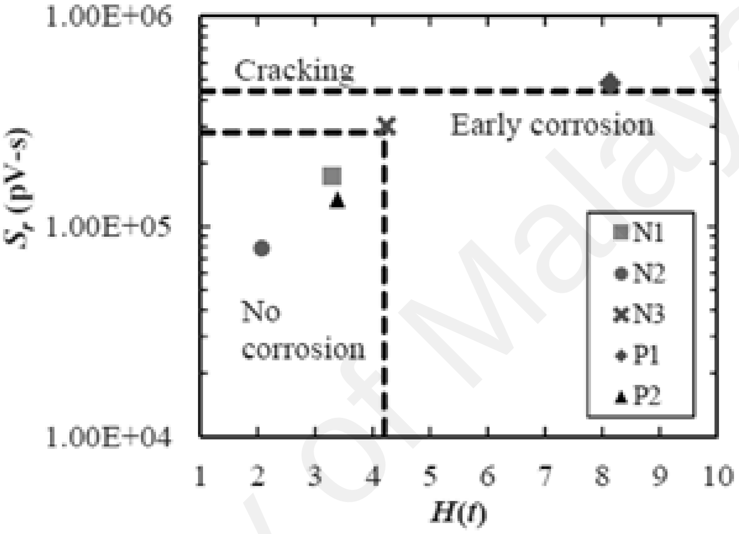

Figure 2. 23: Intensity analysis results (Velez et al., 2014)

2.3.2.7 Relaxation ratio

This refers to the ratio of average energy recorded during the unloading and loading phases of a concrete test (Colombo et al., 2005). The method is based on the effect of the cracks present in the RC structures. If the RC structure contains no cracks, the energy recorded during the unloading phase is low, however, if the cracks exist, the cracks emit significant energy during the unloading phase. Therefore, the greater amount of AE energy collected during the unloading phase compared to the loading phase could be used as an indicator of steel corrosion, if the relaxation ratio is more than 1 (ElBatanouny et al., 2014b).

2.3.3 Signal-based AE for corrosion monitoring

The signal-based technique involved a large number of waveforms that are recorded over a sufficiently short period time (Shiotani et al., 2001; Ohno & Ohtsu, 2010). The most prominent feature of this approach compared to parametric analysis is that it performs better in filtering signal noise, thus offering a better interpretation of the data monitoring in the RC structures (Behnia et al., 2014a).

2.3.3.1 AE source location

AE source location is performed to monitor the onset of steel corrosion, crack initiation due to steel corrosion, crack propagation, and location of steel corrosion in the RC structures. The AE source location is determined using the velocity of the longitudinal wave computed by the time differences among the arrival times of the first longitudinal wave detected by AE sensor (Yun et al., 2010). Figure 2.24 shows the AE source location of high corrosion activity in an RC slab by Ohtsu and Tomoda (2007a). It is reasonable to assume that AE sources are located around the steel reinforcement. This implies that corrosion and activities i.e. cracks and the expansion of corrosion products are readily detected and located by the AE technique.

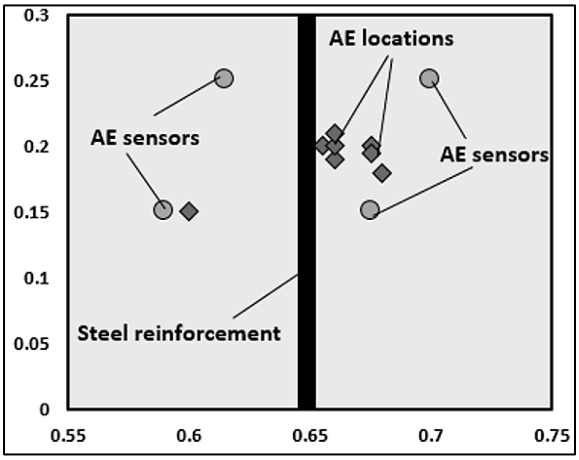

Figure 2. 24: AE source location of corroded RC slab, unit (m) (Ohtsu & Tomoda, 2007a)

2.3.3.2 SiGMA

In order to determine the moment tensor of an AE source, a simplified procedure has been developed and implemented as SiGMA (Simplified Green's functions for Moment Tensor Analysis) by Ohtsu (1998). The analysis consists of a three-dimensional (3D) AE source location procedure and moment tensor analysis of AE sources. The location of the AE source is determined from the differences in arrival time (Yun et al., 2010). Then, the components of the moment tensor are determined from the amplitudes of the first motions at the AE channels (Kawasaki et al., 2013). For this matter, SiGMA is a sophisticated method for estimating the size, orientation, crack type, location, and fracture mode of individual micro-cracking (Shigeishi & Ohtsu, 2001).

Kawasaki et al. (2013) presented the results of SiGMA at Stage 1 and Stage 2 of a cyclic wet-dry of corrosion test in an RC beam, as shown in Figure 2.25. The legend of SiGMA results is shown in Figure 2.25(c). Thirty AE events of cracking mechanisms are detected in Stage 1. These events are located around the steel reinforcement and at around the top side of the RC beam. This phenomenon could be related to the corrosion initiation as shear and mixed-mode cracks. In Stage 2, 19 AE events were determined to close the steel reinforcement with those of corrosion induced crack in the concrete and related to tensile cracks.

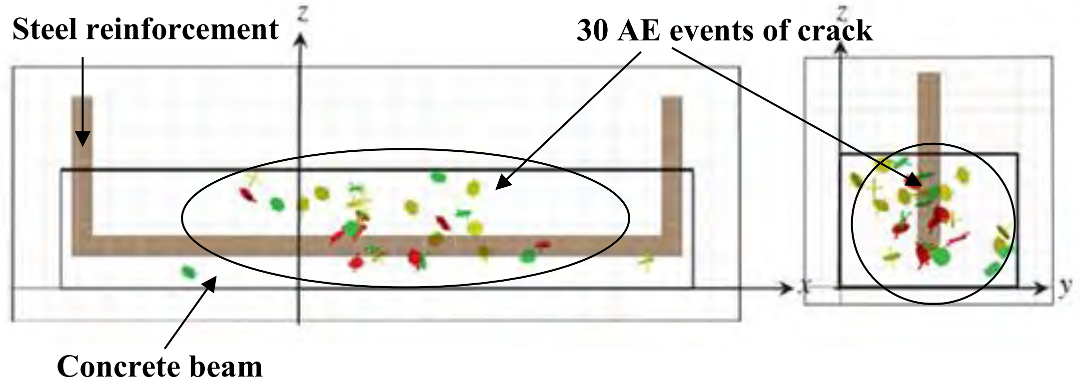

(a) Stages 1 (first 49 days)

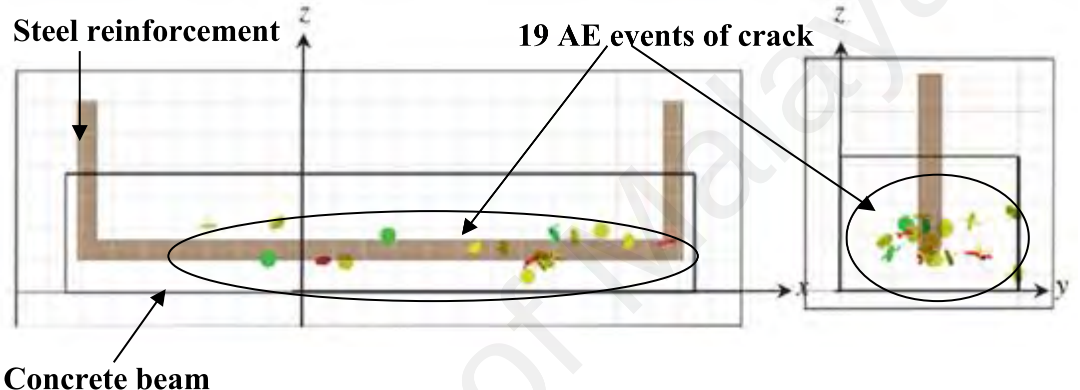

(b) Stages 2 (49-91 days)

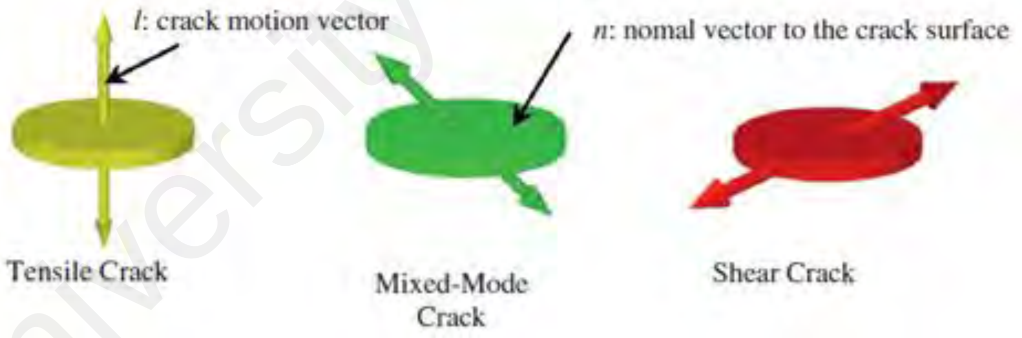

(c) Models of tensile, mixed-mode, and shear crack (Kawasaki et al., 2010)

Figure 2. 25: Results and models of SiGMA data

2.3.3.3 Noise filtering

The noise of AE data can originate from external sources, i.e. environment, traffic, man activities, etc. or be due to instrumental sources. Instrumental or electrical noise is generated by fluctuations occurring in the instrumentation including thermal noise, leakage current instability, and power supply voltage fluctuation (Baranov et al., 2003). Consequently, it is necessary to distinguish between real events related to real sources (such as crack propagation or fracture phenomena) and spurious events related to noise sources.

Kouroussis and Anastassopoulos (2001) proposed Unsupervised Pattern Recognition (UPR) to discriminate the signal and to distinguish real events of noise. The UPR applies mathematical or clustering algorithms in order to divide the set of AE hits into groups or clusters, which are close to one another in the same data set. This algorithm can discriminate the various sources of data that are related to the noise. Thus, Calabrese et al. (2012) carried out an investigation to detect steel corrosion-induced cracking in RC structures. It was focused on the use of multivariate analysis with the aim of establishing a procedure that would allow differentiation between steel corrosion based signals and background noise. Figure 2.26 shows the scheme for clustering methodology for noise removal. The three-step models were implemented using the Matlab software. The results show that more than 60% of detected signals were classified as noise.

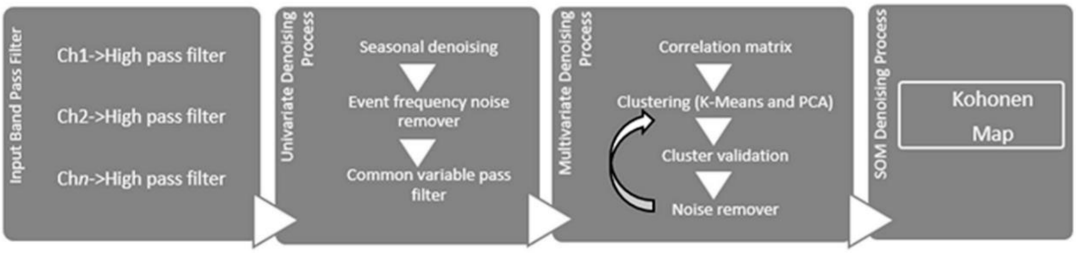

Figure 2. 26: AE noise filtering procedure (Calabrese et al., 2012)

2.4 Summary of AE technique for corrosion monitoring

The AE technique is more effective compared to other NDT methods for monitoring and detecting the steel corrosion in RC structures at an early stage of corrosion as the highlighted characteristics of AE parameters below:

1. The early number of cumulative AE hits can detect the corrosion process at an early stage. If there is a significant increase of cumulative AE hits, it corresponds to the onset of steel corrosion in RC structures.
2. The sudden rise in cumulative signal strength (CSS) and absolute energy (ABS), might indicate crack initiation due to steel corrosion in RC structures.
3. The distribution of RA value and average frequency (AF) also proposed as a means classifying the onset of corrosion and nucleation of cracks. The onset of corrosion is identified by an increase in RA value and a decrease in AF. In addition, the nucleation of cracks is implied by an increase in RA value and a decrease in AF at the next stage. Therefore, the steel corrosion of RC structures can be analyzed according to two stages, i.e. the onset of corrosion and the nucleation of a crack.
4. The *b*-value, *Ib*-value, and intensity analysis (IA) are developed to characterize the damage in RC structures. Previous researchers have indicated that a *b*-value below 1.0 indicates the transition from micro-cracking to macro-cracking. The large fluctuations in *Ib*-value imply that these cracks are generally repeated due to the expansion of corrosion product. On the other hand, IA uses several criteria to identify the condition of the structure (i.e. no corrosion, early corrosion, and cracking).

These capabilities make AE technique a strong candidate to become an efficient NDT method for analyzing and assessing the corroded RC structures occurring in real-time, giving it an advantage over other NDT methods. Therefore, it is necessary to use the AE technique to analyze and assess the steel corrosion in the RC structures subjected to flexural loading.

CHAPTER 3: METHODOLOGY

3.1 Introduction

This chapter introduces the properties of materials and their preparation prior to casting, concrete mixture properties, and experimental test methods which were used toward accomplishing the current research. Three (3) independent experiments were conducted which will be presented in this chapter, respectively. The experiment 1 was conducted to achieve the objectives 1, 2 and 4 while the experiment 2 and 3 were conducted to achieve all of objectives. The different between experiment 2 and 3 was the accelerated corrosion process of the beam specimens. The accelerated corrosion process of experiment 2 and 3 will be explained in the next section 3.2.2.

The research methodology was divided into different stages as follow:

a) Fabrication of RC beam specimens: three experiments.
b) Accelerating steel corrosion of RC beam specimens using impressed current technique.
c) Laboratory tests: test of hardened concrete and mechanical three-point loading test or flexural test.
d) Data acquisitions using AE technique.
e) Data analysis: mechanical properties data and AE data.

Based on data analysis, an assessment of flexural behaviour of steel reinforcement in concrete using AE technique was proposed. The flowchart of the research methodology is shown in Figure 3.1.

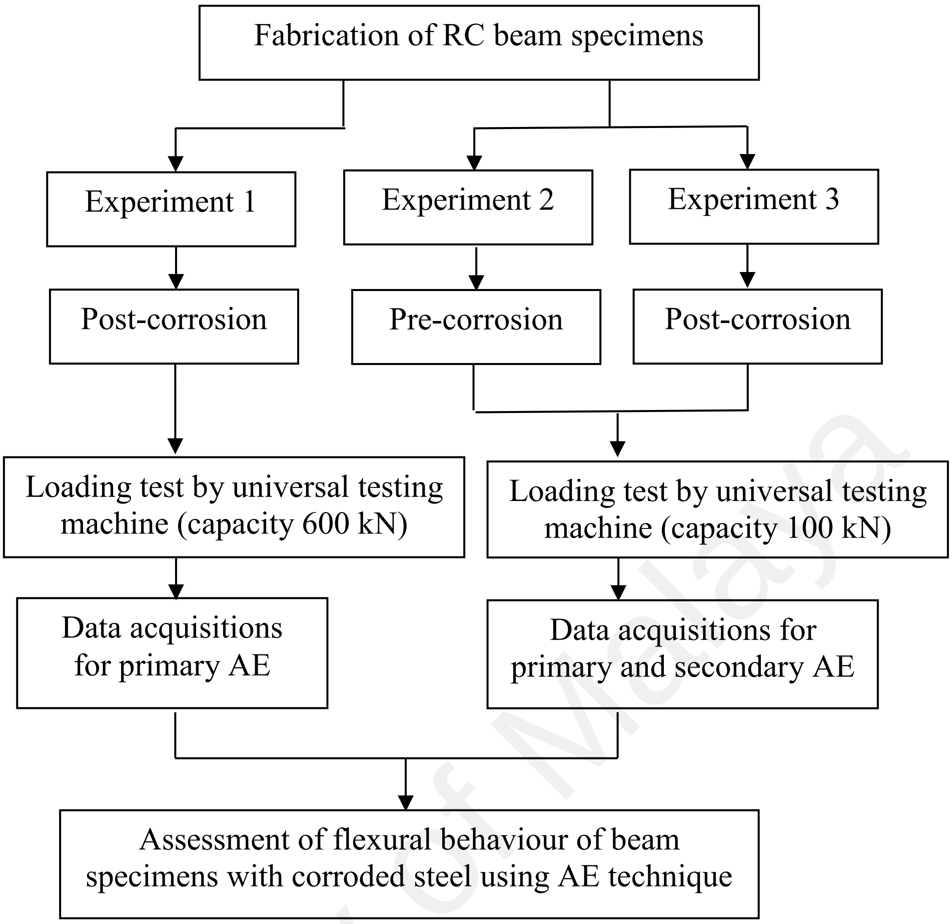

Figure 3. 1: Flowchart of Research Methodology

3.2 Fabrication of Reinforced Concrete (RC) Beams

3.2.1 Concrete beam specimens of Experiment 1

As shown in Figure 3.2, four beam specimens (i.e. 1000 x 150 x 150 mm^3) with 0%, 4.55%, 16.68% and 32.37% of corrosion level were prepared. The concrete specimen was designed in accordance to the British Standard BS 8110-1 (1997) to achieve 30 MPa of compressive strength at 28 days after casting of concrete. Portland cement, uncrushed sand, crushed limestone with a maximum aggregate size of 20 mm are used to prepare the concrete mixture. The dry density of concrete is 2430 kg/m^3. For steel reinforcements, deformed bars of sizes 12 mm and 16 mm complying to BS 4449 (2005) were used as compression and tension steel reinforcements, respectively. The stirrup of size 8 mm and spacing 240 mm was used for shear links. The cover concrete was designed as 36 mm.

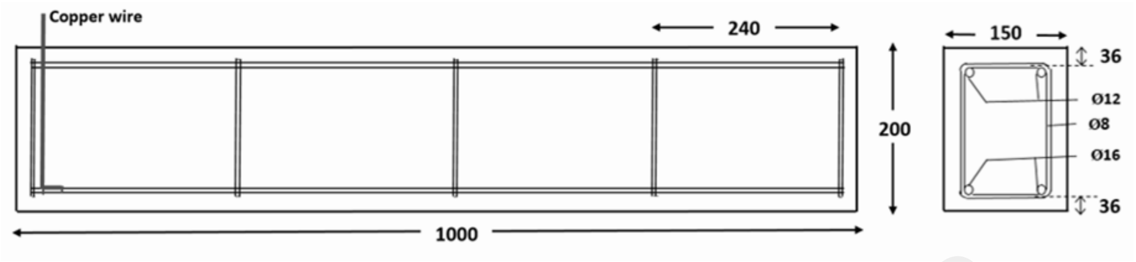

Figure 3. 2: Details of beam specimen of experiment 1 (units are in mm)

The copper wire was connected with steel reinforcement and positive pole of power supply as anode of the accelerated corrosion process. The accelerated corrosion process will be explained in the following section. Table 3.1 gives the proportions of raw materials used for the concrete mix. Figure 3.3 shows the casting of the specimens.

Table 3. 1: Concrete mixture proportions

Concrete Mixture	Quantity	
Cement Content (kg/m^3)	380	
Water to cement ratio	0.5	
Slump value (mm)	65	
	Per m^3	Per one beam (0.0225 m^3)
Cement (kg)	380	8.55
Water (kg/L)	190	4.275
Sand (kg)	780	17.55
Course Aggregate (kg)	1080	24.30

(a) steel reinforcements

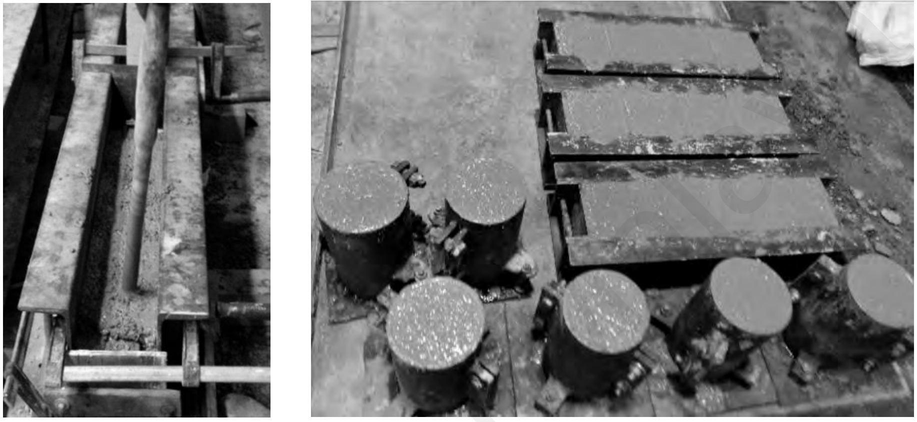

(b) casting of beam (c) cube and cylindrical specimens

Figure 3. 3: The casting of the specimens

Table 3.2 shows the type of specimens and its description. For corroded beam, impressed current technique will be applied, as described in Section 3.3.

Table 3. 2: Specimen descriptions of experiment 1

Specimens	Description
Control	Normal steel reinforcement without corrosion
LC	4.55 % of steel corrosion
MC	16.68 % of steel corrosion
HC	32.37 % of steel corrosion

3.2.2 Concrete beam specimens of Experiment 2 and 3

There are two different types of corrosion process methods for the corroded beam specimens, i.e. pre-corrosion beam specimens for experiment 2 and post-corrosion beam specimens for experiment 3, to quantitatively and qualitatively understand the effect of steel corrosion of the beam specimens on the flexural behaviour. For the pre-corrosion beam specimens, the specimens were prepared using corroded steel reinforcement. For these beam specimens, after the accelerated corrosion process of the steel reinforcements using impressed current technique, the steel reinforcements were cleaned to remove the rust (corrosion products) on its surface, based on the ASTM G1-03 (2003). While for the post-corrosion beam specimens, the steel reinforcement of the beam specimens was corroded after concrete casting. A total of six beam specimens of experiment 2 and six beam specimens of experiment 3 with the same dimension of 100 x 100 x 500 mm^3 were fabricated. The details of the beam specimens are shown in Figure 3.4.

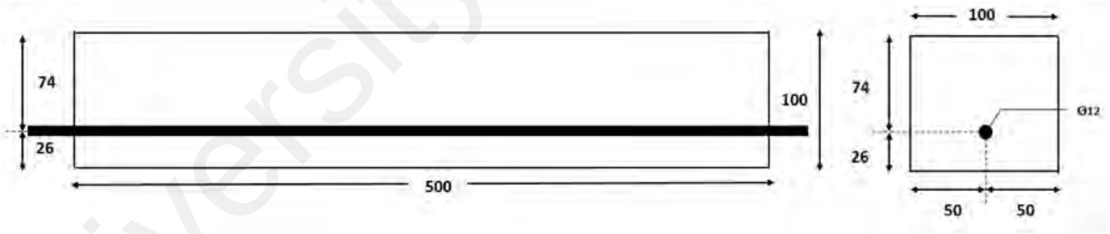

Figure 3. 4: Details of the beam specimen for experiment 2 and 3 (units are in mm)

The beam specimens of the experiments 2 and 3 were designed in the same batch of concrete casting, in accordance to BS 8110-1 (1997) to achieve 28 MPa of compressive strength at 28 days after casting. The dry density of concrete is 2192.91 kg/m^3. The beam specimens with 0%, 8.17%, 9.06%, 24.21%, 27.56%, 50.57% and 0%, 9.54%, 19.84%, 24.60%, 31.91%, 39.84% of corrosion levels were prepared in this study for pre-corroded and post-corrosion beam specimens, respectively. The steel reinforcement of sizes 12 mm in compliance to BS 4449 (2005) was used as tension reinforcement. The bottom cover was 26 mm from the concrete surface.

Table 3. 3: Concrete mixture proportions

Concrete Mixture	Quantity	
Cement Content (kg/m^3)	392.95	
Water to Cement Ratio	0.5429	
Slump value (mm)	67	
	Per m^3	Per beam (0.005 m^3)
Cement (kg)	392.95	1.965
Water (kg)	213.33	1.067
Sand (kg)	1003.76	5.019
Coarse Aggregate (kg)	752.91	3.765

Ordinary Portland cement (OPC), river sand, and crushed granite with a maximum aggregate size of 10 mm were used to prepare the concrete mixture. Table 3.2 gives the proportions of raw materials used for the concrete mixture. Figure 3.5 shows the casting of the beam specimens. Table 3.4 shows the type of specimens and its description. Both concrete casting for experiments 2 and 3 were from the same batch of concrete mix.

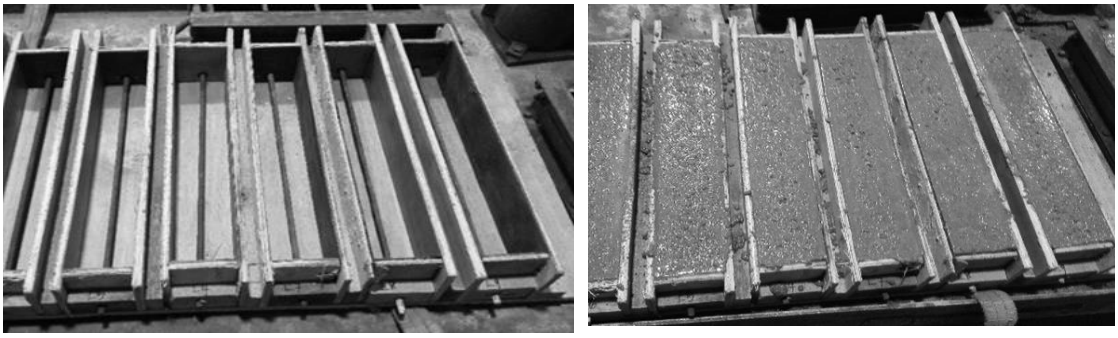

(a) Wooden moulds for beam (b) casting of beams

(c) cylinder specimens (d) cube specimens

Figure 3. 5: The casting of the specimens

Table 3. 4: Specimen descriptions of experiments 2 and 3

Experiment	Specimens	Description
Experiment 2 (pre-corrosion)	S0	Normal steel reinforcement without corrosion
	S8	8.17 % of steel corrosion
	S9	9.06 % of steel corrosion
	S24	24.21 % of steel corrosion
	S28	27.56 % of steel corrosion
	S51	50.57 % of steel corrosion
Experiment 3 (post-corrosion)	S0	Normal steel reinforcement without corrosion
	S10	9.54 % of steel corrosion
	S20	19.84 % of steel corrosion
	S25	24.60 % of steel corrosion
	S32	31.91 % of steel corrosion
	S40	39.84 % of steel corrosion

3.3 Accelerating steel corrosion of concrete beams

Corrosion of steel reinforcement in concrete beams is a long process. This is due to steel reinforcements in concrete is normally coated under a passive layer as a protection on the steel surface. Therefore, to speed up the corrosion of steel reinforcements for further experiment testing, accelerated corrosion technique was used. In this study, the specimens were subjected to accelerated corrosion by an impressed current technique after the completion of the water curing at 28 days of casting. The accelerated corrosion process adopted the impressed current technique that conforms to ASTM G1-03 (2003a) and ASTM G31-72 (2004a). During the accelerated corrosion process for the beams, the control beam was under the flexural loading test at 28th day of concrete age.

Figure 3.6 shows the schematic representation of the accelerated corrosion process. The specimens were partially immersed in 5% sodium chloride (NaCl) solution by volume in a container, i.e. a plastic water tank for experiment 1 and a plastic box for the experiment 2 and 3. The steel reinforcements of the beam specimen were corroded after 28th of concrete casting in the experiment 1 and 3. However, for experiment 2 (pre-corrosion specimens), the steel reinforcements were corroded prior to concrete casting, as shown in Figure 3.6 (c). A direct current (DC) power supply was used in the electrolysis of the chemical solution, from which the positive terminal was connected by the copper wire to the steel reinforcement as the anode. Meanwhile, the negative terminal was connected by an aluminium plate for experiment 1 and steel reinforcement bar for experiment 2 and 3 as the cathode.

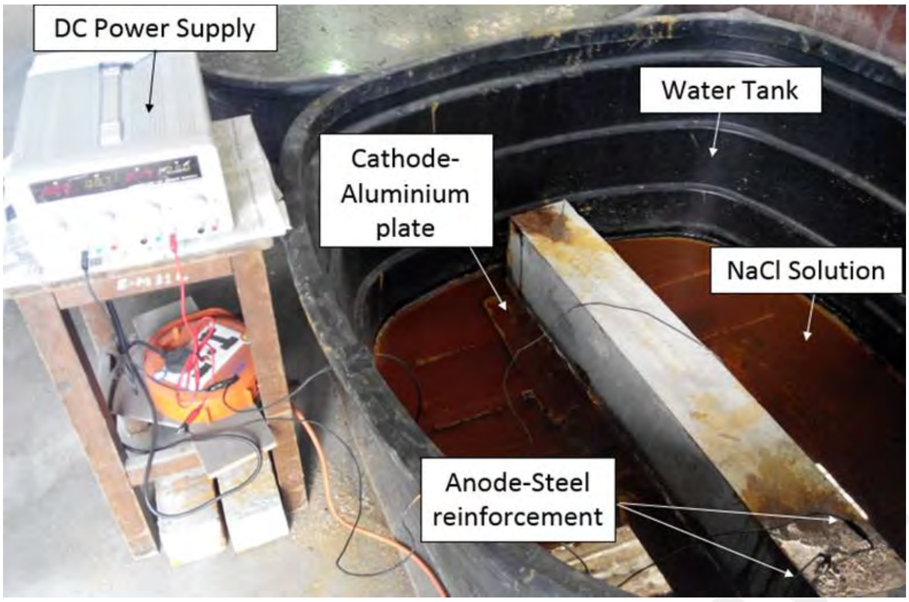

(a) Experiment 1

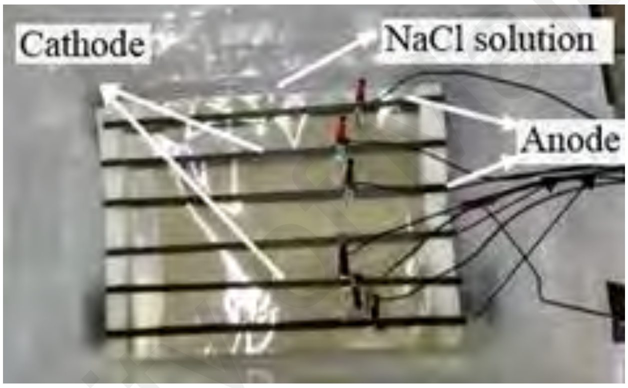

(b) Pre-corrosion of experiment 2

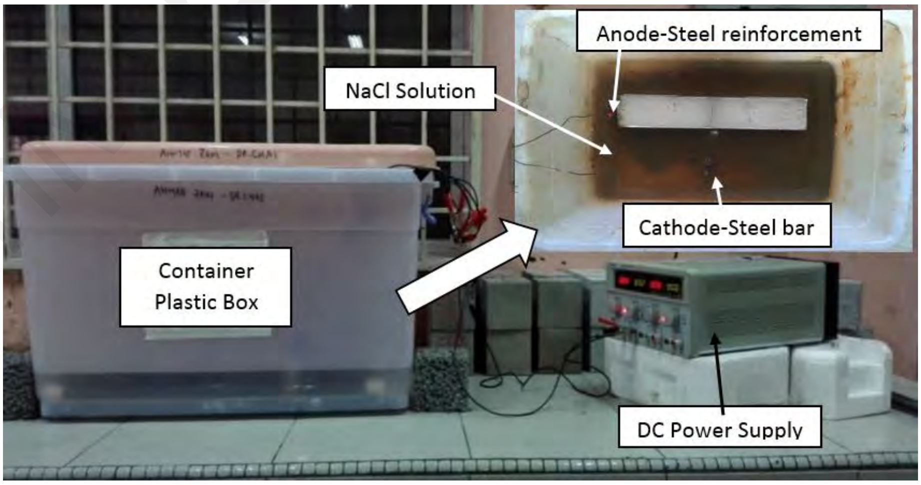

(c) Experiment 3

Figure 3. 6: Experimental setup of the accelerated corrosion process

A constant current was applied in the corrosion process. The corrosion process was continuously monitored until the steel reinforcement was corroded with required mass loss. The mass loss was determined based on converting the current flow using Faraday's law, as shown in Equation 3.1. For the experiment 1, three beam specimens were casted and undergone the post-corrosion process after 28th days curing. Based on the mass loss, they are categorised into the low corrosion (LC), medium corrosion (MC), and high corrosion (HC).

$$\Delta m = \frac{M.I.t}{z.F}, \tag{3.1}$$

Where:

Δm = mass of steel consumed (g, gram),

M = atomic or molecular weight of metal (56 g/mol for steel),

I = current (A, amperes),

t = time current or potentials applied (s, seconds),

z = ionic charge or electrons transferred in the half-cell reaction (2 for steel) and

F = Faraday's constant (96500 A/s).

Therefore, after the flexure tests, the beam specimens of experiment 1 and 3 were hacked to retrieve the corroded steel reinforcements. The reinforcements of all experiments were then cleaned to remove corrosion product (rust) in accordance to ASTM G1-03 (2003a) and weighed to determine the actual mass loss of the reinforcements. Furthermore, especially for experiment 3, the reinforcements were tested to obtain the tensile strength.

3.4 Test for hardened concrete properties

A material are classified as ductile or brittle. Normally, a ductile material has fracture strength lower than its ultimate tensile strength and experiences extensive plastic deformation before fracture. Conversely, a brittle material has fracture strength equivalent to ultimate tensile strength and there is very little or no plastic deformation upon fracture. It will break without any significant deformation and absorb relatively little energy prior to fracture. Usually, if two materials have the same strength and hardness, the one that has the higher ductility is more desirable. The tensile stress-strain behaviours for both ductile and brittle materials are schematically illustrated in Figure 3.7.

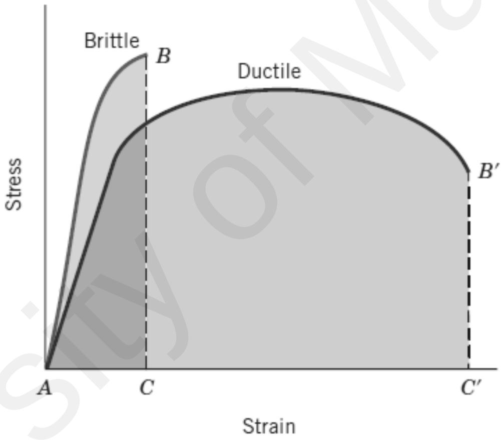

Figure 3. 7: Tensile stress-strain behaviours for brittle and ductile materials

3.4.1 Compressive Strength

The concrete compressive strength was determined in accordance with BS 1881-116 (1983a). The concrete compressive strength test was carried out on the 7th and 28th day. The specimens consist of 100 mm cubes as shown in Figure 3.8 (a). Three cube specimens were tested in order to get the average results. A standard compression testing machine with a maximum capacity of 300 kN (ELE) was used to conduct the tests. The loading rate was set as 2.40 kN/s.

(a) Cube specimen (b) Compression testing machine

Figure 3. 8: Compression test for concrete

3.4.2 Modulus of elasticity

The modulus of elasticity of the concrete specimens was determined in accordance with BS 1881-121 (1983b). The test was carried out at concrete age of 28th day. The specimens used were cylinders of 150 mm in diameter and 300 mm in the height as shown in Figure 3.9 (a). The pacing rate of the test was set at 4.42 kN/s. The modulus of elasticity test setup is shown in Figure 3.9 (b). To compute the value of modulus of elasticity of the concrete, the formula below is used:

$$\text{Modulus of Elasticity} = \text{change in stress / change in strain} \qquad (3.2)$$

$$= (\sigma_2 - \sigma_1)/(\varepsilon_2 - \varepsilon_1)$$

Where:

σ_2 = stress at 0.85 of cube compressive strength/3

σ_1 = basic stress at 0.5 N/mm^2

ε_2 = strain at a stress of σ_2

ε_1 = strain at a stress of σ_1

The longitudinal strains (ε) are calculated on the basis of the deformations measured during each test. The strain $\varepsilon 1$ are recorded after the completion of some preloading and a waiting period of 60 s under the basic stress of 0.5 N/mm^2. After that, reload the specimen to stress σ_2 to specified rate and measurement line record the strain reading σ_1 with 30 s.

(a) Cylinder specimen (b) Compression testing machine

Figure 3. 9: Modulus of elasticity test for concrete

3.5 Data acquisitions

3.5.1 Experiment 1 (Monitoring fracture of steel corroded reinforced concrete members under flexure by acoustic emission technique)

All the beam specimens were subjected to three-point monotonic flexural load using universal testing machine (INSTRON Satec Series) with a maximum capacity of 600 kN, as shown in Figure 3.10. The loading rate of this experiment is 0.15 mm/min.

Figure 3. 10: Universal testing machine (INSTRON Satec Series of 600 kN)

AE monitoring of beam fracture was conducted throughout the load testing. For this step, a six-channel PCI-2 AE System (MITRAS Group, Inc.) was used. The system was connected by six AE sensors of 150 kHz resonant frequency (SR150M) together with 40 dB preamplifiers by Soundwel Co., Ltd, as shown in Figure 3.11. The resonant frequency sensors are suitable for concrete monitoring. The AE sensor converts the mechanical energy carried by the elastic wave into an electrical signal. The sensors were mounted to the surface of concrete using electron wax as the coupling agent.

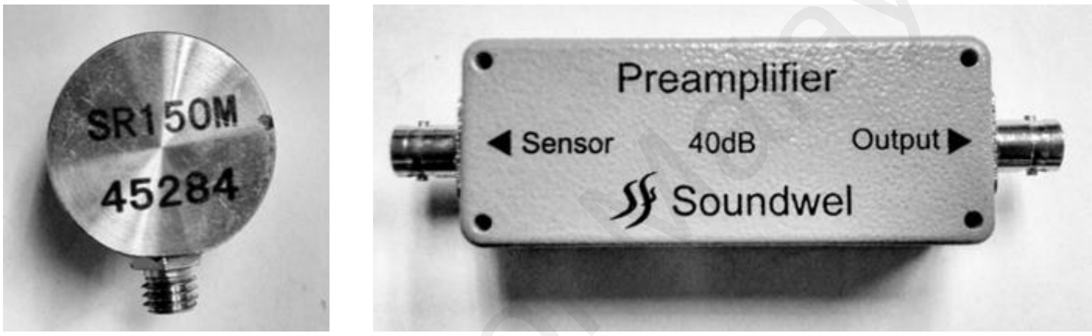

(a) AE sensor (b) Pre-amplifier

Figure 3. 11: AE sensor and pre-amplifier

Figure 3.12 illustrates the sensor placements on the beam specimen. The 6 AE sensors totally used to detect and capture energy emitted from the cracking of the beam specimens when mechanical loading was ongoing. There is no standard for selecting the location of the AE sensors as long as the sensors can trace the wave around the sensors. In the measurements, the sampling rate was set to 2 MHz, with pre-trigger at 256.000 μs and data length at 2k. The hit definition time and hit lockout time were configured as 800 μs and 1000 μs, respectively. To eliminate electrical and mechanical noises generated during monitoring, the threshold level was set at 45 dB.

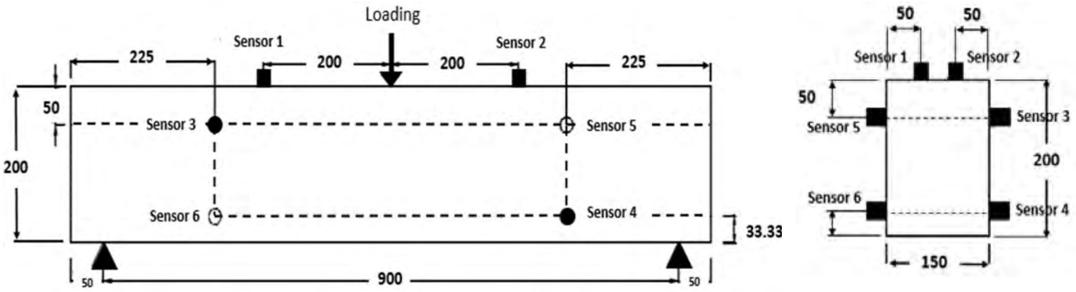

(a) AE sensor placements (units are in mm)

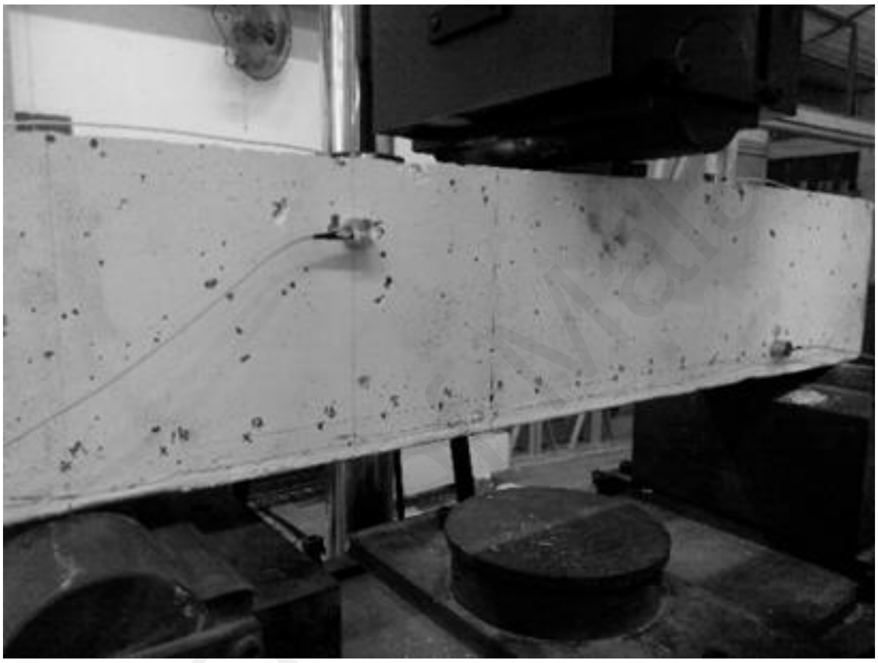

(b) the photograph

Figure 3. 12: AE sensor placements in experiment 1

3.5.2 Experiment 2 and 3 (Reliability of Primary and Secondary AE for Corrosion Evaluation of Concrete Structures)

All the beam specimens of experiment 2 and 3 were subjected to three-point cyclic and monotonic flexural load using a universal testing machine (INSTRON Satec Series) with a maximum capacity of 100 kN, as shown in Figure 3.13. The loading rate of experiments 2 and 3 is 0.1 mm/min. Each specimen was supported at both ends, and the distance between the loading point and each support was 200 mm, as shown in Figure 3.13 (b). The AE monitoring of specimen fracture was conducted throughout the loading test. A six-channel PCI-2 AE System (MITRAS Group, Inc.) was used in this test. The system was connected to the six AE sensors of 150 kHz resonant frequency (SR150M) together with 40 dB preamplifiers by Soundwel Co., Ltd, as shown in Figure 3.11. The sensors were mounted to the surface of the beam specimen using electron wax as the coupling agent.

Figure 3. 13: Universal testing machine (INSTRON Satec Series of 100 kN)

Figure 3.14 illustrates the AE sensor placements on the beam specimen of experiment 2 and 3. The locations for sensors were selected randomly at the vicinity of the steel reinforcements, as long as the sensors can trace the wave around the sensors. For this experiment, the location is outside of the cracks region to avoid the sensors fall down due to cracking of the beams during the loading test. In terms of measurements, the sampling rate was set to 2 MHz, with pre-trigger at 256.000 µs and data length at 2k. The hit definition time and hit lockout time were configured as 800 µs and 1000 µs, respectively. The threshold level was set at 45 dB to eliminate electrical and mechanical noises generated during monitoring.

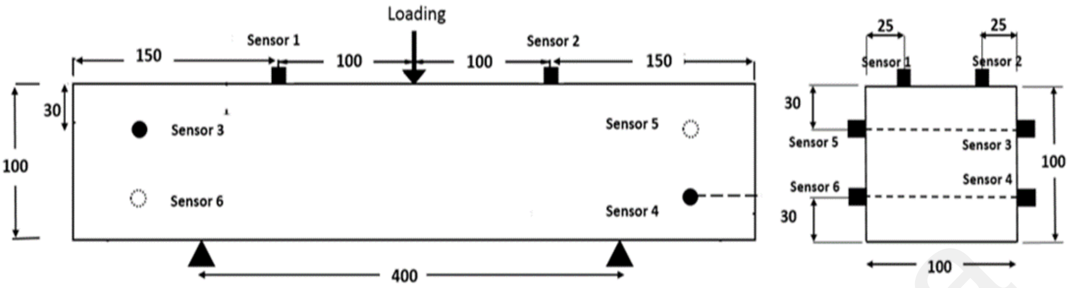

(a) AE sensor placements (units are in mm)

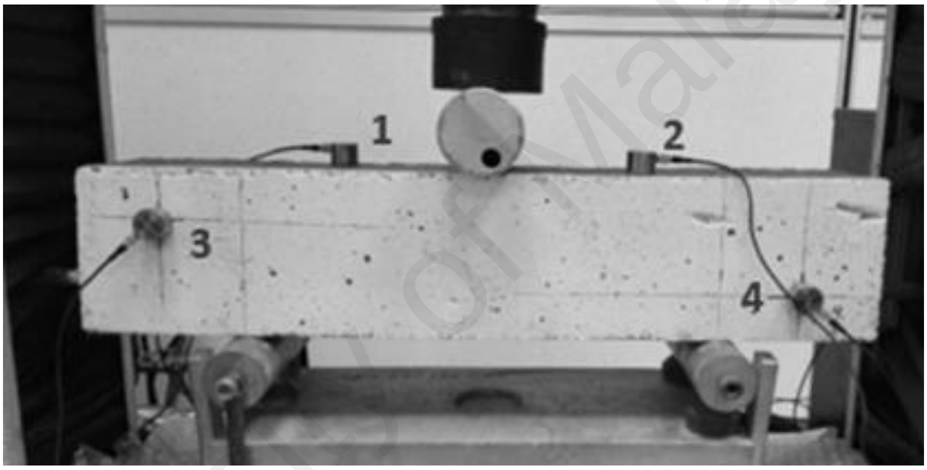

(b) the photograph

Figure 3. 14: AE sensor placements of experiment 2 and 3

3.6 Tensile Test of Steel Reinforcements

Especially, for the experiment 3, the six pieces of steel reinforcements from the crushed post-corrosion beam specimens after load testing were collected for tensile testing using Universal Tensile Machine (INSTRON SATEC Series) with a maximum capacity of 270 kN to evaluate their mechanical properties. The mechanical properties, such as yielding and ultimate capacity were investigated according to the standard ASTM A370 (2017). The tensile test set up is shown in Figure 3.15.

Figure 3. 15: Tensile test of the reinforcement

3.7 Data Analysis

After testing the concrete beams with AE technique, the AE data will be analyzed for AE parameters analysis. The source types of AE monitoring of the specimens can be classified as primary AE and secondary AE (Holford, 2000). The primary AE is related to crack growth and fracture mechanic parameters while in secondary AE comprises all other sources, including the micro-fracture. The secondary AE sources induced by the cyclic load with maximum load level is half of the estimated first visible cracks, that is 4 kN, as shown in Figure 3.16. The loading cycle load is intended to study the effect of significant damage before the first cracking occurs. Furthermore, the number of cycles were chosen based on many references, such as: Riedge and Ziehl (2006). The sources of primary AE are recorded during activities of monotonic loading until failure of the specimens.

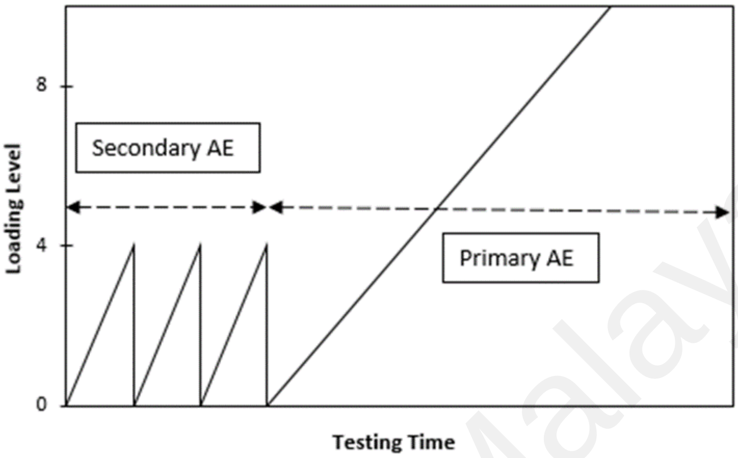

Figure 3. 16: Specimen load testing

CHAPTER 4: RESULTS AND DISCUSSIONS FOR EXPERIMENT 1 MONITORING FRACTURE MECHANISM OF CORRODED RC MEMBERS UNDER FLEXURE

4.1 Introduction

Table 4.1 shows the results of compressive strength and the modulus of elasticity tests for concrete cubes and cylinders of Experiment 1. From the results, the average of 28th day compressive strength is 39.57 MPa. The average modulus of elasticity of cylinder at 28th day after casting is 30.87 GPa.

Table 4. 1: Compressive strength and modulus of elasticity of experiment 1

Age of concrete	Compressive strength (MPa)		Average modulus of elasticity (GPa)
	For one specimen	Average	
7th day	33.79	33.66	-
	33.39		
	33.79		
28th day	38.57	39.47	30.87
	41.27		
	38.57		

After the flexure tests, the beam specimens were hacked to retrieve the steel reinforcements. The steel reinforcements were then cleaned to remove rust in accordance to ASTM G1-03 (2003) and weighed to determine the actual mass loss of steel reinforcement. The mass loss (corrosion level) was calculated as the mass loss of the steel before and after the testing, as shown in Equation 2.13. The corrosion levels of beam specimens were 4.55% for low corrosion (LC) beam, 16.36% for medium corrosion (MC) beam and 32.37% for high corrosion (HC) beam. The cleaned reinforcements with different levels of corrosion are shown in Figure 4.1. The quantitative results are tabulated in Table 4.2.

(a) Control

(b) LC

(c) MC

(d) HC

Figure 4. 1: Condition of reinforcements obtained from beam specimens subject to different levels of corrosion of experiment 1

Table 4. 2: Quantitative results of steel reinforcements of experiment 1

Specimens	Tension Steel	Initial Mass (g)	Final Mass (g)	Mass loss, Δm (g)	Corrosion Level (%)	Average Corrosion Level (%)
Control	1	1769.50	1769.50	0	0	0
	2	1764.03	1764.03	0	0	
LC	1	1795.40	1735.28	60.12	3.35	4.55
	2	1797.20	1775.55	21.65	1.20	
MC	1	1789.55	1623.10	166.45	9.30	16.86
	2	1793.90	1658.32	135.58	7.56	
HC	1	1779.70	1527.87	251.83	14.15	32.37
	2	1780.67	1456.22	324.45	18.22	

4.2 Mechanical Behaviour

Figure 4.2 shows the load against mid-span deflection curves of the beam specimens. The loading rate of the beam specimens is 0.15 mm/min. The failure load dropped from approximately 182.57 kN for the Control beam specimen to less than 150 kN for LC and HC beam specimens, justifying the decrease in beam stiffness as a result of steel corrosion. The stiffness of Control beam specimen decrease from 48.08 to 37.39, 30.99 and 33.17 for LC, MC and HC beam specimens, respectively. The stiffness of each beam specimen is shown in Table 4.3.

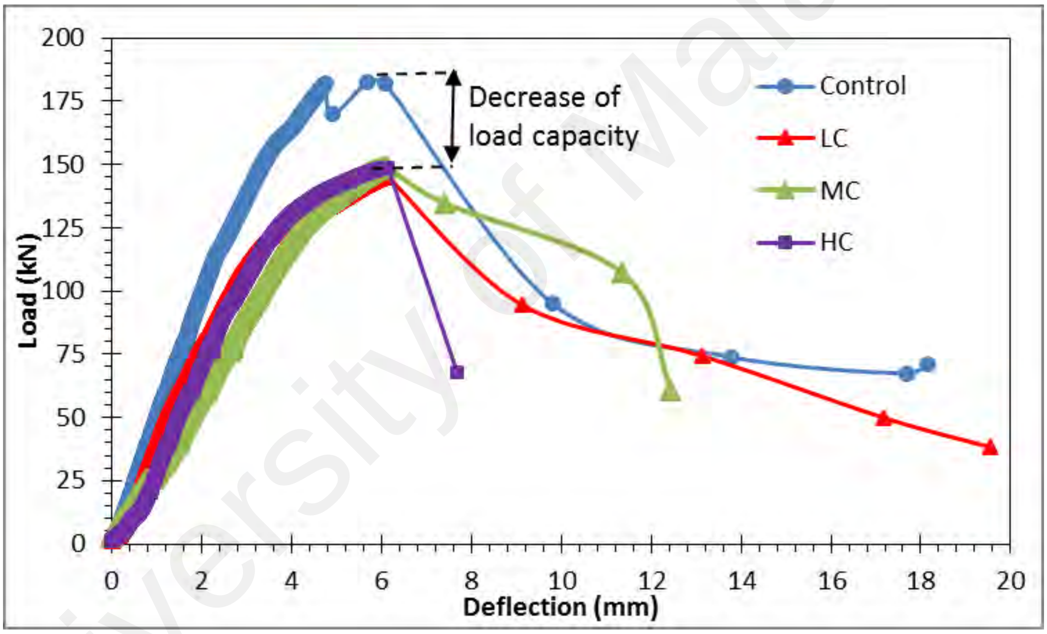

Figure 4. 2: Load versus mid-span deflection of the beam specimens

Table 4. 3: Stiffness of each beam specimen before damage localization

Beam Specimens	Corrosion Level (%)	Load change (kN)	Deflection change (mm)	Stiffness (kN/mm)
Control	0	162.50	3.38	48.08
LC	4.55	133.85	3.58	37.39
MC	16.36	134.91	4.352	30.99
HC	32.37	135	4.07	33.17

Table 4.4 shows the summary of the ductility factor of the beam specimens. It is found that the three corroded (LC, MC, and HC) beam specimens did not register significant difference between their failure loads, which were 147.9 kN, 148.9 and 148.8 kN, respectively. The LC, MC and HC beam specimens show exhibited nearly similar behavior in terms of ductility which was higher than the Control beam specimen.

Table 4. 4: Determination of ductility factor of beam specimen

Beam Specimens	Maximum Load (kN)	Deflection at damage localization, Δ_y (mm)	Peak Deflection, Δ_u (mm)	Ductility factor
Control	182.57	3.68	7.28	1.66
LC	147.90	3.52	6.14	1.67
MC	148.90	3.81	6.13	1.61
HC	148.80	3.61	6.11	1.70

The condition of beam fracture at the end of loading test is shown in Figure 4.3. From observations during testing, all the four beam specimens were found to fail by developing macroscopic fracture in shear, signified by the formation of diagonal crack that eventually penetrated through the specimen height. At the initial stage of loading, the first visible crack was observed from the concrete side face of all the three beam specimens, which propagated from the specimen bottom between loads of 47 kN to 55 kN. As the load increased, more cracks were found propagating vertically from the bottom of the beam specimen to indicate tensile fracture under flexure. Diagonal cracks were also found initiated from concrete above the supports and progressed towards the location where the load was applied, at 95 kN, 87 kN, 80 kN and 100 kN for the Control, LC, MC, and HC beam specimens, respectively. The continuous increase in the load resulted in the start beam fracture localization to form macro-cracks, at 120 kN, 137 kN, 135 kN and 134 kN for the Control, LC, MC and HC beam specimens, respectively.

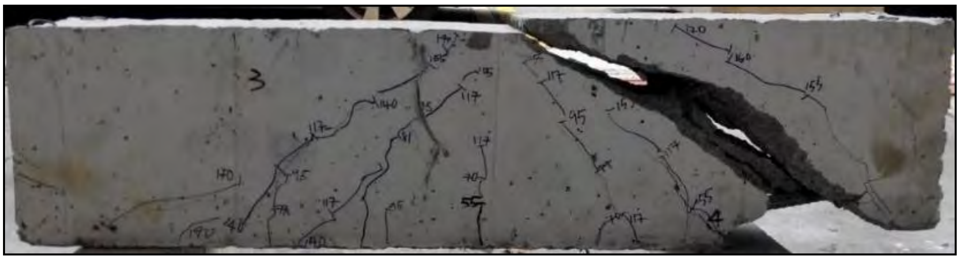

(a) Control

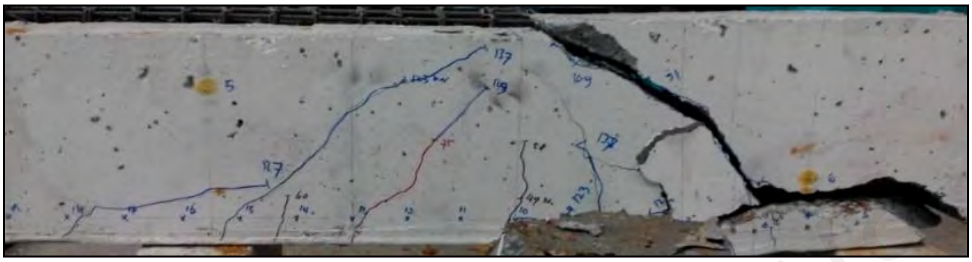

(b) LC

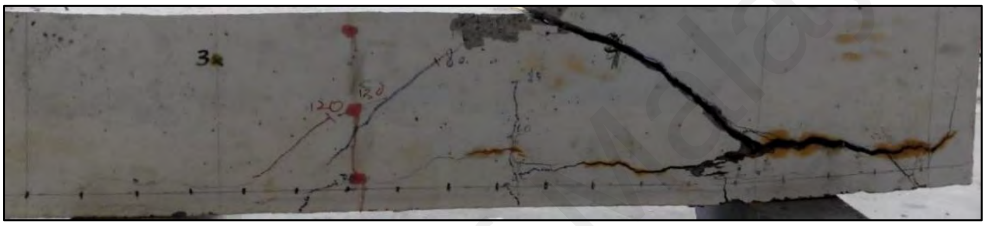

(c) MC

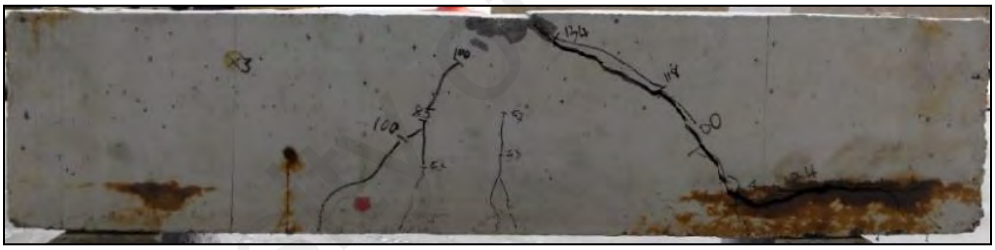

(d) HC

Figure 4. 3: Cracking as observed at failure for beam specimens

For the Control beam specimen, the amount of visible cracks observed until failure occurred was found to be more than the two corroded beam specimens. Photographs showing the progression of the visible damage of the Control beam specimen are presented in Figure 4.4. Rust stain was evident on the side face of MC and HC beam specimen at the proximity of tension reinforcements, where horizontal cracks were also seen. This indicated fracture of the beam specimen by the formation of expansive corrosion product on tensile steel reinforcements. This has resulted in a decrease of bond strength between steel reinforcement and beam specimen, affecting stress distribution within the beam specimen when the flexural load was applied. The doweling action was noticeable during the loading, with which splitting of concrete cover occurred by macroscopic cracking along the steel reinforcements from beam end. The crack was then directed diagonally upwards to the point of loading to form brittle shear failure, which occurrence was similar to that observed for the Control beam specimen.

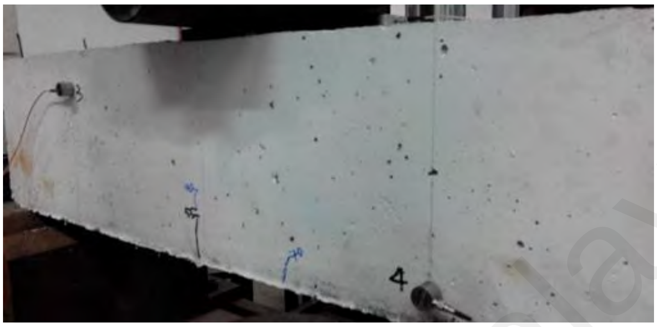

(a) First visible crack

(b) Cracks distribution

(c) damage localization

Figure 4. 4: Progression of the cracks for the Control beam specimen

In general, the fracture of beam specimens can be classified into four damage stages as shown in Figure 4.5, which were suggested by previous study on flexural behavior of RC structures (Bagherifaez et al., 2014). The damage stage can help to characterize the concrete behaviour in relationship between load and deflection with the AE parameters. Analyzing AE data at each stage of damage can help to overcome the overlap among stages and to classify the crack types. Figure 4.5 shows the normalized load (%) against deflection. The normalized load is a technique to treat the classification of load versus deflection curve in four damage stages. The normalized load is the percentage (%) of original load plot per peak load. The damage stage based on a portion of normalized load.

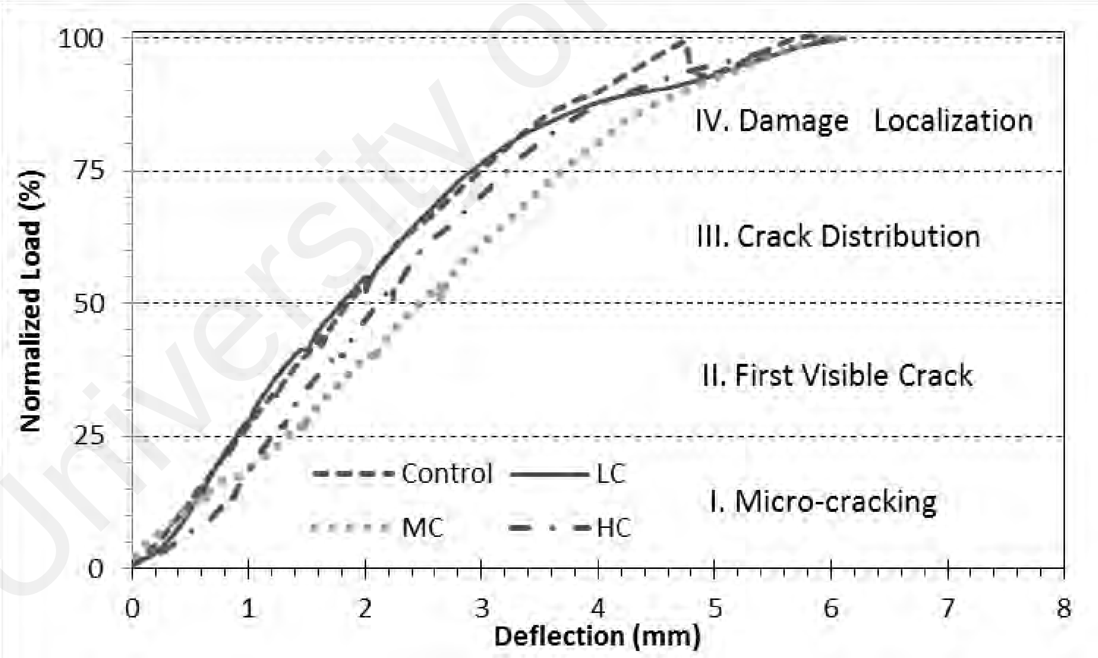

Figure 4. 5: Damage stage classification of the beam specimens

The first visible crack was found at approximately 30-35 % of the ultimate load. Prior to this micro-cracking was considered to have taken place within the beam specimens, whose occurrence could be detected with the AE monitoring. It was also observed that the location of the first visible crack was near to the mid-span of beam specimens. Damage Stage III, known as the crack distribution stage, was detected when load reached approximately 50% of its ultimate load. This process was observed till the flexural moment reached damage Stage IV, with steel reinforcement damage localization and yielding started at approximately 81-86 % of the ultimate load, micro-cracking should have when loading commenced and cracks distributed and coalesced to give localized macroscopic fracture. By considering the definition of stiffness, Figure 4.4 shows that as load increases the slope of load-deflection curve decreased which implies that the stiffness of the beam specimens decreases with the widening of the cracks at mid-span. Apparently, Control beam specimen has more brittle than the other three beam specimens (i.e. LC, MC and HC).

4.3 Characteristics of AE parameters

According to the damage stages defined above, the AE signals from all the beam specimens were divided into 4 sections separately. Table 4.4 presents a summary of characteristics of the AE parameter along the different damage levels. The AE parameters are duration, amplitude, frequency, count, and hits. The duration, amplitude, and frequency in Table 4.5 are presented in average term.

Table 4. 5: AE parameters of Experiment 1

Specimen	Damage Stage	Duration (s)	Amplitude (dB)	Frequency (kHz)	Count	Hits	% Hits
Control	I	627.78	53.99	34.69	495561	24545	2.34
	II	644.3	53.39	46.8	3276353	137375	13.10
	III	652.16	53.72	43.92	6032840	239029	22.80
	IV	860.62	54.49	41.22	20119068	647599	61.76
LC	I	920.41	53.79	28.94	615314	28901	2.92
	II	584.14	53.94	41.53	1718738	81907	8.28
	III	598.39	54.33	47.16	7647192	235638	23.83
	IV	1321.36	55.37	43.14	54285675	642469	64.97
MC	I	558.82	53.31	39.34	188050	10693	7.63
	II	425.74	53.06	42.77	133748	7833	5.59
	III	380.90	53.34	51.91	336598	20579	14.69
	IV	586.21	53.62	46.75	2305684	100951	72.08
HC	I	608.16	54.93	41.07	839871	41947	5.11
	II	455.54	54.58	42.08	1154543	65390	7.97
	III	612.82	54.95	42.98	5567031	227452	27.71
	IV	557.77	55.1	42.23	10427583	486089	59.22

4.3.1 Accumulated AE hits

Figure 4.5 shows the cumulative AE hits versus time. The accumulated AE hits of the tests decrease in terms of increase of corrosion level. However, for MC beam specimen, there is significant decrease in accumulated AE hits. It might be the unpredictable effect of steel corrosion on the beam specimen. The steel corrosion affecting the low of stress distribution within the beam specimen. The stress distribution is a source of the AE data. The MC beam specimen is not feasible for the next discussions due to the low AE data.

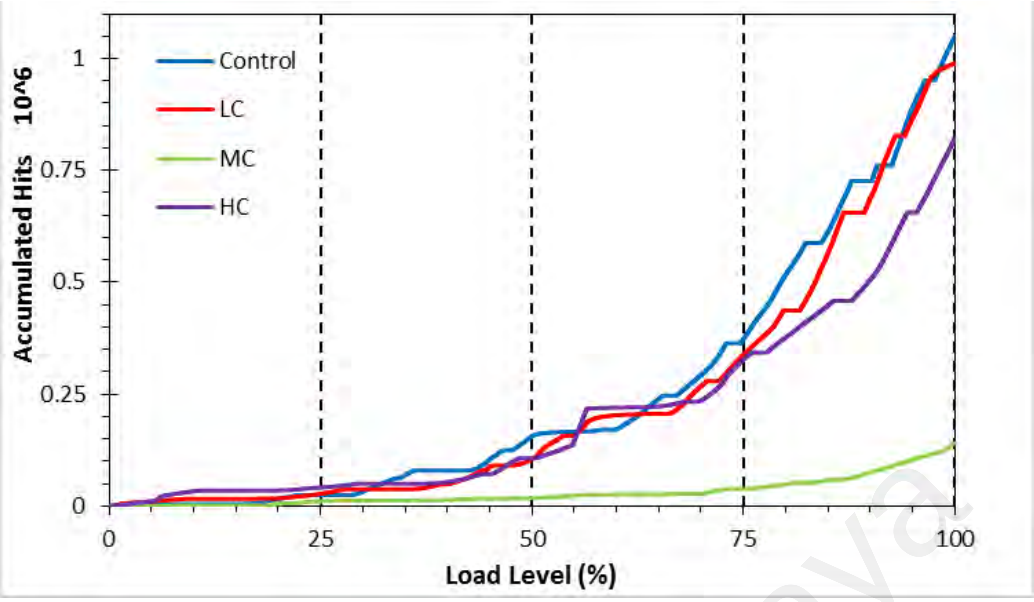

Figure 4. 6: Accumulated AE hits versus load level (%)

Besides MC, all the other specimens (Control, LC and HC beams) show the same trend of accumulated AE hits. At an early damage stage, micro-cracking starts to develop and this is indicated by a number of AE hits, which is increasing as the load increases. When the first visible crack is formed, at 25% of load level, an increase of AE hits rate is observed. At the damage stage II, the Control beam has significant increase AE hits compare to LC and HC beam. As the loading continues, the cracks propagate in the beam specimens in the damage stage III and the AE hits increase gradually until damage localization at 75% of load level. There are significant increase of AE hits of LC and HC beam at the middle of damage stage III. This is due to the formation of severe crack occurs due to steel corrosion. At the early damage IV, a significant increase of AE hits is observed after the damage localization. The accumulated AE hits of Control beam is higher than LC and HC beam at the damage stage IV. The accumulated AE hits increase more than 60% where is from around 0.35 x 10^6 to around 1 x 10^6.

4.3.2 Frequency and Amplitude

Figures 4.7 to 4.9 show the relationship between frequency and amplitude in each damage stage (damage stages I to IV) for the Control, LC and HC beam specimens, respectively. From the figures and Table 4.5, based on the experimental results, the average frequency and amplitude tend to increase from the damage stage I to damage stage IV. There are AE signals characteristics that are of high amplitude and low frequency. The frequency range for the three beams in the sequence of corrosion level are 36 – 45 Hz, 31 – 47 Hz, and 38 – 45 Hz respectively. The linear regression has been provided as well for each damage stage.

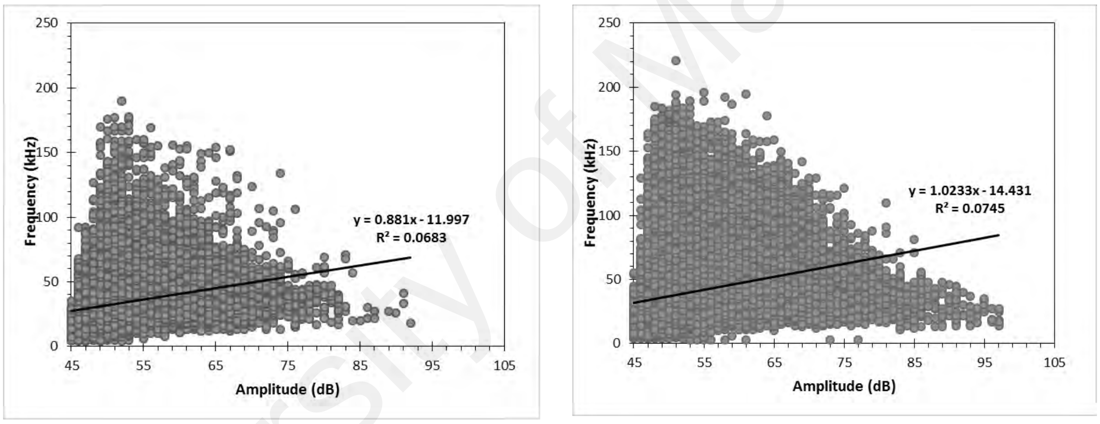

(a) damage stage I

(b) damage stage II

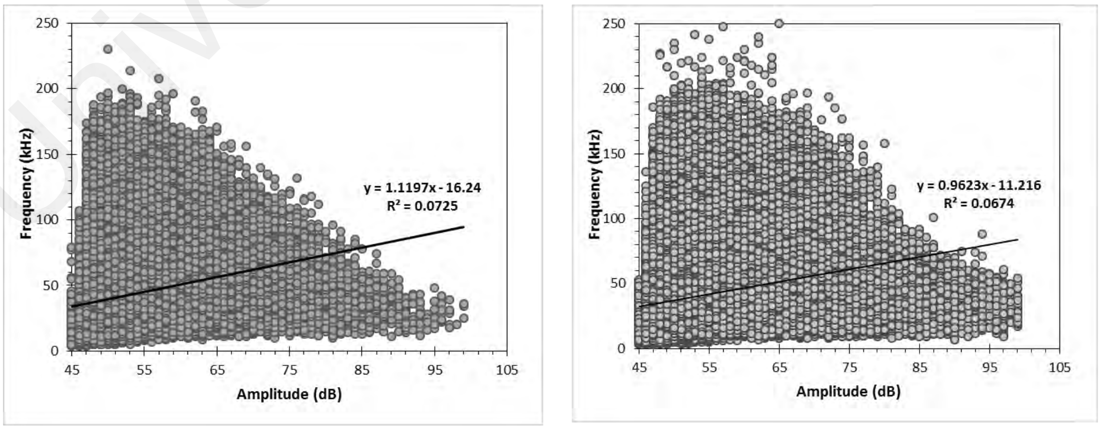

(c) damage stage III

(d) damage stage IV

Figure 4. 7: Typical Frequency and Amplitude of Control beam specimen

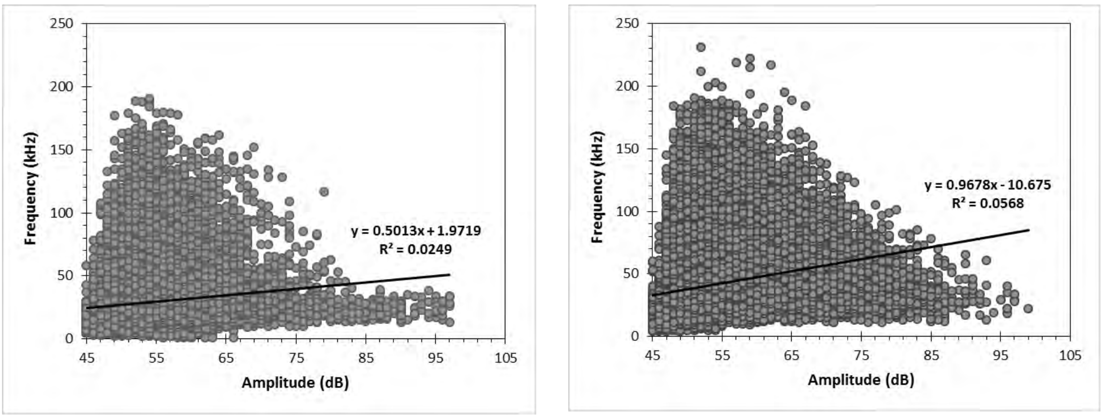

(a) damage stage I

(b) damage stage II

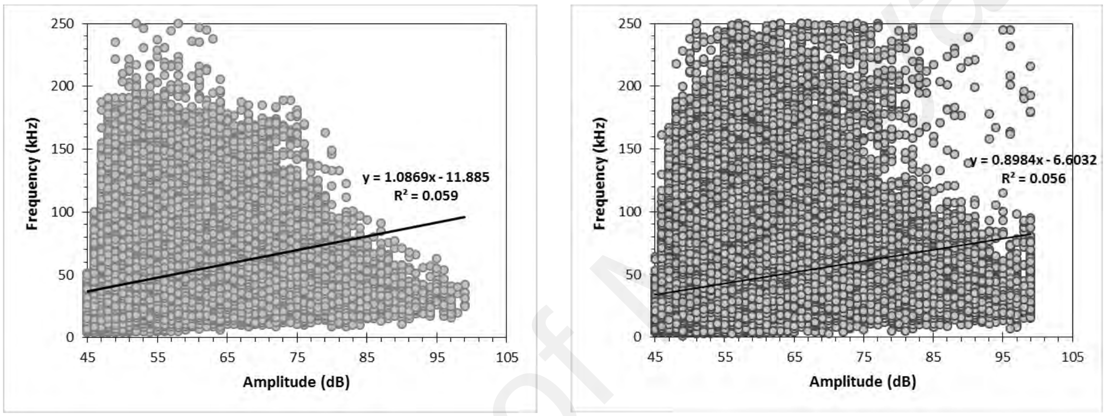

(c) damage stage III

(d) damage stage IV

Figure 4. 8: Typical Frequency and Amplitude of LC beam specimen

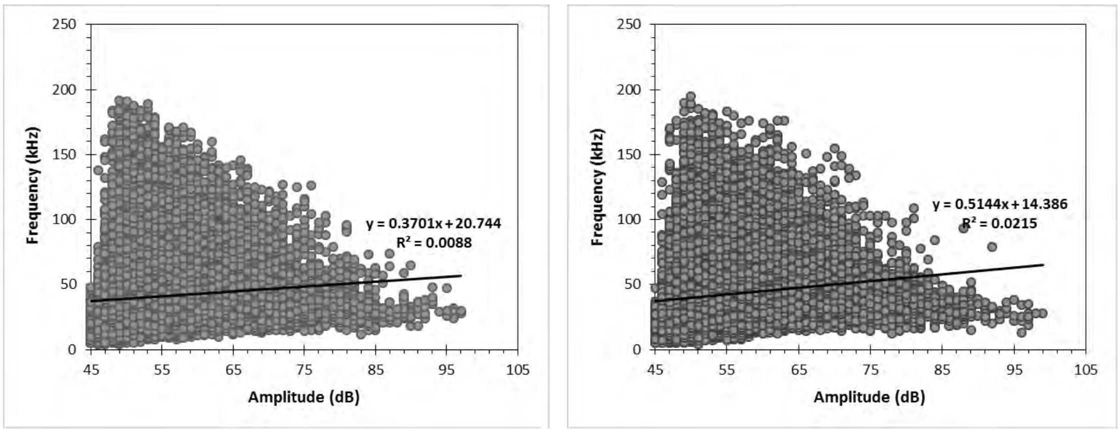

(a) damage stage I (b) damage stage II

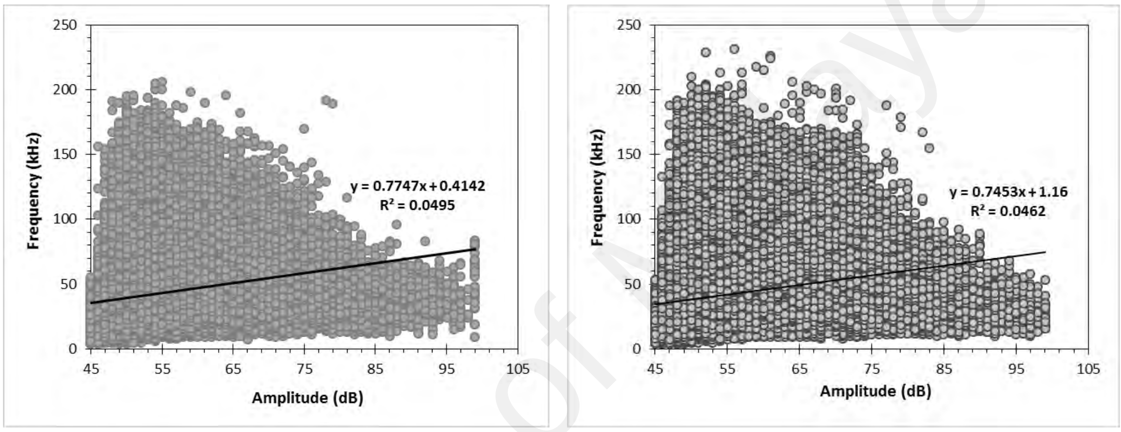

(c) damage stage III (d) damage stage IV

Figure 4. 9: Typical Frequency and Amplitude of HC beam specimen

4.3.3 Duration and Amplitude

The plots of duration versus amplitude from AE signals are given in Figures 4.10 to 4.12. In the case of Control beam specimen, the AE duration, as shown in Table 4.5, was 600 s until an initial crack occurred and then additional tensile cracks and shear cracks were generated on the surface of the beam specimen. When damage stage IV was achieved, the AE duration was 860 s. It is thought that this increment of AE duration may result from the characteristic of the AE signals due to the debonding between the reinforcement and the concrete (Yun et al., 2010). The AE duration due to debonding between the reinforcement and the concrete in damage stage IV was much longer than that due to crack initiation and propagation in damage stage I.

However, in particulars, when the corrosion level increase, the AE duration decreases according to each damage level. The decreasing of the AE duration when an increase in corrosion level. This condition might be due to the lower bond properties of the beam specimens. The lower bond properties are due to the corrosion product (i.e. rust) which emit stresses to produce more cracks and spalling in the bond area.

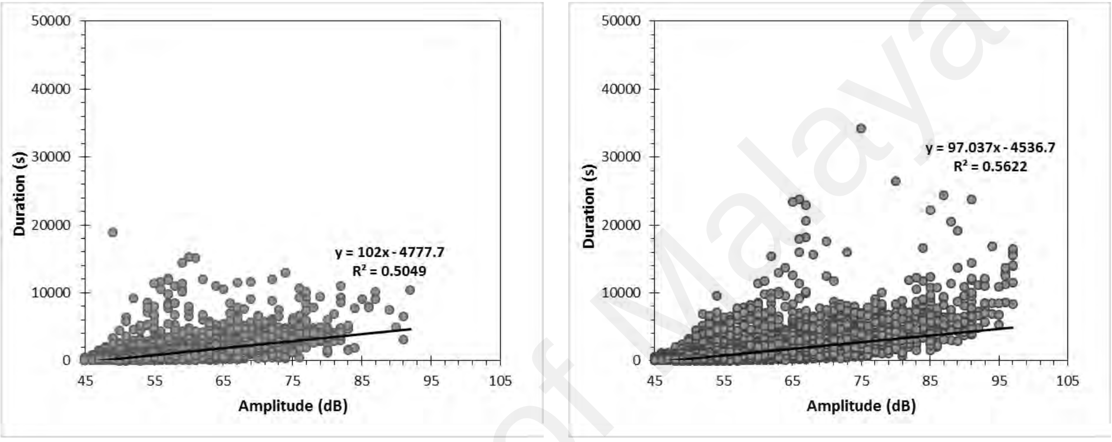

(a) damage stage I (b) damage stage II

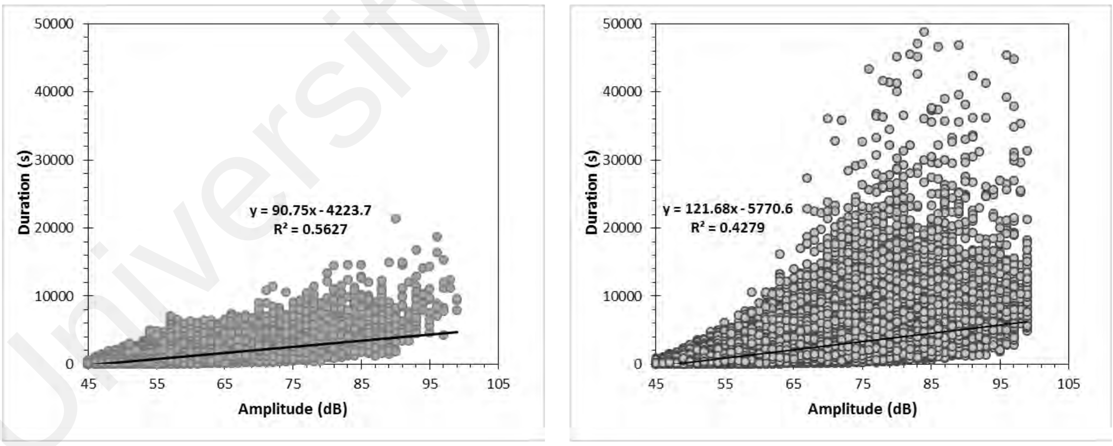

(c) damage stage III (d) damage stage IV

Figure 4. 10: Typical Duration and Amplitude of Control beam specimen

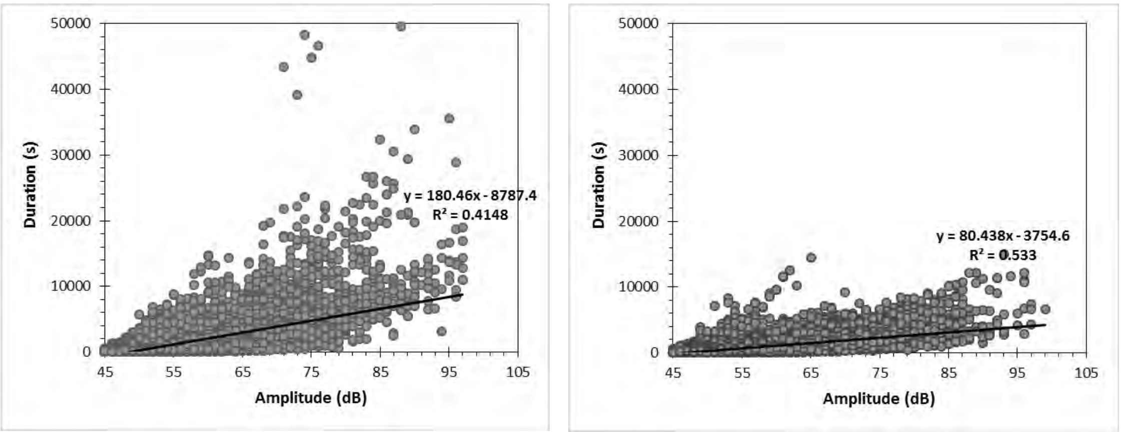

(a) damage stage I

(b) damage stage II

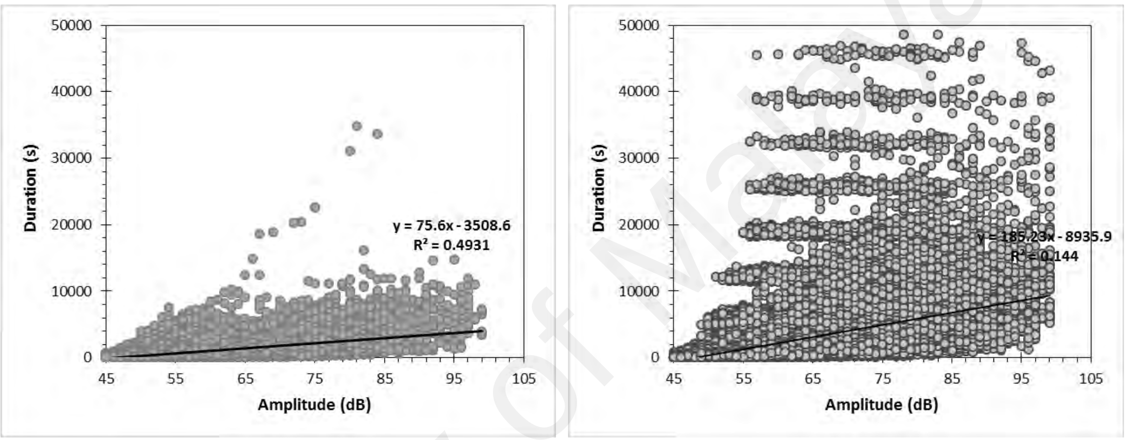

(c) damage stage III

(d) damage stage IV

Figure 4. 11: Typical Duration and Amplitude of LC beam specimen

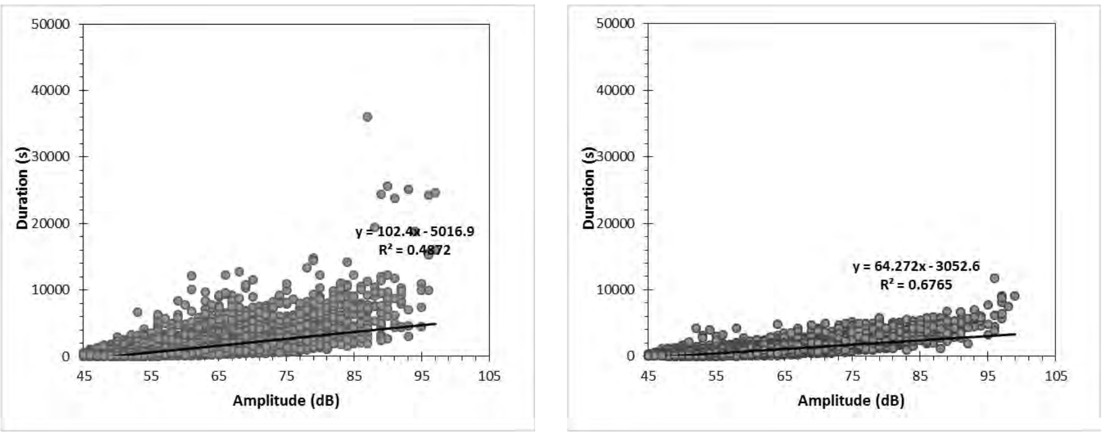

(a) damage stage I (b) damage stage II

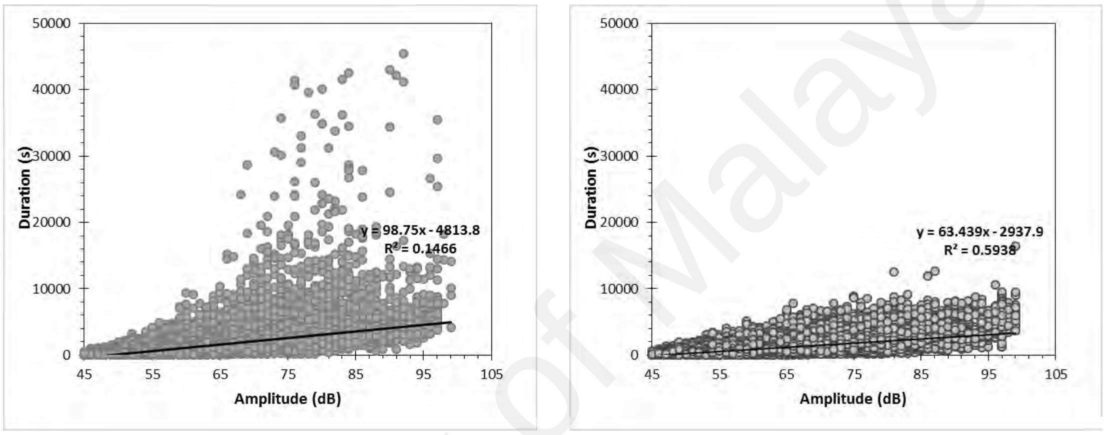

(c) damage stage III (d) damage stage IV

Figure 4. 12: Typical Duration and Amplitude of HC beam specimen

4.3.4 Count and Amplitude

The relationship between count and amplitude greater than 45 dB is given in Figures 4.13 to 4.15 and Table 4.5. There is a tendency for cumulative counts and average amplitude to increase as the damage stage increases on each beam specimen. For all the damage stage, all the beam specimens are in the amplitude range of 45 – 100 dB. The count increases with the evolution of damage up until reach an ultimate load.

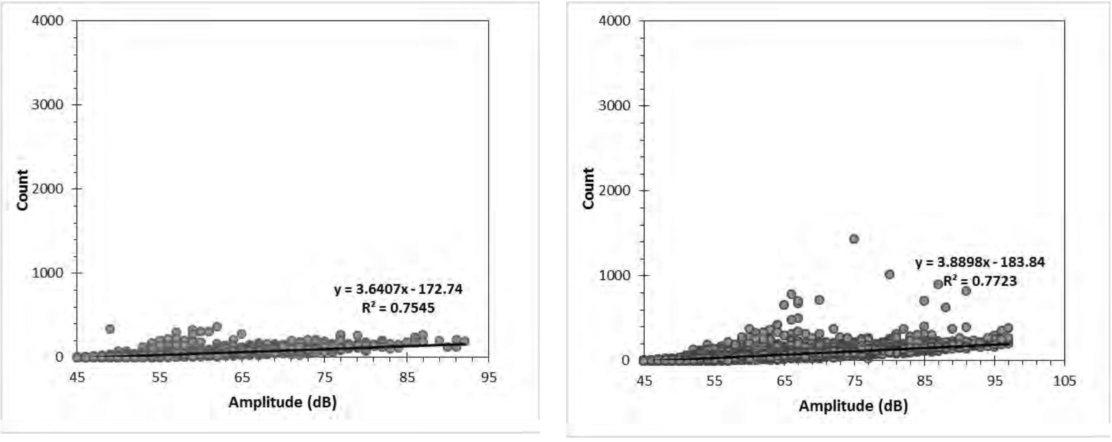

(a) damage stage I (b) damage stage II

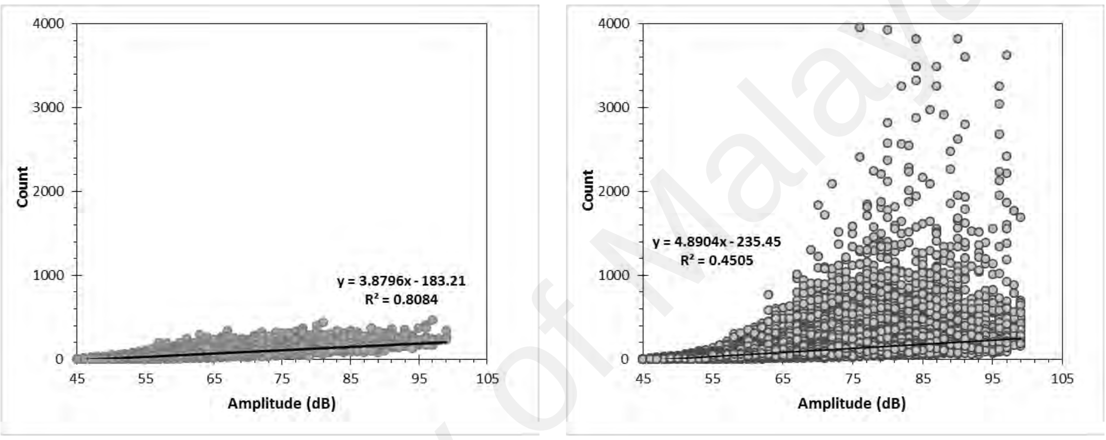

(c) damage stage III (d) damage stage IV

Figure 4. 13: Typical Count and Amplitude of Control beam specimen

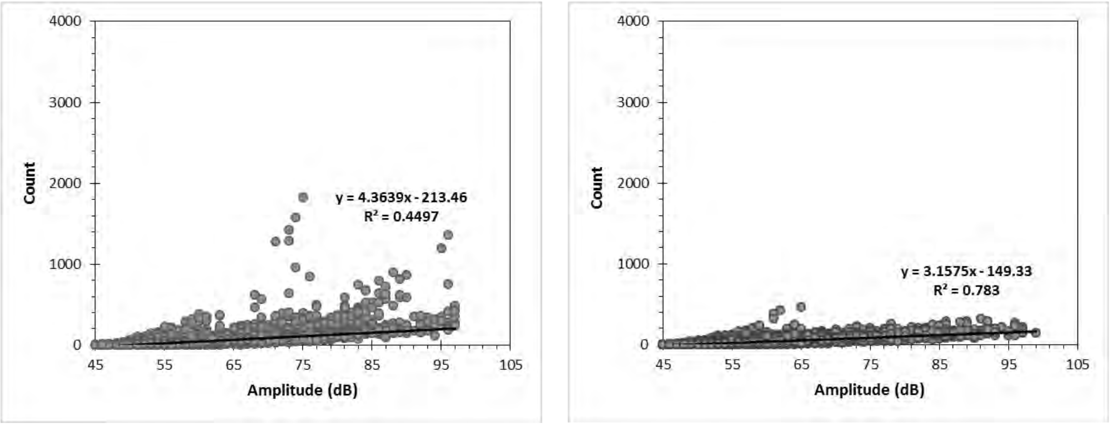

(a) damage stage I (b) damage stage II

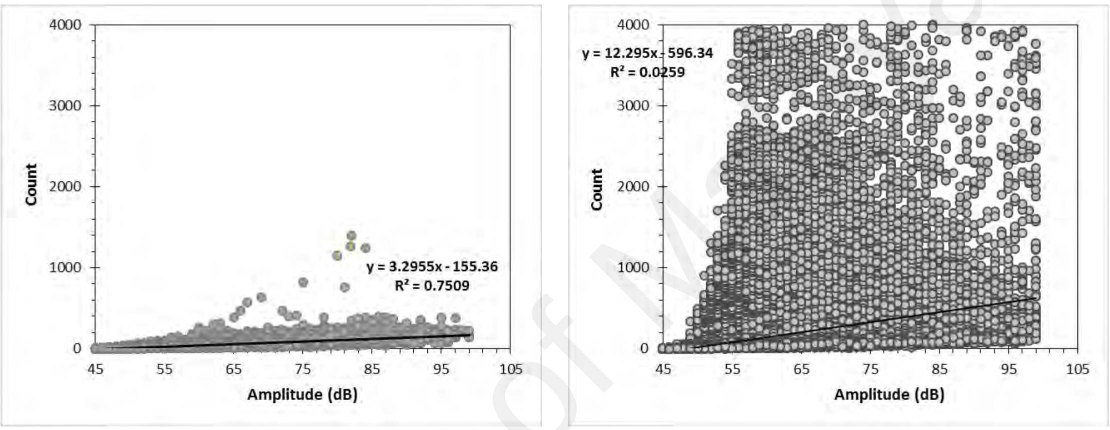

(c) damage stage III (d) damage stage IV

Figure 4. 14: Typical Count and Amplitude of LC beam specimen

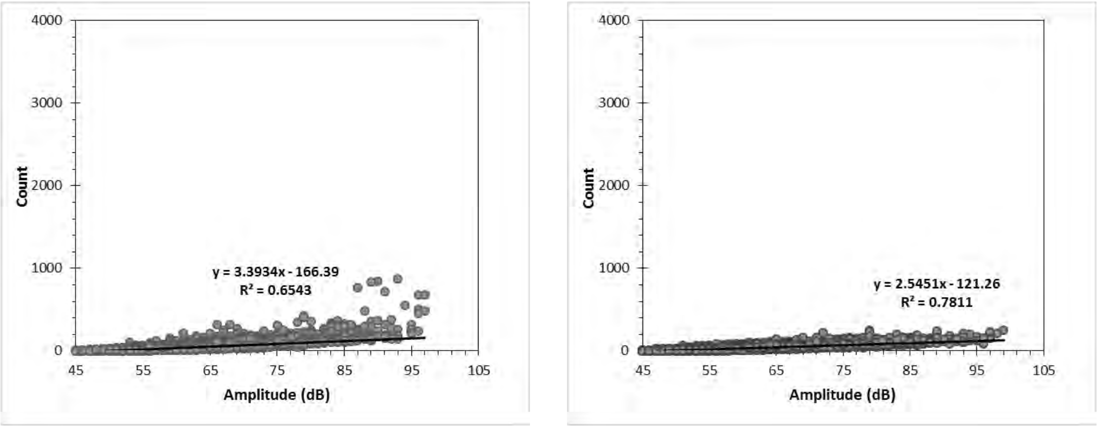

(a) damage stage I (b) damage stage II

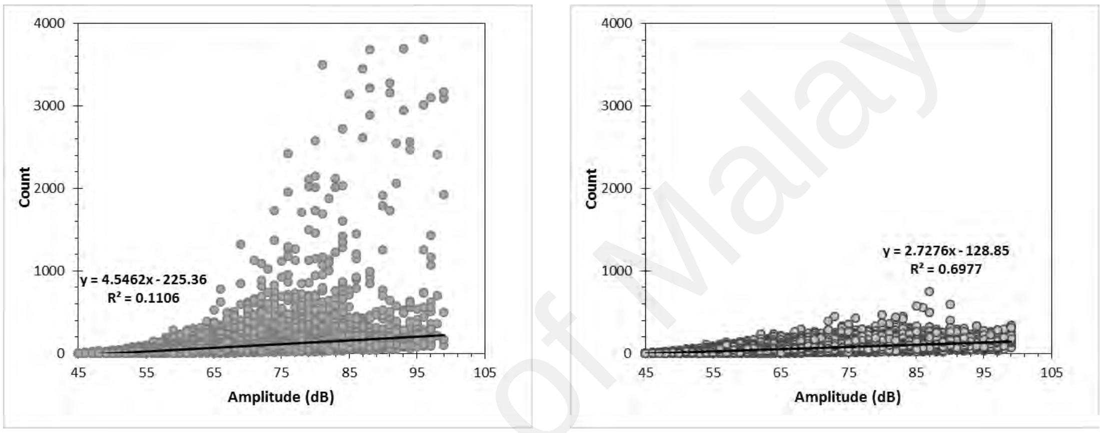

(c) damage stage III (d) damage stage IV

Figure 4. 15: Typical Count and Amplitude of HC beam specimen

4.3.5 Crack classifications – RA value and AF

The change in RA value and average frequency (AF) is used to evaluate the mode of fracture in the beam specimens. The two AE parameters can be computed using Equations (2.16) and (2.17). The characteristics of AE signals are estimated using two parameters, RA value and AF in line with the relevant recommendations. The RA value and AF are defined from the AE parameters, i.e. rise time, peak amplitude, counts, and duration, as given by Equations (2.16) and (2.17).

Previous findings suggested that in tensile mode cracking, AE rise time would be shorter, with higher average frequency but lower RA value as compared with those registered for shear mode cracking (Aggelis, 2011). The variations are mainly attributed to the change in the transmitted energy and its speed, which were correlated in an inversed manner. Hence, the energy speed at the later stages of damage is always slower than that at the earlier stages because of the larger part of energy being transferred in shear waves form (Aldahdooh & Muhamad Bunnori, 2013).

Figure 4.16 gives the plots of RA value and AF against time, computed from the monitored AE data in the current study, by averaging the respective values at every 5% load increment. It can be seen from the plots that in general, after the first load level (5% of ultimate load), the RA value experienced a decrease and AF value abruptly increased before gradually rose back in subsequent load levels. From the relationship, tensile cracks were observed from the beginning of the load. For the Control beam specimen, the RA value and AF register steady increase after not long after load was applied, as recorded from the middle of damage Stage I (10% of ultimate load) to the early stage of damage Stage IV (80% of ultimate load), during which micro-fracture in tensile crack mode were observed to propagate extensively and coalesced, at the same time shear cracking started to initiate.

On the other hand, the RA value and AF of LC beam specimen gradually increased from the end of damage Stage I (20% of ultimate load). Starting from damage Stage III (50% of ultimate load), the RA value dropped, in contrast to the marked increase in AF to imply the occurrence of beam rupture by cracking and corrosion activities (Aggelis, 2011). The crack mode was classified as the tensile cracks at the bond of tension reinforcements in beam specimen.

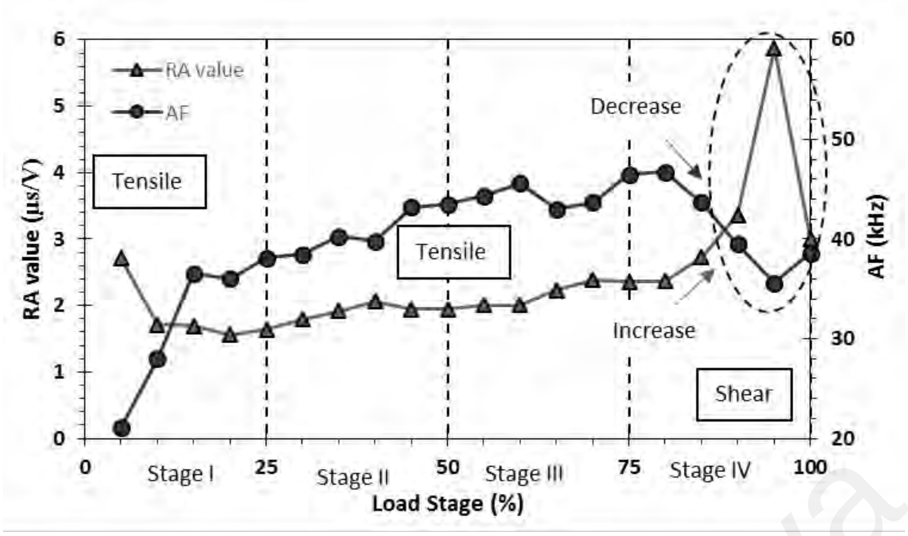

(a) Control

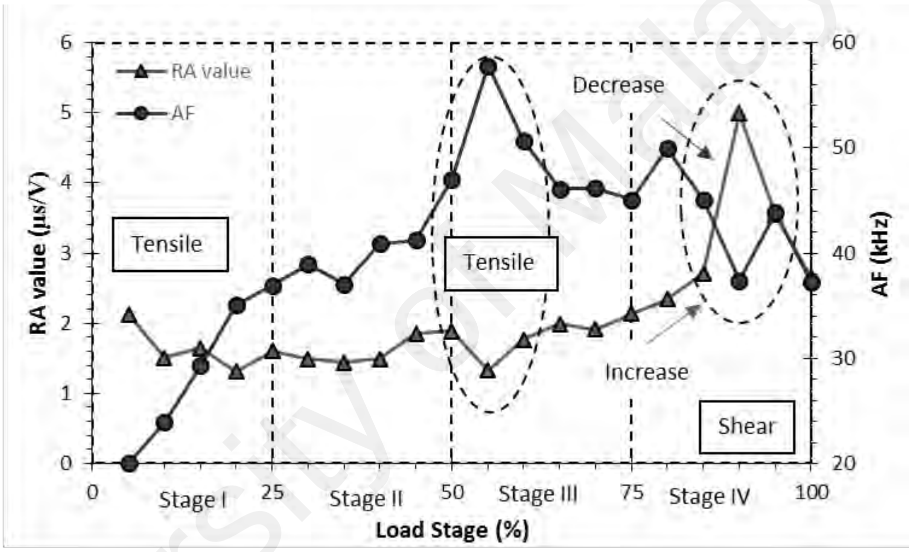

(b) LC

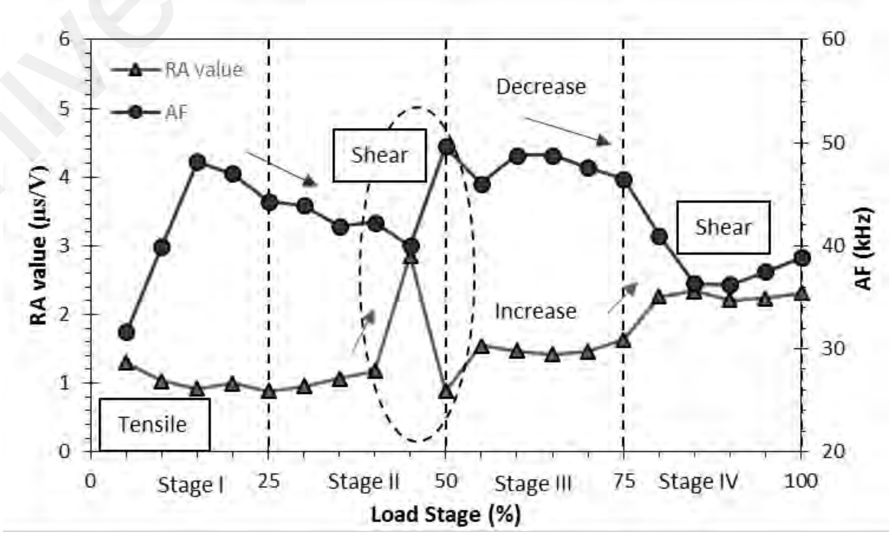

(c) HC

Figure 4. 16: Variation of RA value and AF with load for beam specimens

The highest recorded RA value is obtained from the last damage stage of the Control and LC beam specimens, as shown in Figures 4.16 (a) and (b). This indicates a trend for shear crack development and progression due to ultimate fracture. For the HC beam specimen, however, the highest RA value and the decrease AF occur towards the end of the damage Stage II, which at this condition the shear cracks have been observed to start propagating from the tension side of the beam specimen, at the proximity of the steel reinforcements. After reaching the peak, the RA value marked a sharp decrease before increasing gradually from the damage Stage III. There is a relatively large increase in RA value at the start of damage Stage IV, but the magnitude is lower than that obtained earlier. This implies that the most corrosion-induced cracks were progressed further and nucleated at the end of damage Stage II compared with the damage Stage IV. According to the RA value and AF of the AE parameters, the effect of increase corrosion level of the beam specimens was confirmed by the lower magnitude of RA value. In the HC beam specimen, the magnitude of RA value was lowest and nucleated at an earlier stage than Control and LC beam specimens.

The average RA value was calculated for each stage of damage for all beam specimens with reference to the work reported by Aldahdooh et al. (2013). From Figure 4.17 that shows the results of computation, the average RA value increased with the development of damage for all the beam specimens. In damage Stage I, the average RA value decreased with the increase of the corrosion level. This stage was associated with the initial or micro-cracking until the formation of the first visible crack. The feasible interpretation of this result was related to the mechanical behavior of the beam specimens, as the corrosion level increased for a given load, the number of tensile cracks decreased. Because of that, the RA value tends to decrease and the AF is high.

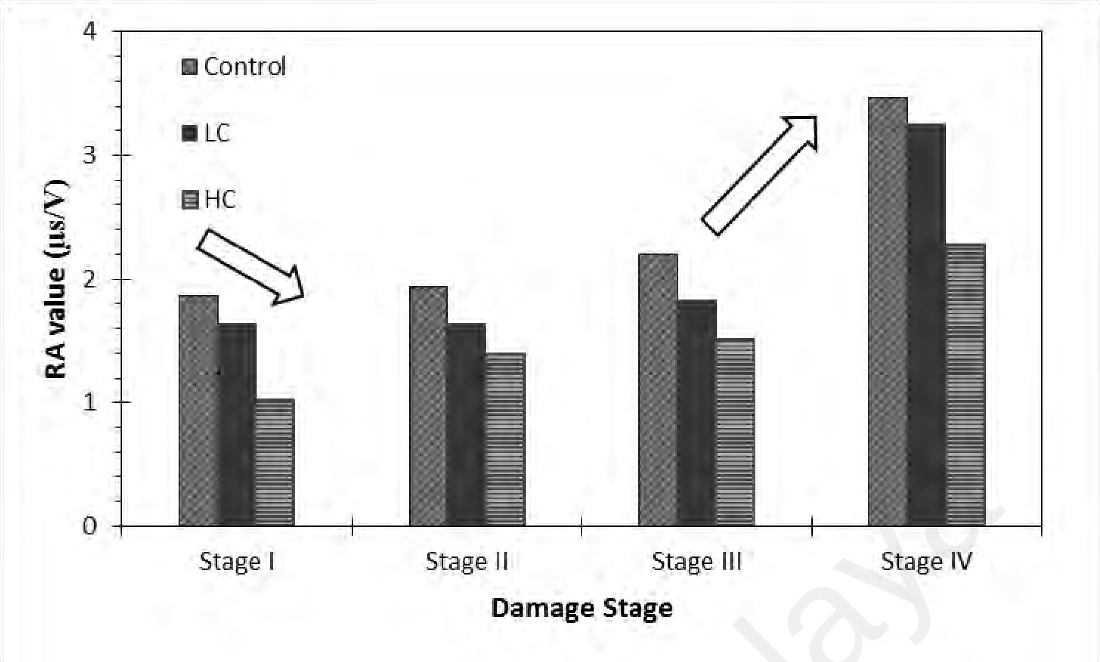

Figure 4. 17: Average RA value at each load stage of the beam specimens

The average RA value acquired from this damage stage is useful as an early indicator of the imminent formation of visible cracking due to the deterioration by steel corrosion activity. In overall, the average RA value is also lower for higher corrosion level, however, when the shear cracks initiated, the RA value increased evidently as shown in damage Stage IV.

Figure 4.18 shows RA value vs. AF distribution of the AE data per 5% of the ultimate load. The dashed lines are the linear regression line of the distribution of RA value and AF data of the beam specimens. It is shown that as the corrosion level becomes higher (from Control beam to LC and HC beam specimens), there is a collective increase in AF and decreases in RA value of the beam specimen. On the other hand, it also indicated of the transition of the beam dominating fracture behavior, which shifts from tensile to shear as the damage stage increased (from damage Stage I to IV) in accordance to the classification method was suggested previously.

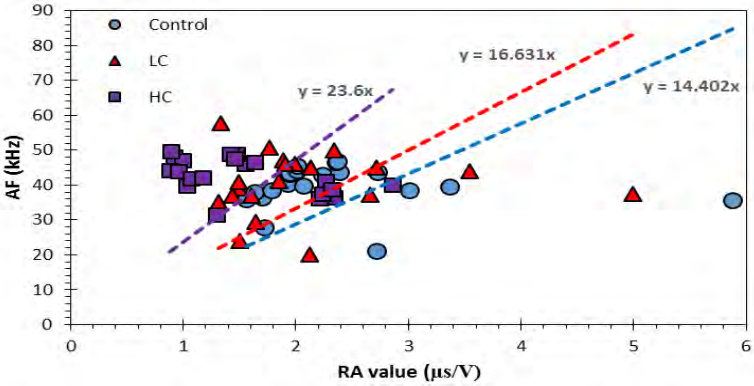

(a) All

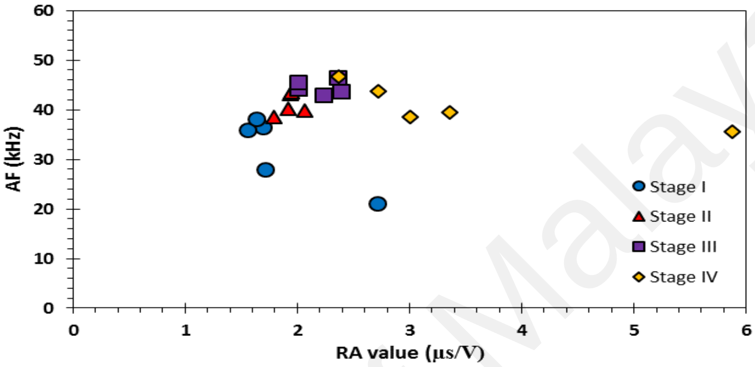

(b) Control

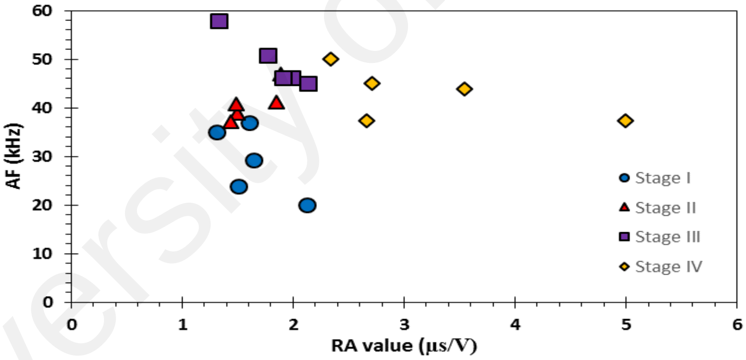

(c) LC

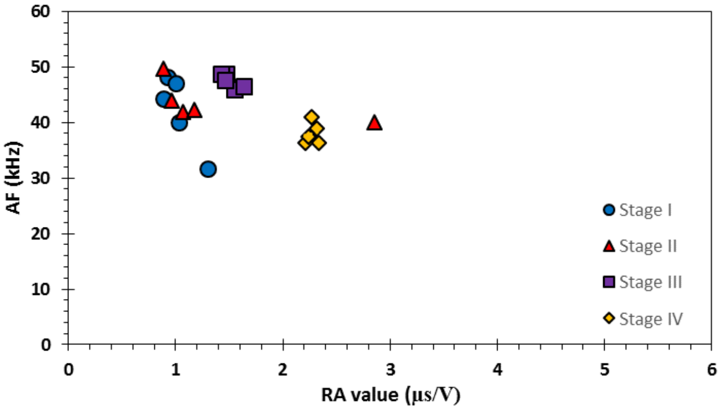

(d) HC

Figure 4. 18: RA value versus AF for beam specimens

4.3.6 Damage evaluation - Index of Damage

Table 4.6 shows the total AE energy recorded in all the damage stages of the beam specimens. From the table, the total AE energy recorded for the HC beam specimen was the lowest among three. On the other hand, the total AE energy increased with progression of the damage stage. The total AE energy was the highest for damage Stage IV, indicating that macroscopic fractures have taken place. However, for the HC beam specimen, the total AE energy damage Stages II and III were comparable. In addition, the total AE energy obtained for damage Stage IV of the specimen was markedly lower than the other two beam specimens. These findings imply that the formation of new cracks in the HC beam specimen was relatively fewer than the other two beam specimens and the majority of cracking could have occurred during the steel corrosion process that was not monitored by AE.

Table 4. 6: Total AE energy for each damage stage

Beam Specimen	Stage I	Stage II	Stage III	Stage IV	Total
Control	697,205	2,949,516	7,243,477	16,442,895	27,333,093
LC	979,874	2,987,582	5,061,069	34,539,102	43,567,627
HC	899,470	5,858,081	5,086,416	7,271,464	19,115,431

The ID from each damage stage is given in Figure 4.19. The suggested index was calculated by dividing the cumulative AE energy obtained from the respective load levels (percentage of the instantaneous load in relative to failure load) with that were acquired at ultimate failure. At damage Stage I, the ID is higher when the corrosion level of the beam specimen increased, as shown in Figure 4.19 (b). However, the ID of LC beam specimen is slightly higher than that of HC beam specimen. This result was probably due to the effect of steel corrosion of LC beam specimen to the structural performance of the beam specimen higher than HC beam specimen. The AE energy measured from this damage stage was closely associated with the actual condition of corroded beam specimens before the occurrence of visible cracking to signify the initiation of permanent damage.

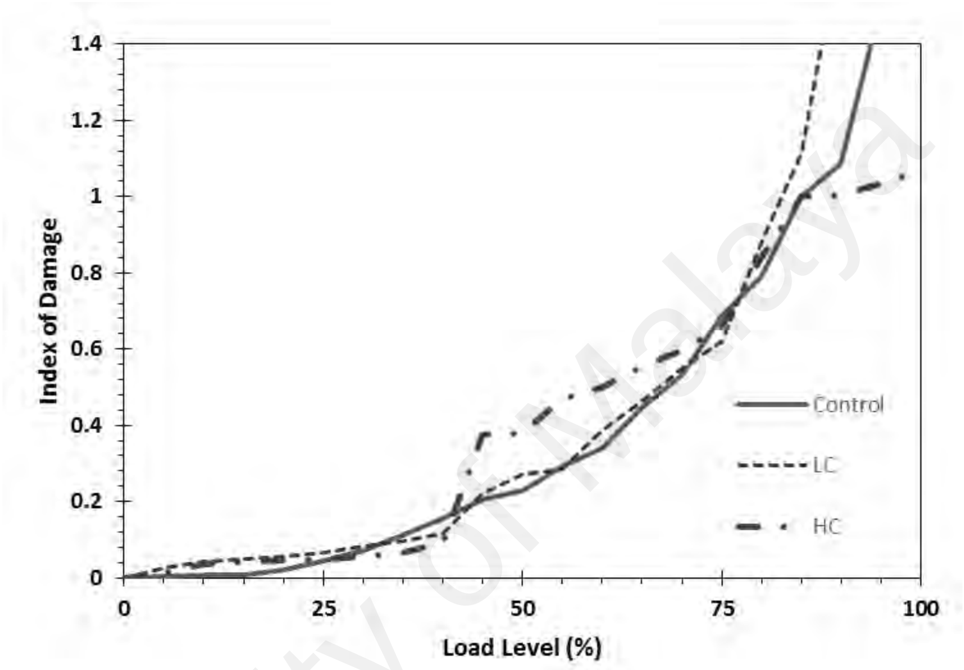

(a) Each load level (%)

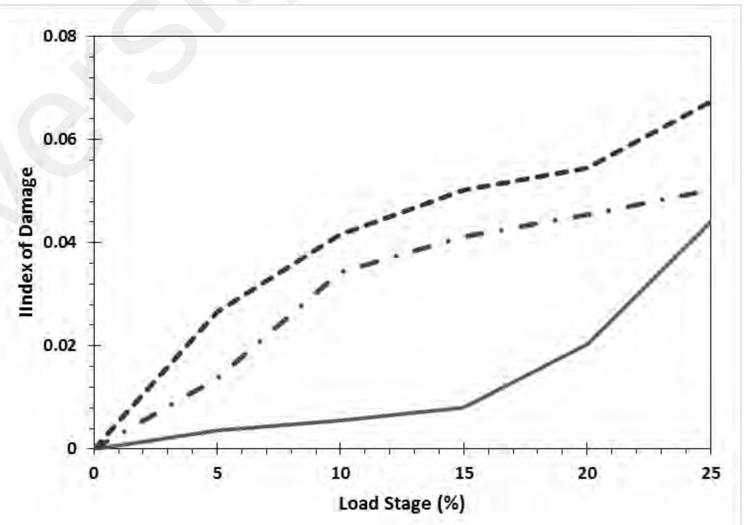

(b) Damage Stage I

Figure 4. 19: ID distributions

From damage Stage II to III, the ID for the HC beam specimen increased and became the highest among three beam specimens. An explicit pattern for the development of ID was found, which can be described as a sudden change in slope of the data line that could be related to the occurrence of fractures, especially the ones that occurred at the interface between concrete and steel reinforcements. The fracture was considered to be dominant in damage Stages II and III. In damage Stage IV, after yielding point, the increase in the data slope could be clearly pointed for the Control and LC beam specimens, manifesting relatively high AE activities that were generated from the extensive cracking and fracturing towards the ultimate failure of the beam specimen.

4.4 Damage Statistical Model by Mesoscopic Element Probability Function

As observed, the AE total energy could provide DI pertaining to each load level. However, the need for total AE energy and reproduction of AE data is a drawback for practical application of this index in real structures. Therefore, a damage statistical model was developed to overcome the above-mentioned drawback using AE energy data as a variable. Figure 4.20 (a) shows the computed Weibull damage function and AE energy versus displacement for the control beam. A fitted trend line which used to facilitate regression is also shown in the logarithmic chart as in Figure 4.20 (b).

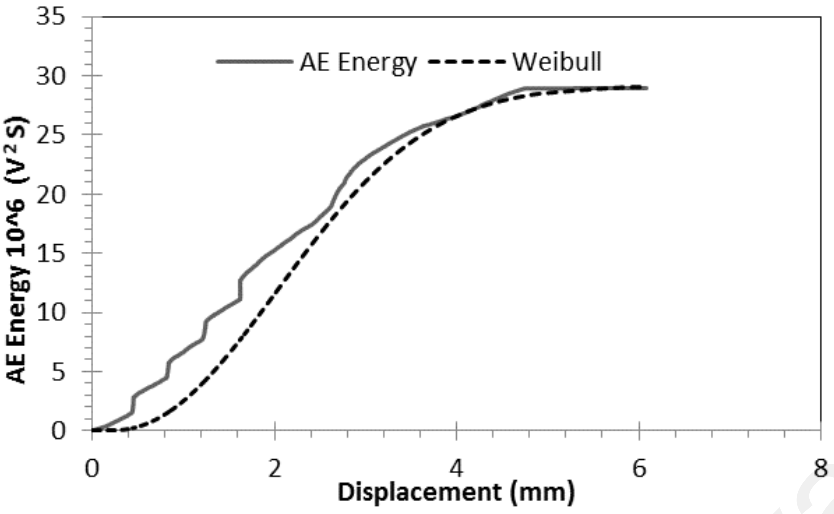

(a) Weibull damage distribution and AE Energy versus displacement

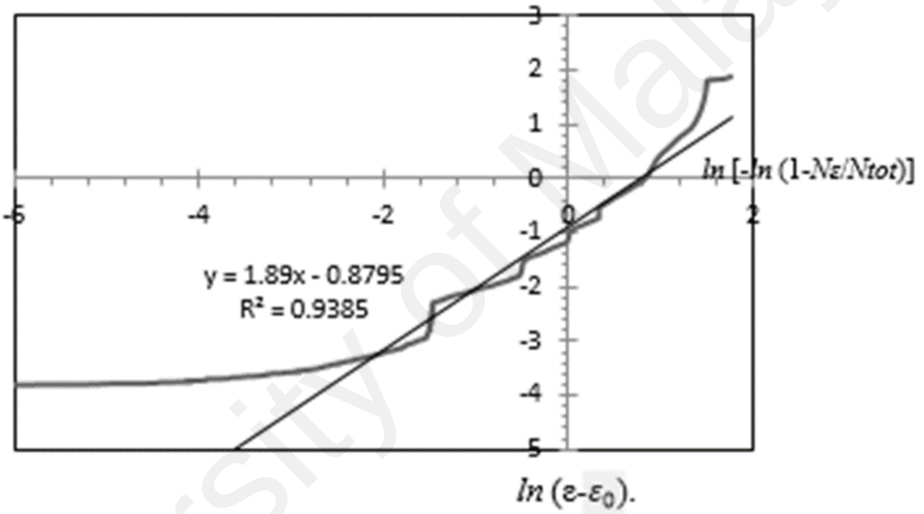

(b) Weibull function calibration

Figure 4. 20: Weibull damage function of Control Beam

The parameters *m*, *n*, $R^{2,}$ and ε_0 were calibrated as 1.89, 0.41, 0.9385 and 0.0366, respectively. The obtained Weibull damage parameters were used to estimate AE energy to verify the accuracy and efficiency of the proposed model. As depicted in Figure. 4.20 (a), the average absolute relative difference between cumulative AE energy and Weibull distribution curve is about 2.443% which is fairly acceptable. Therefore, the Weibull parameters were calibrated for the other two corroded beams so that the damage probability function could be obtained for all beam specimens. The calibrated Weibull parameters by AE energy data are presented in Table 4.7.

Table 4. 7: Parameters for Weibull damage functions

Specimen	m	n	R^2	Error %
Control	1.89	0.41	0.9385	6.15
LC	1.69	0.4	0.9249	7.51
HC	1.53	0.41	0.9136	8.64

Table 4.7 shows the calibrated Weibull parameters obtained by AE energy data, which is the reflection of the mechanical performance of the beam specimens. It can be seen that the variation in *n* among the three beam specimens is negligible, probably due to the dimensions or size of beam specimens as *n* is related to size scale. On the contrary, it was obvious that the *m* changes in accordance with any change imposed to material properties and strength. It can be said that the change of *m* value was governed by fractal properties. In other words, a higher value of *m* suggests the higher strength of the material. This has been reflected by the plots given in Figures 4.21 (a) and (b) where damage probability of all the beam specimens, computed using cumulative AE energy data, is plotted against displacement and load. These figures show that the probability of failure occurrence is higher for HC beam specimen at a lower load level compared to the other two beam specimens.

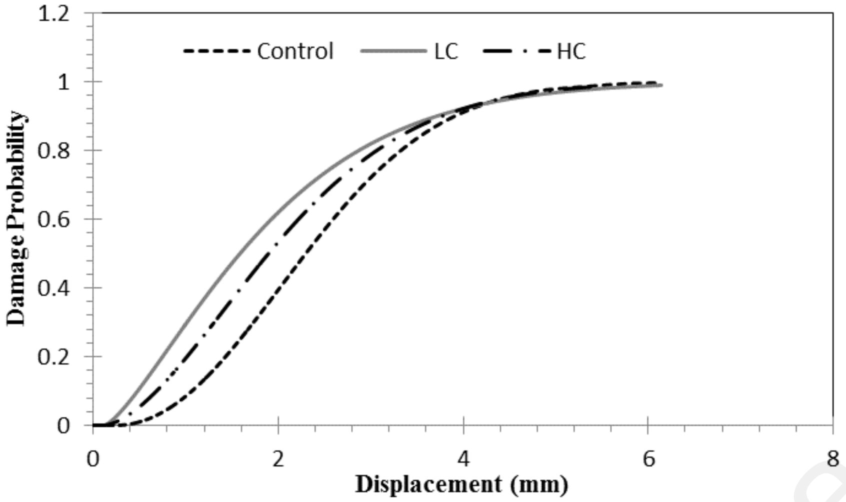

(a) damage probability function versus displacement

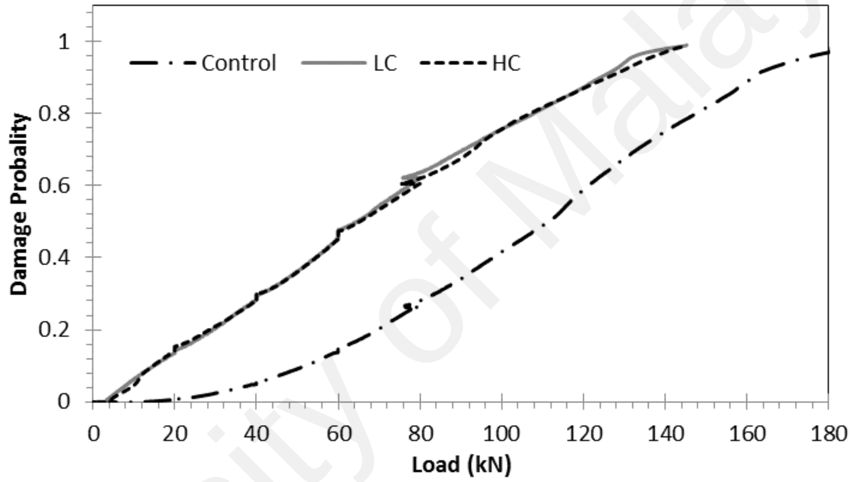

(b) damage probability function versus load of all beam specimens load

Figure 4. 21: Damage probability function

With the successful utilization of AE energy data to define Weibull damage function for characterizing the mechanical performance of corroded beam specimens, it is deduced that certain statistical relationships between material behavioral change and AE parameters may provide a useful mechanical characterization of a structure from the early stage of fracture occurrence. The findings also provide insights into using AE monitoring technique in predicting the structural behavior of steel corroded beam specimens under service load. More studies will be required to further examine the reliability of this statistical approach and the feasibility of using other AE parameters.

4.5 *I*b-value

Figures 4.22 to 4.25 show *I*b-value for the three beam specimens. Figures 4.22 to 4.24 show *I*b-value of each sensor of the beam specimens. The solid line is trend line to describe the trend of *I*b-value. It can be clearly observed that an increasing *I*b-value trend is followed by fluctuation and then a decreasing trend.

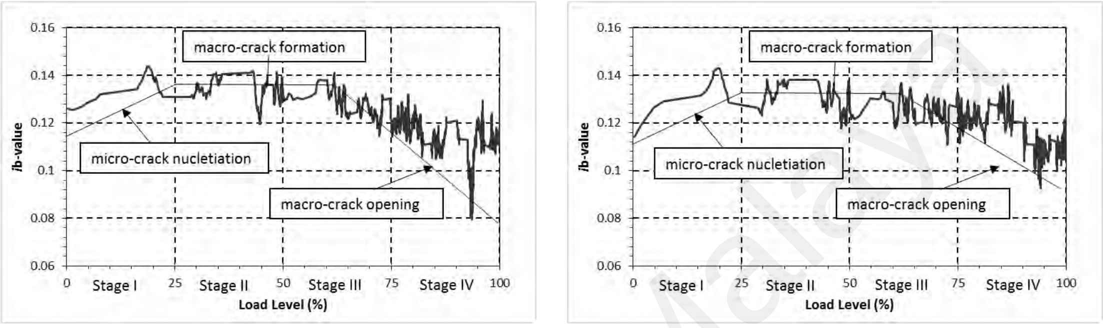

(a) Sensor 1 (b) Sensor 2

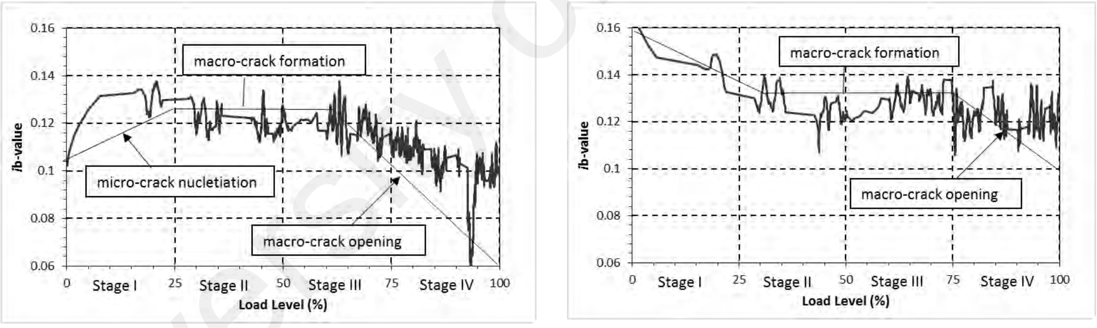

(c) Sensor 3 (d) Sensor 4

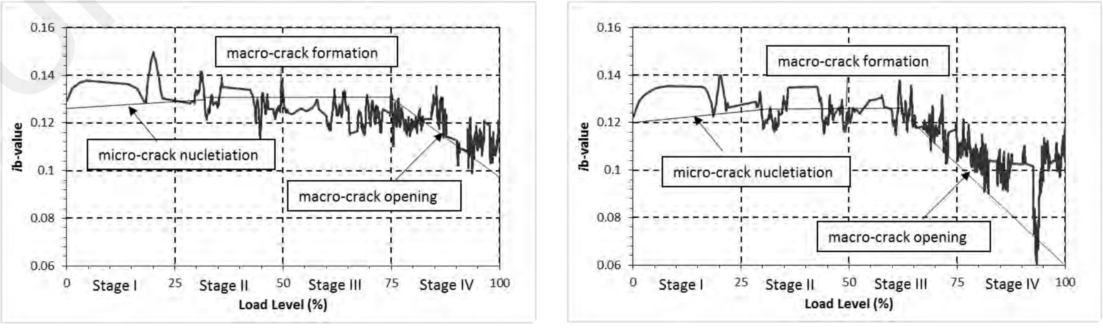

(e) Sensor 5 (f) Sensor 6

Figure 4. 22: *I*b-value of Control beam specimen

However, for some sensors, i.e. sensor 4 of Control beam specimen, and sensor 3 and 6 of LC beam specimen have different trend of *I*b-value. From the figures, the *I*b-value started with decrease at the damage stage I. This might indicate the high AE events at the tension reinforcement side near the position of the sensors.

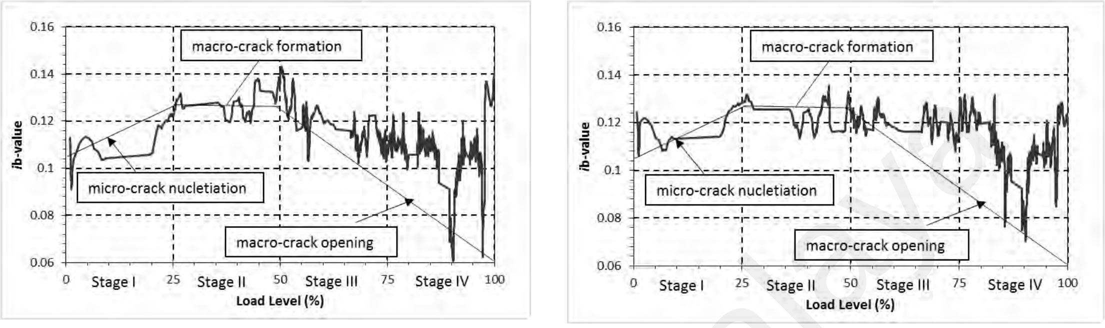

(a) Sensor 1 (b) Sensor 2

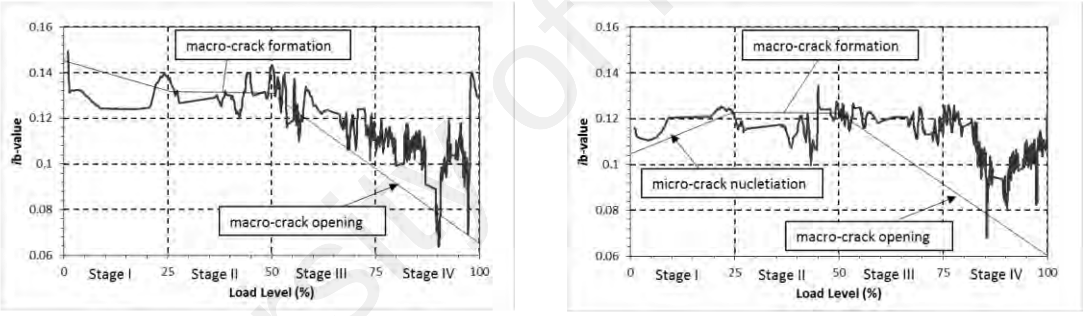

(c) Sensor 3 (d) Sensor 4

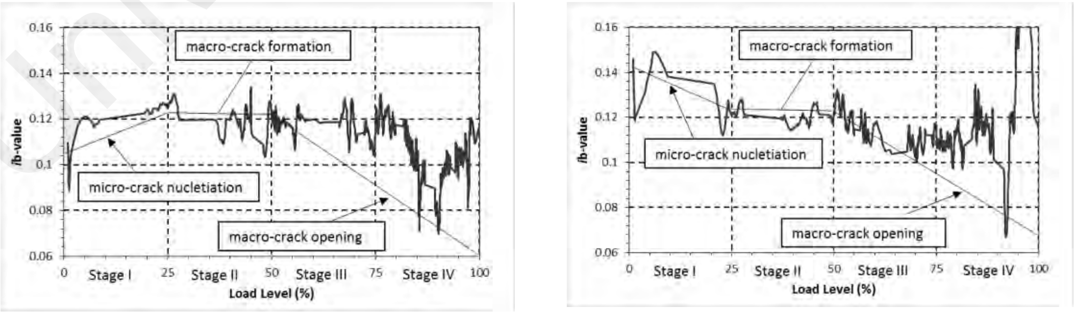

(e) Sensor 5 (f) Sensor 6

Figure 4. 23: *I*b-value of LC beam specimen

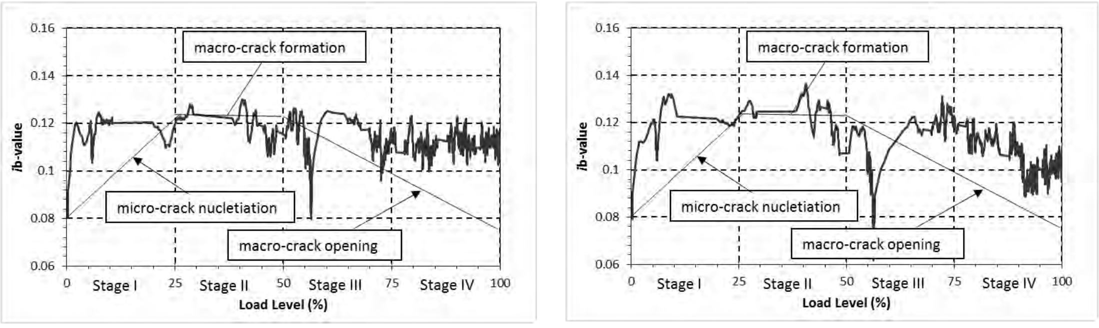

(a) Sensor 1 (b) Sensor 2

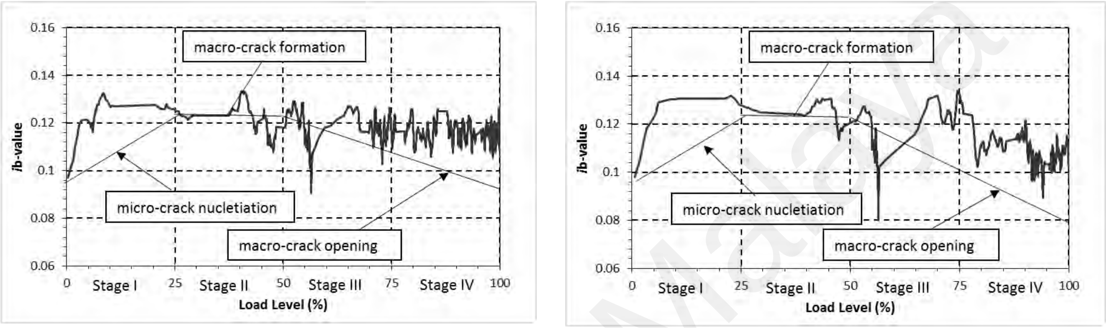

(c) Sensor 3 (d) Sensor 4

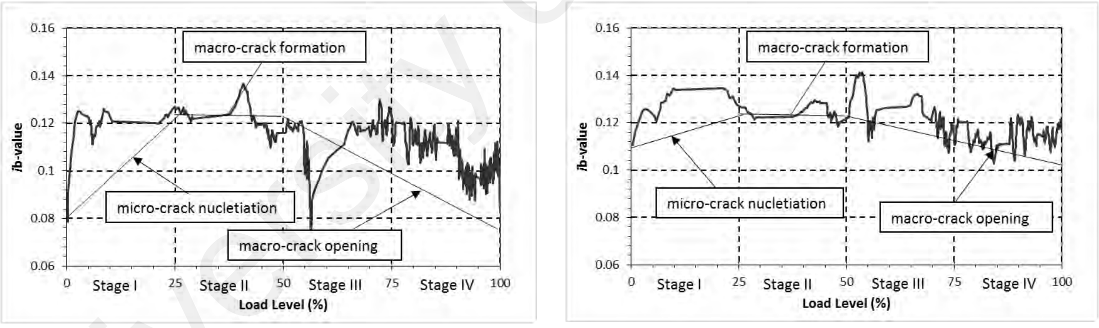

(e) Sensor 5 (f) Sensor 6

Figure 4. 24: Ib-value of HC beam specimen

Figure 4.25 shows *I*b-value of all sensor of the three beam specimens. It can be clearly observed that same trend of the *I*b-value like Figures 4.22 to 4.24. From Figure 4.25 (b), which is the Control beam, we can infer that micro-cracks formation was dominant in the damage stage I, which show the increasing trend of *I*b-value. Then it began to localize as macro cracks in damage stage II and III with a fluctuation region. After that, the *I*b-value started to decrease at the end of damage stage III and damage stage IV as macro cracks opening happened. The similar trend shows in other beam specimens as well, however, for the HC beam specimen, the *I*b-value started to decrease earlier at the end of damage stage II. This indicated that the macrocracks opening earlier at the tension reinforcement side of the beam specimen. Higher *I*b-value reflect small AE events where lower of *I*b-value implies active nucleation of large AE events (Ohtsu et al., 2007; Ohtsu & Uddin, 2008). The lowest *I*b-value of the beam specimens were 0.076, 0.064, and 0.067, respectively. The lowest *I*b-value occurs at the damage stage IV for all beam specimens except HC beam specimen. For the HC beam specimen, the lowest *I*b-value occurs at the early of damage stage III.

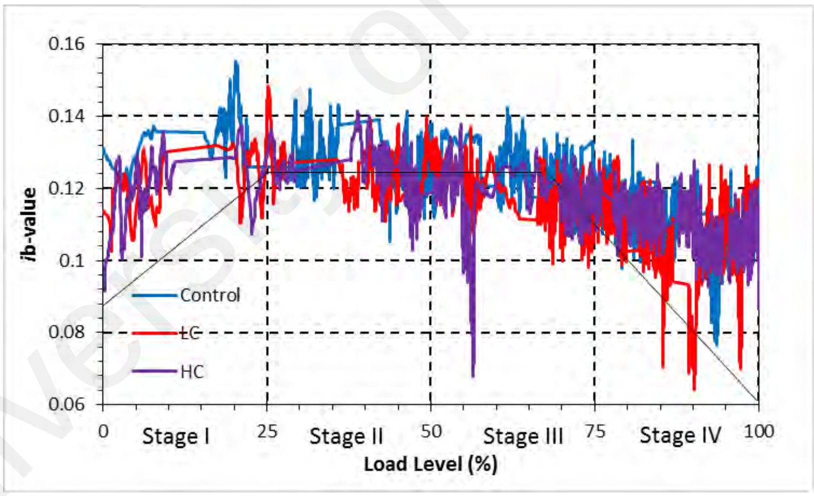

(a) All

Figure 4. 25: Ib-value of beam specimens

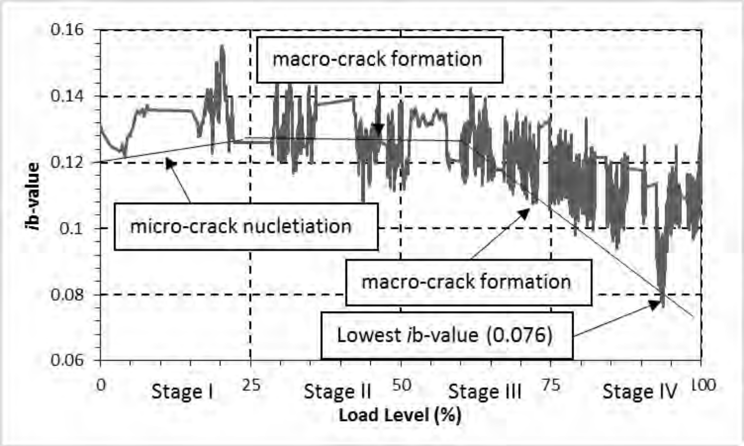

(b) Control

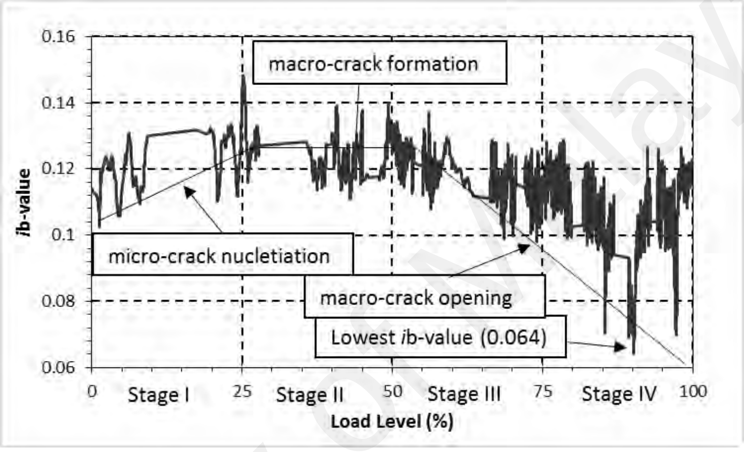

(c) LC

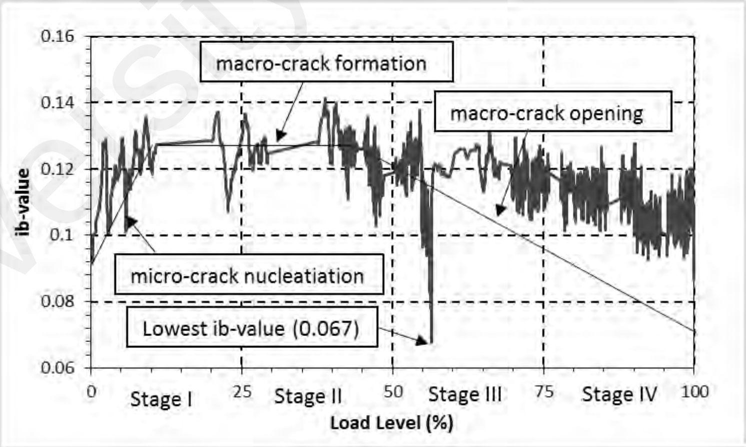

(d) HC

Figure 4. 25: Continued

4.6 Intensity Analysis (IA)

The maximum value of Hi and Sr from each damage stage in the experiment are plotted in Figure 4.26 and 4.27. The intensity analysis-based criteria for assessing the steel corrosion in concrete has been developed by Velez et al. (2014). However, the Hi and Sr data does not match in the divided criteria of the assessment chart.

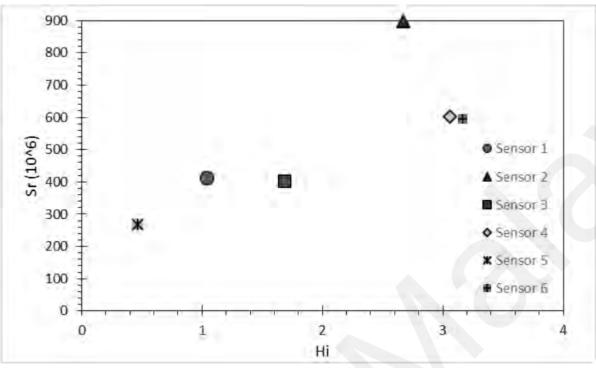

(a) Control

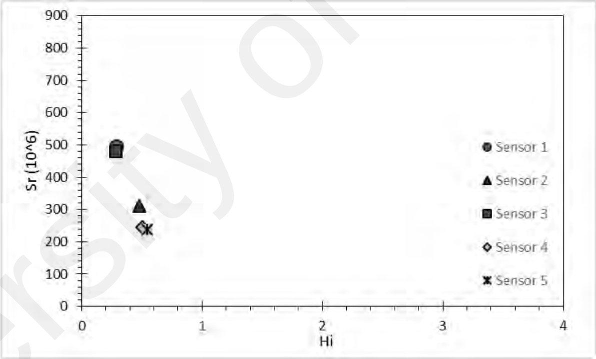

(b) LC

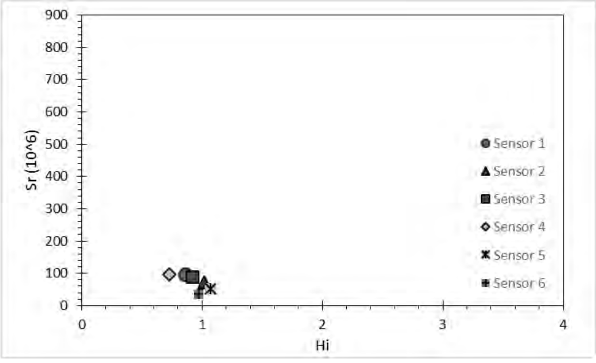

(c) HC

Figure 4. 26: Intensity analysis of each sensor of the beam specimens

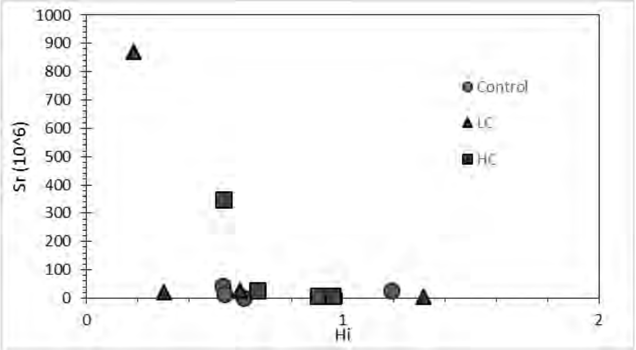

(a) All

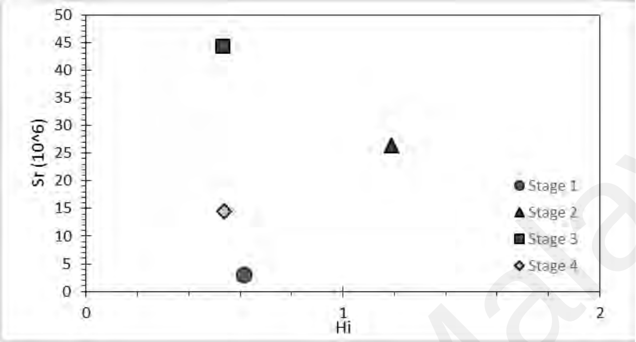

(b) Control

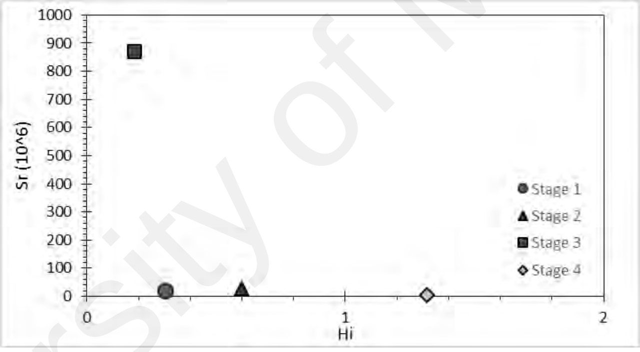

(c) LC

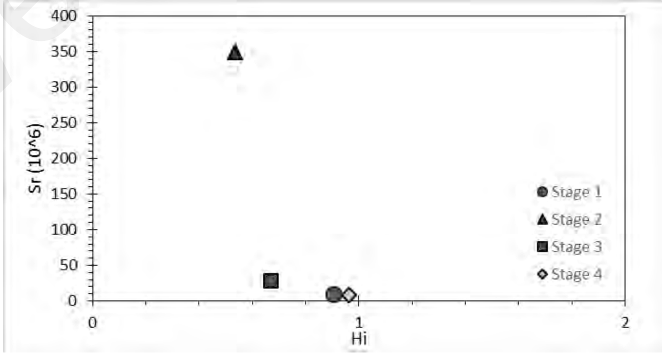

(d) HC

Figure 4. 27: Intensity analysis of each damage stages of the beam specimens

Actually, Figure 4.26 and 4.27, the Hi and Sr data have been analyzed based on the distribution plot. From figure 4.26, the distribution of Hi and Sr for each sensor tends to decrease in terms of increase of corrosion levels. However, this trend is not acceptable for quantifying the structural significant of an AE event. Thereafter, the Hi and Sr based on damage stage were analyzed for the beam specimens.

From Figure 4.27, at the damage stage I, the severity of the beam specimen is low as there is only micro-cracking in the beam specimen before the first visible crack occurs. Figure 4.27 (a) shows when at damage stage I, the severity is the lowest and recognized as a micro-cracking stage. Then, after the damage stage II, the first visible crack occurs, which represented the crack propagation. There is the highest value of severity index at damage stage III as the crack distribution of the beam specimens. However, for the highest corroded beam specimen as shown in Figure 4.22 (d), the highest plot of intensity chart (high Hi and Sr index) occurs at damage level II due to the crack have been observed to start distributing at tension reinforcement side of the beam specimen.

4.7 Summary of experiment 1

The AE technique is used for monitoring and evaluating the influence of corrosion on the structural behaviour of steel beam specimens under three-point flexure test for primary AE. In this experiment, the steel reinforcement was corroded using the post-corrosion method. Analysis of the AE data reveals distinguishable trends for RA value and AF for different corrosion levels. In addition, the index of damage (ID) derived from the AE energy parameters obtained during the early stage of damage was found to be useful as an indicator for evaluating the corroded beam specimens at initial loadings. Moreover, based on the analysis, it is noted that the tensile fracture became more dominant with an increase in corrosion levels. However, this experiment has not been carried out in the area of fracture behaviour of the AE technique for secondary AE. The secondary AE data are needed to know the behaviour due to friction between the interface of steel reinforcement and concrete before first visible cracks occur. Therefore, in experiment 2 and 3, the primary and secondary AE techniques are utilized to evaluate the fracture behaviour of corroded beam specimens subjected to flexural loading.

CHAPTER 5: RESULTS AND DISCUSSIONS FOR EXPERIMENT 2 RELIABILITY OF PRIMARY AND SECONDARY AE FOR CORROSION EVALUATION OF PRE-CORROSION CONCRETE STRUCTURES

5.1 Introduction

Table 5.1 shows the results of compressive strength and modulus of elasticity tests done for concrete casted for experiment 2 and 3. The concrete of experiment 2 and 3 were casting in same batch. As shown in the table, both the 7th day and 28th day compressive strengths are higher than the design strength of 28 MPa. The concrete already met its characteristic strength at the age of 7th day. Apart from that, the average modulus of elasticity of concrete is 26.49 GPa.

Table 5. 1: Compressive strength and modulus of elasticity of concrete

Age of concrete	Compressive strength (MPa)		Average modulus of elasticity (GPa)
	For one specimen	Average	
7th day	30.85	29.40	-
	27.11		
	30.25		
28th day	35.14	37.31	26.49
	37.79		
	38.99		

After the accelerated corrosion test of steel reinforcements using impressed current technique, the steel reinforcements were cleaned to remove the rust (corrosion products) on the surface based on the ASTM G1-03 (2003). The cleaned steel reinforcements are shown in Figure 5.1. The quantitative results are as tabulated in Table 5.2. According to Table 5.2, there were six steel reinforcements of corrosion levels ranging from 0% to 51% that were used in this experiment for the casting of the beam specimens.

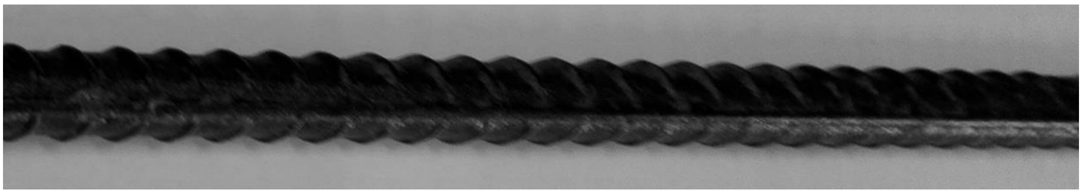

(a) S0

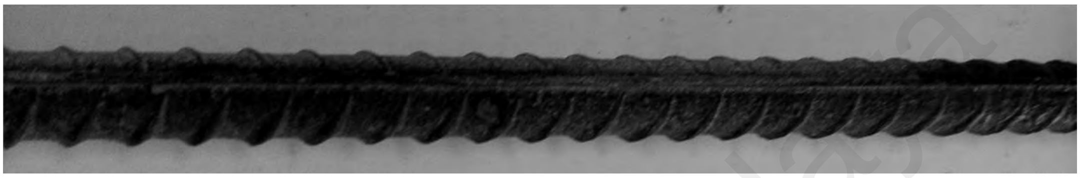

(b) S8

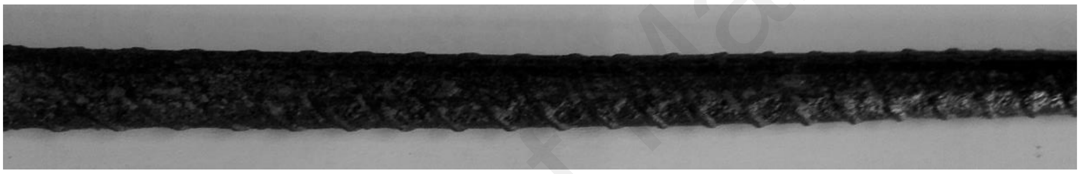

(c) S9

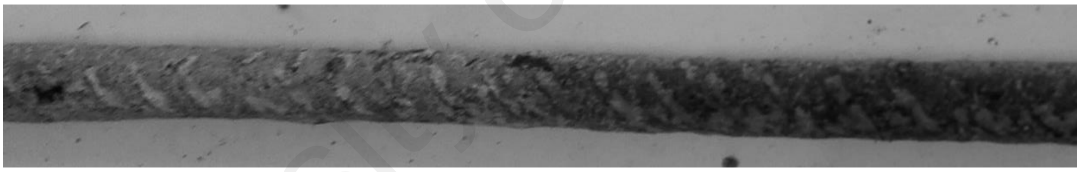

(d) S24

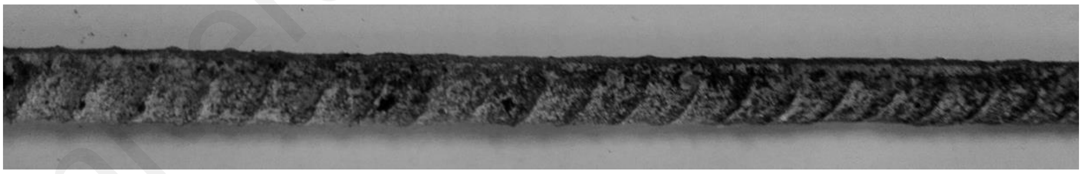

(e) S28

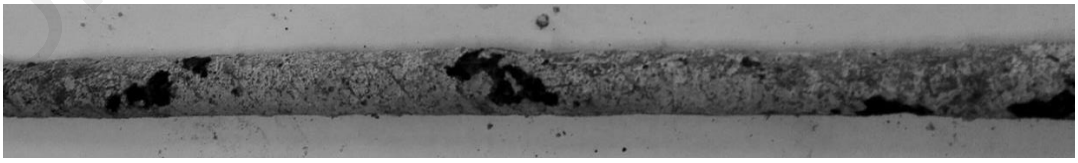

(f) S51

Figure 5. 1: Condition of steel reinforcements after accelerated corrosion test of experiment 2

Table 5. 2: Quantitative results of accelerated corrosion process of experiment 2

No	Beam specimens	Initial mass, M_i (g)	Final mass, M_f (g)	Mass loss, Δm (g)	Corrosion Level (%)
1	S0	520	520	0	0.00
2	S8	514	472	42	8.17
3	S9	508	462	46	9.06
4	S24	504	382	122	24.21
5	S28	508	368	140	27.56
6	S51	522	258	264	50.57

5.2 Mechanical Behaviour

From Figure 5.2, it can be seen that most of the beam specimens experienced brittle failure while the specimen with the highest corrosion level of S51 beam specimen experienced significant yielding before failure, which means it failed in ductile failure. Theoretically, the S0 beam specimen should fail in ductile failure which means that the section is under-reinforced. The steel reinforcement may reach its yield strength before the concrete reaches its strength. In this mode of failure, the steel reinforcement yields, the beam sags and large tensile cracks become visible before the reinforcement finally fails.

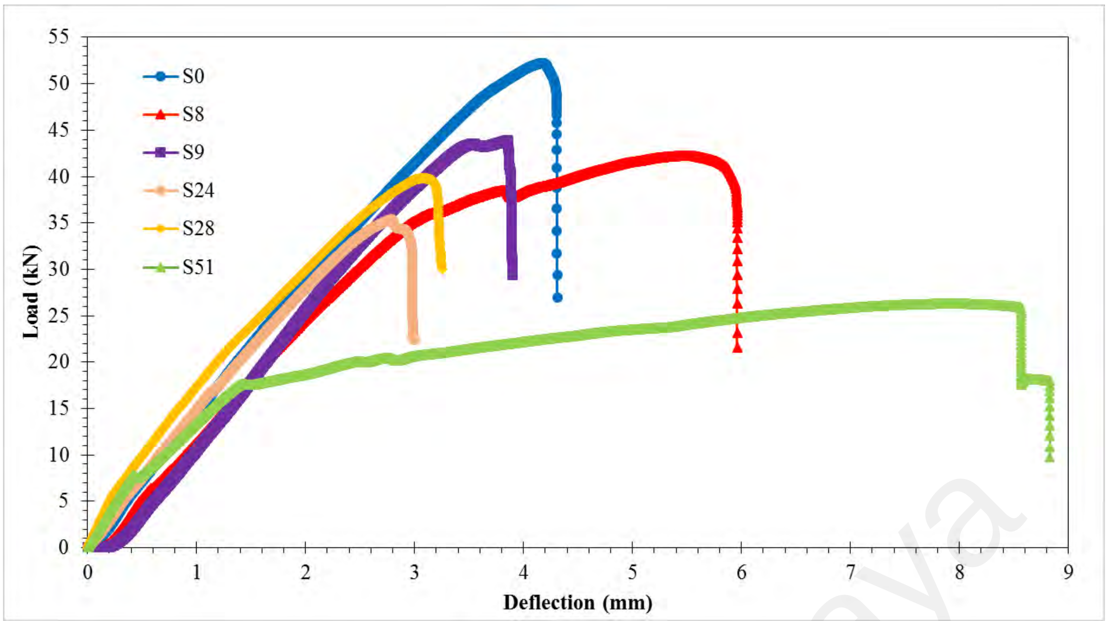

Figure 5. 2: Load against mid-span deflection of the beam specimens

However, the S0 beam specimen failed in brittle failure which signifies that the section is most probably balanced-reinforced. The concrete reached its ultimate strength and crushed at the same time when the steel reinforcement yielded. According to the observation, the S0 beam specimen failed in a sudden with the concrete failing in compression. This mode of failure is not preferable as it gives little or no warning before failure. This failure mode is low in safety.

However, as the corrosion levels increase, it can be observed from Figure 5.2 that there is a shifting of dominant failure mode from brittle to ductile. It may be due to the steel corrosion (i.e. pitting corrosion) of steel reinforcement which increased the ductility of the beam specimens. Steel reinforcement yielding became more pronounced with the increment of corrosion level, inferring higher "working stress" (the stress to which material may be safely subjected in the course of ordinary use) sustained by steel reinforcement as a result of reduction in effective cross section area. Table 5.3 shows the peak load and maximum displacement of the six beam specimens. The load capacities of the beams specimens decreased as the corrosion levels increased. Besides that, the peak displacement of the beam specimens basically shows a decreasing trend except the S8 beam specimen. The S51 beam specimen with the highest corrosion level has the highest displacement value of 8.83 mm which means that it experienced significant yielding before it failed.

Table 5. 3: Maximum load and maximum displacement for six beam specimens

Corrosion level (%)	Ultimate Peak load (kN)	Peak displacement (mm)
0	52.21	4.31
8	42.25	5.96
9	43.87	3.90
24	39.80	3.25
28	35.39	3.00
51	26.29	8.83

By plotting peak load against corrosion level as shown in Figure 5.3, the increase of corrosion level of steel reinforcement was found in linear with the decreasing load capacity of the corroded beam specimens. The regression value, R^2 of the linear graph with negative gradient is 0.934 which is highly acceptable as it is near to 1. In addition, this experimental result confirmed that the beam specimen’s loss capacity was linked to the cross-section loss at the failure location.

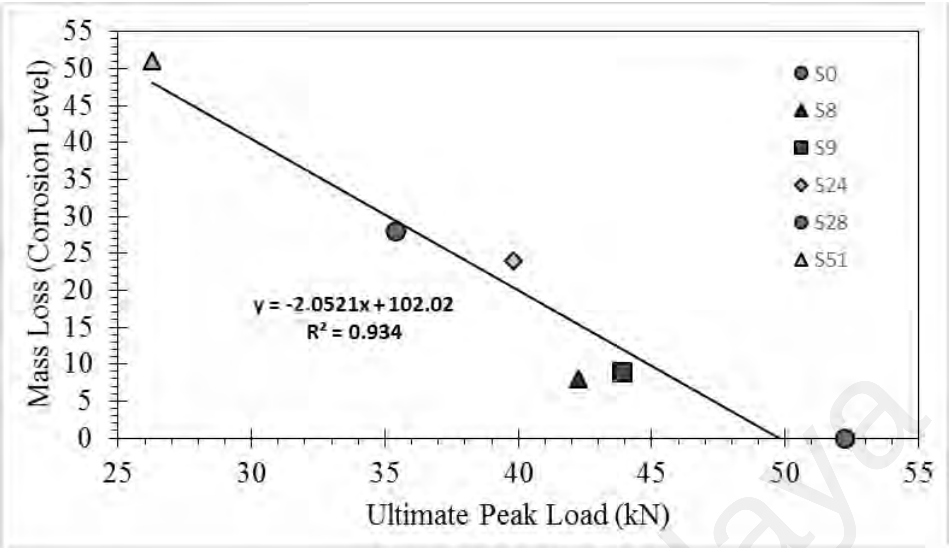

Figure 5. 3: Loss of ultimate strength against mass loss of the beam specimens

Ductility is a mechanical property of material that signifies the degree of plastic deformation a material can sustain prior to fracture or failure. Due to the corrosion levels of the beam specimens are different, this parameter is determined based on its deflection. Table 5.4 shows the summary of the ductility factor for each specimen.

Table 5. 4: Determination of ductility factor

Beam specimens	Maximum (peak) load (kN)	Deflection at yield, Δ_y (mm)	Peak Deflection, Δ_u (mm)	Ductility factor
S0	52.21	3.75	4.31	1.15
S8	42.25	3.00	5.96	1.99
S9	43.87	3.11	3.90	1.25
S24	39.80	2.59	3.25	1.26
S28	35.39	2.54	3.00	1.18
S51	26.29	1.41	8.83	6.26

The ductility factor ranges from 1.15 to 6.26 of all beam specimens. They are more to brittle and less ductile with the narrow range of difference in the ductility factor. However, the ductility factor for corrosion level of S8 and S51 beam specimens are higher which are 1.99 and 6.26, respectively. It means that these two beam specimens have higher ductility among all the beam specimens and hence S51 beam specimen experienced large yielding before they failed. This may due to tensile steel reinforcement of the beam specimen managed to function much better during the loading process. Therefore, it was able to undergo appreciable plastic deformation before failure. Apart from that, pitting corrosion may have contributed to the increase of the ductility of the beam specimen. This is because the S51 beam specimen experienced the most severe pitting corrosion and it has the highest ductility factor among all the beam specimens.

From Figure 5.4, all the beam specimens failed with shear cracks at support with few numbers of cracks in the middle part of the beams that can be observed. However, S51 beam specimen with the highest corrosion level failed with single number of cracks in the middle part of the beam. As the loading process progressed, the cracks started to develop from the support and it propagated accordingly to the top of the middle span by increasing in crack width till failure happened. On the other hand, the cracks formation of the S51 beam specimen was most probably due to the lowest cross section of steel reinforcement and existence of pitting corrosion pits that act as precursors to cracking.

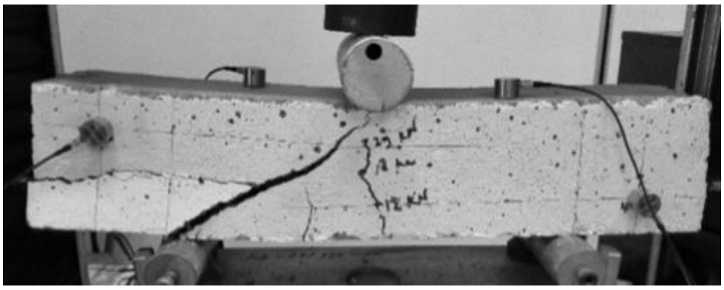

(a) S0

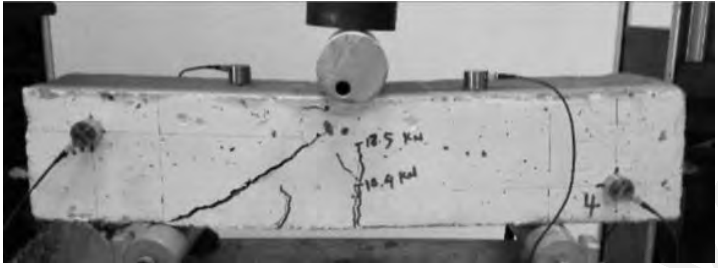

(b) S8

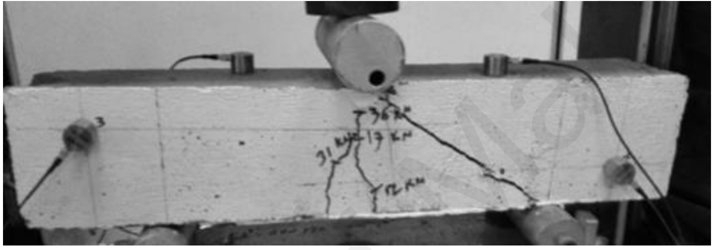

(c) S9

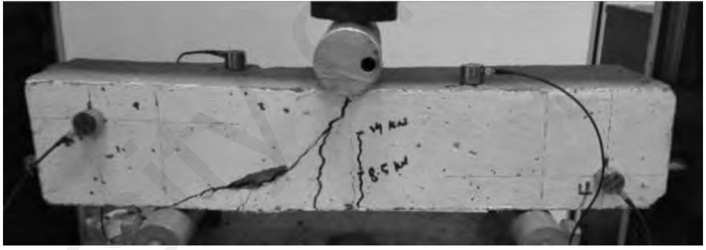

(d) S24

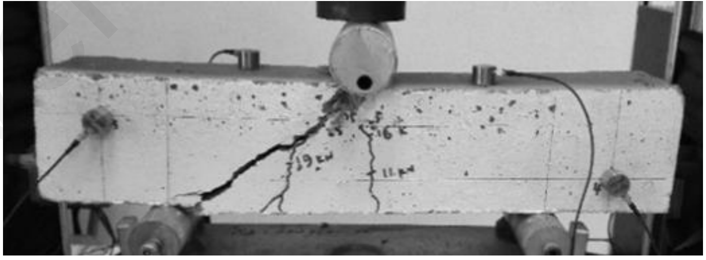

(e) S28

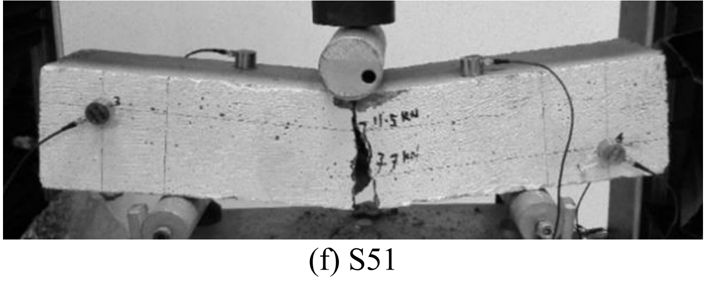

(f) S51

Figure 5. 4: Condition of beam specimens after failure

Pitting corrosion will influence the fatigue strength and life of the structures by reducing the average material thickness that influences the nominal stress in the structure (Jakubowski, 2011). It also induces the roughness of the material surface that leads to local stress concentrations at some locations on the surface. With this, the stress cannot be distributed to the whole steel reinforcement but concentrated on certain locations that experienced pitting corrosion. In addition, it causes crack and failure to occur at the particular location. Due to this experiment is based on the pre-corrosion, hence the bond strength does not decrease and has no effect on all of the phenomenon. The cracking progression of the S8 beam specimen is shown in Figure 5.5.

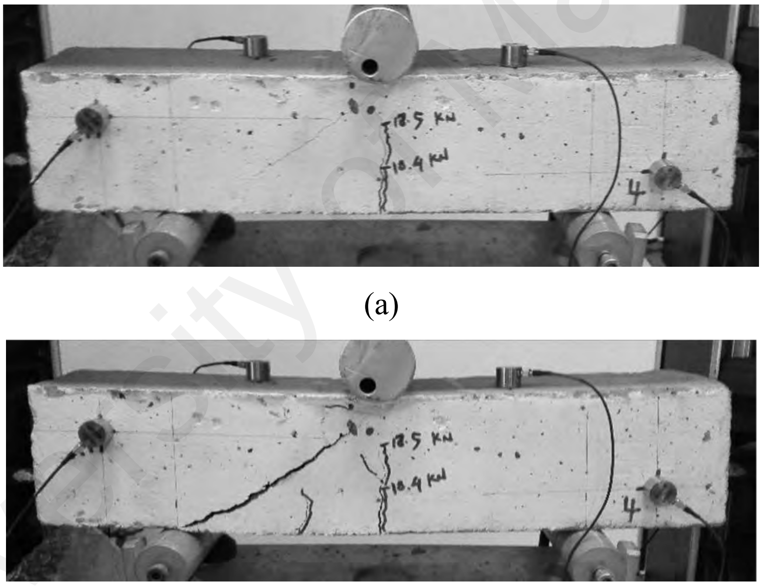

(a)

(b)

Figure 5. 5: The crack progression of the S8 beam specimen of experiment 2

Based on the load and deflection curves as well as the observations, as shown in Figure 5.2, the development of the beam damage was classified into the following three general levels: damage level 1 (micro-cracking), damage level 2 (first visible crack and crack distribution), and damage level 3 (damage classification).

5.3 Primary AE results

Table 5.5 presents a summary of the primary AE parameters of the pre-corrosion specimens along the three different damage levels (i.e. damage level 1, 2 and 3). The primary AE parameters of the specimens are duration, amplitude, average frequency, hits, and counts.

Table 5. 5: Primary AE parameters of experiment 2

Beam Specimens	Damage Level	Duration (x1000 µs)	Amp (dB)	Ave Freq (kHz)	Hits	% of Total Hits	Counts
S0	1	13.492	33.93	19.39	15905	10.91	5335290
	2	7.576	36.73	24.98	94692	64.95	21847676
	3	7.051	37.77	24.65	35196	24.14	6677251
S8	1	5.042	37.69	25.47	19347	4.53	2172830
	2	6.108	38.16	26.40	144663	33.84	18825270
	3	6.720	38.88	25.86	263497	61.64	43238546
S9	1	6.800	35.48	18.74	38378	25.74	7340042
	2	6.635	35.29	18.02	107531	72.12	18735510
	3	9.366	31.65	7.98	3195	2.14	292463
S24	1	7.598	37.14	20.28	16045	5.72	2189279
	2	6.720	37.73	22.54	202012	72.07	28856714
	3	6.853	37.60	22.20	62262	22.21	9856692
S28	1	10.263	38.93	23.48	39145	20.20	12188031
	2	6.822	37.48	21.51	154659	79.80	25198747
	3	-	-	-	-	-	-
S51	1	15.805	43.14	29.29	5910	3.20	3278323
	2	6.290	39.23	29.54	45566	24.67	5770389
	3	7.048	38.66	28.89	133190	72.12	16649453

5.3.1 Accumulated AE Hits

Figure 5.6 shows the relationship between the accumulated AE hits and load level (%) of the beam specimens. In general, the accumulated AE hits increase as the increase corrosion level of the specimens due to loss of cross section. However, the corrosion beam specimens (i.e. S8, S9, S24, S28 and S 51 of beam specimens) experienced different trend of the accumulated AE hits. This may due to the presence of different pitting corrosion in the steel reinforcement that caused high AE activity of the beam specimens.

In general, as the load is applied, the AE hits appear to increase prior to the first visible cracks. After the formation of the first visible crack at the range of 10% to 20% of the load level, the rate of AE hits significantly increases. Afterward, as the loading continues, the cracks propagate, and the AE hits gradually increase until beam specimen failure occurs. However, for S9 beam specimen, the AE hits activity increase insignificantly (stagnant) at around 2 x 10^5 after 50% of load level. This trend happen probably due to the stressing and majority of cracking, especially longitudinal cracking along the steel reinforcement, which has already been dissipated by the steel corrosion.

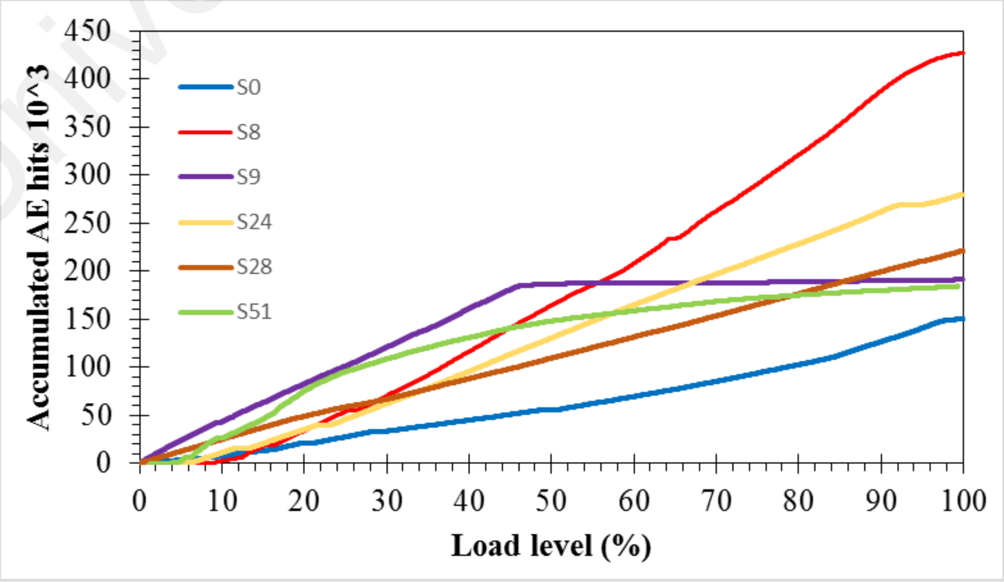

Figure 5. 6: Cumulative AE hits against load level (%)

5.3.2 Crack Classification – RA value and AF

To study on the fracture mechanism of the beam specimens in a more detailed way, average frequency (AF) and RA values of both AE parameters were plotted against time as shown in Figure 5.7. For the S0 beam specimen, from the beginning of loading, shear cracks are observed due to high RA and low AF values. This indicates that high density events occurred within the concrete at the tension area (Kawasaki et al., 2014). Then, after first few loads to the end of damage level 1 (when first visible crack occurred), RA value decreases and AF value increases significantly. This indicates that the micro-fractures were propagated extensively.

After the first visible crack occurred, RA value tends to increase while AF value tends to decrease which signifies shear cracks occurrence than tensile cracks. This indicates the nucleation and progress of further crack inside the concrete. After 17 kN of this load, both RA and AF values fluctuated which means that mixture of shear and tensile cracks occurred. During the early of damage level 3 which was occurred slightly after the yielding, the RA value increases and AF value decreases which suggest shear cracks. It indicates the progress of cracking due to ultimate failure of the beam specimen.

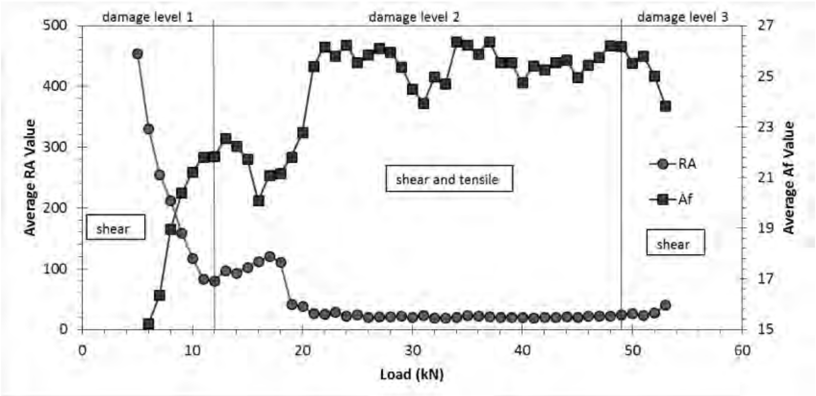

(a) S0

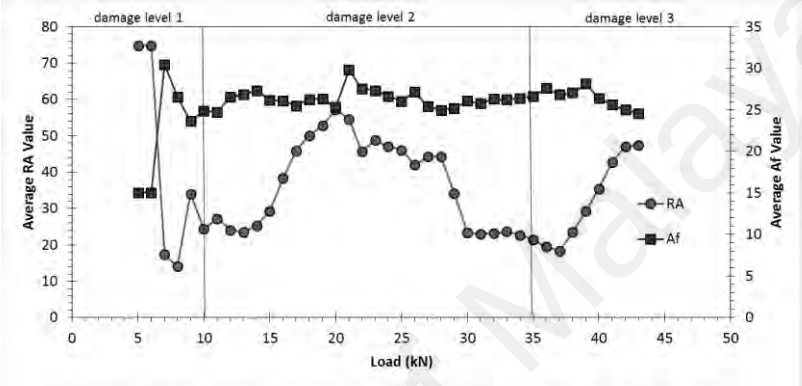

(b) S8

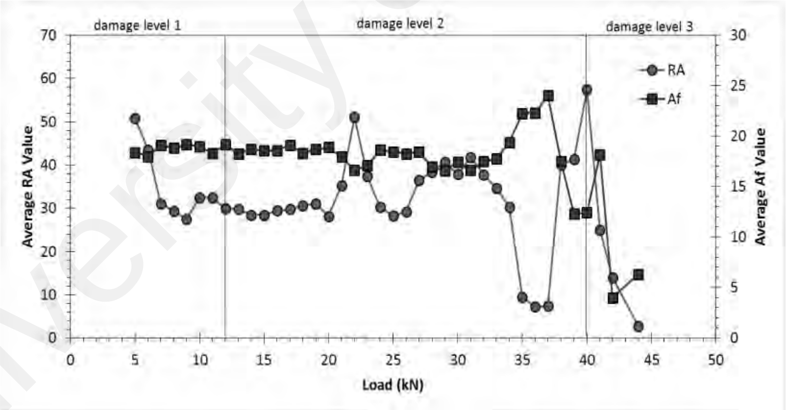

(c) S9

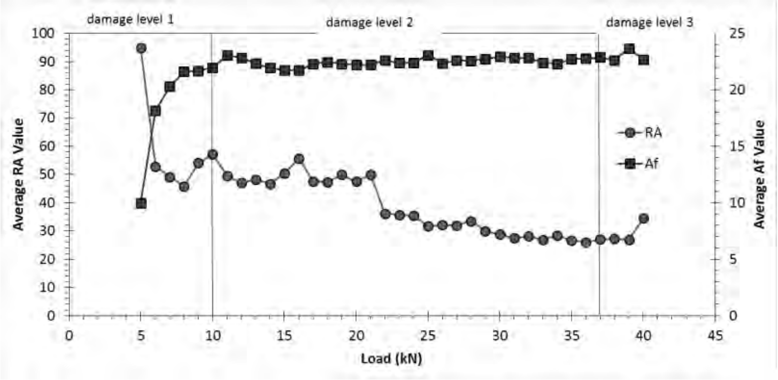

(d) S24

Figure 5. 7: Average RA and AF values against load of the beam specimens

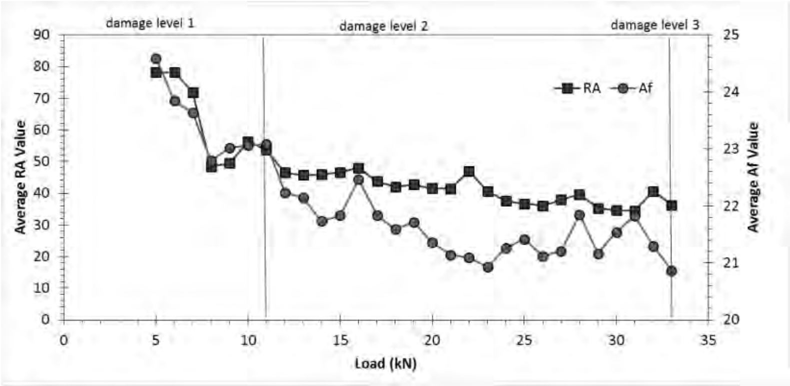

(e) S28

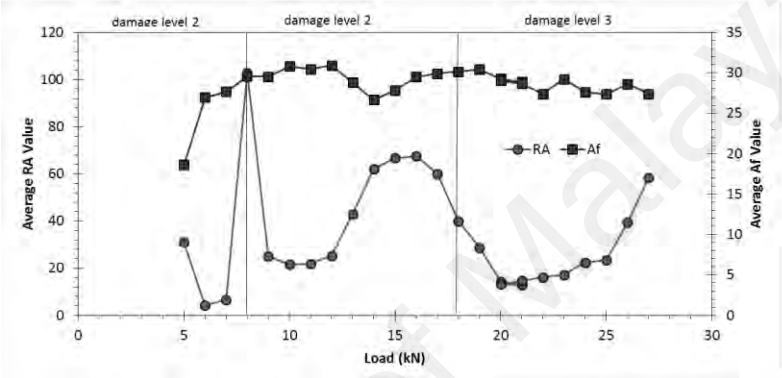

(f) S51

Figure 5. 7: Continued

Overall of the corroded beams specimens (i.e. S8, S9, S24, S28, and S51 beam specimens), they illustrate a similar trend to the S0 beam specimen at the damage level 1. However, there are a significant increase of RA and decrease of AF at the middle of damage level 2. The shear cracks have been observed to start propagating from the tension side of the RC beam, at the proximity of the steel reinforcements. While for the S28 beam specimen, after the first visible crack, both the RA and AF values fluctuate until the end of the loading process. It can be interpreted that mixture of shear and tensile cracks occurred evenly until ultimate failure.

On the other hand, for the S51 beam specimen with the highest corrosion, when the first crack occurred, there was a sudden increase of RA value and high AF value were observed which signifies the occurrence of tensile cracks. This condition indicates that the macro-fracture occurred at the tensile reinforcement area. As mentioned before, there was a presence of significant pitting corrosion at the middle part of steel reinforcements. The pitting corrosion helps the tensile crack to propagate extensively. At damage level 2, a mixture of tensile and shear cracks occurred and there were significant increase of RA and decrease of AF at the end of this stage. There were shear cracks happened at tensile steel area due to the extensive yielding of steel reinforcement. After the yielding point which is at damage level 3, the beam specimen at tensile cracks due to the decreasing of RA and AF values was being observed. At the end of damage level 3, the relationship switched to shear crack. The significant increase of RA value and decrease of AF before the beam failed were observed. This phenomenon might be associated with the steel reinforcement yielding until it broke into two parts.

Aggelis et al. (2011) explained that the wave modes excited by crack types (i.e. shear and tensile cracks). For shear cracks, even though longitudinal waves may still be excited, most of the energy is transmitted as shear waves which are slower. As a result, most of the energy (or maximum amplitude) arrives later than the first longitudinal arrivals resulting in high RA value. However, for tensile cracks, they cause a transient volumetric change inside the material and convert the released energy mainly into a longitudinal (dilatational) wave. Thus, the excited pulse containing longitudinal waves of large amplitude are faster than any other type of cracks and the resulting RA value is low. From Figure 5.8, it can be observed that as the corrosion level gets higher, in the average AF value increases and average RA value of the beam specimen decreases. This indicates the transition of beam dominating fracture behaviour which shifts from shear region to tensile region as the corrosion level increases.

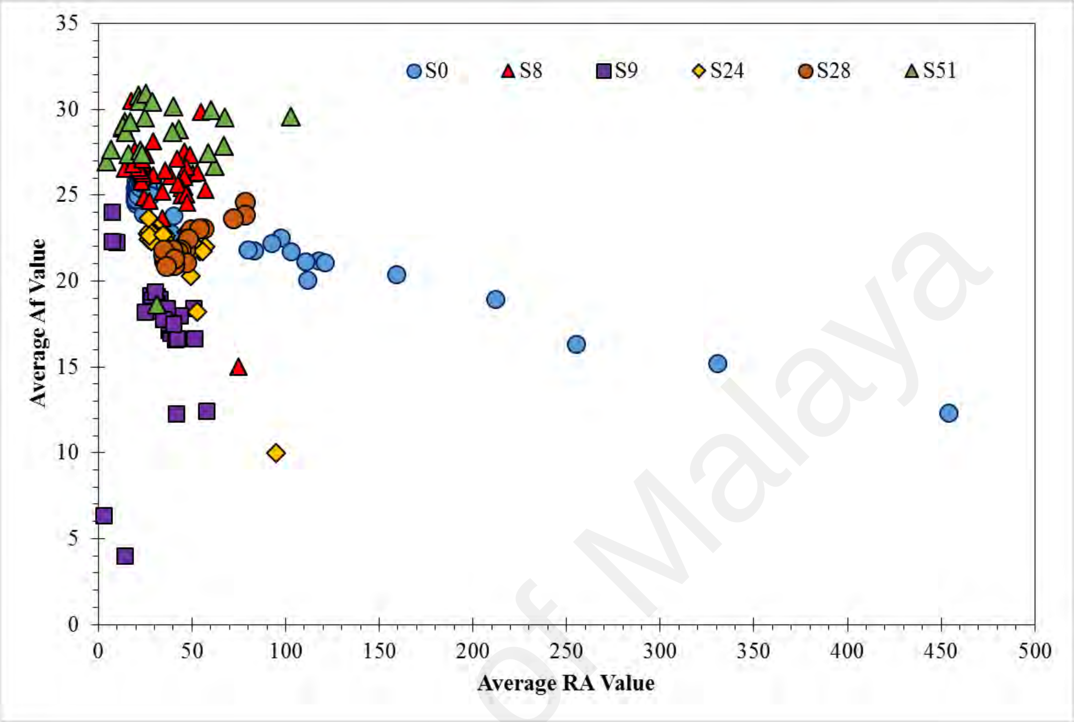

Figure 5. 8: Average AF against average RA value

5.3.3 Intensity Analysis

The intensity chart is plotted with the values of the historic index (Hi) and severity index (Sr) for each sensor and each damage level of various corrosion of the beam specimens, as shown in Figures 5.9 and 5.10 respectively. In general, intensity values that are clustered towards the top are associated with the phenomena of high structural significant events, whereas less structural significant events were concentrated near the bottom of the chart (MacGregor & Ghoneim, 1995). However, there is no significant trend of the intensity chart from Figure 5.9.

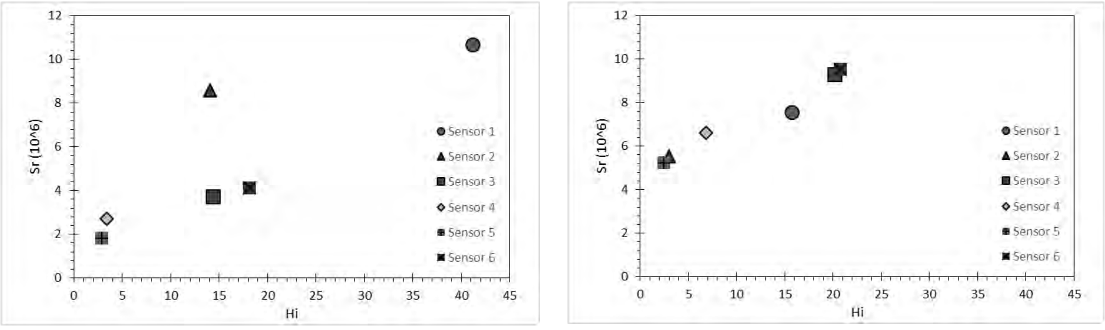

(a) S0 (b) S8

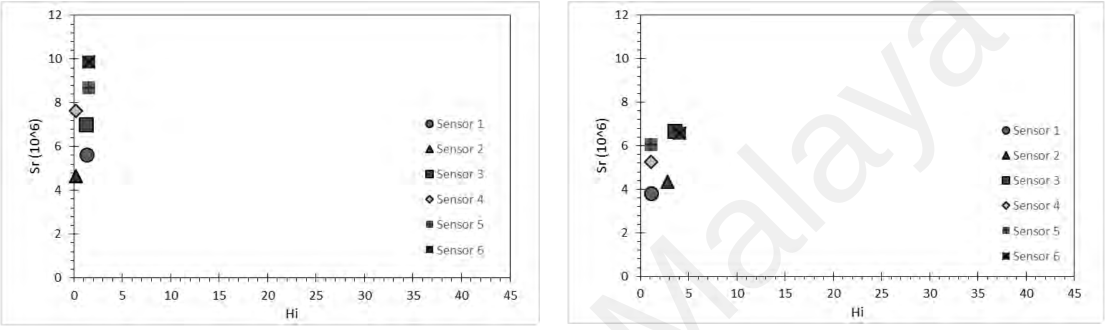

(c) S9 (d) S24

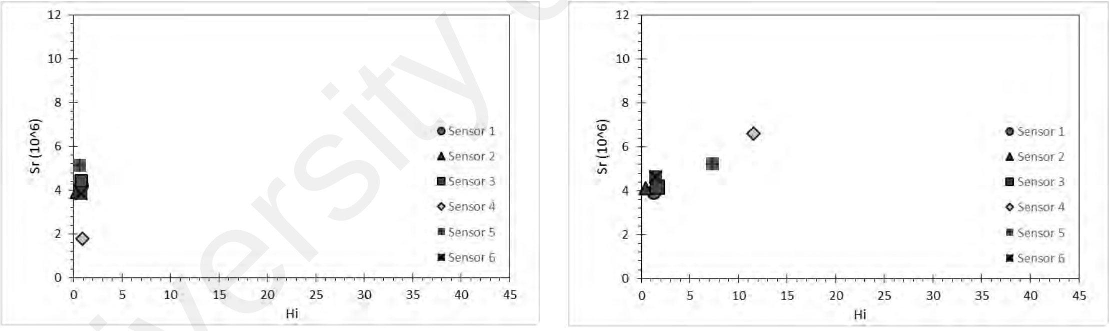

(e) S28 (f) S51

Figure 5. 9: Intensity chart at each sensor of the beam specimens

From the Figure 5.10, at the damage level 1, the severity of the beam is the lowest for all the corroded beam specimens compared to the other two damage levels (i.e. damage level 2 and 3). This is due to that there were only micro-cracking occurs in the beam before the first visible crack exists.

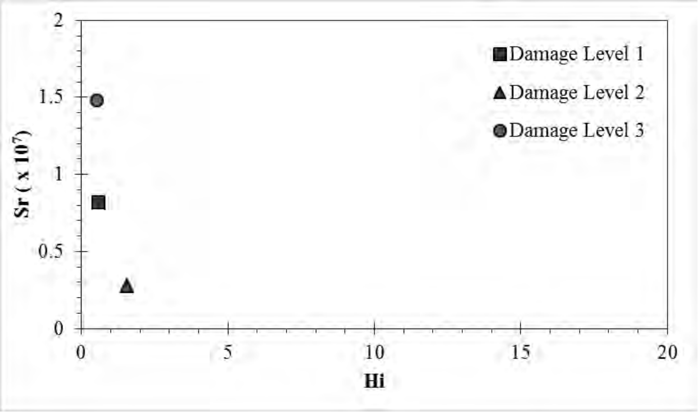

(a) S0

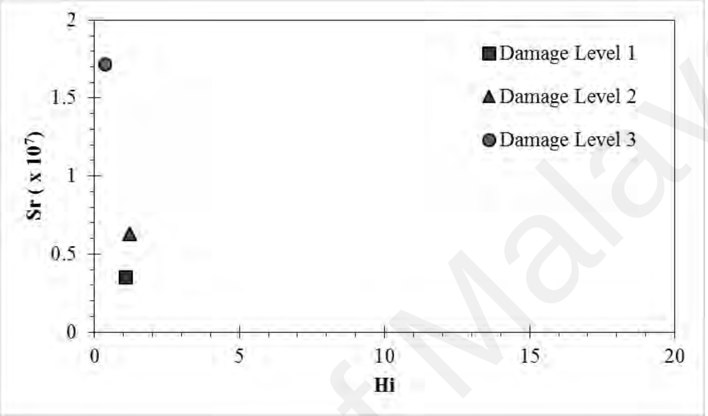

(b) S8

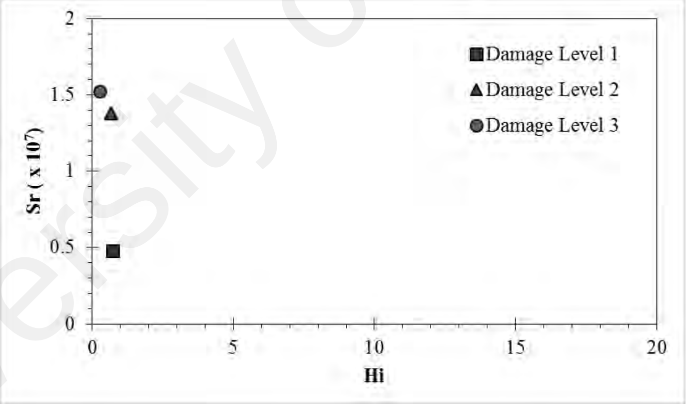

(c) S9

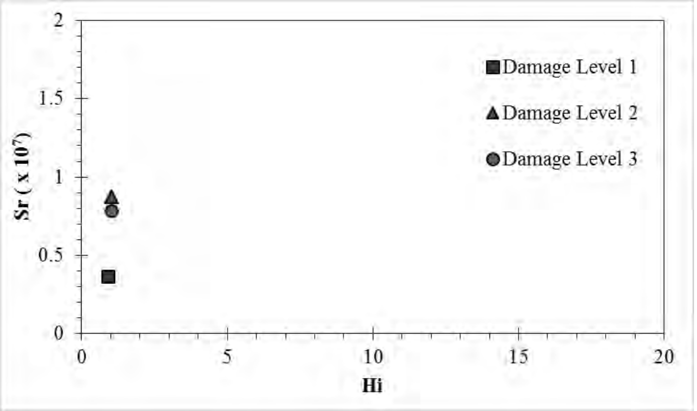

(d) S24

Figure 5. 10: Intensity chart at each damage level of the beam specimens

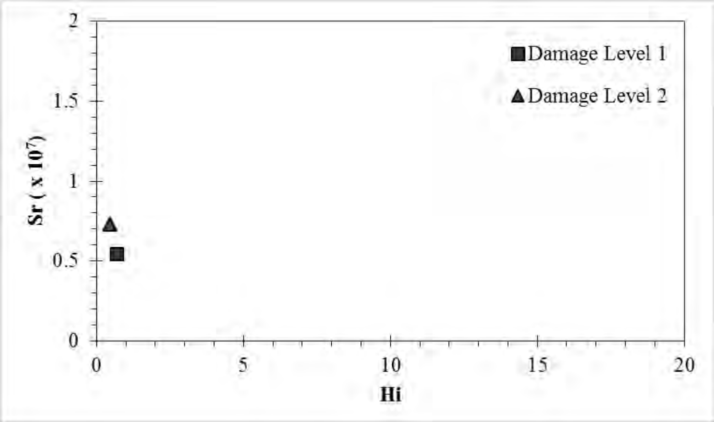

(e)S28

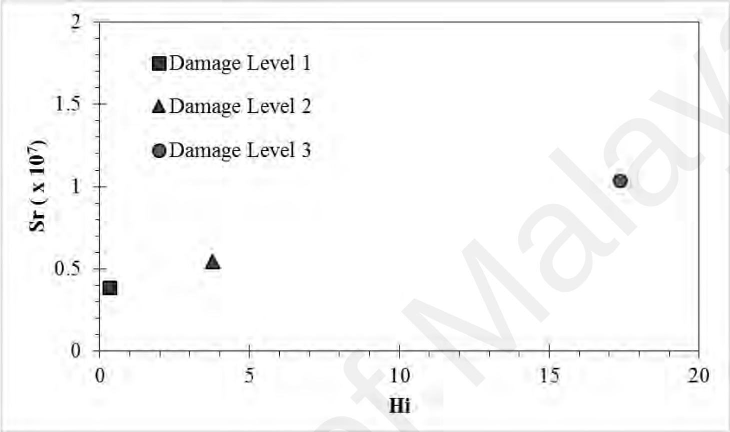

(f)S51

Figure 5. 10: Continued

At damage level 2, as load increases and the first visible crack is occurred on the face of the specimen, a significant increase in Sr value is observed. The higher Sr value and/or higher Hi value is obtained at damage level 2, which confirms that greater amount of damage occurs at this damage level. In this damage level, propagation of shear and tensile cracks occur continuously and progressively. In addition, for damage level 3, where yielding and the cracks start to localize to form major cracks. As the width of cracks increases, the value of Sr for all the beam specimens increases considerably also. The damage severity stage is identified to be in damage level 3 which is known as serious fracture of the beam specimens. One essential point to be mentioned and discussed here is that for the beam specimens, they have the highest Sr value at its damage level 3. Therefore, the highest Hi and/or Sr values as given by the beam specimens can be used as an indication to the severity of the damage experienced by the beam specimens.

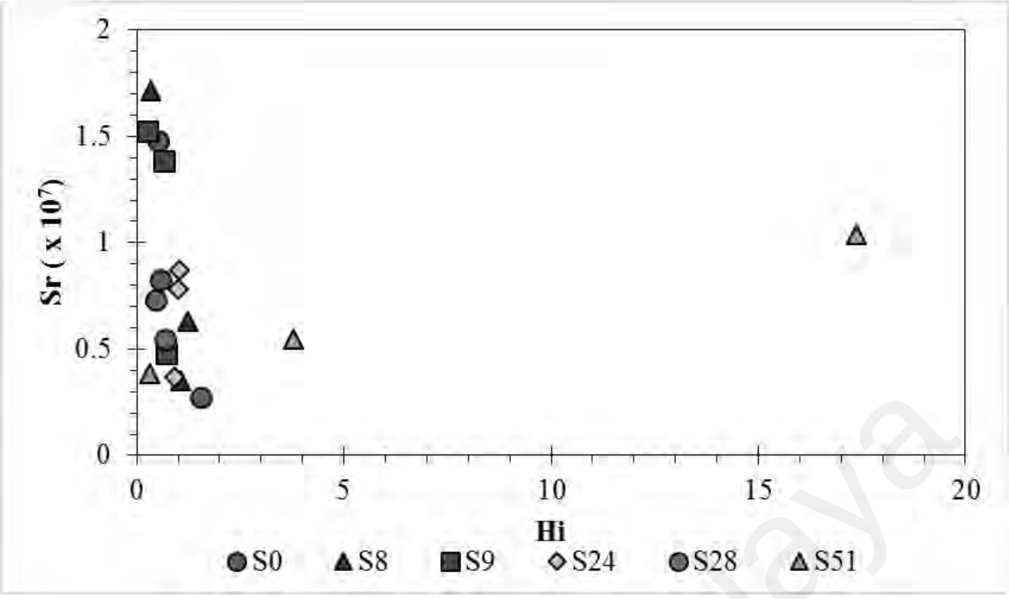

Figure 5. 11: Intensity analysis chart for all the beam specimens

5.3.4 *I*b-value

Figure 5.12 shows the *I*b-value of S0 beam before and after filtering. Savitzky-Golay smoothing was used to filter the *I*b-value data of the beam specimen. The filter has two options for parameters, namely polynomial fit (N) and window length (F). This filter is also suitable for a variable that is both slowly varying as well as corrupted by random noise. Replacing each data point by some kind of local average of surrounding data points to smoothen the noisy data is beneficial in increasing the signal-to-noise ratio without distorting the signal. Averaging can reduce the level of noise without influencing the value obtained because nearby points measure near the same underlying value.

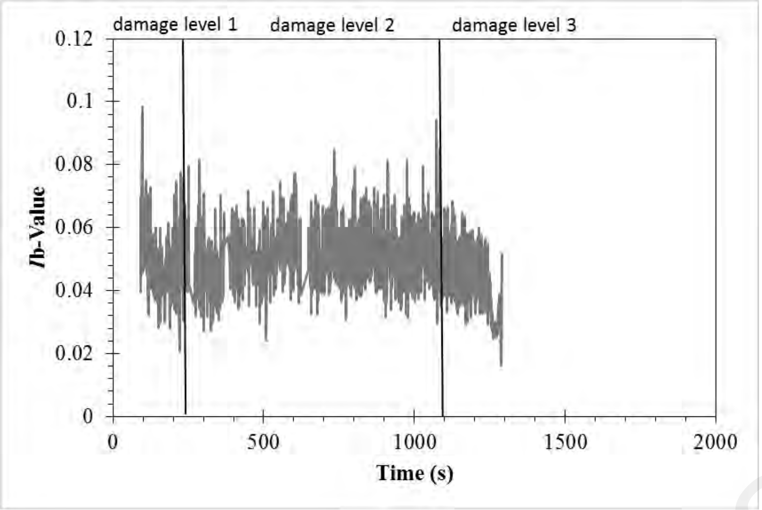

(a) Before filtering

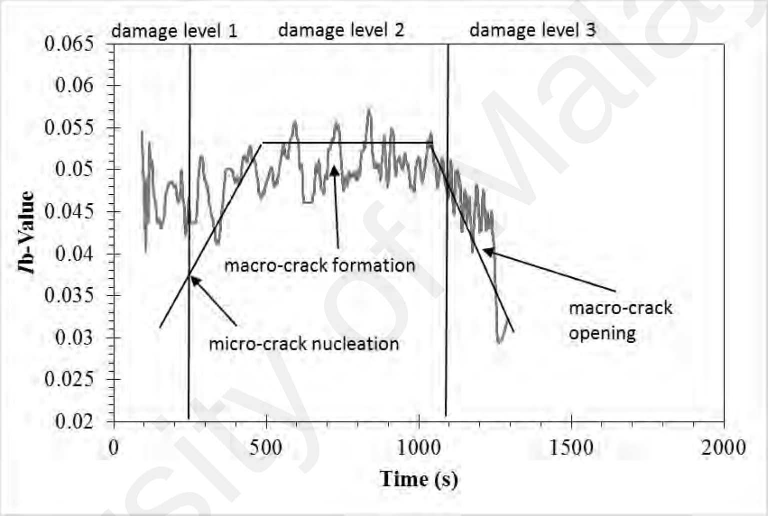

(b) After filtering

Figure 5. 12: *I*b-value of S0 beam specimen

Figure 5.12 (b) and 5.13 shows filtered *I*b-value for the six beam specimens. The solid line is trend line to describe the trend of *I*b-value. It can be clearly observed that all the beam specimens show a similar trend, except for S51 beam specimen with 51% of corrosion level. For the S0 beam specimen, trend established is that there is an increase in *I*b-value during damage level 1 followed by a slight fluctuation of *I*b-value during damage level 2 and then lastly decreasing in *I*b-value during damage level 3. This means that the micro-cracks formation were dominant before the first cracks that occur during damage level 1 due to the steady rise of *I*b-value. Once the first cracks occur at damage level 2, the cracks began to localize as macro-cracks. At damage level 3, *I*b-value decreases due to macro cracks start to open. A decreasing trend of *I*b-value can be known as a serious damage alert.

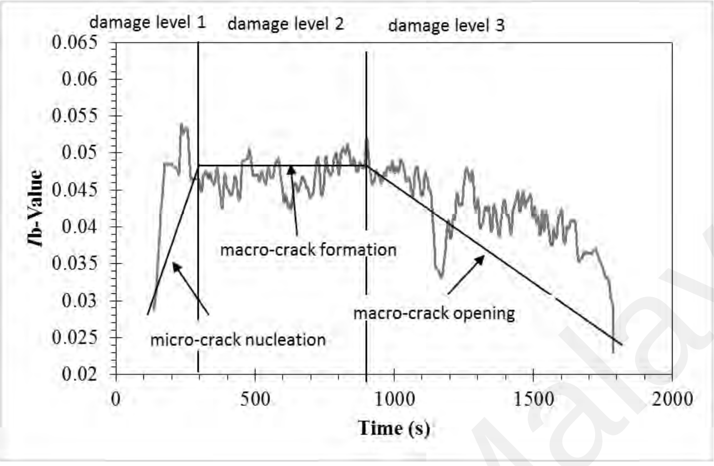

(a) S8

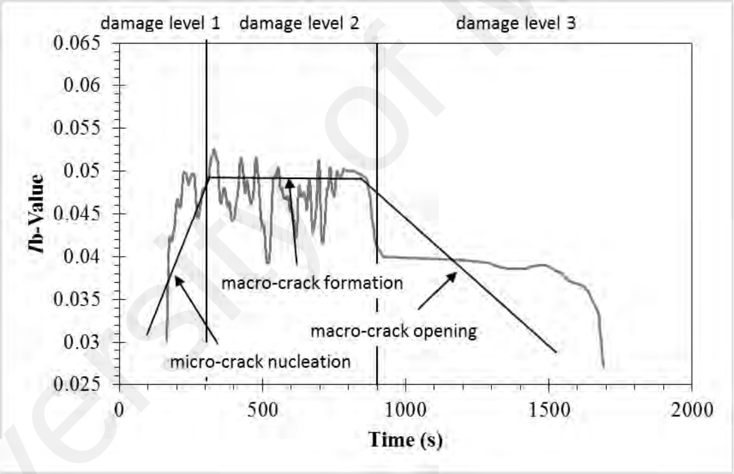

(b) S9

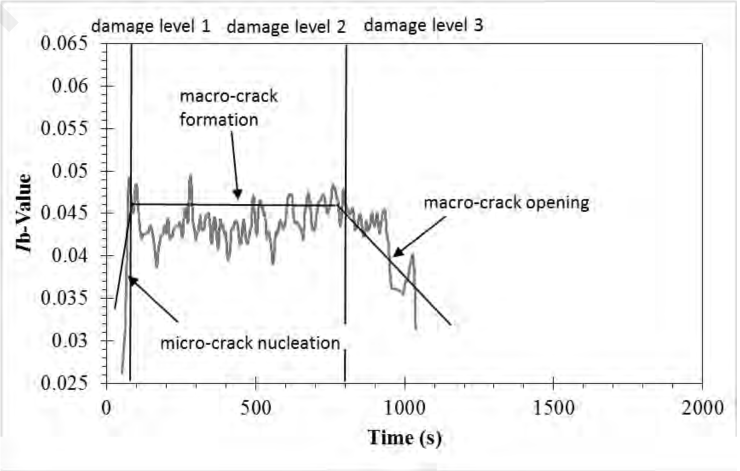

(c) S24

Figure 5. 13: Ib-value against time of the beam specimens

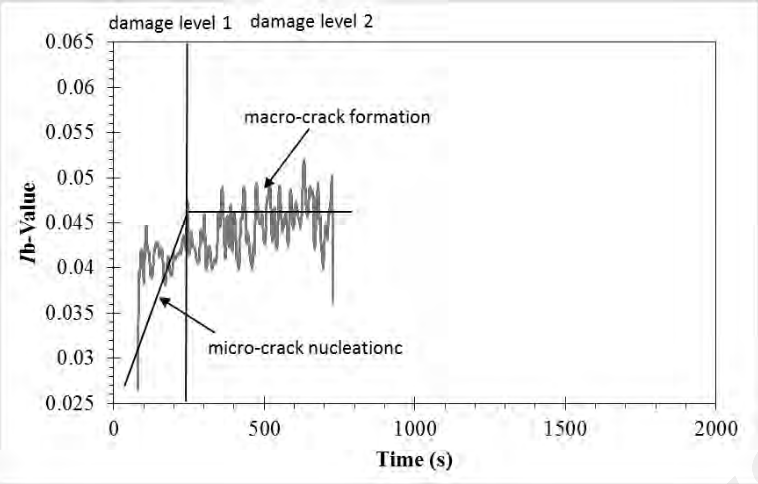

(d) S28

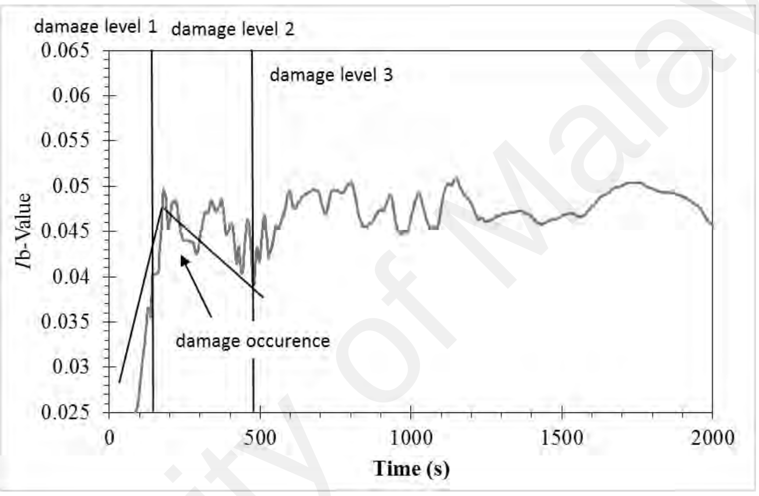

(e) S51

Figure 5.13: Continued

Different from all other specimens, S51 beam specimen with the highest corrosion level shows a significant drop in *I*b-value at the early of damage level 2. The drop of *I*b-value provides an indication of damage occurrence. The cross section reduction due to corrosion affects the crack opening of the beam specimen at tension reinforcement area. When the first visible crack occurred, at the early of damage level 2, the *I*b-value decreases until at early of damage level 3 and then remain its fluctuation until the failure of the beam specimen. This signifies that after the first visible crack, macro-crack propagated until failure. The *I*b-value of each sensor of the beam specimens is shown in Appendix A.

5.4 Secondary AE Results

Table 5.6 presents a summary of the secondary AE parameters of the beam specimens along the three different cycles (i.e. cycle 1, 2, and 3) of loading. The loading rate of secondary AE is 0.1 mm/min. The secondary AE parameters are duration, amplitude, average frequency, hits and counts.

Table 5. 6: Secondary AE parameters of experiment 2

Beam specimens	Cycle	Duration (x1000 µs)	Amp (dB)	Ave Freq (kHz)	Hits	% of Total Hits	Counts
S0	1	23.572	29.58	14.08	8992	52.87	2986932
	2	24.848	23.23	7.26	5148	30.27	986366
	3	24.023	22.61	6.77	2868	16.86	532277
S8	1	5.843	39.11	26.10	2392	90.16	273595
	2	5.461	40.03	19.90	172	6.48	20095
	3	8.318	34.02	18.90	89	3.35	13647
S9	1	24.033	34.28	19.25	14667	61.59	8640423
	2	16.408	23.27	5.55	5595	23.50	531306
	3	14.821	23.70	5.91	3551	14.91	311610
S24	1	7.196	35.22	14.80	10528	93.92	1068947
	2	5.610	27.22	7.17	192	1.71	6610
	3	6.770	27.59	8.20	490	4.37	25582
S28	1	38.696	29.49	22.50	4837	35.94	6012840
	2	33.668	23.54	11.23	4182	31.07	1879292
	3	30.228	22.71	9.09	4440	32.99	1440196
S51	1	9.644	45.37	19.92	143	76.88	27824
	2	12.926	34.45	14.30	33	17.74	8128
	3	30.330	39.00	18.30	10	5.38	6825

5.4.1 Cumulative Signal Strength (CSS)

Figure 5.14 shows the curve of CSS with time for all the six beam specimens. In general, the CSS rate decreases from cycle 1 to cycle 3. It means that the AE activities decrease due to the limitation of AE activities during uncracked beam as the beam specimen was subjected up to 4 kN load, at which it is 50% of the theoretical first visible cracking load. However, for S24 beam specimen, it has CSS rate that decreases from cycle 1 to cycle 2 but then increases from cycle 2 to cycle 3. Therefore, to evaluate the damage of beam specimens, the CSS ratio is proposed.

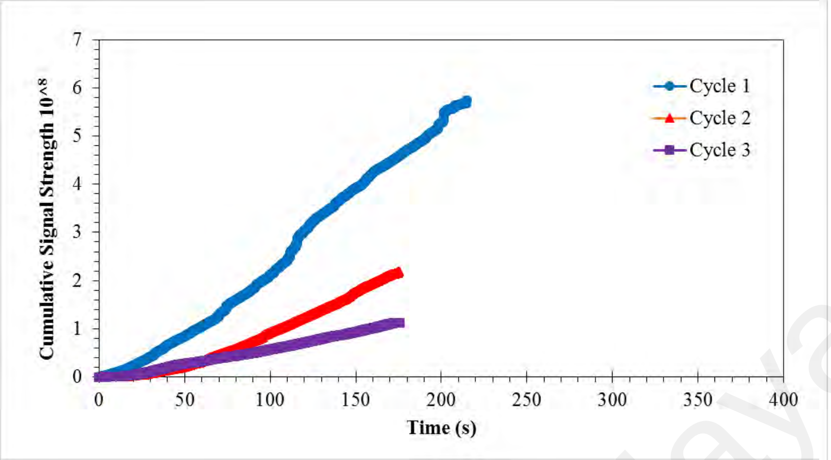

(a) S0

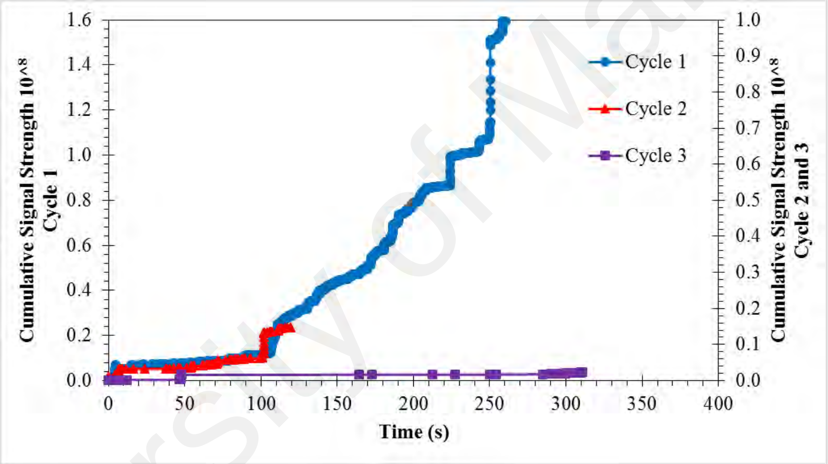

(b) S8

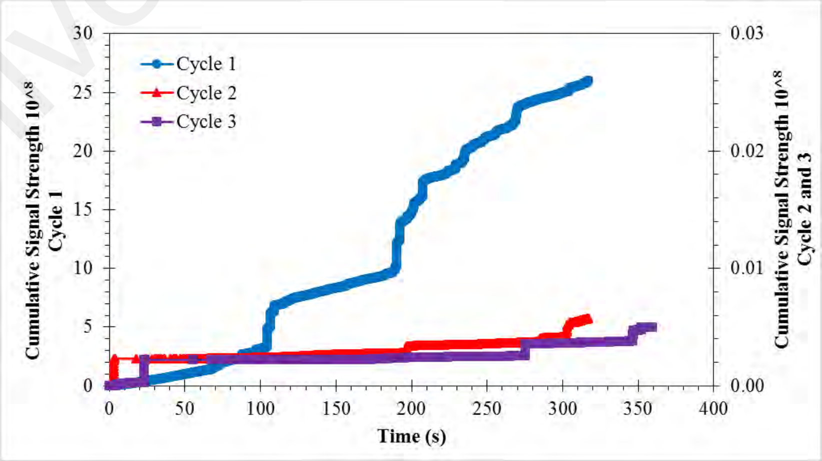

(c) S9

Figure 5. 14: Cumulative signal strength (pVs) against time of the beam specimens

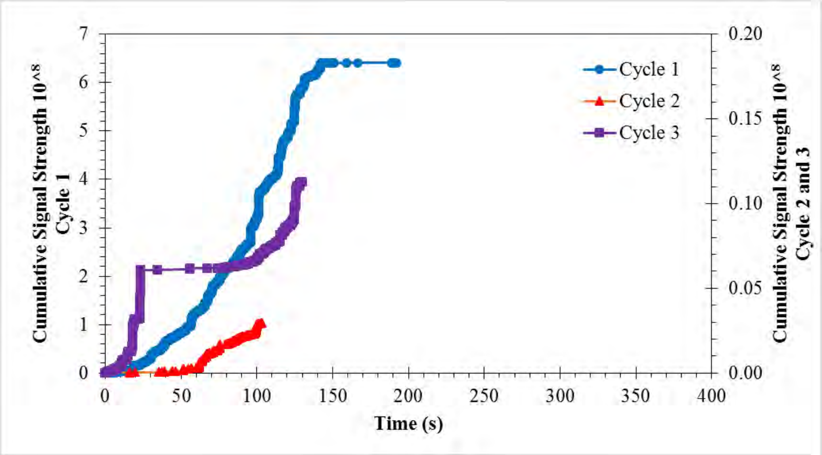

(d) S24

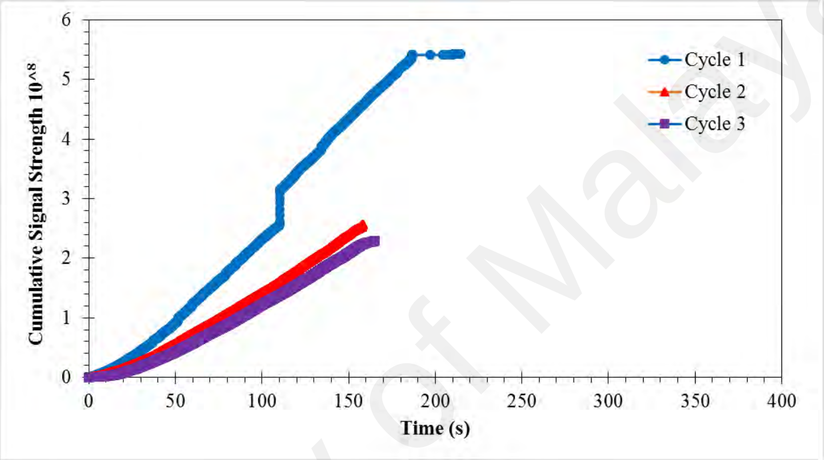

(e) S28

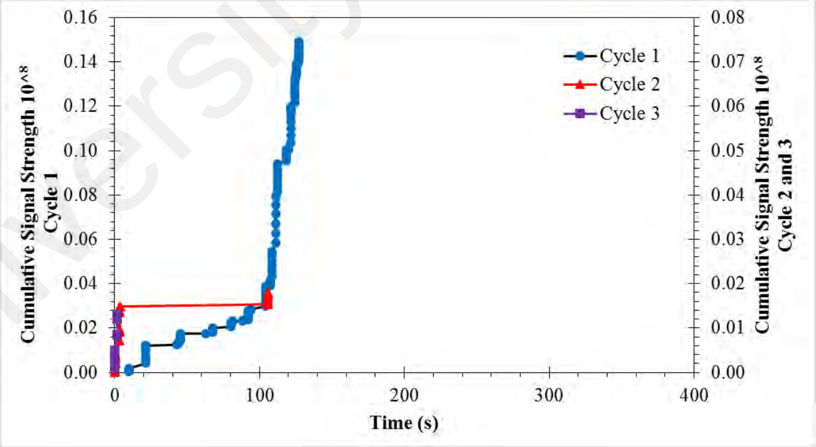

(f) S51

Figure 5.14: Continued

A study done by Ridge and Ziehl (2006) proposed an evaluation criterion based on the cumulative signal strength (CSS) ratio of RC beams that were strengthened with carbon fibre reinforced polymer (CFRP). It is defined as the peak CSS at the end of the reload hold period divided by the peak CSS at the end of the initial load hold period. The study suggested that a peak CSS ratio between 30% and 50% was an appropriate value to select as an indication of significant damage. Table 5.7 shows the CSS ratio for all the six beam specimens. The suggested ratio of CSS ratio based on the study done by Ridge and Ziehl (2006) is not suitable in this case. This is due to the CSS ratios obtained for all specimens that are not absolutely within the range 30-50% for significant damage due to corrosion. It can be contributed to the sensitivity of individual sensors, attachment methods of sensors, concrete material, and steel corroded of pre-corrosion beam specimens of this study that are different from the study by Ridge and Ziehl (2006).

Table 5. 7: CSS ratio

Beam Specimens	Cycle	CSS	CSS Ratio 1 (%)	CSS Ratio 2 (%)
S0	Cycle 1	5.75E+08	38.09	51.60
	Cycle 2	2.19E+08		
	Cycle 3	1.13E+08		
S8	Cycle 1	1.59E+08	9.18	16.51
	Cycle 2	1.46E+07		
	Cycle 3	2.41E+06		
S9	Cycle 1	2.60E+09	0.02	87.43
	Cycle 2	5.73E+05		
	Cycle 3	5.01E+05		
S24	Cycle 1	6.41E+08	0.46	384.35
	Cycle 2	2.94E+06		
	Cycle 3	1.13E+07		
S28	Cycle 1	5.43E+08	47.33	89.49
	Cycle 2	2.57E+08		
	Cycle 3	2.30E+08		
S51	Cycle 1	1.49E+07	12.15	71.82
	Cycle 2	1.81E+06		
	Cycle 3	1.30E+06		

However, from the results obtained, by comparing with the S0 beam specimen, it can be deduced that S28 and S51 beam specimens with higher corrosion levels experienced very significant damage. This is due to both of them having much higher CSS ratio compared to the S0 beam specimen, especially for the CSS ratio obtained using cycle 2 and 3 values, which are more than 70%. This is supported with the findings from the mechanical loading test where these two specimens failed at the lowest peak load for S28 and S51 beam specimens. On the other hand, the result for S9 and S24 beam specimens, their first CSS ratios were the lowest with less than 1% but their second CSS ratio was very significant with the percentage of more than 87%. Actually, the high value of CSS ratio is related to the damage growth of the beam specimens (Reidg and Ziehl, 2006). The lowest CSS ratio might imply the steel corroded beam has no effect on the damage growth of the beam specimens at the first CSS ratio.

5.4.2 *I*b-value

Figure 5.15 shows the *I*b-value for the three selected beam specimens, i.e. S0, S9 and S28 beam specimens. These three beam specimens are selected due to significant trend of *I*b-value that can be established as the corrosion levels increase. It can be clearly seen that the beam specimens experienced steel corrosion have a trend different from S0 beam specimen. For the S0 specimen, the trend established that the *I*b-value that tends to increase from the cycle 1 to cycle 3 of loading, as shown in Figure 5.15 (a). However, for S9 and S28 beam specimens, the *I*b-value tends to decrease from cycle 1 to cycle 3 of loading in terms of increasing in corrosion level. This signifies the occurrence of damage from cycle 1 to cycle 3 of loading. It indicates that the occurrence of damage generated due to loss in cross section of the beam specimens. The cross section of S28 beam specimen is lower than S9 beam specimen.

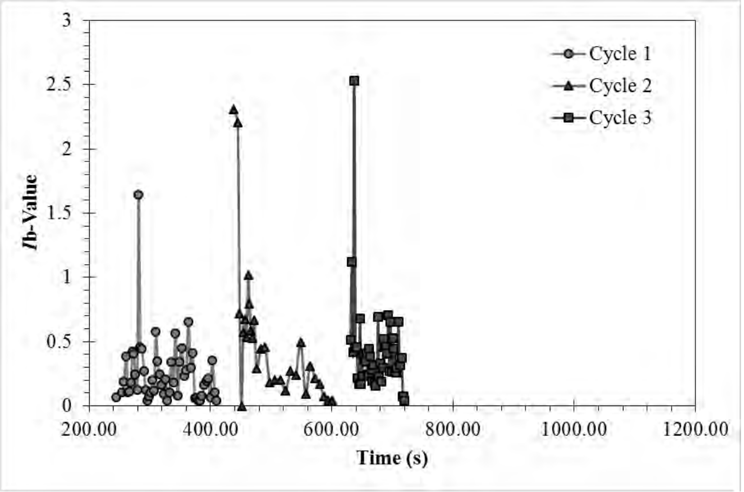

(a) S0

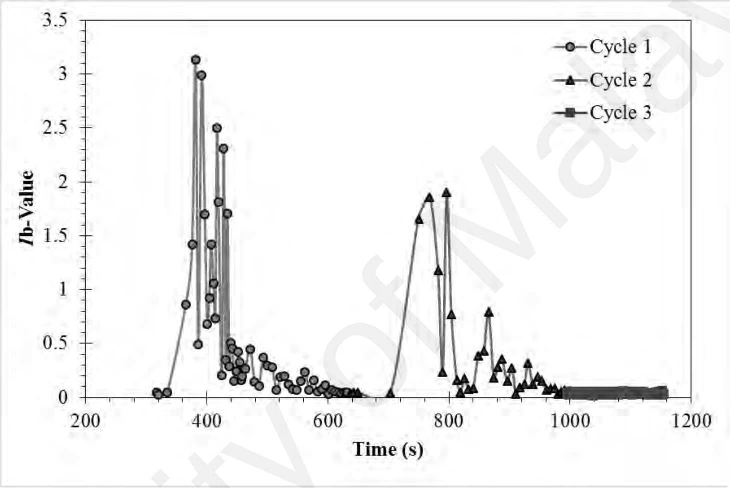

(b) S9

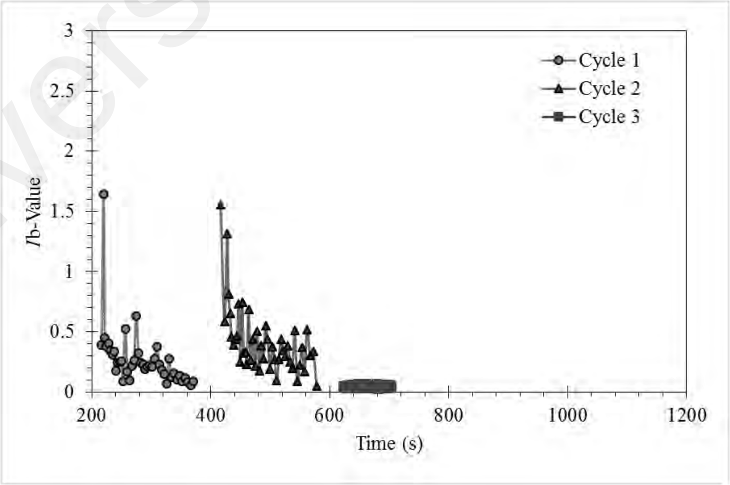

(c) S28

Figure 5. 15: Ib-value against time graph of the beam specimens

5.5 Summary of experiment 2

This experiment deliberates the mechanical behaviour of the RC beam specimens with pre-corroded steel reinforcement, together with the AE monitoring results for primary and secondary AE signals analysis. The results obtained in this experiment showed the great potential of the AE technique to be used in the corrosion evaluation of the beam specimens. The AE parameters used in this experiment provide some useful information and trend that could be illustrated on the corrosion level experienced by the corrosion beam specimens, as discussed in this experiment. However, these findings are not applicable to a real corroded structure that are subjected to water and chloride attack. In addition, there is only one factor contributing to the loss of concrete strength, which is the decrement in the cross section of the steel reinforcement of the pre-corrosion beam specimens. Thereafter, based on the limitation gained in the second experiment, the third experiment was utilized for post-corrosion beam specimens.

CHAPTER 6: RESULTS AND DISCUSSIONS FOR EXPERIMENT 3 RELIABILITY OF PRIMARY AND SECONDARY AE FOR CORROSION EVALUATION OF POST-CORROSION CONCRETE STRUCTURES

6.1 Introduction

The compressive strength after 28th day concrete casting and modulus of elasticity tests for concrete cubes and cylinders of Experiment 3 are same with the experiment 2, due to the same batch of concrete casting. The average compressive strength and average modulus of elasticity of concrete are 37.30 MPa and 26.49 GPa, respectively. After the flexure tests, the beam specimens were hacked to retrieve the steel reinforcements. The steel reinforcements were then cleaned to remove rust in accordance to ASTM G1 (2003) and weighed to determine the actual mass loss of steel reinforcement in accordance to Equation 2.13. The corrosion levels or mass loss of concrete beams were 9.54%, 19.84%, 24.60%, 31.91% and 39.84%. The cleaned reinforcements with various levels of corrosion are shown in Figure 6.1. There were six steel reinforcements of the beam specimens range from 0% to 40% used in this experiment. The corrosion levels of beam specimens were 0% for S0, 9.54% for S10, 19.84% for S20, 24.60% for S25, 31.91% for S32 and 39.84% for S40 as shown in Table 6.1.

Table 6. 1: Quantitative results of accelerated corrosion process

Beam specimens	Initial mass, M_i (g)	Final mass, M_f (g)	Mass loss, Δm (g)	Corrosion level (%)
S0	514	514	0	0.00
S10	524	474	50	9.54
S20	512	420	92	19.84
S25	524	386	138	24.60
S32	514	350	164	31.91
S40	502	302	200	39.84

(a) S0

(b) S10

(c) S20

(d) S25

(e) S32

(f) S40

Figure 6. 1: Condition of steel reinforcements

6.2 Mechanical Behaviour

Figure 6.2 shows the load against mid-span deflection curves of the beam specimens. The corroded specimens have a lower stiffness than the non-corroded specimen, that is, S0 beam specimen. The ultimate load of the S0 beam specimen was approximately 40.2 kN, and the ultimate deflection was 3.14 mm. Although the other beam specimens were damaged by corrosion, the ultimate load and deflection of the corroded specimens were lower than the S0 beam specimen. The all of beam specimens failed in brittle failure which signifies that the section is most probably balanced-reinforced. The specimen reached its ultimate strength and crushed at the same time when yield of the steel reinforcements. According to the visual observation, the specimens suddenly failed when the concrete failed in compression. This type of failure is not preferable as there is no warning before the failure.

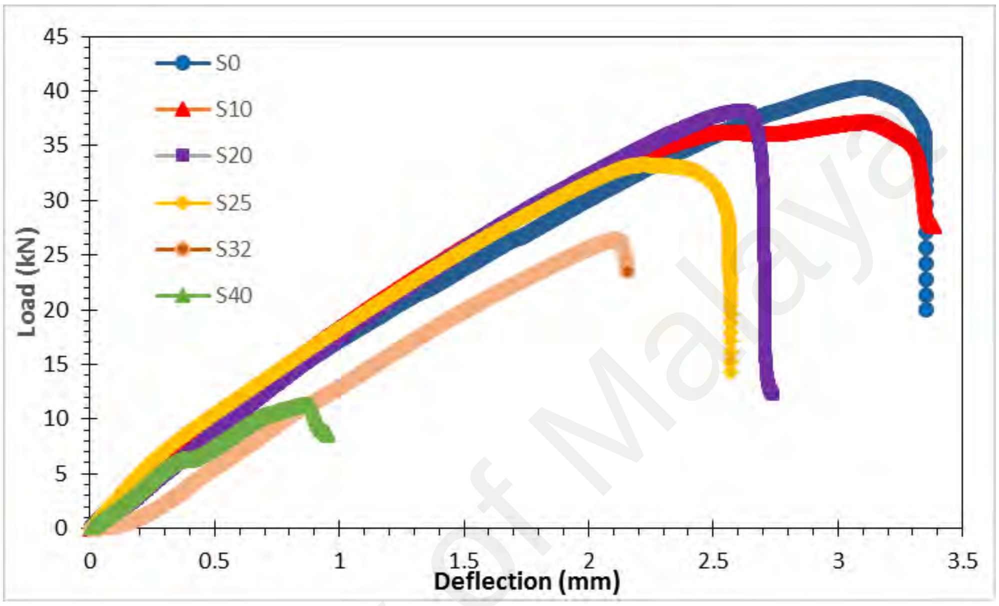

Figure 6. 2: Load versus mid-span deflection of the beam specimens

By plotting mass loss or corrosion level against loss of ultimate strength, the increase in corrosion level of steel reinforcements was found to be linearly consistent with the decrease in the ultimate strength of the corroded beam specimens. The regression value (R^2 of the linear graph) is 0.8271, which is highly acceptable because it is near to one. For example, 10% and 40% of mass loss corresponded to 94.55 % and 35.14 % of ultimate strength, respectively. This experimental result confirmed that the loss of ultimate strength of the specimens was linked to the mass loss due to corrosion, as shown in Figure 6.3.

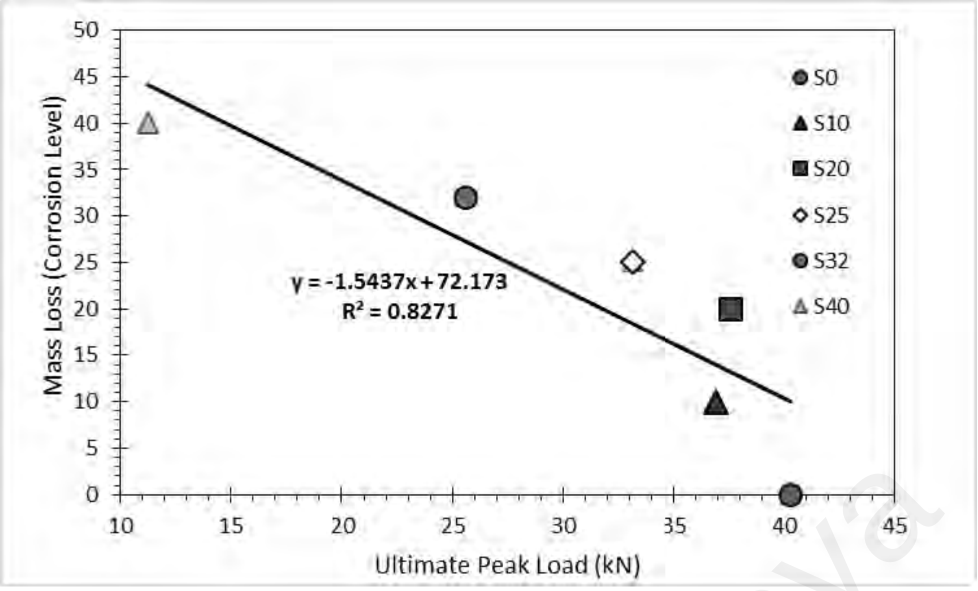

Figure 6. 3: Loss of ultimate strength against mass loss of the beam specimens

Figure 6.4 shows the fracture condition of the specimens at the end of loading tests. From the observations, a half of the specimens, except S20, S25, and S40, failed in shear failure. This finding indicates the fracture of the corroded specimens through the formation of expansive corrosion product or rust of the steel reinforcements. This fracture resulted in a decrease in bond strength between the steel reinforcement and the concrete, thereby affecting the stress distribution dominant on the middle part of the specimen developed from the bottom to the upper surface when the loading was applied. In general, the first visible crack of the specimens was observed on the concrete side face between 7 and 11 kN. As the load increased, additional cracks were found developing upwards from the bottom surface of the beam specimen. Shear cracks were also found starting from above the supports, propagating in a diagonal way towards the location where the load was applied, at between 10.3 and 37 kN.

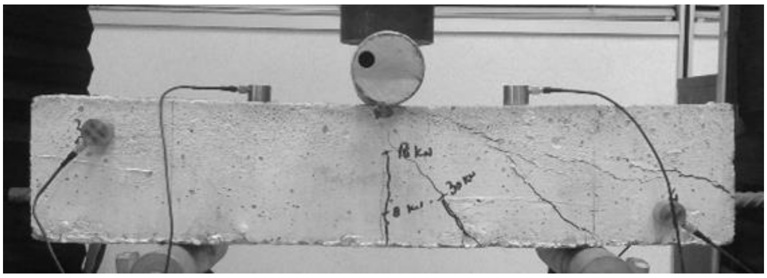

(a) S0

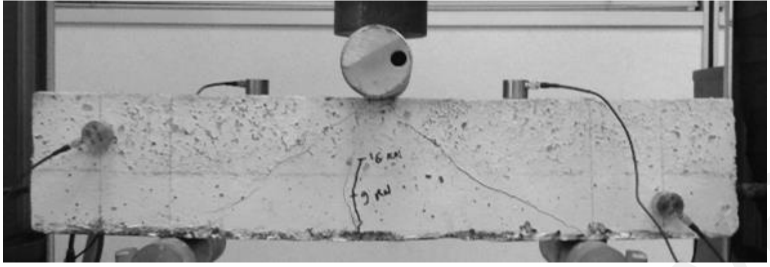

(b) S10

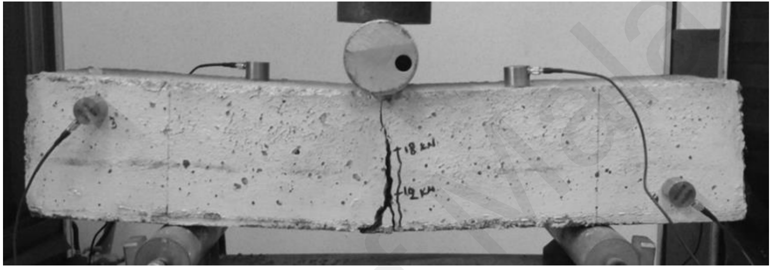

(c) S20

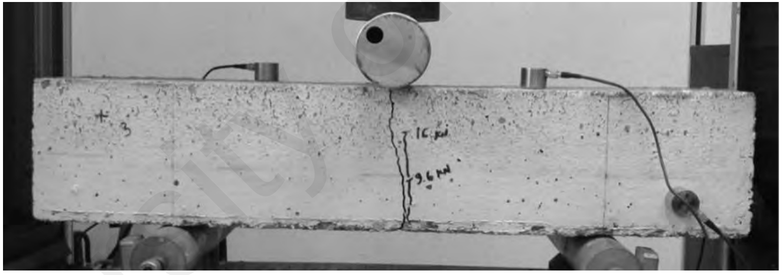

(d) S25

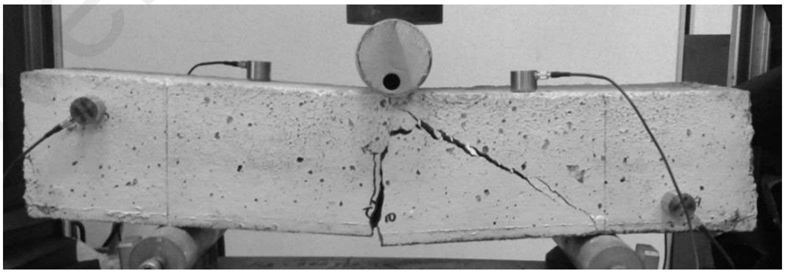

(e) S32

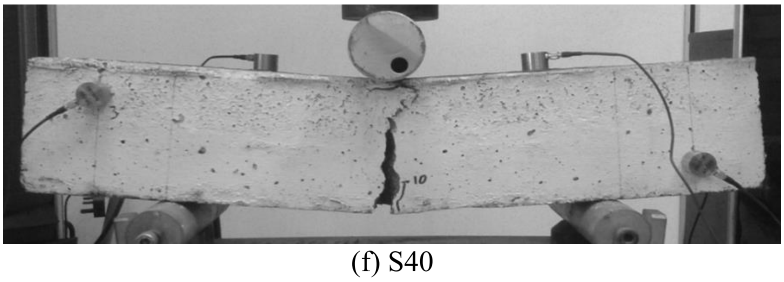

(f) S40

Figure 6. 4: Concrete beam specimens after failure

Based on the load and deflection curves as well as the observations, the development of the beam damage was classified into the following three general levels: damage level 1 (micro-cracking), damage level 2 (first visible crack and crack distribution), and damage level 3 (yielding and or damage classification). Figure 6.5 shows the crack progression of S32 beam specimen.

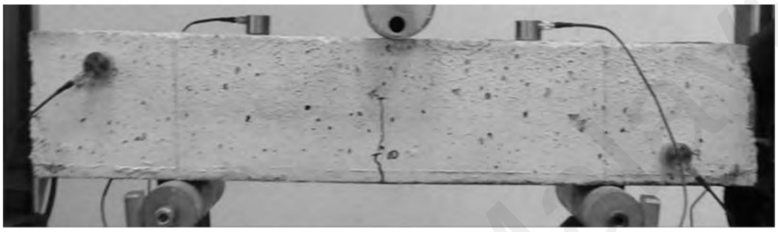

(a) First visible crack

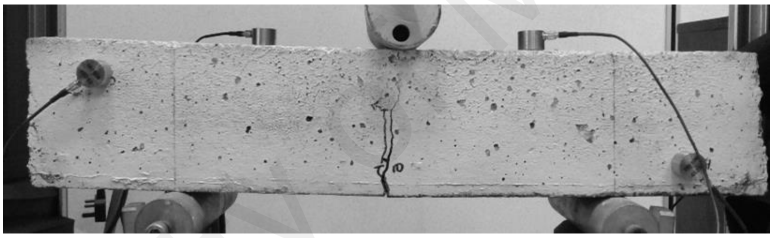

(b) Crack propagation

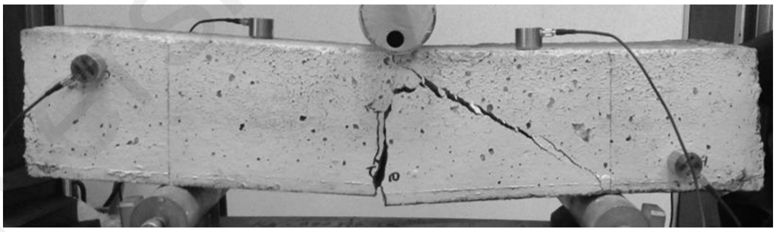

(c) Damage localization

Figure 6. 5: The crack progression of the S32 beam specimen of experiment 3

6.3 Mechanical Performance of Steel Reinforcements

A few tensile tests were performed to assess the influence of corrosion on the mechanical properties of steel reinforcements. Non-corroded steel reinforcement was extracted from S0 beam specimen. A total of five pieces of corroded steel reinforcements were extracted from S10, S20, S25, S32, and S40 of beam specimens and were subjected to the tensile test. Load and time curves of the tensile test are shown in Figure 6.6. Based on the curve, the corroded steel reinforcements reached their yield strength at a low load. The yield point of the steel reinforcement is the point when non-linear (elastic and plastic) deformation begins. The corroded steel reinforcements directly shifted from elastic to the hardening stage (Yu et al., 2015). The corroded steel reinforcements showed more brittle properties than the non-corroded steel reinforcement.

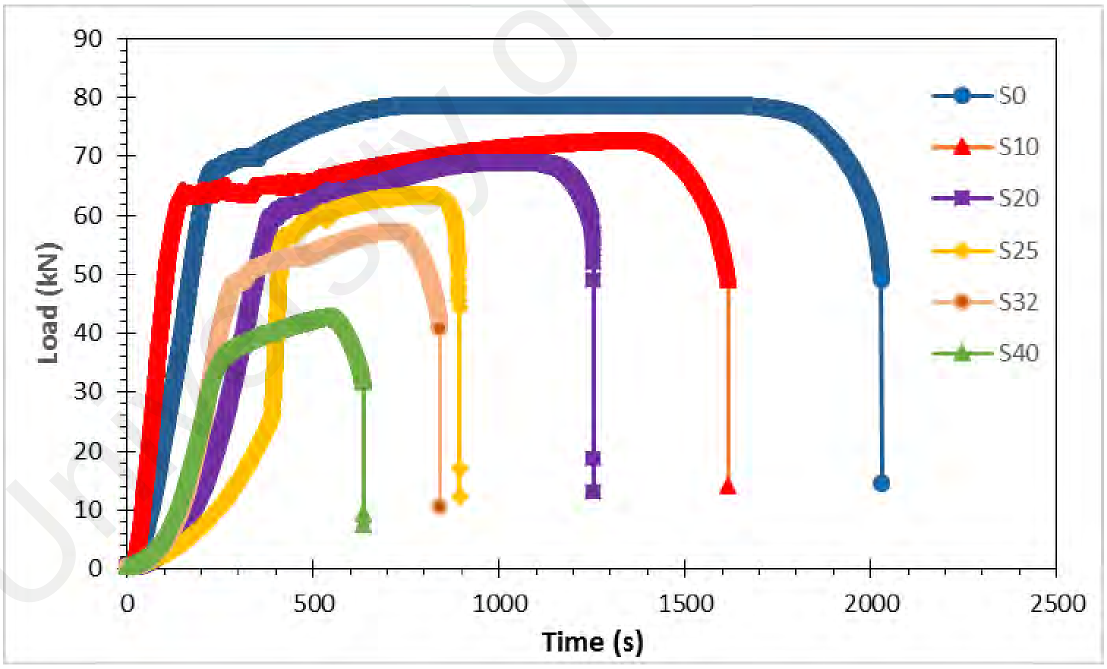

Figure 6. 6: Load vs. time curve of tensile test of steel reinforcements

The mechanical behavior of the steel reinforcements had obviously been affected by the corrosion, including the yield and ultimate capacities, which indicates that residual stress of corroded steel reinforcements decreases with the loss of cross-section. The yield and ultimate capacities decrease in terms of increase in the corrosion level of steel reinforcements. The ultimate and yield strengths of non-corroded steel reinforcement were considered to be 77.09 kN and 796.52 MPa, respectively.

The loss of ultimate strength and yield capacity of the highest corroded steel reinforcements were considered to be 45.59% and 45.61%, respectively. This experimental result confirmed that the loss of ultimate strength and yield capacity of the steel reinforcements was linked to the corrosion level. The mechanical behavior details of the steel reinforcements as shown in Table 6.2.

Table 6. 2: Mechanical behavior of the steel reinforcements

Steel Reinforcements	Ultimate Strength (kN)	Loss of ultimate strength (%)	Yield Strength (Mpa)	Loss of yield strength (%)
S0	77.09	0.00	796.52	0.00
S10	71.31	7.51	743.94	6.60
S20	67.80	12.06	707.96	11.12
S25	62.29	19.20	673.92	15.39
S32	56.30	26.97	584.90	26.57
S40	41.95	45.59	433.21	45.61

6.4 Primary AE data

Table 6.3 presents a summary of the primary AE parameters of the beam specimens along the three different damage levels. In general, Table 6.4 demonstrates an increasing tendency for the average amplitude and AF as the damage level increases on each beam specimens, except for S40 beam specimen. The discussions of the AE parameters, such as accumulated AE hits, RA value, AF, counts, and *I*b-value, are provided in the following sections. Figures 6.7 to 6.13 are the AE parameters from the AE signals of the beam specimens.

Table 6. 3: Primary AE parameters of experiment 3

Beam Specimens	Damage Levels	Duration (x1000 μs)	Amplitude (dB)	Ave Frequency (kHz)	Hits	Total Hits (%)	Counts
S0	1	10645.41	36.62	25.36	63765	45.70	18288162
	2	7164.38	35.47	23.57	63138	45.25	12552707
	3	17944.79	38.59	26.75	12617	9.04	8481434
S10	1	13334.18	35.98	18.12	13110	8.86	3119164
	2	13384.88	38.14	23.16	37186	25.13	13193249
	3	9800.78	39.17	22.11	97672	66.01	26174912
S20	1	10315.42	29.71	10.52	6587	6.65	500054
	2	9952.02	38.14	23.77	59160	59.71	14565296
	3	6106.09	38.82	25.99	33330	33.64	5542896
S25	1	10433.87	25.98	6.73	867	0.92	38616
	2	9809.49	37.51	22.78	67430	71.26	15383446
	3	5171.42	38.67	26.28	26324	27.82	3390177
S32	1	12565.06	31.55	13.90	6993	12.69	767414
	2	11987.61	39.00	20.91	32030	58.12	7317488
	3	8091.86	39.63	23.27	16083	29.19	2554563
S40	1	51089.89	24.11	12.73	1565	25.12	1092900
	2	33557.12	34.86	19.94	2819	45.24	1397818
	3	21276.97	21.74	3.95	1847	29.64	167479

6.4.1 Accumulated AE Hits

Figure 6.7 shows the relationship between the accumulated AE hits and load level (%) of the beam specimens. The accumulated AE hits decrease as the corrosion level of the specimens increases. In general, as the load is applied, the AE hits appear to increase prior to the first visible cracks. After the formation of the first visible crack at the range of 10% to 30% of the load level, the rate of AE hits rapidly increases. Afterward, as the loading continues, the cracks propagate, and the AE hits gradually increase until beam specimen failure occurs. Based on the history of accumulated AE hits, the trend of the accumulated AE hits can provide useful information in evaluating the damage level of the corroded beam specimens. This trend may be attributed to the stressing and majority of cracking, especially longitudinal cracking along the steel reinforcement, which has already been dissipated by the steel corrosion.

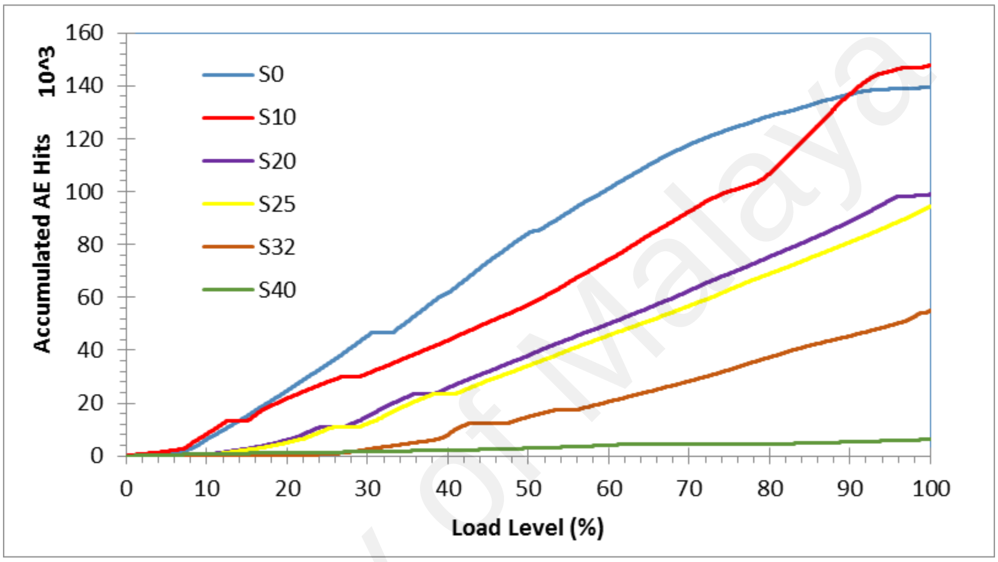

Figure 6. 7: Accumulated AE hits versus load level (%) of beam specimens

The correlation between accumulated AE hits and ultimate peak load or ultimate strength is shown in Figure 6.8. A decrease in ultimate strength was found to be linear with the decrease in accumulated AE hits of the specimens. The ultimate strength and accumulated AE hits were controlled by corrosion level of the beam specimens. The R^2 of the linear graph is 0.9223, which is acceptable because the value is almost 1 (one).

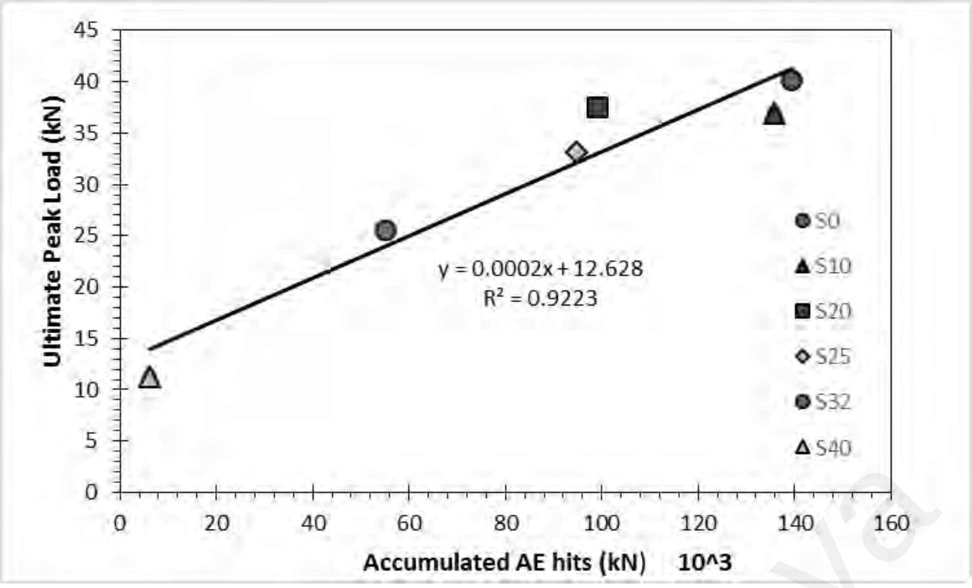

Figure 6. 8: Accumulated AE hits against ultimate peak load of beam specimens

6.4.2 Crack classification – RA value and AF

Figure 6.9 and 6.10 show RA value vs. AF distribution of the AE data at every 1 kN increment load. The RA value is defined as the ratio of the waveforms rise time to the amplitude, as shown in Equation 2.16. The AF feature is calculated from the number of threshold crossing of waveforms divided by duration, as shown in Equation 2.17. Based on the linear regression for each data group, it is suggested that as the corrosion level becomes higher, there is a collective increase in AF and decrease in RA value of the beam specimen. It also indicates the transition of the beam dominating fracture type, which shifts from shear crack to tensile crack. However, for highest corrosion level, there is a decrease and increase in RA value due to the shear crack progression of the beam specimen.

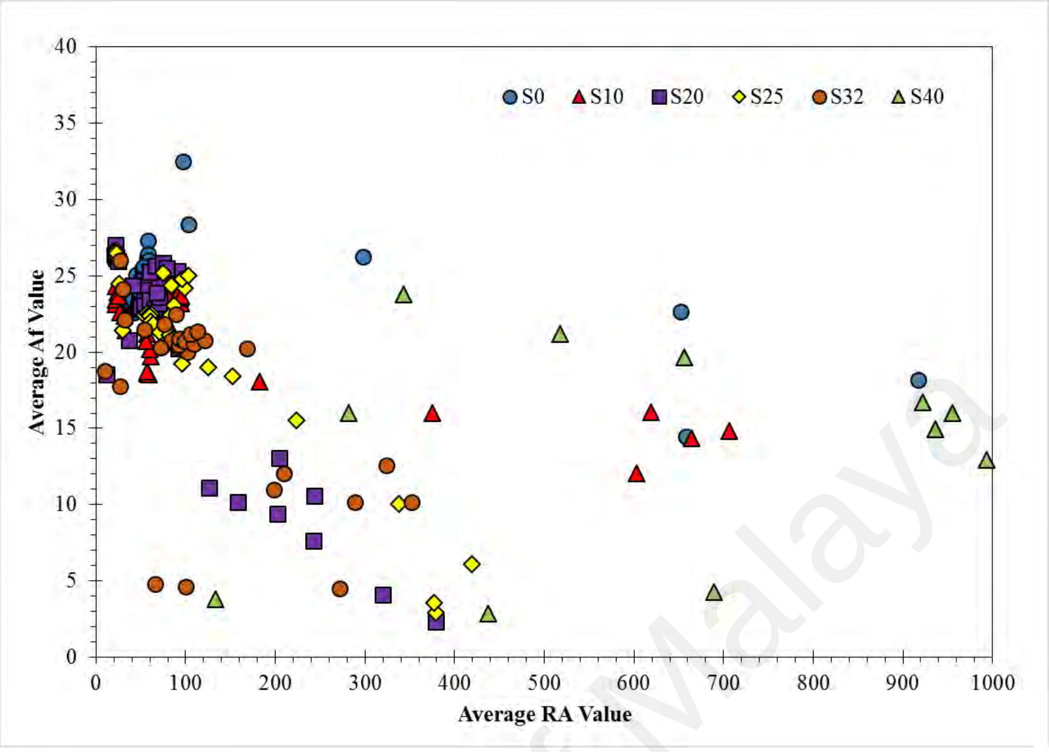

Figure 6. 9: RA value and AF of the concrete beam specimens

Figure 6.10 shows RA value vs. AF distribution of the AE data per damage level. Based on the linear regression of the RA value and AF data, it is suggested that as the increase of the damage level (from damage level 1 (D1), damage level 2 (D2) to damage level 3 (D3)), there is a significant increase in AF and decrease in RA value. In general, there are shifts from shear region to tensile region as the damage level increase.

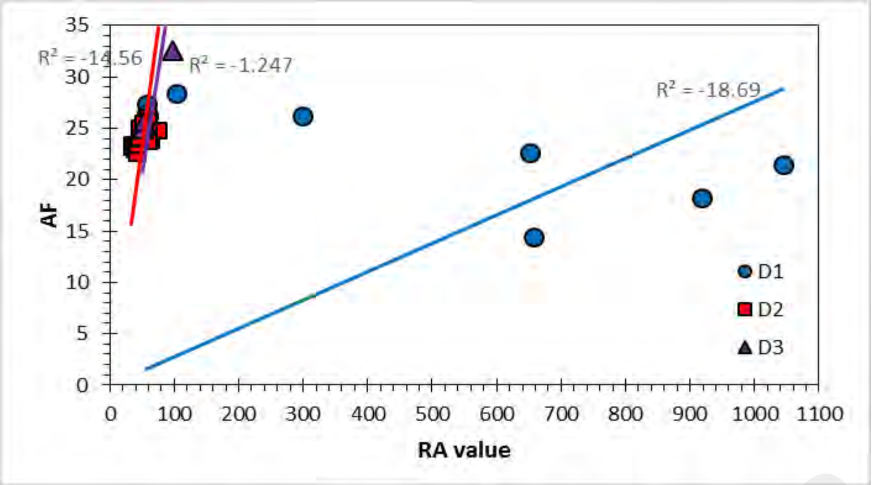

(a) S0

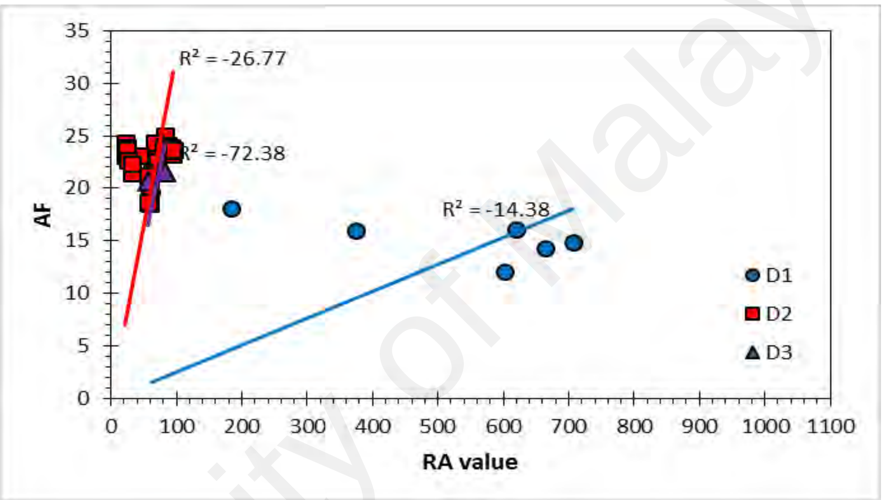

(b) S10

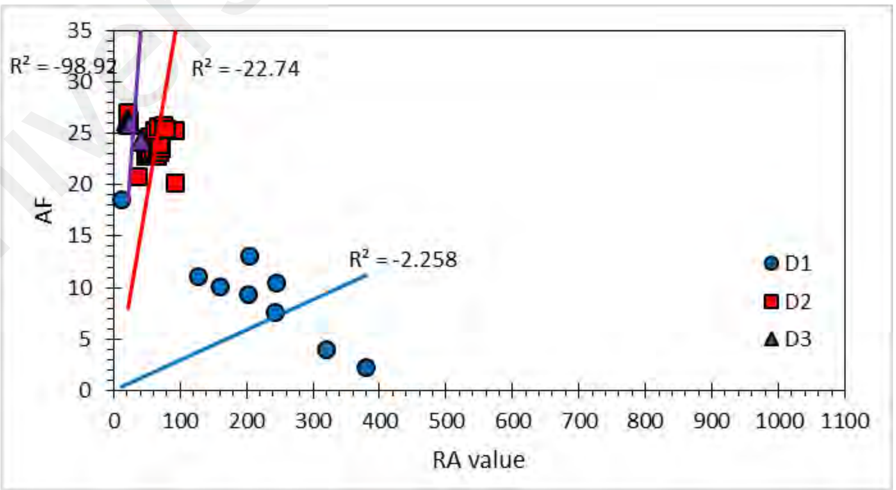

(c) S20

Figure 6. 10: RA vs. AF of the concrete beam specimens per damage level

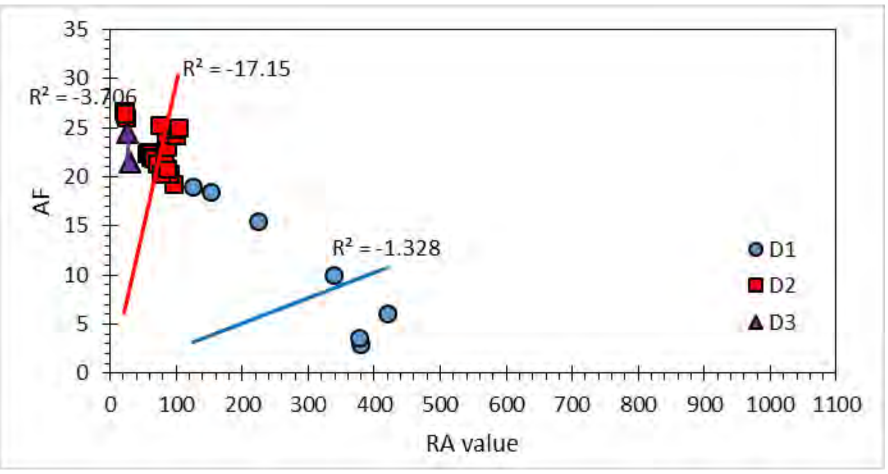

(d) S25

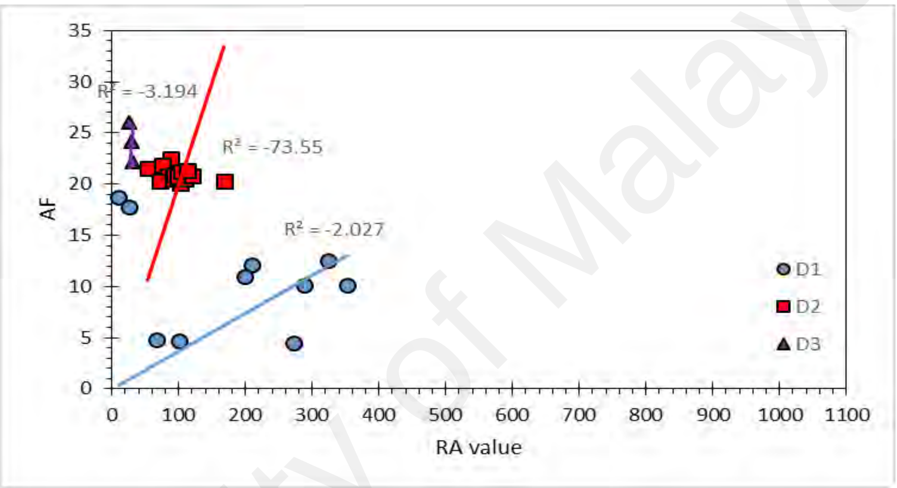

(e) S32

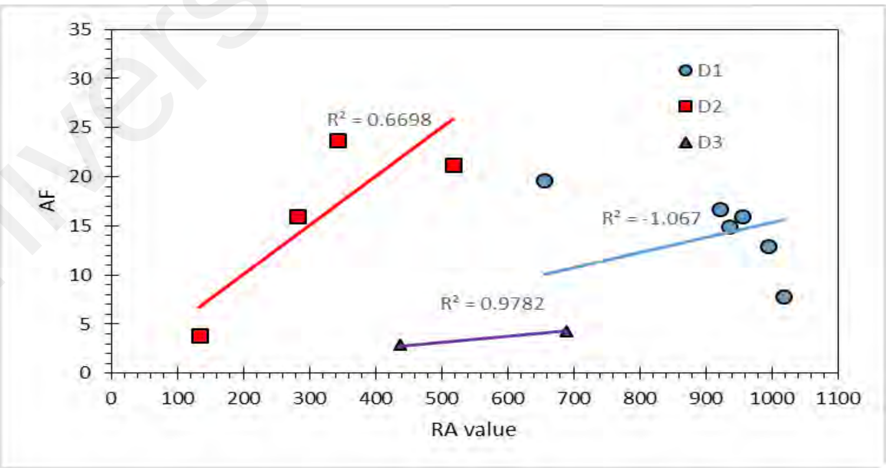

(f) S40

Figure 6. 10: Continued

Figure 6.11 provides the plots of RA value and AF versus time, which were computed from the monitored AE data in the current study, by averaging the respective values at every 1 kN load increment. The development of the beam damage was classified into general levels. The solid line was plotted as the boundary of each damage level. At damage level 1, the high in RA value and low in AF value indicate the occurrence of high density damage events within the concrete at the tension reinforcement area. As previously mentioned, the high RA value and low AF correspond to the shearing mode of cracks. After the load reached the first visible cracks, the explosive decreased RA value and the AF increased before gradually rising again in subsequent levels.

At damage level 2, the crack mode switched to tensile cracks after the first visible crack. The RA value was restored at the load level until the RA value suddenly experienced an explosive which might indicate a strong tensile crack opening of the beam specimens in the damage level 2. Furthermore, the other AE parameters, such as count and ib-value, are necessary to analyze and evaluate the decrease in RA value. The load level of the RA value drop of non-corroded beam specimen (S0) occurred in the middle part of damage level 2. However, as the corrosion level of the specimens increased, the drop of RA value occurred toward the end of the damage level 2. This condition occurred due to the delayed tensile cracks opening by the steel corrosion of the specimens. In addition, the number of RA value drop increased due to the increase in corrosion level of the beam specimens, as shown in Table 6.4.

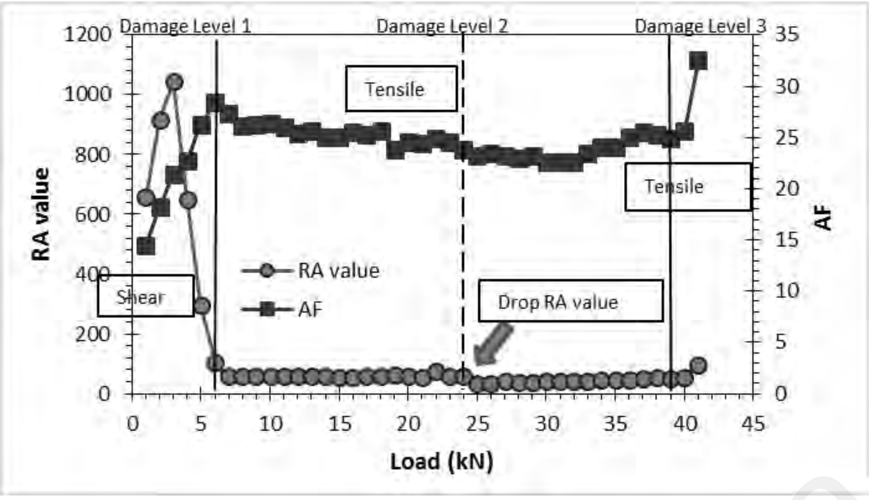

(a) S0

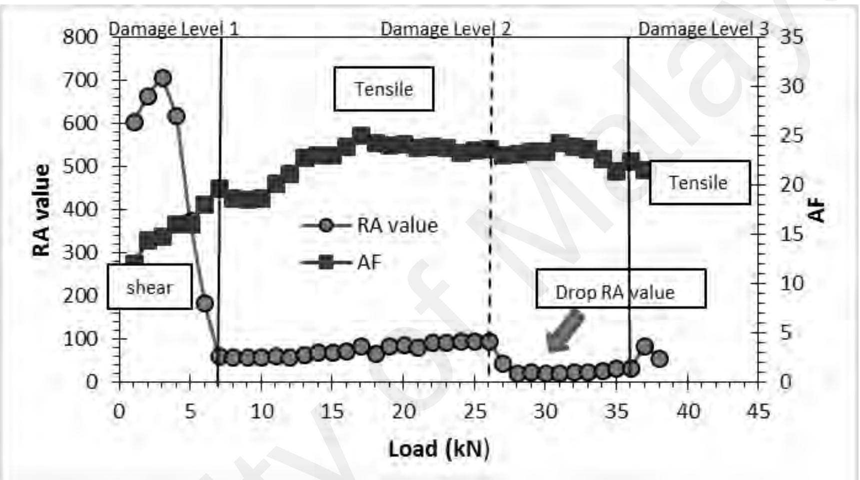

(b) S10

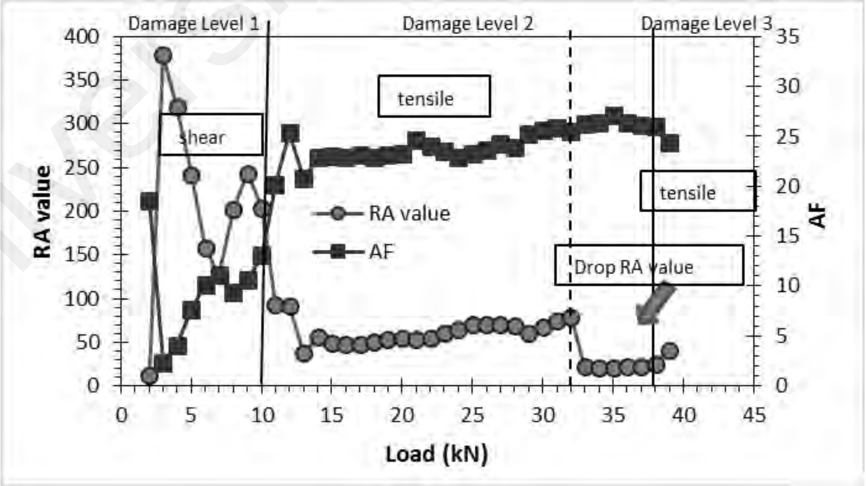

(c) S20

Figure 6. 11: RA-AF distributions of the concrete beam specimens vs. load at three different damage stages

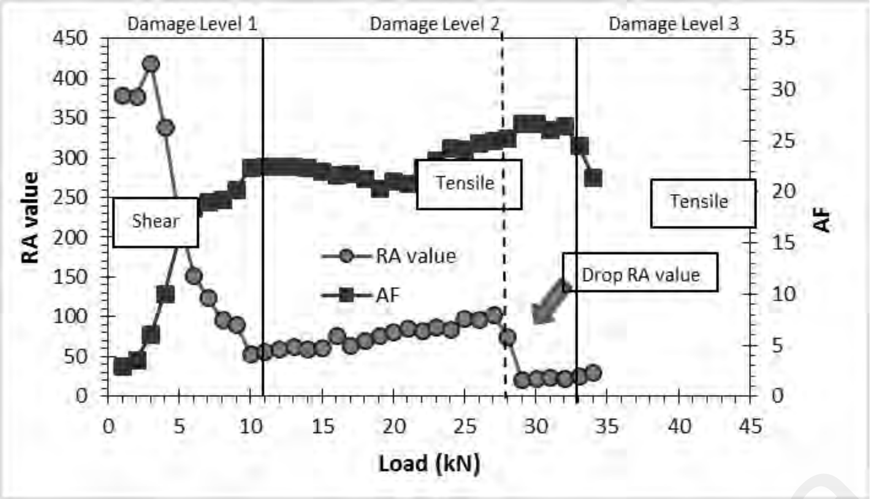

(d) S25

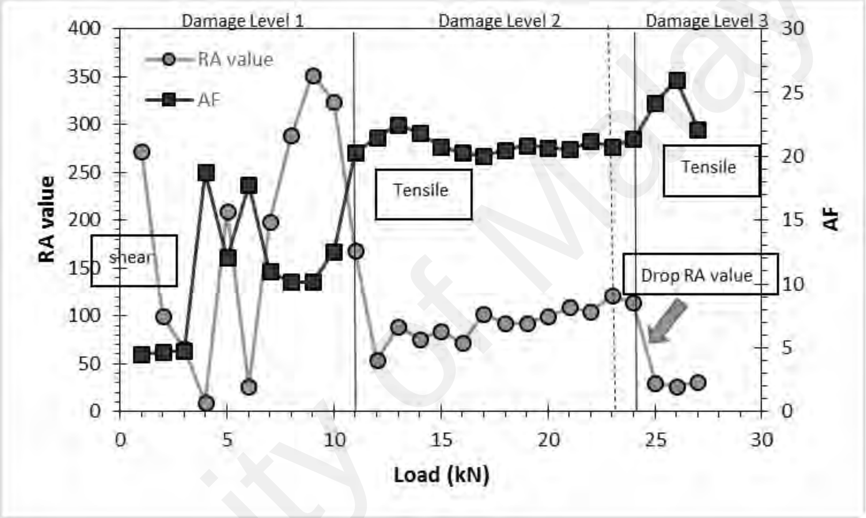

(e) S32

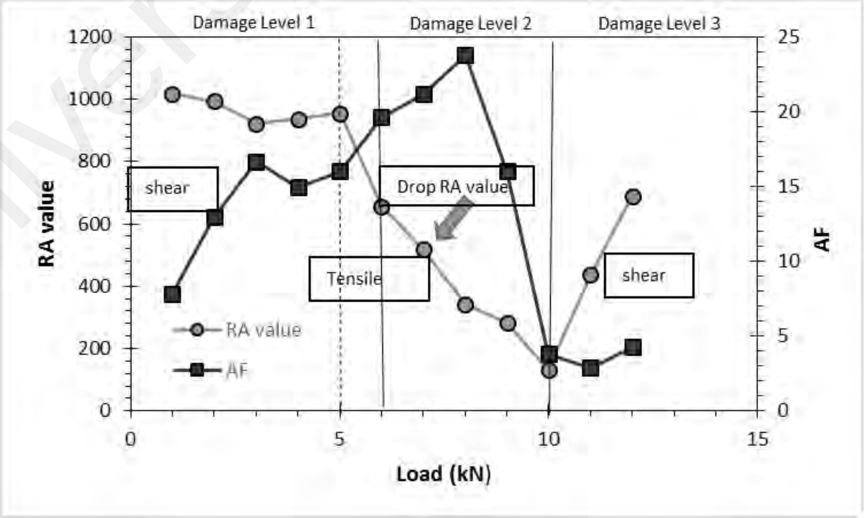

(f) S40

Figure 6. 11: Continued

Table 6. 4: Drop of RA value

Beam Specimens	Drop of RA Value
S0	25.33
S10	51.01
S20	57.09
S25	81.99
S32	91.20
S40	673.24

6.4.3 Amplitude versus Load

A typical amplitude vs. load curve according to three damage levels is shown in Figure 6.12. As mentioned in the previous section, there is boundary line of separate damage levels. The dashed line at damage level 2 is load level where the significant drop in RA value occurred. The rate of AE amplitude is progressively increasing at first load level (damage level 1), from about 20's kN to around 35 kN to 40 kN. This concerning mechanical behaviour, before first visible crack develops, the amplitude increases by several dB.

After first visible cracks, the amplitude did not show any significant change as can be seen at the damage level 2. The amplitude value is around 35 kN to 40 kN. Only in one specimen (S40), the significant decrease in amplitude after first visible cracks. In particulars at damage level 3, there is no significant change of amplitude after yielding and damage localization, except the non-corroded beam specimen (S0) and the lowest corrosion beam specimen (S10). However, for the highest corrosion level (S40), the amplitude is stored at a level around 22 dB after the significant increase in amplitude (from 39 dB to 22 dB).

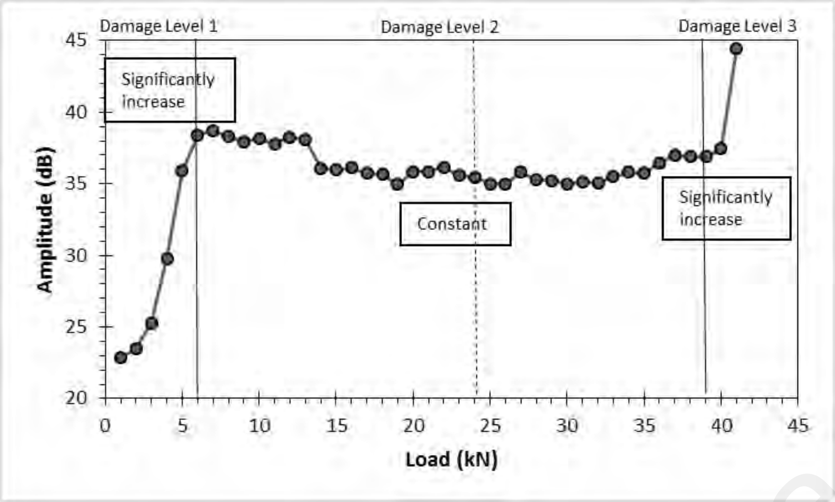

(a) S0

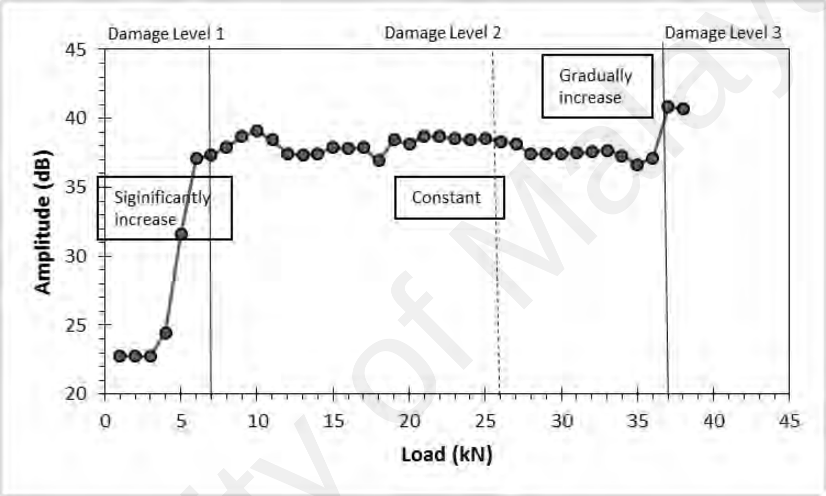

(b) S10

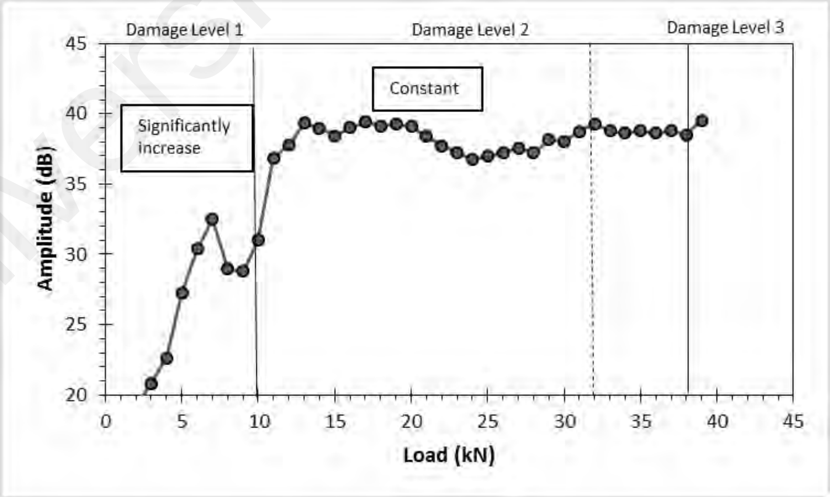

(c) S20

Figure 6. 12: Amplitude vs. load of the beam specimens

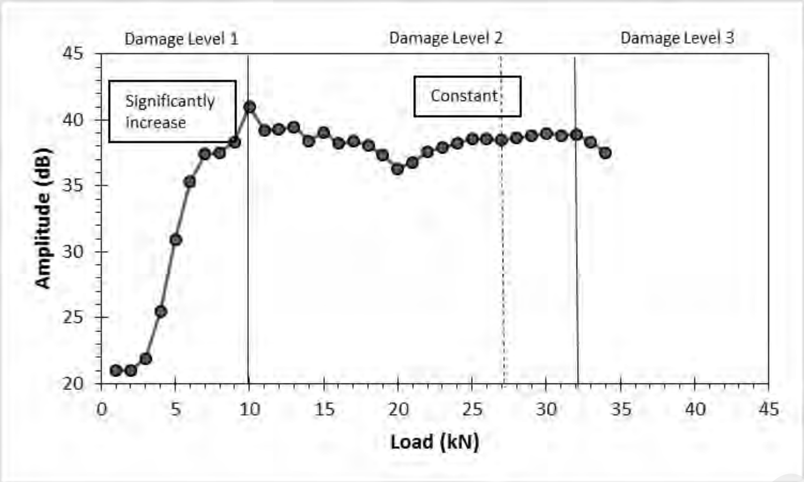

(d) S25

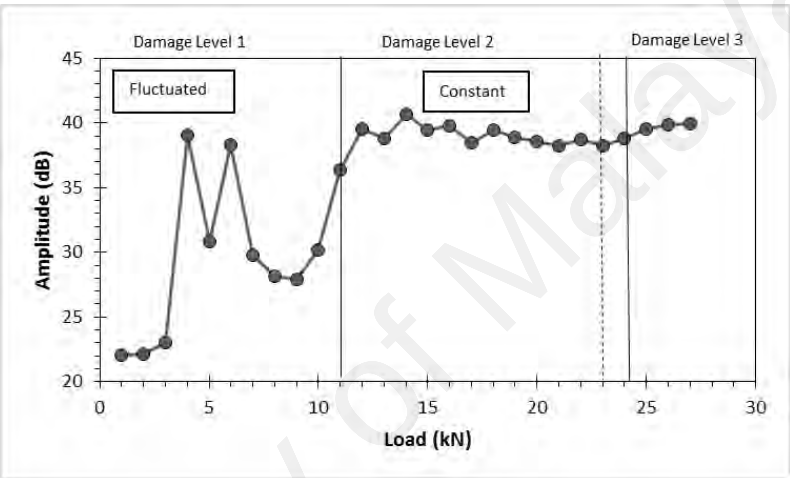

(e) S32

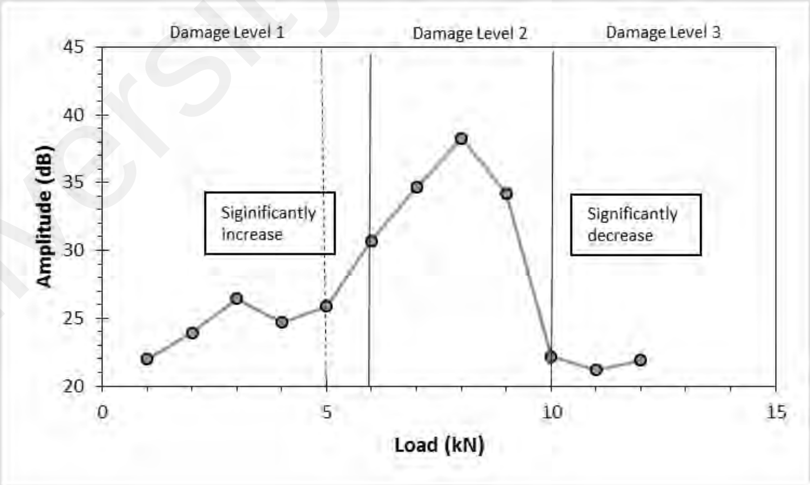

(f) S40

Figure 6. 12: Continued

6.4.4 Count versus Load

Figure 6.13 shows the count and load according to three damage levels. At damage level 1, two beam specimens (non-corroded (S0) and low corrosion (S10)) showed large fluctuation in the count rate, which indicates the development of a large number of cracks. However, for other beam specimens (S20, S25, and S32), the count began to increase at an early load level. At damage level 2, the significant drop in the count occurred at the dashed line. As shown in the figure, the dashed line represents the load level where a significant drop in RA value occurred. This drop is attributed to the crack opening of the specimens. By contrast, the count tends to increase again after a drop of count until the failure of the beam specimens. The significant decrease of count is shown in Table 6.5.

Table 6. 5: Decrease of count

Beam Specimens	Drop of count
S0	128.18
S10	271.64
S20	205.54
S25	253.58
S32	134.49
S40	1146.18

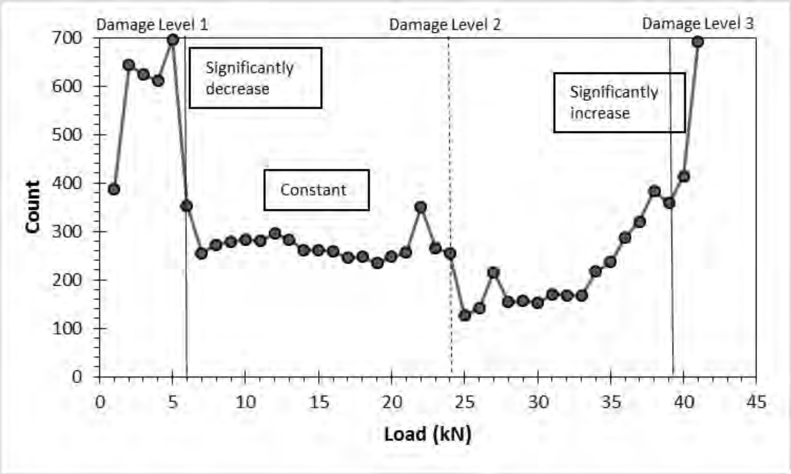

(a) S0

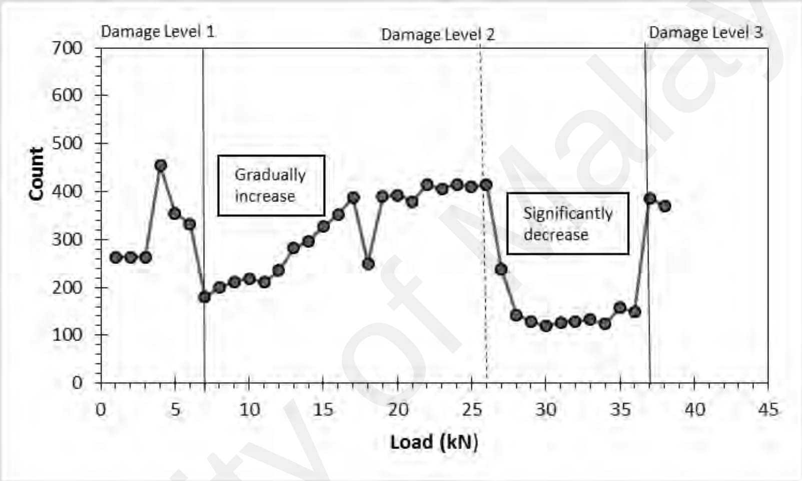

(b) S10

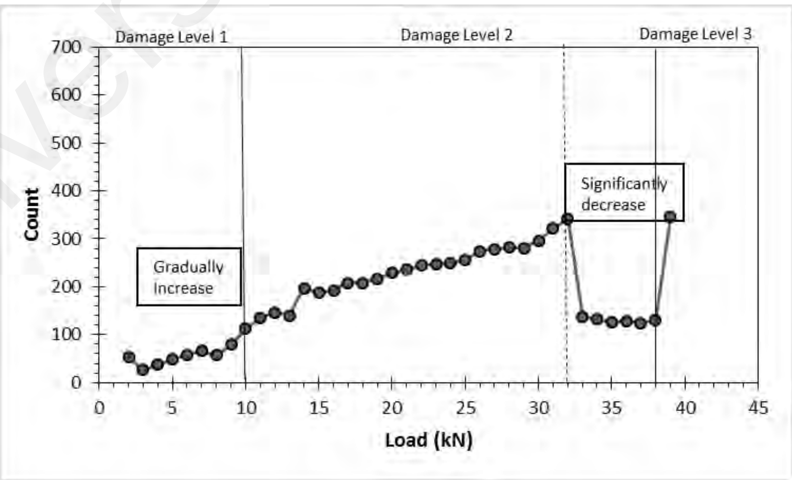

(c) S20

Figure 6. 13: Count vs. load of the beam specimens

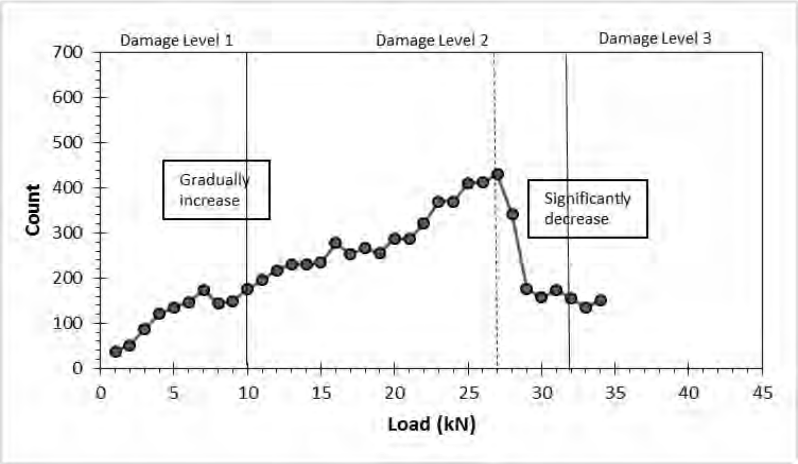

(d) S25

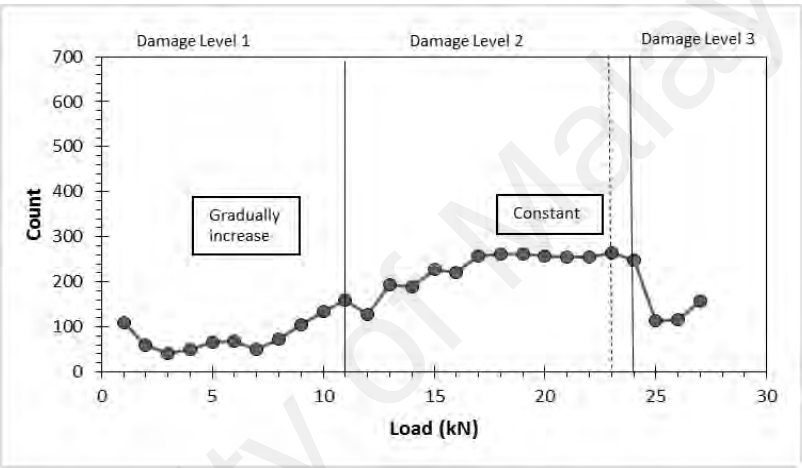

(e) S32

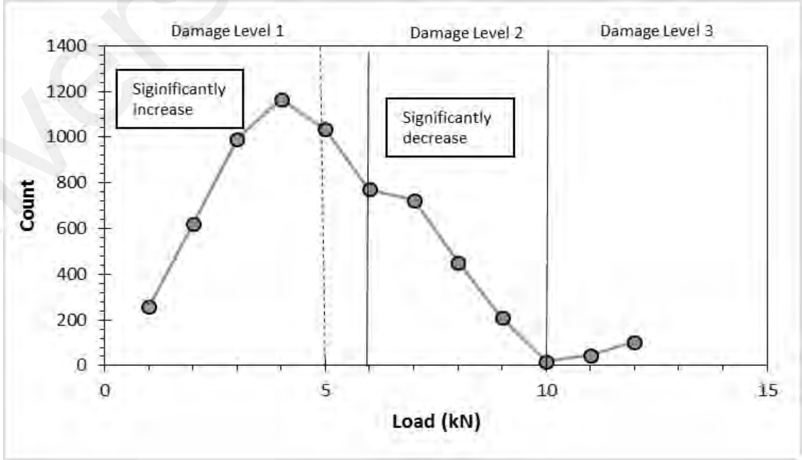

(f) S40

Figure 6. 13: Continued

6.4.5 *I*b-value

In Figure 6.14 (a), the *I*b-value history is depicted from non-beam specimen before filtering. Savitzky-Golay smoothing was used to filter the *I*b-value data of the beam specimens as described in Section 5.3.4. The filtered *I*b-value of non-corroded beam specimen is shown in Figure 6.14 (b).

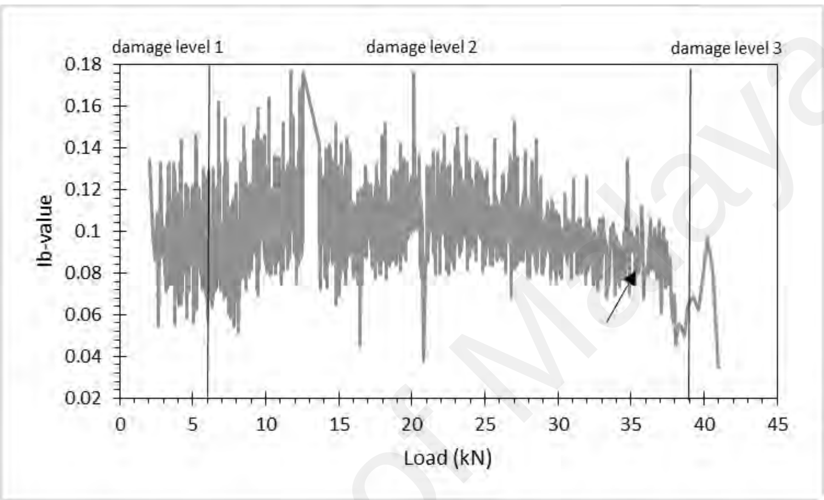

(a) before filtering

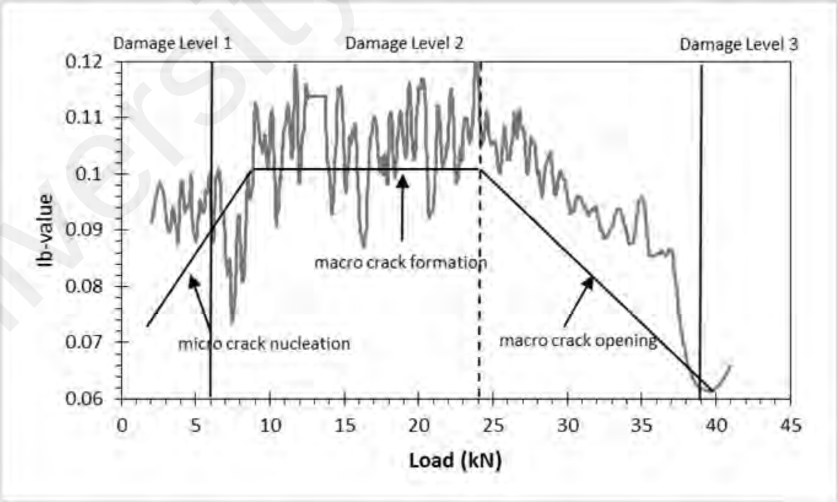

(b) after filtering

Figure 6. 14: Ib-value of S0 beam specimen

Figure 6.15 shows filtered *I*b-value for the corroded specimens. As also mentioned in previous section, the solid line is a boundary of the damage levels. The dashed line is the load when the significant drop of RA value. All the specimens clearly show a similar trend. An established trend shows that an increasing *I*b-value exists during damage level 1, followed by a slight fluctuation of *I*b-value during damage level 2 and a decrease in *I*b-value at the dashed line. As previously mentioned, the dashed line indicates the level where RA value drop occurs. This finding means that the micro-cracks formation was dominant before the occurrence of first cracks during damage level 1 due to the steady rise of the *I*b-value.

Once the first visible cracks occurred at damage level 2, the cracks began to localize as macro-cracks. At the dashed line, *I*b-value decreases due to the opening of macro-cracks. A decreasing trend of *I*b-value can be considered a serious damage alert of the beam. However, the S40 beam specimen with the highest corrosion level (39.84%) shows different trends of the *I*b-value distribution, and a significant drop in *I*b-value occurs at damage level 1. The drop of *I*b-value provides an indication of damage occurrence at an early damage level. This finding might imply that the high loss of cross section due to corrosion affects the crack opening of the beam specimen at tension steel reinforcement. The *I*b-value of each sensor of the beam specimens is shown in Appendix B.

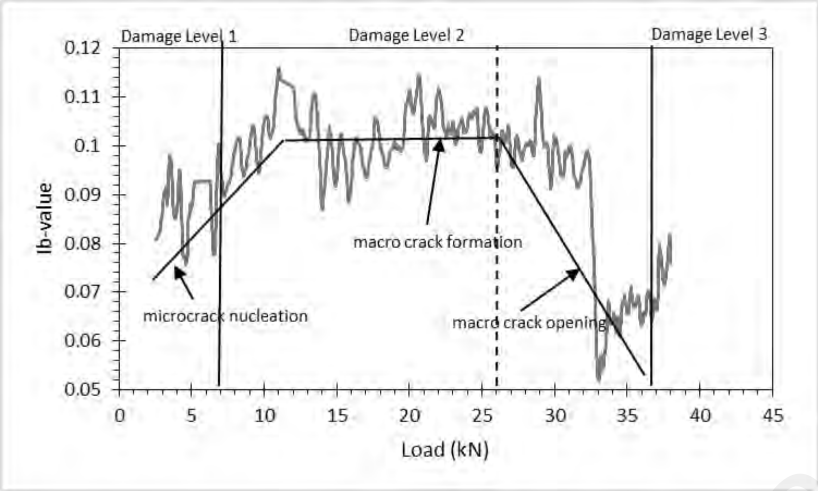

(a) S10

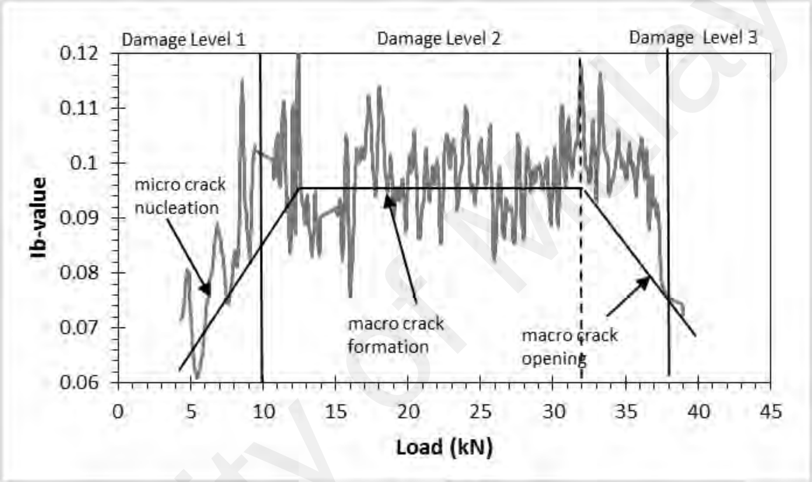

(b) S20

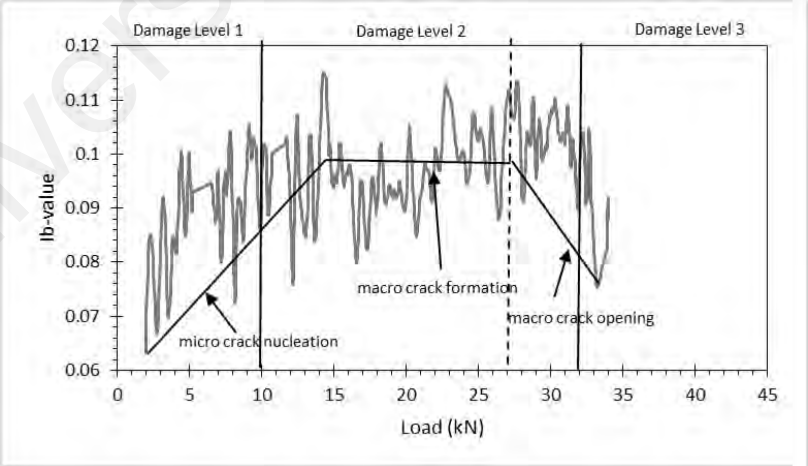

(c) S25

Figure 6. 15: *I*b-value of concrete beam specimens after filtering vs. load

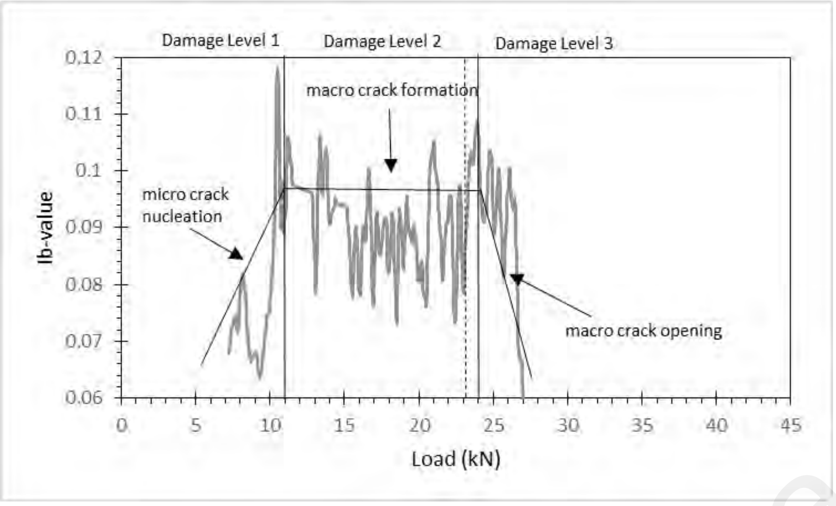

(d) S32

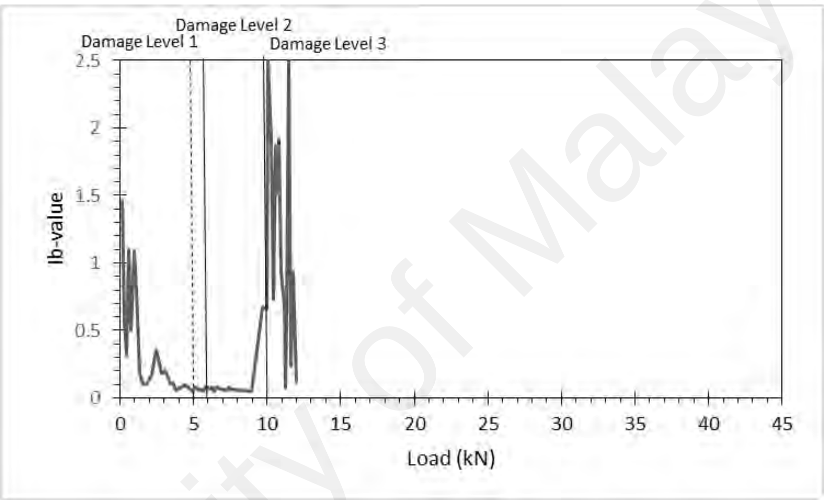

(e) S40

Figure 6. 15: Continued

6.4.6 Intensity Analysis

As described in Section 5.3.3, the intensity chart is plotted based on Hi and Sr values. Figures 6.16 and 6.17 show intensity chart of each sensor and each damage levels of the beam specimens, respectively. From the figures, the Hi and Sr values of the beam specimens tend to decrease in terms of increase of the corrosion levels. There is less significant different of Hi and Sr values among the sensors and damage levels of the S40 beam specimen. There are less structural significant events of each sensor of the highest corroded beam specimen.

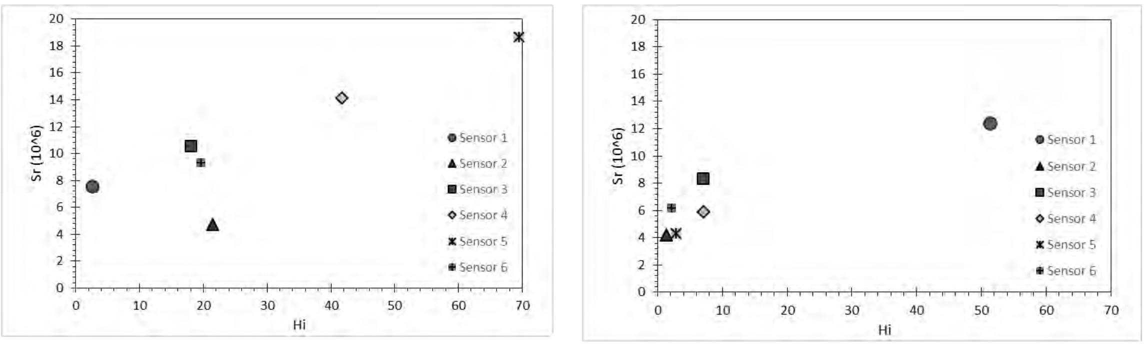

(a) S0

(b) S10

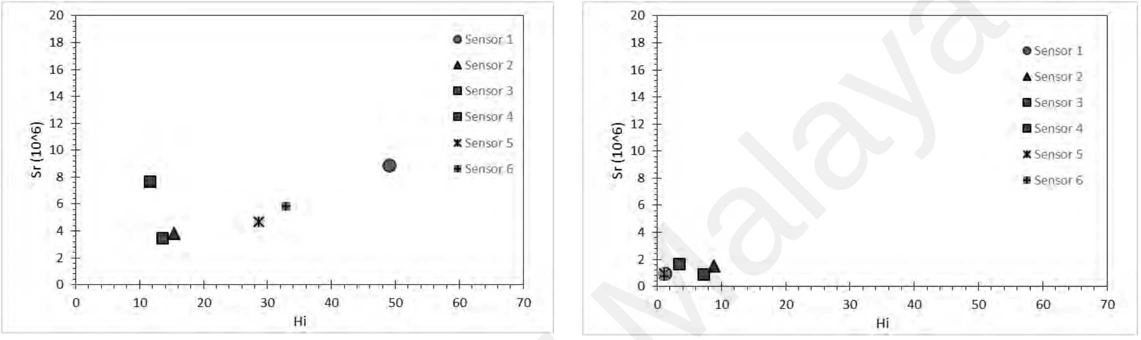

(c) S20

(d) S25

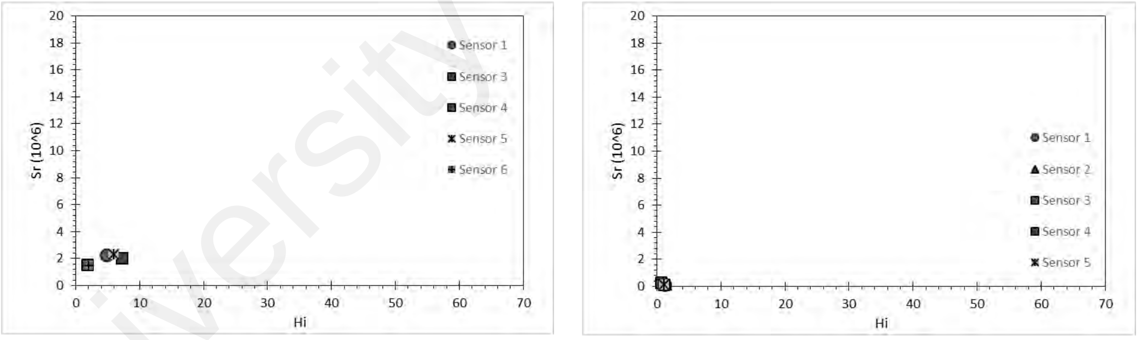

(e) S32

(f) S40

Figure 6. 16: Intensity Chart of each sensor of the beam specimens

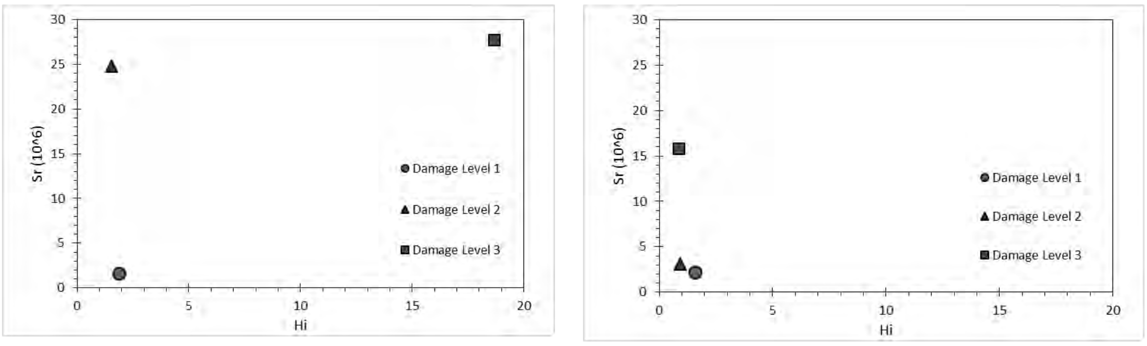

(a) S0

(b) S10

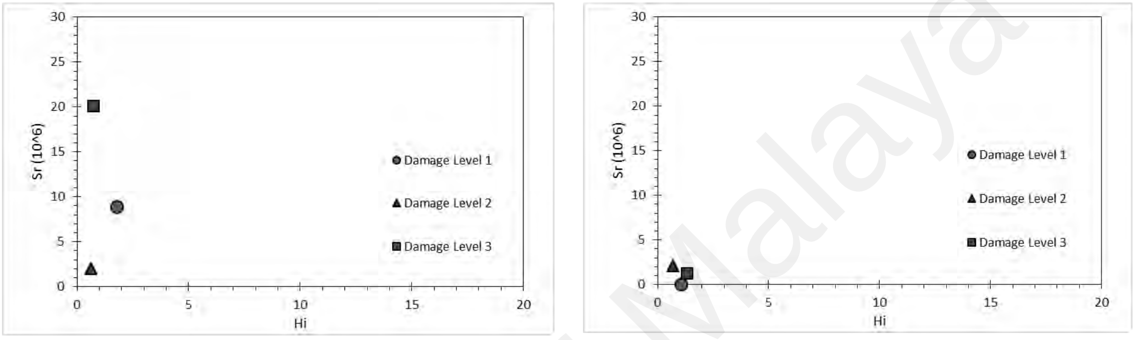

(c) S20

(d) S25

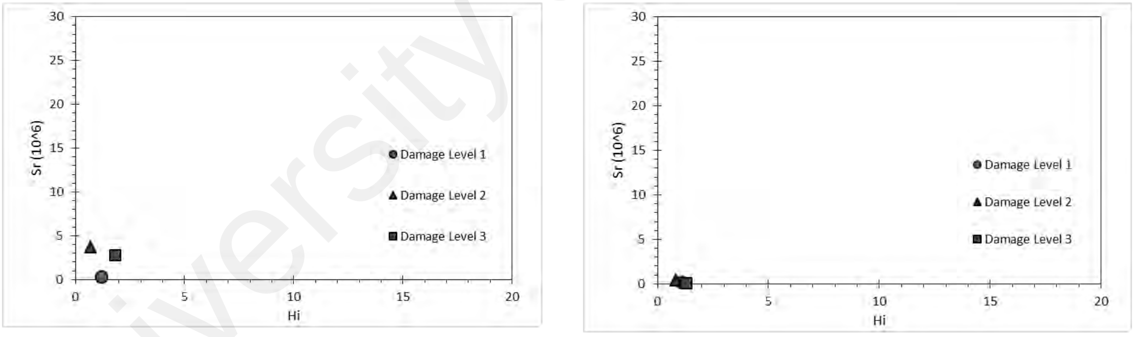

(e) S32

(f) S40

Figure 6. 17: Intensity chart at each damage level of the beam specimens

6.5 Secondary AE Data

The AE signals of secondary AE data from all the beam specimens with three cycles of cyclic load. The loading rate of each cycle of the secondary AE is 0.1 mm/min. Table 6.6 presents a summary of AE characteristics of the secondary AE along the different corrosion levels of the beam specimens. In general, the amplitude, AF, and accumulated AE hits, and counts decrease from cycle 1 to 3 of each beam specimen.

Table 6. 6: Secondary AE parameters of experiment 3

Beam Specimens	Cycle	Duration (x1000 μs)	Amplitude (dB)	Ave Frequency (kHz)	Hits	% of Total Hits	Counts
S0	1	22423.767	36.01	24.30	9861	72.34	5354071
	2	52936.880	25.51	17.06	1693	12.42	1569340
	3	50446.173	23.55	13.64	2077	15.24	1696582
S10	1	13045.545	36.75	16.05	13201	83.77	2117324
	2	22973.417	24.66	7.43	2009	12.75	275669
	3	18352.024	24.07	6.97	548	3.48	46990
S20	1	13567.432	29.39	9.42	4366	85.89	370200
	2	10701.089	28.50	8.55	347	6.83	31492
	3	10866.623	25.69	6.35	370	7.28	15690
S25	1	15540.200	34.91	16.74	10221	81.05	1924186
	2	19867.423	23.62	5.79	1635	12.97	154339
	3	13598.895	25.32	6.39	754	5.98	45425
S32	1	10176.896	31.48	13.41	4647	85.74	338698
	2	24773.168	27.82	9.30	357	6.59	71448
	3	24023.565	25.50	6.33	416	7.68	57994
S40	1	39972.339	31.06	17.43	4361	41.66	2490280
	2	15315.883	21.19	2.93	2957	28.25	31037
	3	21376.909	21.26	3.51	3150	30.09	33997

6.5.1 Cumulative Signal Strength (CSS)

Figure 6.18 shows the curve of CSS in relation with time for all the beam specimens. In general, the CSS rate in the first cycle is higher than the repeated cycles. This result means that the AE activities decrease due to the new cracks not to be generated as the beam specimen was subjected up to 4 kN of the load or 50% estimated load of the first visible cracking. Evaluating the damage of the beam specimens by CSS ratio is useful because the CSS ratio due to cracking is related to the increase in the load level and presence of existing cracks.

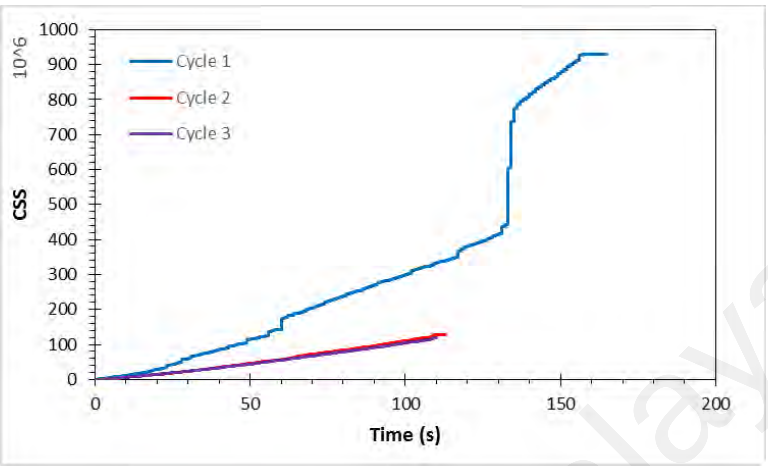

(a) S0

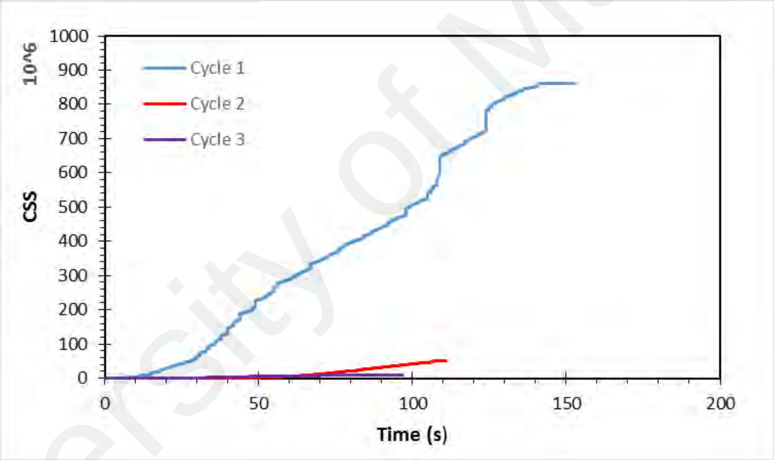

(b) S10

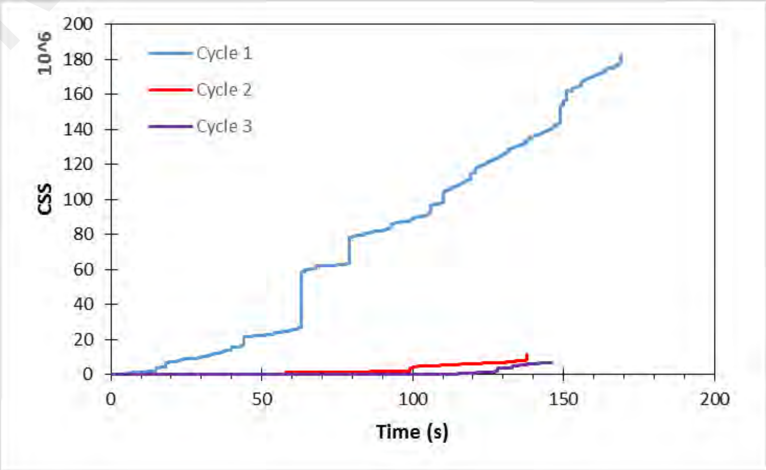

(c) S20

Figure 6. 18: CSS against time of the beam specimens

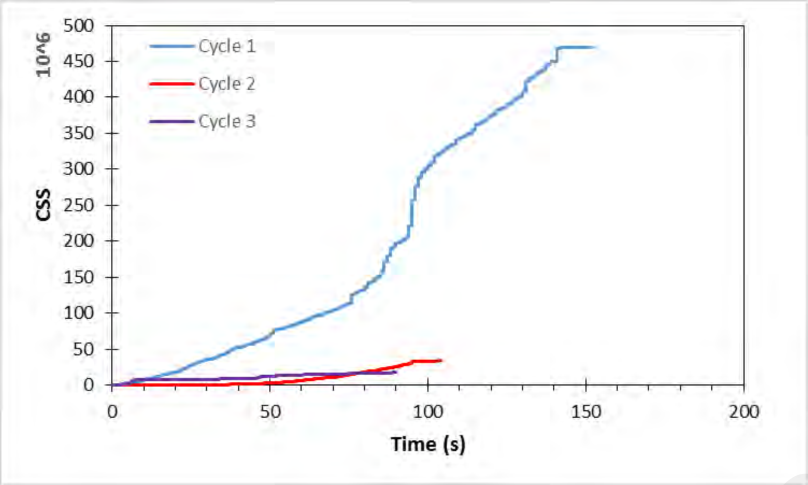

(d) S25

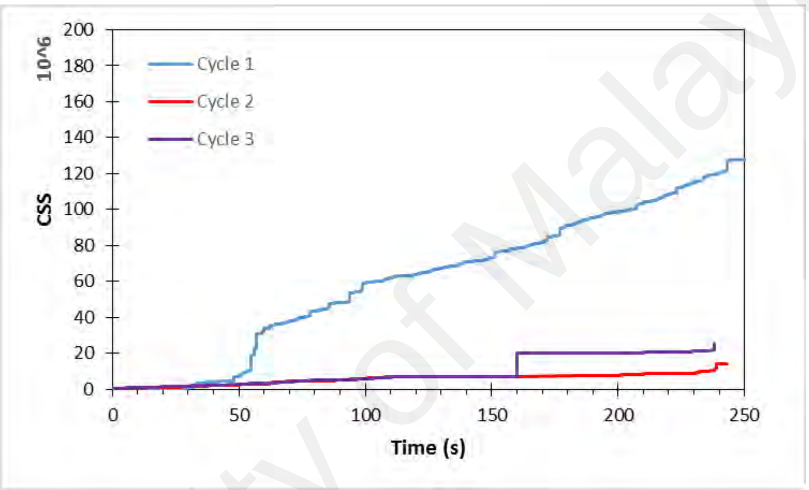

(e) S32

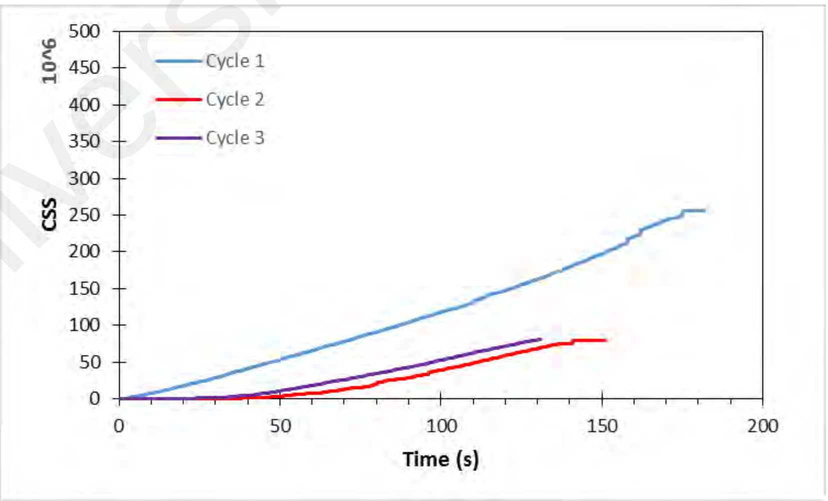

(f) S40

Figure 6. 18: Continued

A reference, a study conducted by Ridge and Ziehl (2006) proposed an evaluation criterion based on the CSS ratio of beam specimens strengthened with carbon fibre reinforced polymer (CFRP). Their study suggested that a peak CSS ratio between 30 and 50% was an appropriate value to indicate significant damage. Table 6.8 shows the CSS ratio for all the beam specimens. CSS ratio 1 is defined as the peak CSS at the end of cycle 2 divided by the peak CSS at the end of cycle 1. Meanwhile CSS ratio 2 is defined as the peak CSS ratio at the end of cycle 3 divided by the peak CSS at the end of cycle 2. As shown in the table, the CSS ratio 1 is in the range 5%–31% for all specimens. Based on the study of Ridge and Ziehl (2006), no indication of significant damage exists for CSS ratio 1. Moreover, evaluating the corroded beam specimens is unsuitable. For CSS ratio 2, the ratio is between 17.42% and 116.22%. The highest CSS ratio implies that the steel corroded beam has a significant damage on the beam specimens.

Table 6. 7: CSS ratio

Beam Specimens	Cycle	CSS	CSS ratio 1 (%)	CSS ratio 2 (%)
S0	Cycle 1	1.71E+08	5.24	17.42
	Cycle 2	8.95E+06		
	Cycle 3	1.56E+06		
S10	Cycle 1	8.62E+08	5.96	20.05
	Cycle 2	5.14E+07		
	Cycle 3	1.03E+07		
S20	Cycle 1	1.82E+08	6.32	59.11
	Cycle 2	1.15E+07		
	Cycle 3	6.80E+06		
S25	Cycle 1	4.69E+08	7.22	60.58
	Cycle 2	3.39E+07		
	Cycle 3	2.05E+07		
S32	Cycle 1	1.28E+08	11.09	106.98
	Cycle 2	1.42E+07		
	Cycle 3	1.52E+07		
S40	Cycle 1	2.56E+08	30.97	116.22
	Cycle 2	7.93E+07		
	Cycle 3	9.22E+07		

Figure 6.17 shows that CSS ratio increases with the increase in corrosion level of the specimens. As previously mentioned, the high CSS ratio might be a beneficial indication of significant damage to the beam specimens. It is a simple way to quickly conduct a damage assessment of cyclic load test of the beam specimen before the occurrence of the first visible cracks. an RC specimen. Appropriately, calculating the CSS ratio of the beam specimens can help predict the corrosion level experienced by the specimens.

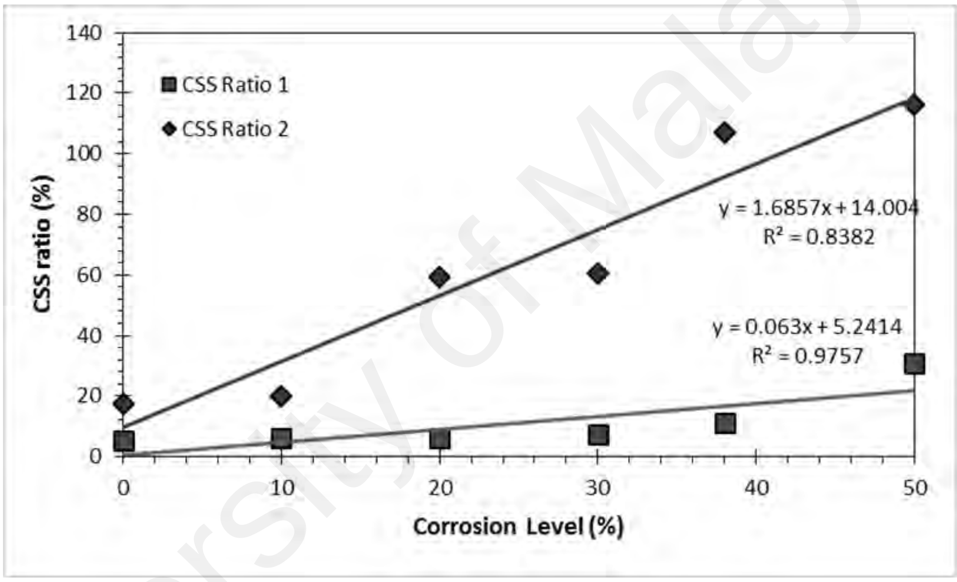

Figure 6. 19: CSS ratio vs. corrosion level (%)

6.5.2 *I*b-value

Table 6.8 shows the minimum *I*b-value of the beam specimens for each cycle. The *I*b-value of each cycle increases from cycle 1 to 3. In addition, the *I*b-value decreases with the increase in corrosion levels. The decrease in *I*b-value might indicate that the beam specimens with high corrosion level have a significant damage due to the steel corrosion of beam specimens at a low load level or early stage of loading.

Table 6. 8: *I*b-value of secondary AE

Beam Specimens	Min *I*b-value		
	Cycle 1	Cycle 2	Cycle 3
S0	0.050	0.078	0.132
S10	0.048	0.089	0.124
S20	0.038	0.073	0.075
S25	0.035	0.074	0.069
S32	0.033	0.073	0.066
S40	0.035	0.078	0.070

6.5.3 Intensity Analysis (IA)

Figure 6.20 and Table 6.9 show the intensity analysis of the beam specimens. Cycle 1 has the highest Hi and Sr values for all beam specimens. The high Hi and Sr values indicate that high activities of significant AE events occur during cycle 1 compared to subsequent two cycles. This is the first time that such specimens are subjected to load testing. In addition, this finding means that the AE activities decrease due to the new cracks, which have not been significantly generated yet during cycles 2 and 3.

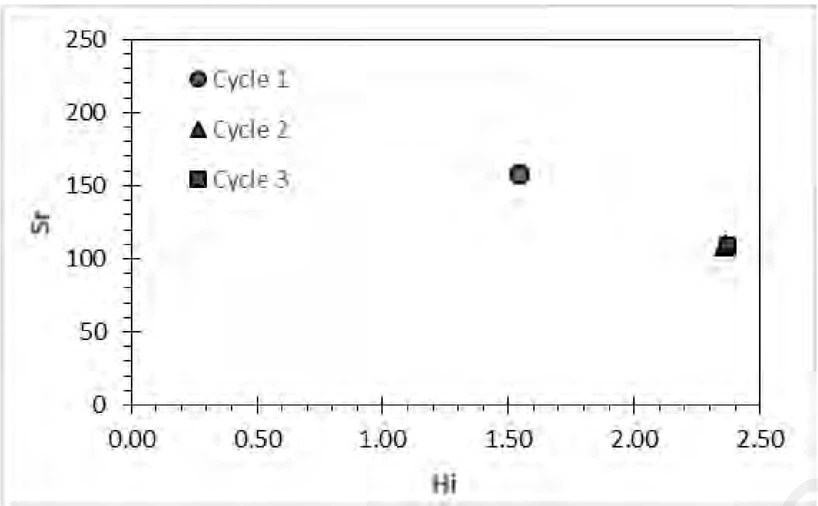

(a) S0

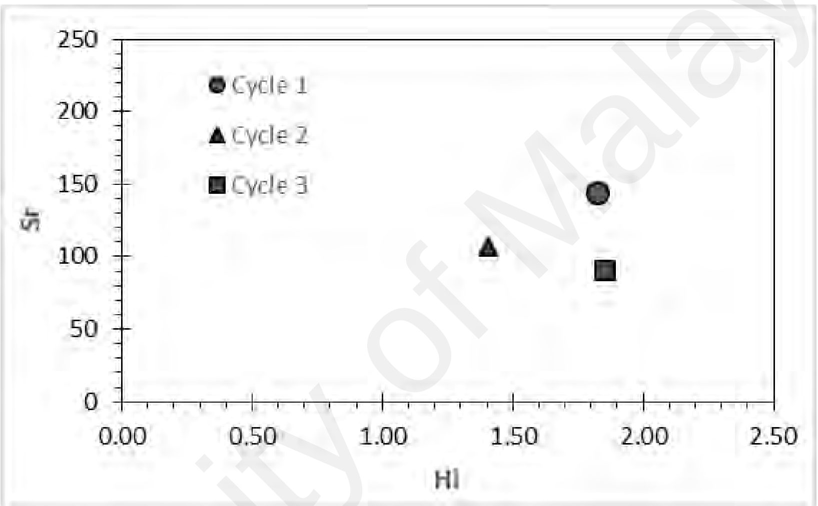

(b) S10

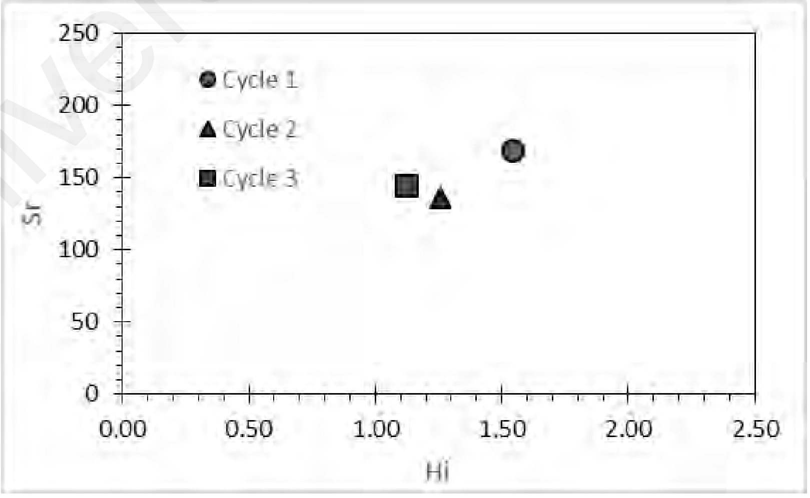

(c) S20

Figure 6. 20: Intensity chart at each cycle of beam specimens

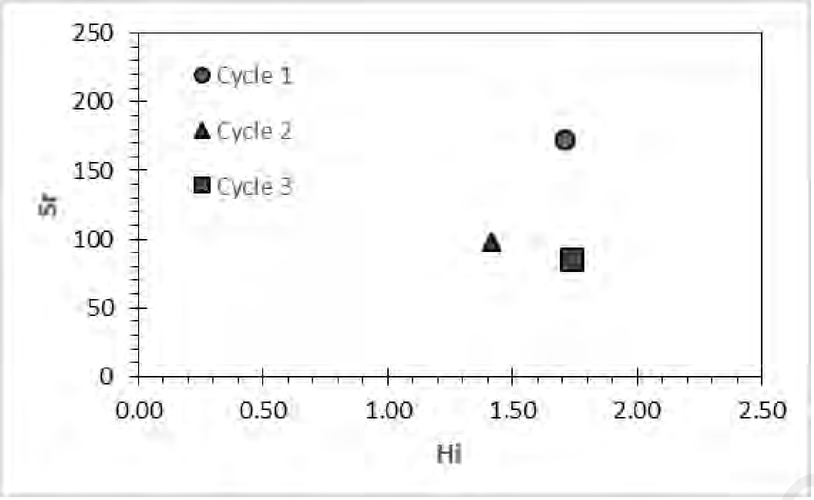

(d) S25

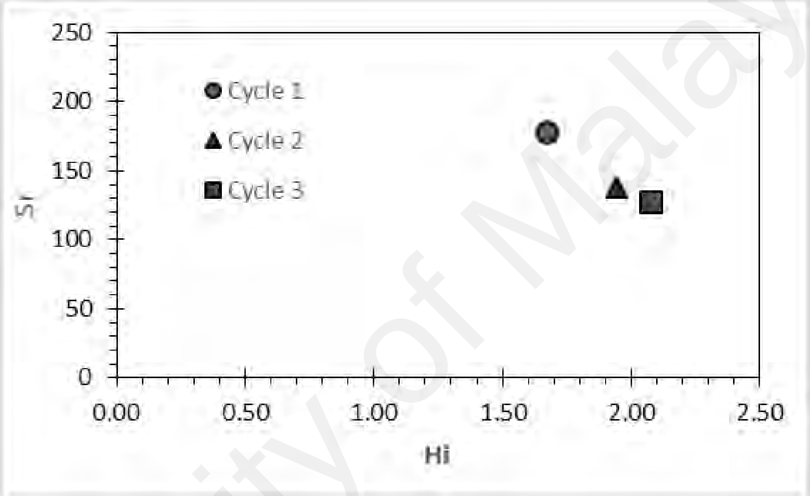

(e) S32

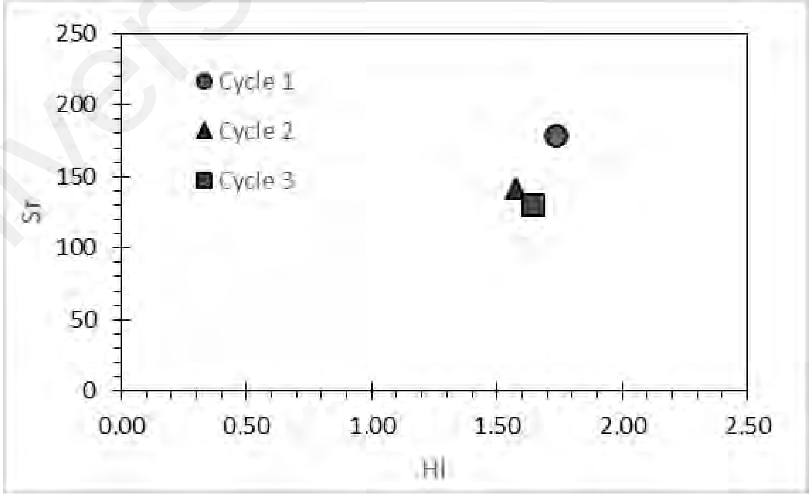

(f) S40

Figure 6. 20: Continued

Table 6. 9: Intensity analysis of secondary AE

Beam Specimens	Cycle	Hi	Sr
S0	Cycle 1	1.54	157.92
	Cycle 2	2.36	109.18
	Cycle 3	2.37	109.02
S10	Cycle 1	1.83	144.36
	Cycle 2	1.40	107.28
	Cycle 3	1.85	91.26
S20	Cycle 1	1.54	169.00
	Cycle 2	1.25	135.80
	Cycle 3	1.12	145.14
S25	Cycle 1	1.71	172.90
	Cycle 2	1.42	98.04
	Cycle 3	1.74	85.64
S32	Cycle 1	1.67	177.80
	Cycle 2	1.94	138.24
	Cycle 3	2.07	127.64
S40	Cycle 1	1.73	179.24
	Cycle 2	1.57	141.32
	Cycle 3	1.64	130.36

6.6 Linear Discriminant Analysis (LDA)

The LDA performs well in many applications. The basic idea of LDA is simple: for each class to be identified, calculate a (different) linear function of the attributes. The class function yielding the highest score represents the predicted class. There are many linear classification models, and they are different largely in how the coefficients are established. LDA does not require multiple passes over the data for optimization. Also, it naturally handles problems with two classes and more. It can provide an estimation of probability for each of the candidate class (Jusman et al., 2016).

The LDA solves a general Eigen-problem. Suppose there are C classes and *n* number of d-dimensional training samples, and n_c denotes the number of training samples of class c. Let 1 denotes an all-one vector of proper length. The equations for within-class scatter matrix, *Sw*, between-class scatter matrix, *Sb* and total scatter matrix, *St*, are:

$$S_w = \frac{1}{n}\sum_{c=1}^{C}\left(\hat{X}_c - m_c 1^T\right)\left(\hat{X}_c - m_c 1^T\right)^T \quad , \tag{6.1}$$

$$S_b = \frac{1}{n}\sum_{c=1}^{C} n_c (m_c - m)(m_c - m)^T \quad , \tag{6.2}$$

$$S_t = \frac{1}{n}\left(\hat{X} - m1^T\right)\left(\hat{X} - m1^T\right)^T \quad , \tag{6.3}$$

Where:

$\hat{X} \in R^{dxn}$ = the data matrix in which the columns are training samples,

$\hat{X}_c$ = the data matrix of training samples belonging to the class *c*,

m = the mean vector of all training samples,

m_c = the mean vector of training samples belonging to the class *c*, and

T = denotes matrix transpose.

The LDA computes a linear transformation matrix $W \in R^{d\times(C-1)}$, and usually $d \gg C$. The transformation matrix projects data from the original high-dimensional space into a low-dimensional space, maximizing the between-class distance while minimizing the within-class distance. Traditional LDA finds the optimal transformation matrix W_{LDA} by solving the optimization problem (Jusman et al., 2016).

$$W_{LDA} = arg_W \max trace(W^T S_b W (W^T S_t W)^{-1}) \tag{6.4}$$

According to Galloway (1975), when the total scatter matrix St is non-singular, the solution W_{LDA} consists of the top eigenvectors of the matrix $(S_t^{-1}S_b)$ that corresponds to non-zero eigenvalues. When the total scatter matrix St does not have a full rank, W_{LDA} consists of the eigenvectors of $(S_t^+S_b)$ corresponding to the non-zero eigenvalues, where S_t^+ denotes the pseudo-inverse of S_t (Weszka et al., 1976).

The description of data used for the classification of LDA is tabulated in Table 6.10. The data are obtained from the AE parameters, i.e. RA value of the concrete beam specimens. The data are classified into six classes based on the corrosion levels of the beam specimens. Class 1 is for S0, class 2 is for S10, class 3 is for S20, class 4 is for S25, class 5 is for S32 and class 6 is for S40 beam specimens. For LDA classification data, each beam specimens are also classified to six classes based on the class of LDA. The LDA was applied to classify RA value data of the beam specimens. Table 6.10 shows the classification results of LDA. In this study, a system uses validity measures of the test with six classes.

Table 6. 10: Data classifications to test system of LDA

Beam Specimens	Class 1	Class 2	Class 3	Class 4	Class 5	Class 6
S0	6472	601	796	18	0	0
S10	2746	3272	1116	0	0	0
S20	1953	1367	1952	0	0	0
S25	1553	698	1070	232	0	0
S32	2368	165	232	0	0	0
S40	601	4	18	0	0	0

Table 6.11 shows the classification of AF features of the beam specimens. The table shows that initially the classified data are predominantly classified as a class they are. The S0 beam specimen failed in the shear crack, the high percentage of S0 beam specimen and Class 1 is assumed as shear crack. Overall, the class 1 of the beam specimens are classified as shear crack and the class 2 to 6 are classified as tensile crack. Table 6.13 the classification data based on LDA data in terms of the type of crack. The S0, S32, and S40 beam specimen dominant as shear crack while for S10, S20, S25 dominant as tensile crack. The type of cracks of the beam specimens is almost same with the observations. More studies will be required to further examine the reliability of the LDA using other AE parameters.

Table 6. 11: Type of cracks classification based on LDA

Beam Specimens	Shear Cracks (%)	Tensile Cracks (%)
S0	82.06	27.94
S10	38.50	61.50
S20	37.04	62.96
S25	43.46	56.54
S32	85.64	14.36
S40	96.46	3.54

6.7 Summary of experiment 3

The beam specimens of experiment 3 were designed to be the same as the beam specimens of experiment 2 except for the steel reinforcement corrosion methods as discussed earlier. The beam specimens of experiment 3 were also subjected to monotonic and cyclic mechanical loading for primary and secondary AE, respectively. There are two factors contributing to the loss of the concrete strength of the post-corrosion beam specimens, i.e. loss of cross section and loss of bond strength. The increase in corrosion level or cross section of steel reinforcements was found to be linearly consistent with the decrease in the concrete strength of the beam specimens. On the other hand, a decrease in bond strength was found to be linear with the decrease in accumulated AE hits of the specimens. The results of the post-corrosion beam specimens indicate that the beam transition dominates the fracture behavior, which shifts from shear to tensile region as the corrosion level increases. For secondary AE, the CSS ratio increases as the corrosion level increases. This finding indicates that the occurrence of damage was due to loss in cross section and loss in bond strength of the post-corrosion beam specimens.

CHAPTER 7: CONCLUSIONS AND RECOMMENDATIONS

7.1 Conclusions

Based on the AE technique results obtained from testing of the three experiments of the corroded RC beam specimens under flexure loading, the conclusions drawn from this study can be summarized as follows:

1. RA value and AF of the AE parameters are useful in association with fracture mechanisms of the corroded RC beam specimens. Based on general observations, the corroded RC beam specimens failed in shear failure. Based on the AE data, the RA value and AF were successfully used to evaluate the fracture mechanisms in the beam specimens.
    a) For experiment 1, the highest recorded RA value of the beam specimens was obtained from the last damage stage (stage IV). However, for the most corroded beam specimen, the highest RA value occurred at the end of the damage stage II. The highest RA value is associated with the shear cracks and lowest RA value represents the development of tensile cracks. The shear cracks were observed to start propagating from the tension side, as a result of deteriorated cohesion between steel reinforcements and concrete due to corrosion.
    b) For experiment 2 and 3, shear cracks were observed due to high RA value and low AF at damage level 1. This result indicates that high-intensity events occurred within the concrete at the tension reinforcement area due to corrosion. Therefore, especially for experiment 3, the RA value suddenly experienced a significant drop in damage level 2, which indicates a tensile crack opening in the beam specimens.

2. The damage of the corroded RC beam specimens could be sufficiently characterized by the accumulated AE hits and *I*b-value of primary AE data and CSS ratio and ib-value of secondary AE data. These methods show great potential in becoming an effective tool for evaluation and continuous monitoring of the corroded RC structures by primary and secondary AE, especially for the post-corrosion beam specimens.

   a) For primary AE, the experimental result confirmed that the loss of ultimate strength of the beam specimens was linked to the decrease of accumulated AE hits. This trend of accumulated AE hits can be attributed to the stressing and cracking at tension reinforcement which has already been dissipated by corrosion. However, for pre-corrosion beam specimens, the accumulated AE hits increase in terms of corrosion level of steel reinforcements. This may due to the presence of pitting corrosion in the steel reinforcement that caused high AE activity of the beam specimens. On the other hand, the filtered *I*b-value increased during damage level 1, followed by a slight fluctuation of *I*b-value during damage level 2, and then decreased in *I*b-value at the load level of a significant drop of RA value. A decreasing trend in *I*b-value can be considered a serious damage alert.
   b) For secondary AE, the specimen with higher corroded beam specimens experienced very significant damage due to higher CSS ratio compared to the non-corroded beam specimen. The high CSS ratio might be a beneficial indication of significant damage to the corroded beam specimens. By contrast, the *i*b-value tends to decrease with the increase in the corrosion level of the beam specimens. This result indicates that the occurrence of significant damage due to the steel corrosion of the beam specimens at an early stage of loading.

3. There are two factors contributing to the loss of strength by steel corrosion in RC beam specimens; loss of cross-section (mass loss) and loss of ultimate strength or

bond strength. The increase in corrosion level or mass loss of steel reinforcements of the corroded beam specimens was found to be linearly consistent with the decrease in the ultimate strength. On the other hand, a decrease in the ultimate strength of the beam specimens was found to be linear with the decrease in accumulated AE hits, except for pre-corrosion beam specimens. The ultimate strength and accumulated AE hits were controlled by corrosion level or mass loss of the post-corrosion beam specimens.

4. The statistical and signal processing methods have been successfully established for identification and quantification of the corroded RC beam specimens using the Weibull damage function and linear discriminant analysis (LDA).
    a) For experiment 1, the Weibull fracture parameters were calibrated using AE energy data so that the failure probability function was successfully computed through which the remaining flexural capacity of the beam specimens was estimated. The probability of the failure occurrence is higher for the highest corroded beam specimen at a lower load level.
    b) For experiment 3, linear discriminant analysis (LDA) was performed using RA value data and the identification of the classification type based on the percentage of the cracks was successfully computed. Based on the classification, the higher corroded beam specimens were dominant in shear cracks compared to the lower corroded beam specimens.

7.2 Recommendations

There are still some significant drawbacks in the utilization of AE technique of corroded RC structures for which extensive researches could be recommended. The following concerns can be considered in future studies which are highly required to be answered.

1. The artificial climate environment is an alternative technique for accelerated corrosion in RC structures. The technique accelerated corrosion of RC structures in an artificial climate room controlled by computer system. Further studies should also be conducted for verifying the behaviour of AE parameters in corroded RC structures due to this accelerated corrosion process.
2. A comparative study between corrosion created in a short time (accelerated corrosion process) in laboratory and corrosion formed over time should be understood in the future studies.
3. Larger structures in real time are subjected to higher loading variations, as well as various loading configurations. Therefore, in future study, loading configuration should be considered seriously. With the variation of the loading rate and configuration, the developed AE analysis tools presented in the study could be applied.
4. AE parametric analysis may not reveal the whole details of fracture of the corroded RC structures. To this end, application of some signal processing process such as wavelets analysis in de-noising process and analyzing the waveforms energy rather than converted signals parameters could be significance in future studies.
5. Attenuation was an issue in these tests, performing a study on the attenuation with the corroded RC structures would help for further comprehension. Possible attenuation tests could be performed by testing the amplitude and frequency content of recorded signal by known sources over a variety of travel distances.
6. Future researchers should put emphasis on classifying AE source by differentiating between AE signals due to corrosion and signals due to load related deteriorations.

REFERENCES

Aballe, A., Bethencourt, M., Botana, F. J., Marcos, M., & Sánchez-Amaya, J. M. (2004). Influence of the degree of polishing of alloy AA 5083 on its behaviour against localised alkaline corrosion. *Corrosion Science, 46*(8), 1909-1920.

Abul, K. A., Ahmad, S., & Syed, A. A. (2007). Residual Strength of Corrosion-Damaged Reinforced Concrete Beams. *ACI Materials Journal, 104*(1), 40-47.

Aggelis, D. G. (2011). Classification of cracking mode in concrete by acoustic emission parameters. *Mechanics Research Communications, 38*(3), 153-157.

Aggelis, D. G., Kordatos, E. Z., Soulioti, D. V., & Matikas, T. E. (2010). Combined use of thermography and ultrasound for the characterization of subsurface cracks in concrete. *Construction and Building Materials, 24*(10), 1888-1897.

Aggelis, D. G., Soulioti, D. V., Sapouridis, N., Barkoula, N. M., Paipetis, A. S., & Matikas, T. E. (2011). Acoustic emission characterization of the fracture process in fibre reinforced concrete. *Construction and Building Materials, 25*(11), 4126-4131.

Ahmad, S. (2003). Reinforcement corrosion in concrete structures, its monitoring and service life prediction - A review. *Cement and Concrete Composites, 25*(4–5), 459-471.

Ahmad, S. (2009). Techniques for inducing accelerated corrosion of steel in concrete. *Arabian Journal for Science and Engineering, 34*(2 C), 95-104.

Al-Dulaijan, S. U., Al-Zahrani, M. M., Saricimen, H., Maslehuddin, M., Shameem, M., & Abbasi, T. A. (2002). Effect of rebar cleanliness and repair materials on reinforcement corrosion and flexural strength of repaired concrete beams. *Cement and Concrete Composites, 24*(1), 139-149.

Al-Saidy, A. H., Al-Harthy, A. S., Al-Jabri, K. S., Abdul-Halim, M., & Al-Shidi, N. M. (2010). Structural performance of corroded RC beams repaired with CFRP sheets. *Composite Structures, 92*(8), 1931-1938.

Aldahdooh, M. A. A., & Muhamad Bunnori, N. (2013). Crack classification in reinforced concrete beams with varying thicknesses by mean of acoustic emission signal features. *Construction and Building Materials, 45*, 282-288.

Almusallam, A. A. (2001). Effect of degree of corrosion on the properties of reinforcing steel bars. *Construction and Building Materials, 15*(8), 361-368.

Almusallam, A. A., Ahmad S. Al-Gahtani, Abdur Rauf Aziz, & Rasheeduzzafar. (1996). Effect of reinforcement corrosion on bond strength. *Construction and Building Materials, 10*(2), 123-129.

Almusallam, A. A., & Al-Gahtani, A. S. (1996). Effect of reinforcement corrosion on flexural behavior of concrete slabs. *Journal of Materials in Civil Engineering, 8*(3), 123-127.

Alvarez, M. G., Lapitz, P., & Ruzzante, J. (2012). Analysis of acoustic emission signals generated from SCC propagation. *Corrosion Science 55*(0), 5-9.

Andrade, C., & Gonzalez, J. A. (1978). Quantitative measurements of corrosion rate of reinforcing steels embedded in concrete using polarization resistance measurements. *Werkstoffe und Korrosion, 29*(8), 515-519.

Andrade, C., Keddam, M., Novoa, X. R., Perez, M. C., Rangel, C. M., & Takenouti, H. (2001). Electrochemical behaviour of steel rebars in concrete: Influence of environmental factors and cement chemistry. *Electrochimica Acta, 46*(24-25), 3905-3912.

Andrade, C., M.C.Alonso, & J.A.Gonzalez. (1990). An initial effort to use corrosion rate measurements for estimating rebar durability corrosion rates of steel in concrete. In V. C. Neal S. B., and David W, editor (Ed.), *Corrosion rates of steel in concrete* (pp. 29-37.). Philadelphia: ASTM.

Apostolopoulos, C. A., & Michalopoulos, D. (2007). Impact of Corrosion on Mass Loss, Fatigue and Hardness of BSt500s Steel. *Journal of Materials Engineering and Performance, 16*(1), 63-67.

Arndt, R., & Jalinoos, F. (2009). *NDE for corrosion detection in reinforced concrete structures-benchmark approach*. Paper presented at the Non-destructive Testing In Civil Engineering (NDTCE'09).

Assouli, B., Ballivy, G., & Rivard, P. (2008). Influence of environmental parameters on application of standard ASTM C876-91: Half cell potential measurements. *Corrosion Engineering Science and Technology, 43*(1), 93-96.

ASTM. (1989). ASTM C-597-83: Standard test method for pulse velocity through concrete (pp. p. 289): American Society of Testing Materials.

ASTM. (1998). ASTM C-610-98A: Definitions of Terms Relating to Acoustic Emission: American Society of Testing Materials.

ASTM. (2003a). ASTM G1-03: Standard Practice for Preparing, Cleaning, and Evaluating Corrosion Test Specimens: American Society of Testing Materials.

ASTM. (2003b). G1-Standard Practice for Preparing, Cleaning, and Evaluating Corrosion Test Specimens.

ASTM. (2004a). ASTM G31-72: Standard Practice for Laboratory Immersion Corrosion Testing of Metals: American Society of Testing Materials.

ASTM. (2004b). G3 -72-Standard Practice for Laboratory Immersion Corrosion Testing of Metals.

ASTM. (2017). ASTM A370-17: Standard Test Methods and Definitions for Mechanical Testing of Steel Products: American Society for Testing and Materials.

Baek, S., Xue, W., Feng, M. Q., & Kwon, S. (2012). Nondestructive corrosion detection in RC through integrated heat induction and IR thermography. *Journal of Nondestructive Evaluation, 31*(2), 181-190.

Bagavathiappan, S., Lahiri, B. B., Saravanan, T., Philip, J., & Jayakumar, T. (2013). Infrared thermography for condition monitoring - A review. *Infrared Physics & Technology, 60*(0), 35-55.

Bagherifaez, M., Behnia, A., Majeed, A. A., & Hwa Kian, C. (2014). Acoustic Emission Monitoring of Multicell Reinforced Concrete Box Girders Subjected to Torsion. The Scientific World Journal, *2014*, 13.

Ballim, Y., & Reid, J. C. (2003). Reinforcement corrosion and the deflection of RC beams - an experimental critique of current test methods. *Cement and Concrete Composites, 25*(6), 625-632.

Baranov, V. M., Kapralov, E. Y., & Karasevich, V. A. (2003). Acoustic and electrochemical noise methods in extreme-condition fatigue tests. *Measurement Techniques 46*(10), 994-999.

Barnes, C. L., Trottier, J.-F., & Forgeron, D. (2008). Improved concrete bridge deck evaluation using GPR by accounting for signal depth-amplitude effects. *NDT & E International, 41*(6), 427-433.

Baronio, G., Berra, M., Bertolini, L., & Pastore, T. (1996). Steel corrosion monitoring in normal and total-lightweight concretes exposed to chloride and sulphate solutions Part I: Potential measurements. *Cement and Concrete Research, 26*(5), 683-689.

Basheer, L., Kropp, J., & Cleland, D. J. (2001). Assessment of the durability of concrete from its permeation properties: a review. *Construction and Building Materials, 15*(2-3), 93-103.

Beattie, A. G. (1983). Acoustic emission, principles and instrumentation. *J Acoust. Emission, 2*(1-2), 34.

Behnia, A., Chai, H. K., & Shiotani, T. (2014a). Advanced structural health monitoring of concrete structures with the aid of acoustic emission. *Construction and Building Materials, 65*, 282-302.

Behnia, A., Chai, H. K., Yorikawa, M., Momoki, S., Terazawa, M., & Shiotani, T. (2014b). Integrated non-destructive assessment of concrete structures under flexure by acoustic emission and travel time tomography. *Construction and Building Materials*, *67*(B), 202-215.

Bertocci, U., & Huet, F. (1995). Noise analysis applied to electrochemical systems. *Corrosion, 51*(2), 131-144.

Broomfield, J. P. (1996). Field measurement of the corrosion rate of steel in concrete using a microprocessor controlled unit with a monitored guard ring for signal confinement. *ASTM Special Technical Publication, 1276*, 91-106.

BS. (1983a). BS 1881-116: Testing concrete. Method for determination of compressive strength of concrete cubes: British Standards Institution.

BS. (1983b). BS 1881-121: Testing concrete. Method for determination of static modulus of elasticity in compression: British Standards Institution.

BS. (1997). BS 8110-1: Structural use of concrete. Code of practice for design and construction: British Standards Institution.

BS. (2005). BS 4449: Specification Steel for the reinforcement of concrete. Weldable reinforcing steel. Bar, coil and decoiled product. : British Standards Institution.

Bungey, J. H. (1991). Ultrasonic testing to identify alkali-silica reaction in concrete. *British Journal of Non-Destructive Testing, 33*(5), 227-231.

Bungey, J. H., & Millard, S. G. (1996). *Testing of concrete in structures (3rd ed.)*. London; New York: Blackie Academic & Professional.

Büyüköztürk, O. (1998). Imaging of concrete structures. *NDT & E International, 31*(4), 233-243.

Cabrera, J. G. (1996). Deterioration of concrete due to reinforcement steel corrosion. *Cement and Concrete Composites, 18*(1), 47-59.

Calabrese, L., Campanella, G., & Proverbio, E. (2012). Noise removal by cluster analysis after long time AE corrosion monitoring of steel reinforcement in concrete. *Construction and Building Materials, 34*(0), 362-371.

Calabrese, L., Campanella, G., & Proverbio, E. (2013a). Identification of corrosion mechanisms by univariate and multivariate statistical analysis during long term acoustic emission monitoring on a pre-stressed concrete beam. *Corrosion Science, 73*(0), 161-171.

Calabrese, L., Campanella, G., & Proverbio, E. (2013b). Identification of corrosion mechanisms by univariate and multivariate statistical analysis during long term acoustic emission monitoring on a pre-stressed concrete beam. *Corrosion Science, 73*, 161-171.

Carino, N. J. (1999). Nondestructive techniques to investigate corrosion status in concrete structures. *Journal of Performance of Constructed Facilities, 13*(3), 96-106.

Carino, N. J., Sansalone, M., & Hsu, N. N. (1986). Flaw detection in concrete by frequency spectrum analysis of impact-echo waveforms. *International Advances in Nondestructive Testing, 12*, 117-146.

Carpinteri, A., Lacidogna, G., & Niccolini, G. (2011). Damage analysis of reinforced concrete buildings by the acoustic emission technique. *Structural Control and Health Monitoring, 18*(6), 660-673.

Cavalier, P. G., & Vassie, P. R. (1981). Investigation and repair of reinforcement corrosion in a bridge deck. *Proceedings of the Institution of Civil Engineers (London) Part 1 - Design & Construction*, Vol. 70 (pt 1), pp. 461-480.

Chen, W., & Dong, X. (2012). Modification of the wavelength-strain coefficient of FBG for the prediction of steel bar corrosion embedded in concrete. *Optical Fiber Technology, 18*(1), 47-50.

Christodoulou, C. (2009). *Electrochemical treatments of corroded reinforcement in concrete.* The 2nd International Conference on Concrete Repair, Rehabilitation and Retrofitting, ICCRRR 2009.

Chung, L., Najm, H., & Balaguru, P. (2008). Flexural behavior of concrete slabs with corroded bars. *Cement and Concrete Composites, 30*(3), 184-193.

Chung, L., Paik, I. K., Cho, S. H., & Roh, Y. S. (2006). Infrared thermographic technique to measure corrosion in reinforcing bar. *Key Engineering Materials, 321-323 l*, 821-824.

Clark, M. R., McCann, D. M., & Forde, M. C. (2003). Application of infrared thermography to the non-destructive testing of concrete and masonry bridges. *NDT & E International, 36*(4), 265-275.

Clear, K. C. (1982). *Time to corrosion of reinforcing steel in concrete slabs*.

Clear., K. C. (1989). Measuring rate of corrosion of steel in field concrete structures. *Transportation Research Record,* (1211), 28-37.

Colombo, S., Forde, M. C., Main, I. G., & Shigeishi, M. (2005). Predicting the ultimate bending capacity of concrete beams from the relaxation ratio analysis of AE signals. *Construction and Building Materials, 19*(10), 746-754.

Colombo, S., Main, I. G., & Forde, M. C. (2003). Assessing damage of reinforced concrete beam using "b-value" analysis of acoustic emission signals. *Journal of Materials in Civil Engineering, 15*(3), 280-286.

Cusson, D., Lounis, Z., & Daigle, L. (2011). Durability Monitoring for Improved Service Life Predictions of Concrete Bridge Decks in Corrosive Environments. *Computer-Aided Civil and Infrastructure Engineering, 26*(7), 524-541.

Dunn, S. E., Young, J. D., Hartt, W. H., & Brown, R. P. (1984). Acoustic emission characterization of corrosion induced damage in reinforced concrete. *Corrosion, 40*(7), 339-343.

El Maaddawy, T., & Soudki, K. (2007). A model for prediction of time from corrosion initiation to corrosion cracking. *Cement and Concrete Composites, 29*(3), 168-175.

El Maaddawy, T. A., & Soudki, K. A. (2003). Effectiveness of Impressed Current Technique to Simulate Corrosion of Steel Reinforcement in Concrete. *Journal of Materials in Civil Engineering, 15*(1), 41-47.

ElBatanouny, M. K., Larosche, A., Mazzoleni, P., Ziehl, P. H., Matta, F., & Zappa, E. (2012a). Identification of cracking mechanisms in scaled FRP reinforced concrete beams using acoustic emission. *Experimental Mechanics.*

ElBatanouny, M. K., Mangual, J., Velez, W., Ziehl, P. H., Matta, F., & Gonzalez, M. (2012b). *Monitoring corrosion in prestressed concrete beams using acoustic emission technique.* The SPIE - The International Society for Optical Engineering.

ElBatanouny, M. K., Mangual, J., Ziehl, P. H., & Matta, F. (2014a). Early corrosion detection in prestressed concrete girders using acoustic emission. *Journal of Materials in Civil Engineering, 26*(3), 504-511.

ElBatanouny, M. K., Ziehl, P. H., Larosche, A., Mangual, J., Matta, F., & Nanni, A. (2014b). Acoustic emission monitoring for assessment of prestressed concrete beams. *Construction and Building Materials, 58*, 46-53.

Elfergani, H. A., Pullin, R., & Holford, K. M. (2013). Damage assessment of corrosion in prestressed concrete by acoustic emission. *Construction and Building Materials, 40*(0), 925-933.

Elsener, B., Andrade, C., Gulikers, J., Polder, R., & Raupach, M. (2003). Half-cell potential measurements - Potential mapping on reinforced concrete structures. *Materials and Structures, 36*(7), 461-471.

Elsener, B., Wojtas, H., & Bohni, H. (1994). Inspection and monitoring of reinforced concrete structures - electrochemical methods to detect corrosion. *Insight: Non-Destructive Testing and Condition Monitoring, 36*(7), 502-506.

Ervin, B., Kuchma, D., Bernhard, J., & Reis, H. (2009). Monitoring corrosion of rebar embedded in mortar using high-frequency guided ultrasonic waves. *Journal of Engineering Mechanics, 135*(1), 9-19.

Fang, C., Lundgren, K., Chen, L., & Zhu, C. (2004). Corrosion influence on bond in reinforced concrete. *Cement and Concrete Research, 34*(11), 2159-2167.

Fang, X., Chen, L., & Pan, J. (2014). Comparative study of on-site corrosion monitoring for concrete by different methods. *Advanced Materials Research, 838-841*, 2066-2070.

Fowler, T. J., Blessing, J. A., & Strauser, F. E. (1992). Intensity analysis. *Proc. 4th Int. Symp. Acous. Emiss. from composite materials*, 16-27.

Fukuyama, T., Nagai, H., & Noguchi, T. (2009). *Corrosion monitoring of reinforcing bars by electrochemical noise measurement.* The 4th International Conference on Structural Health Monitoring of Intelligent Infrastructure, SHMII.

Galloway, M. M. (1975). Texture analysis using gray level run lengths. *Computer Graphics and Image Processing, 4*(2), 172-179.

Gao, J., Wu, J., Li, J., & Zhao, X. (2011). Monitoring of corrosion in reinforced concrete structure using Bragg grating sensing. *NDT & E International, 44*(2), 202-205.

Geng, J., Wu, J., & Zhao, X. (2009). *Simulation of fiber Bragg grating sensor for rebar corrosion.* SPIE - The International Society for Optical Engineering.

Gonzalez, J. A., Miranda, J. M., Birbilis, N., & Feliu, S. (2005). Electrochemical techniques for studying corrosion of reinforcing steel: Limitations and advantages. *Corrosion, 61*(1), 37-50.

Gostautas, R. S., Ramirez, G., Peterman, R. J., & Meggers, D. (2005). Acoustic emission monitoring and analysis of glass fiber-reinforced composites bridge decks. *Journal of Bridge Engineering, 10*(6), 713-721.

Goueygou, M., Piwakowski, B., Fnine, A., Kaczmarek, M., & Buyle-Bodin, F. (2004). NDE of two-layered mortar samples using high-frequency Rayleigh waves. *Ultrasonics, 42*(1-9), 889-895.

Grosse, C. U., Reinhardt, H. W., & Finck, F. (2003). Signal-based acoustic emission techniques in civil engineering. *Journal of Materials in Civil Engineering, 15*(3), 274-279.

Gutenberg, B., & Richter, C. F. (1954). *Seismicity of the Earth and Associated Phenomena*: Princeton University Press.

Ha, T.-H., Muralidharan, S., Bae, J.-H., Ha, Y.-C., Lee, H.-G., Park, K.-W., & Kim, D.-K. (2007). Accelerated short-term techniques to evaluate the corrosion performance of steel in fly ash blended concrete. *Building and Environment, 42*(1), 78-85.

Halabe, U. B. (1990). *Condition assessment of reinforced concrete structures using electromagnetic waves.* (Ph.D Thesis), Massachusetts Institute of Technology, United States - Massachusetts.

Hashimoto, M., Miyajima, S., & Murata, T. (1992). An experimental study of potential fluctuation during passive film breakdown and repair on iron. *Corrosion Science 33*(6), 905-915.

Hassan, M. R. A., Bakar, M. H. A., Dambul, K., & Adikan, F. R. M. (2012). Optical-based sensors for monitoring corrosion of reinforcement rebar via an etched Cladding Bragg grating. *Sensors (Switzerland), 12*(11), 15820-15826.

Holford, K. M. (2000). Acoustic Emission–Basic Principles and Future Directions. Strain, *36*(2), 51-54.

Holloway, L., Birbilis, N., & Forsyth, M. (2004). *Long term monitoring of a reinforced concrete remediation method in a marine environment.* European Corrosion Conference: Long Term Prediction and Modelling of Corrosion (EUROCORR).

Holloway, L., Karajayli, P., & Birbilis, N. (2009). *Galvanostatic pulse corrosion rate monitoring for steel in concrete.* 49th Annual Conference of the Australasian Corrosion Association: Corrosion and Prevention.

Hong, S., Lai, W.-L., & Helmerich, R. (2014). Experimental monitoring of chloride-induced reinforcement corrosion and chloride contamination in concrete with ground-penetrating radar. *Structure and Infrastructure Engineering*, 1-12.

Hong, S. X., Lai, W. L., & Helmerich, R. (2012). *Monitoring accelerated corrosion in chloride contaminated concrete with ground penetrating radar.* 14th International Conference on Ground Penetrating Radar.

Ii, Chung, L., Paik, I. K., & Roh, Y. S. (2004). Non-destructive evaluation techniques of reinforcing steel corrosion using infrared thermography. *Key Engineering Materials, 270-273*, 1592-1597.

Ing, M., Austin, S., & Lyons, R. (2005). Cover zone properties influencing acoustic emission due to corrosion. *Cement and Concrete Research 35*(2), 284-295.

Inoue, H., Moriya, R., & Nishimura, R. (2008). Extreme-value distribution of the metastable-pit depth estimated by potential noise method. *Journal of the Society of Materials Science, Japan, 57*(11), 1097-1100.

Ismail, M. A., Soleymani, H., & Ohtsu, M. (2006, 5-6 September). *Early detection of corrosion activity in reinforced concrete slab by AE technique.* The 6th Asia-Pasific Structural Engineering and Construction Conference (APSEC 2006), Kuala Lumpur, Malaysia.

Ismail, M. E., Ismail, M., & Ohtsu, M. (2008). *Non-destructive evaluation of corrosion activity in reinforced concrete slab.* 4th International Structural Engineering and Construction Conference (ISEC-4) - Innovations in Structural Engineering and Construction.

Jakubowski, M. (2011). Influence of pitting corrosion on strength of steel ships and offshore structures. *Polish Maritime Research, 18*(4), 54-58.

JCMS-IIIB5706. (2003). Monitoring Method for Active Cracks in Concrete by Acoustic Emission (pp. 6). Japan: Federation of Construction Material Industries.

John, G., Hladky, K., Gaydecki, P., & Dawson, J. (1992). *Recent developments in inspection techniques for corrosion damaged concrete structures.* the ASTM Special Technical Publication.

Jung, Y.-C., Na, W.-B., Kundu, T., & Ehsani, M. (2000). *Damage detection in concrete using Lamb waves.* SPIE - The International Society for Optical Engineering.

Jusman, Y., Ng, S. C., Hasikin, K., Kurnia, R., Osman, N. A. A., & Teoh, K. H. (2016). A system for detection of cervical precancerous in field emission scanning electron microscope images using texture features. *Journal of Innovative Optical Health Sciences*.

Kabir, S., & Zaki, A. (2011). *Detection and quantification of corrosion damage using ground penetrating radar (GPR).* The Progress in Electromagnetics Research Symposium.

Kawasaki, Y., Tomoda, Y., & Ohtsu, M. (2010). AE monitoring of corrosion process in cyclic wet–dry test. *Construction and Building Materials, 24*(12), 2353-2357.

Kawasaki, Y., Wakuda, T., Kobarai, T., & Ohtsu, M. (2013). Corrosion mechanisms in reinforced concrete by acoustic emission. *Construction and Building Materials, 48*(0), 1240-1247.

Kim, W. (2003). *Ground penetrating radar application for non-destructive testing: Bridge deck inspection and dowel bar detection.* (Ph.D Thesis), University of Missouri - Rolla, United States, Missouri.

Klysz, G., Balayssac, J. P., & Laurens, S. (2004). Spectral analysis of radar surface waves for non-destructive evaluation of cover concrete. *NDT & E International, 37*(3), 221-227.

Kobayashi, K., & Banthia, N. (2010). *Detection of reinforcement corrosion with a new non-destructive test method using induction heating.* 6th International Conference on Concrete under Severe Conditions (CONSEC'10).

Kobayashi, K., & Banthia, N. (2011). Corrosion detection in reinforced concrete using induction heating and infrared thermography. *Journal of Civil Structural Health Monitoring, 1*(1-2), 25-35.

Koleva, D. A., De Wit, J. H. W., Van Breugel, K., Lodhi, Z. F., & Van Westing, E. (2007). Investigation of corrosion and cathodic protection in reinforced concrete: I. Application of electrochemical techniques. *Journal of the Electrochemical Society, 154*(4), P52-P61.

Komlos, K., Popovics, S., NÃrnbergerovÃ, T., BabÃl, B., & Popovics, J. S. (1996). Ultrasonic pulse velocity test of concrete properties as specified in various standards. *Cement and Concrete Composites, 18*(5), 357-364.

Kordatos, E. Z., Strantza, M., Soulioti, D. V., Matikas, T. E., & Aggelis, D. G. (2011). *Combined NDT methods for characterization of subsurface cracks in concrete.* SPIE - The International Society for Optical Engineering.

Kouroussis DA, & AA., A. (2001). Advances in classification of acoustic emission sources. *Les Journées COFREND, Reims*.

Kwon, S. J., Xue, H., Feng, M. Q., & Baek, S. (2011). *Nondestructive corrosion detection in concrete through integrated heat induction and IR thermography.* SPIE - The International Society for Optical Engineering.

Lai, W. L., Kind, T., & Wiggenhauser, H. (2011a). *Detection of accelerated reinforcement corrosion in concrete by ground penetrating radar.* 13th International Conference on Ground Penetrating Radar (GPR).

Lai, W. L., Kind, T., & Wiggenhauser, H. (2011b). Frequency-dependent dispersion of high-frequency ground penetrating radar wave in concrete. *NDT & E International, 44*(3), 267-273.

Lai, W. L., Kou, S. C., Tsang, W. F., & Poon, C. S. (2009). Characterization of concrete properties from dielectric properties using ground penetrating radar. *Cement and Concrete Research 39*(8), 687-695.

Lapitz, P., Ruzzante, J., & Alvarez, M. G. (2007). AE response of α-brass during stress corrosion crack propagation. *Corrosion Science 49*(10), 3812-3825.

Lau, K. T. (2003). Fibre-optic sensors and smart composites for concrete applications. *Magazine of Concrete Research, 55*(1), 19-34.

Law, D. W., Millard, S. G., & Bungey, J. H. (2001). Use of galvanostatic pulse measurements on active reinforcing steel in concrete to assess corrosion rates. *British Corrosion Journal, 36*(1), 75-80.

Lee, C., Bonacci, J. F., Thomas, M. D. A., Maalej, M., Khajehpour, S., Hearn, N., Sheikh, S. (2000). Accelerated corrosion and repair of reinforced concrete columns using carbon fibre reinforced polymer sheets. *Canadian Journal of Civil Engineering, 27*(5), 941-948.

Lee, H.-S., Noguchi, T., & Tomosawa, F. (2002). Evaluation of the bond properties between concrete and reinforcement as a function of the degree of reinforcement corrosion. *Cement and Concrete Research, 32*(8), 1313-1318.

Lee, J. R., Yun, C. Y., & Yoon, D. J. (2010). A structural corrosion-monitoring sensor based on a pair of prestrained fiber Bragg gratings. *Measurement Science and Technology, 21*(1).

Leelalerkiet, V., Shimizu, T., Tomoda, Y., & Ohtsu, M. (2005). Estimation of corrosion in reinforced concrete by electrochemical techniques and acoustic emission. *Journal of Advanced Concrete Technology, 3*(1), 137-147.

Legat, A. (2007). Monitoring of steel corrosion in concrete by electrode arrays and electrical resistance probes. *Electrochimica Acta 52*(27), 7590-7598.

Legat, A., & Govekar, E. (1994). Detection of corrosion by analysis of electrochemical noise. *Fractals, 02*(02), 241-244.

Legat, A., Leban, M., & Bajt, Ž. (2004). Corrosion processes of steel in concrete characterized by means of electrochemical noise. *Electrochimica Acta, 49*(17–18), 2741-2751.

Lei, Y., & Zheng, Z.-P. (2013). Review of physical based monitoring techniques for condition assessment of corrosion in reinforced concrete. *Mathematical Problems in Engineering, 2013*, 14.

Li, D., Zhang, S., Yang, W., & Zhang, W. (2014). Corrosion monitoring and evaluation of reinforced concrete structures utilizing the ultrasonic guided wave technique. *International Journal of Distributed Sensor Networks*.

Liang, M. T., & Su, P. J. (2001). Detection of the corrosion damage of rebar in concrete using impact-echo method. *Cement and Concrete Research, 31*(10), 1427-1436.

Liang, M. T., Wang, K. L., & Liang, C. H. (1999). Service life prediction of reinforced concrete structures. *Cement and Concrete Research, 29*(9), 1411-1418.

Lu, C., & Peiyu, Y. (2000). An algorithm of galvanostatic pulse method to determine the corrosion status of reinforcement in concrete. *Corrosion Science, 42*(4), 675-686.

Luo X, Haya H, Inaba T, Shiotani T, & Y., N. (2002). *Experimental study on evaluation of breakage in foundations using train-induced acoustic emission.* Structural Engineering World Congress.

MacGregor, J., & Ghoneim, M. (1995). Design for Torsion. *Structural Journal, 92*(2), 211-218.

Maierhofer, C. (2003). Nondestructive Evaluation of Concrete Infrastructure with Ground Penetrating Radar. *Journal of Materials in Civil Engineering, 15*(3), 287-297.

Malhotra, V. M., Carino, N.J. (1991). *CRC handbook on nondestructive testing of concrete*: CRC Press.

Mangat, P., & Elgarf, M. (1999). Bond characteristics of corroding reinforcement in concrete beams. *Materials and Structures, 32*(2), 89-97.

Mangual, J., ElBatanouny, M. K., Velez, W., Ziehl, P., Matta, F., & Gonzalez, M. (2012, 12-15 March). *Characterization of corrosion damage in prestressed concrete using acoustic emission.* Sensors and Smart Structures Technologies for Civil, Mechanical, and Aerospace Systems 2012, Pts 1 and 2, San Diego, CA.

Mangual, J., ElBatanouny, M. K., Ziehl, P., & Matta, F. (2013). Acoustic emission-based characterization of corrosion damage in cracked concrete with prestressing strand. *ACI Materials Journal, 110*(1), 89-98.

Manning, D. G., & Holt, F. B. (1980). Detecting delamination in concrete bridge decks. *Concrete International, 2*(11), 34-41.

Mansfeld, F., Sun, Z., & Hsu, C. H. (2001). Electrochemical noise analysis (ENA) for active and passive systems in chloride media. *Electrochimica Acta 46*(24-25), 3651-3664.

Mansfeld, F., & Xiao, H. (1993). Electrochemical noise analysis of iron exposed to NaCl solutions of different corrosivity. *Journal of The Electrochemical Society, 140*(8), 2205-2209.

Mariaca, L., Bautista, A., Rodríguez, P., & González, J. A. (1997). Use of electrochemical noise for studying the rate of corrosion of reinforcements embedded in concrete. *Materials and Structures, 30*(10), 613-617.

Maslehuddin, M., Al-Zahrani, M. M., Al-Dulaijan, S. U., Abdulquddus, Rehman, S., & Ahsan, S. N. (2002). Effect of steel manufacturing process and atmospheric corrosion on the corrosion-resistance of steel bars in concrete. *Cement and Concrete Composites, 24*(1), 151-158.

Melchers, R. E., & Li, C. Q. (2006). Phenomenological modeling of reinforcement corrosion in marine environments. *ACI Materials Journal 103*(1), 25-32.

Miller, R. K., & Mc Intire, P. (1987). *Acoustic emission testing* (Vol. 5).

Miller, T. H., Yanagita, T., Kundua, T., Grill, J., & Grill, W. (2009). *Nondestructive inspection of reinforced concrete structures.* SPIE - The International Society for Optical Engineering.

Mills, D., Mabbutt, S., & Bierwagen, G. (2003). Investigation into mechanism of protection of pigmented alkyd coatings using electrochemical and other methods. *Progress in Organic Coatings, 46*(3), 176-181.

Nagiub, A., & Mansfeld, F. (2001). Evaluation of corrosion inhibition of brass in chloride media using EIS and ENA. *Corrosion Science, 43*(11), 2147-2171.

Neville, A. (1995). Chloride attack of reinforced concrete: an overview. *Materials and Structures, 28*(2), 63-70.

Neville, M. (1996). *Properties of Concrete* (Fourth and Final Edition ed.): Addison Wesley Longman Limited.

Newton, C. J., & Sykes, J. M. (1988). A galvanostatic pulse technique for investigation of steel corrosion in concrete. *Corrosion Science, 28*(11), 1051-1074.

Nounu, G., & Chaudhary, Z.-U. L. H. (1999). Reinforced concrete repairs in beams. *Construction and Building Materials, 13*(4), 195-212.

Ohno, K., & Ohtsu, M. (2010). Crack classification in concrete based on acoustic emission. *Construction and Building Materials, 24*(12), 2339-2346.

Ohtsu, M. (1987). Mathematical theory of acustic emission and moment tensor solution. *Zairyo/Journal of the Society of Materials Science, 36*(408), 7.

Ohtsu, M. (1996). The history and development of acoustic emission in concrete engineering. *Magazine of Concrete Research, 48*(4), 321-330.

Ohtsu, M. (2010). Recommendation of RILEM TC 212-ACD: acoustic emission and related NDE techniques for crack detection and damage evaluation in concrete. *Materials and Structures, 43*(9), 1187-1189.

Ohtsu, M., Okamoto, T., & Yuyama, S. (1998). Moment Tensor Analysis of Acoustic Emission for Cracking Mechanisms in Concrete. *Structural Journal, 95*(2).

Ohtsu, M., & Tomoda, Y. (2007a). *Acoustic emission techniques for rebar corrosion in reinforced concrete.* Advances in Construction Materials.

Ohtsu, M., & Tomoda, Y. (2007b). Corrosion process in reinforced concrete Identified by acoustic emission. *Materials Transactions, 48*(6), 1184-1189.

Ohtsu, M., & Tomoda, Y. (2008a). Phenomenological model of corrosion process in reinforced concrete identified by acoustic emission. *ACI Materials Journal 105*(2), 194-199.

Ohtsu, M., & Tomoda, Y. (2008b). Phenomenological model of corrosion process in reinforced concrete identified by acoustic emission. *ACI Materials Journal, 105*(2), 194-199.

Ohtsu, M., Tomoda, Y., & Suzuki, T. (2007). *Damage evaluation and corrosion detection in concrete by acoustic emission.* Proceedings of the 6th International Conference on Fracture Mechanics of Concrete and Concrete Structures.

Ohtsu, M., & Uddin, F. A. K. M. (2008). Mechanisms of Corrosion-induced Cracks in Concrete at Meso- and Macro-Scales. *Journal of Advanced Concrete Technology, 6*(3), 419-429.

Ohtsu, M., & Yuyama, S. (2000). *Recommended practice for in-situ monitoring of concrete structures by acoustic emission*. 15th International Acoustic Emission Symposium.

Ohtsu., M., & Yamamoto, T. (1997). Compensation procedure for half-cell potential measurement. *Construction and Building Materials, 11*(7-8), 395-402.

Ono, K. (2010). Application of acoustic emission for structure diagnosis. *Konferencja Naukowa*, 317-341.

Page, C. L., & Treadaway, K. W. J. (1982). Aspects of the electrochemistry of steel in concrete. *Nature, 297*(5862), 109-111.

Parameswaran, L., Kumar, R., & Sahu, G. K. (2008). Effect of carbonation on concrete bridge service life. *Journal of Bridge Engineering, 13*(1), 75-82.

Patil, S., Karkare, B., & Goyal, S. (2014). Acoustic emission vis-Ã-vis electrochemical techniques for corrosion monitoring of reinforced concrete element. *Construction and Building Materials, 68*(0), 326-332.

Pieper, D., Donnell, K. M., Ghasr, M. T., & Kinzel, E. C. (2014). *Integration of microwave and thermographic NDT methods for corrosion detection.* AIP Conference.

Polder, R., Andrade, C., Elsener, B., Vennesland, O., Gulikers, J., Weidert, R., & Raupach, M. (2000). Test methods for on site measurement of resistivity of concrete. *Materials and Structures 33*(234), 603-611.

Polder, R. B. (2001). Test methods for on site measurement of resistivity of concrete - A RILEM TC-154 technical recommendation. *Construction and Building Materials, 15*(2-3), 125-131.

Poonguzhali, A., Shaikh, H., Dayal, R. K., & Khatak, H. S. (2008). A review on degradation mechanism and life estimation of civil structures. *Corrosion Reviews, 26*(4), 215-294.

Poursaee, A., & Hansson, C. M. (2008). Galvanostatic pulse technique with the current confinement guard ring: The laboratory and finite element analysis. *Corrosion Science, 50*(10), 2739-2746.

Raad, J., Aktan, H., & Usmen, M. (1997). *Laboratory for non destructive evaluation of civil structures.* ASEE Annual Conference.

Rao, M. V. M. S., & Prasanna Lakshmi, K. J. (2005). Analysis of b-value and improved b-value of acoustic emissions accompanying rock fracture. *Current Science, 89*(9), 1577-1582.

Rasheeduzzafar, Al-Saadoun, S. S., & Al-Gahtani, A. S. (1992). Corrosion cracking in relation to bar diameter, cover, and concrete quality. *Journal of Materials in Civil Engineering, 4*(4), 327-342.

Reichling, K., Raupach, M., Broomfield, J., Gulikers, J., L'Hostis, V., Kessler, S., TachÃ, G. (2013a). Full surface inspection methods regarding reinforcement corrosion of concrete structures. *Materials and Corrosion, 64*(2), 116-127.

Reichling, K., Raupach, M., Broomfield, J., Gulikers, J., Nygaard, P. V., Schneck, U., & Sergi, G. (2013b). Local detailed inspection methods regarding reinforcement corrosion of concrete structures. *Materials and Corrosion, 64*(2), 128-134.

Rhazi, J., Dous, O., & Laurens, S. (2007). *A new application of the GPR technique to reinforced concrete bridge decks*. 4th Middle East NDT conference and Exhibition, Kingdom of Bahrain.

Ridge, A. R., & Ziehl, P. H. (2006). Evaluation of strengthened reinforced concrete beams: cyclic load test and acoustic emission methods. *ACI Structural Journal, 103*(6), 832.

Robert, A. (1998). Dielectric permittivity of concrete between 50 Mhz and 1 Ghz and GPR measurements for building materials evaluation. *Journal of Applied Geophysics, 40*(1-3), 89-94.

Rodriguez, P., Ramirez, E., & Gonzalez, J. A. (1994). Methods for studying corrosion in reinforced concrete. *Magazine of Concrete Research, 46*(167), 81-90.

Sadowski, L. (2010). New non-destructive method for linear polarisation resistance corrosion rate measurement. *Archives of Civil and Mechanical Engineering, 10*(2), 109-116.

Sadowski, L. (2013). Methodology for assessing the probability of corrosion in concrete structures on the basis of half-cell potential and concrete resistivity measurements. *The Scientific World Journal*.

Saetta, A. V., Schrefler, B. A., & Vitaliani, R. V. (1993). The carbonation of concrete and the mechanism of moisture, heat and carbon dioxide flow through porous materials. *Cement and Concrete Research, 23*(4), 761-772.

Sakr, K. (2005). Effect of cement type on the corrosion of reinforcing steel bars exposed to acidic media using electrochemical techniques. *Cement and Concrete Research, 35*(9), 1820-1826.

Samarkova, K., Chobola, Z., & Stefkova, D. (2014a). The corrosion status of reinforced concrete structure monitoring by impact echo method. *Advanced Materials Research, 875-877*, 445-449.

Samarkova, K., Chobola, Z., & StefkovÃ, D. (2014b). Using of impact-echo methods to assessment of reinforced concrete structures corrosion. *Applied Mechanics and Materials, 446-447*, 1400-1404.

Samarkova, K., Chobola, Z., Stefkova, D., & Kusak, I. (2014c). Impact-echo methods to assessment corrosion of reinforced concrete structures. *Applied Mechanics and Materials, 627*, 268-271.

Samarkova, K., Stefkova, D., & Chobola, Z. (2014d). Monitoring of reinforced concrete structure corrosion by using impact-echo method. *Advanced Materials Research*, *1000*, 239-242.

Sansalone, M. J., & Streett, W. B. (1997). *Impact echo nondestructive evaluation of concrete & masonry*. Ithaca, NY: Bullbrier Press.

Saricimen, H., Ashiru, O. A., Jarrah, N. R., Quddus, A., & Shameem, M. (1998). Effect of Inhibitors and Coatings on Rebar Corrosion. *Materials Performance, 37*(5), 32-38.

Sathiyanarayanan, S., Natarajan, P., Saravanan, K., Srinivasan, S., & Venkatachari, G. (2006). Corrosion monitoring of steel in concrete by galvanostatic pulse technique. *Cement and Concrete Composites, 28*(7), 630-637.

Sbartai, Z. M., Laurens, S., Balayssac, J. P., Arliguie, G., & Ballivy, G. (2006a). Ability of the direct wave of radar ground-coupled antenna for NDT of concrete structures. *NDT and E International, 39*(5), 400-407.

Sbartai, Z. M., Laurens, S., Balayssac, J. P., Ballivy, G., & Arliguie, G. (2006b). Effect of concrete moisture on radar signal amplitude. *ACI Materials Journal, 103*(6), 419-426.

Sbartai, Z. M., Laurens, S., Rhazi, J., Balayssac, J. P., & Arliguie, G. (2007). Using radar direct wave for concrete condition assessment: Correlation with electrical resistivity. *Journal of Applied Geophysics, 62*(4), 361-374.

Sharma, S., & Mukherjee, A. (2010). Longitudinal guided waves for monitoring chloride corrosion in reinforcing bars in concrete. *Structural Health Monitoring, 9*(6), 555-567.

Sharma, S., & Mukherjee, A. (2011). Monitoring corrosion in oxide and chloride environments using ultrasonic guided waves. *Journal of Materials in Civil Engineering, 23*(2), 207-211.

Sharma, S., & Mukherjee, A. (2013). Nondestructive evaluation of corrosion in varying environments using guided waves. *Research in Nondestructive Evaluation, 24*(2), 63-88.

Shi, J. J., Sun, W., & Geng, G. Q. (2011). Steel corrosion in simulated concrete pore solutions using a galvanostatic pulse method. *Beijing Keji Daxue Xuebao/Journal of University of Science and Technology Beijing, 33*(6), 727-733.

Shigeishi, M., & Ohtsu, M. (2001). Acoustic emission moment tensor analysis: Development for crack identification in concrete materials. *Construction and Building Materials, 15*(5-6), 311-319.

Shiotani, T. (2006). Evaluation of long-term stability for rock slope by means of acoustic emission technique. *NDT & E International, 39*(3), 217-228.

Shiotani, T., & Ohtsu, M. (1999). Prediction of slope failure based on AE activity. *ASTM Special Technical Publication*, 156-172.

Shiotani, T., Ohtsu, M., & Ikeda, K. (2001). Detection and evaluation of AE waves due to rock deformation. *Construction and Building Materials, 15*(5-6), 235-246.

Sohn, H., Park, G., Wait, J. R., Limback, N. P., & Farrar, C. R. (2004). Wavelet-based active sensing for delamination detection in composite structures. *Smart Materials and Structures, 13*(1), 153-160.

Song, H. W., & Saraswathy, V. (2007). Corrosion monitoring of reinforced concrete structures - A review. *International Journal of Electrochemical Science, 2*(1), 1-28.

Song., G., & Shayan, A. (1998). *Corrosion of steel in concrete: causes, detection and prediction*.

Soutsos, M. N., Bungey, J. H., Millard, S. G., Shaw, M. R., & Patterson, A. (2001). Dielectric properties of concrete and their influence on radar testing. *NDT & E International, 34*(6), 419-425.

Swarup, J., & Sharma, P. C. (1996). Electrochemical techniques for the monitoring of corrosion of reinforcement in concrete structures. *Bulletin of Electrochemistry, 12*(1-2), 103-108.

Tachibana, Y., Kajikawa, Y., & Kawamura, M. (1989). Behaviour of RC beams damaged by corrosion of reinforcement. *Doboku Gakkai Rombun-Hokokushu/Proceedings of the Japan Society of Civil Engineers* (402 pt 5-10), 105-114.

Titus, T. N. K., Reddy, D. V., Dunn, S. E., & Hartt, W. H. (1988, 13-17 September). *Acoustic emission crack monitoring and prediction of remaining life of corroding reinforced concrete beams.* 4th European Conference Non-destructive Testing, London, UK.

Tuutti, K. (1979). Service Life of Structures with Regard to Corrosion of Embedded Steel. *Metal Construction, 1*, 293-301.

Uomoto, T., Tsuji, K., & Kakizawa, T. (1985). Deterioration Mechanism of Concrete Structures caused by Corrosion of Reinforcing Bars. *Trans of the Jpn Concr Inst, 6*, 163-170.

Vallee, R., Fredrick, S., Asatryan, K., Fischer, M., & Galstian, T. (2004). Real-time observation of Bragg grating formation in As2S 3 chalcogenide ridge waveguides. *Optics Communications, 230*(4-6), 301-307.

Vedalakshmi, R., Balamurugan, L., Saraswathy, V., Kim, S. H., & Ann, K. Y. (2010). Reliability of galvanostatic pulse technique in assessing the corrosion rate of rebar in concrete structures: Laboratory vs field studies. *KSCE Journal of Civil Engineering, 14*(6), 867-877.

Vedalakshmi, R., & Thangavel, K. (2011). Reliability of electrochemical techniques to predict the corrosion rate of steel in concrete structures. *Arabian Journal for Science and Engineering, 36*(5), 769-783.

Velez, W., Matta, F., & Ziehl, P. (2013). *Acoustic emission characterization of early corrosion in prestressed concrete exposed to salt water.* The 11th International Conference on Structural Safety and Reliability (ICOSSAR) 2013.

Velez, W., Matta, F., & Ziehl, P. (2014). *Acoustic emission intensity analysis of corrosion in prestressed concrete piles.* AIP Conference Proceedings.

Washer, G. (2012). Advances in the use of thermographic imaging for the condition assessment of bridges. *Bridge Structures - Assessment, Design & Construction, 8*(2), 81-90.

Washer, G., Bolleni, N., & Fenwick, R. (2010). Thermographic imaging of subsurface deterioration in concrete bridges. *Transportation Research Record*, 27-33.

Wells, D. (1970). An acoustic apparatus to record emissions from concrete under strain. *Nuclear Engineering and Design, 12*(1).

Weszka, J. S., Dyer, C. R., & Rosenfeld, A. (1976). A Comparative Study of Texture Measures for Terrain Classification. *IEEE Transactions on Systems, Man, and Cybernetics, SMC-6*(4), 269-285.

Wiggenhauser, H., & Reinhardt, H. W. (2010). *NDT in civil engineering: Experience and results of the for 384 research group.* AIP Conference.

Wojtas, H. (2004). Determination of corrosion rate of reinforcement with a modulated guard ring electrode: Analysis of errors due to lateral current distribution. *Corrosion Science, 46*(7), 1621-1632.

Xiao, H., & Mansfeld, F. (1994). Evaluation of coating degradation with electrochemical impedance spectroscopy and electrochemical noise analysis. *Journal of The Electrochemical Society, 141*(9), 2332-2337.

Xu, J., & Yao, W. (2010). Corrosion detection of steel in concrete by use of galvanostatic pulse technique. *Journal of the Chinese Society of Corrosion and Protection, 30*(3), 181-186.

Yeih, W., & Huang, R. (1998). Detection of the corrosion damage in reinforced concrete members by ultrasonic testing. *Cement and Concrete Research, 28*(7), 1071-1083.

Yingshu, Y., Yongsheng, J., & Surendra, P. S. (2007). Comparison of Two Accelerated Corrosion Techniques for Concrete Structures. *ACI Structural Journal, 104*(3), 344-347.

Yoon, D. J., Weiss, W. J., & Shah, S. P. (2000). Assessing damage in corroded reinforced concrete using acoustic emission. *Journal of Engineering Mechanics, 126*(3), 273-283.

Yu, A., Zhao, Y., & Wang, L. (2014). Acoustic emission(AE) online monitoring test on corrosion in reinforced concrete. *Jianzhu Cailiao Xuebao/Journal of Building Materials, 17*(2), 291-297.

Yu, J. G., Luo, J. L., & Norton, P. R. (2002). Investigation of hydrogen induced pitting active sites. *Electrochimica Acta, 47*(25), 4019-4025.

Yu, L., François, R., Dang, V. H., L'Hostis, V., & Gagné, R. (2015). Structural performance of RC beams damaged by natural corrosion under sustained loading in a chloride environment. *Engineering Structures, 96*, 30-40.

Yuan, Y., & Ji, Y. (2009). Modeling corroded section configuration of steel bar in concrete structure. *Construction and Building Materials, 23*(6), 2461-2466.

Yuan, Y., Zhang, X., & Ji, Y. (2006). Comparative study on structural behavior of deteriorated reinforced concrete beam under two different environments. *Tumu Gongcheng Xuebao/China Civil Engineering Journal, 39*(3), 42-46.

Yun, H.-D., Choi, W.-C., & Seo, S.-Y. (2010). Acoustic emission activities and damage evaluation of reinforced concrete beams strengthened with CFRP sheets. *NDT & E International, 43*(7), 615-628.

Yuyama, S., Yokoyama, K., Niitani, K., Ohtsu, M., & Uomoto, T. (2007). Detection and evaluation of failures in high-strength tendon of prestressed concrete bridges by acoustic emission. *Construction and Building Materials, 21*(3), 491-500.

Zhang, W., Wang, X., Gu, X., & Shang, D. (2006). Comparative study on structural performance of reinforced concrete beams subjected to natural corrosion and accelerated corrosion. *Dongnan Daxue Xuebao (Ziran Kexue Ban)/Journal of Southeast University (Natural Science Edition), 36*(SUPPL. 2), 139-144.

Zhao, B., Li, J.-H., Hu, R.-G., Du, R.-G., & Lin, C.-J. (2007). Study on the corrosion behavior of reinforcing steel in cement mortar by electrochemical noise measurements. *Electrochimica Acta, 52*(12), 3976-3984.

Zheng, Z., Sun, X., & Lei, Y. (2009). Monitoring corrosion of reinforcement in concrete structures via fiber Bragg grating sensors. *Frontiers of Mechanical Engineering in China, 4*(3), 316-319.

LIST OF PUBLICATIONS AND PAPER PRESENTED

Published:

Zaki A., Chai H.K., Aggelis D.A. (2015), Alver N. *Non-Destructive Evaluation for Corrosion Monitoring in Concrete: A Review and Capability of Acoustic Emission Technique*. Sensors, 15(8), 19069-1910. (ISI/SCOPUS Cited Publication).

Zaki A., Chai H.K., Behnia, A., Aggelis, D.G., Tan, J.Y, Ibrahim, Z. (2017), *Monitoring Fracture of Steel Corroded Reinforced Concrete Members under Flexure by Acoustic Emission Technique*. Construction and Building Materials, Vol. 136, 609-618. *(*ISI/SCOPUS Cited Publication).

Under preparation:

Zaki A., Ibrahim, Z., Chai H.K., Aggelis, D.A. *Reliability of Primary and Secondary AE for Corrosion Evaluation of Concrete Structures.*

Proceedings:

Zaki A., Tan, J.Y., Chai H.K., Aggelis D.A. *Assessment of Corrosion Damage using Acoustic Emission Technique under Load Testing*. The 7th Asia Pacific Young Researchers and Graduates Symposium, University of Malaya, Kuala Lumpur, Malaysia; 08/2015 (Non-ISI/SCOPUS Cited Publication).